



**HAL**  
open science

# Development of polypeptide-based multifunctional nano-assemblies for a theranostic approach

Vusala Ibrahimova

► **To cite this version:**

Vusala Ibrahimova. Development of polypeptide-based multifunctional nano-assemblies for a theranostic approach. Organic chemistry. Université de Bordeaux; Université catholique de Louvain (1970-..), 2016. English. NNT: 2016BORD0115 . tel-01370743

**HAL Id: tel-01370743**

**<https://theses.hal.science/tel-01370743>**

Submitted on 23 Sep 2016

**HAL** is a multi-disciplinary open access archive for the deposit and dissemination of scientific research documents, whether they are published or not. The documents may come from teaching and research institutions in France or abroad, or from public or private research centers.

L'archive ouverte pluridisciplinaire **HAL**, est destinée au dépôt et à la diffusion de documents scientifiques de niveau recherche, publiés ou non, émanant des établissements d'enseignement et de recherche français ou étrangers, des laboratoires publics ou privés.

THÈSE EN COTUTELLE PRÉSENTÉE  
POUR OBTENIR LE GRADE DE

**DOCTEUR EN SCIENCES DE  
L'UNIVERSITÉ CATHOLIQUE DE LOUVAIN**

**ET**

**DE L'UNIVERSITÉ DE BORDEAUX**

FACULTÉ DES SCIENCES ÉCOLE DOCTORALE EN SCIENCES (Université  
catholique de Louvain)

ÉCOLE DOCTORALE DES SCIENCES CHIMIQUES (Université de Bordeaux)

SPECIALITE ORGANIQUE ET CHIMIE DES POLYMERES

Par Vusala IBRAHIMOVA

---

**Development of Polypeptide-Based Multifunctional Nano-  
Assemblies for a Theranostic Approach**

---

Sous la direction de Prof. Charles-André FUSTIN et Prof. Sébastien  
LECOMMANDOUX

Soutenue le 31 août 2016

**Membres du jury :**

M. FUSTIN, Charles André	Professeur, Université catholique de Louvain	Examineur
M. GOHY, Jean-François	Professeur, Université catholique de Louvain	Examineur
Mme. JEROME, Christine	Professeur, Université de Liège	Rapporteur
M. LAFARQUE, David	Docteur, SERVIER	Examineur
M. LECOMMANDOUX, Sébastien	Professeur, Bordeaux INP	Examineur
M. NICOLAS, Julien	DR CNRS, Université de Paris Sud	Rapporteur
Mme. RAVAINÉ, Valérie	Professeur, Université de Bordeaux	Président
M. ELIAS, Benjamin	Professeur, Université catholique de Louvain	Invité
M. McCLENAGHAN, Nathan	DR CNRS, Université de Bordeaux	Invité

# Development of Polypeptide- Based Multifunctional Nano- Assemblies for a Theranostic Approach

VUSALA İBRAHIMOVA

Août 2016

Thèse présentée en vue de l'obtention  
du grade de docteur en sciences

Faculté des sciences

Université catholique de Louvain

## PREAMBLE

This PhD had been performed within the framework of the International Doctoral School in Functional Materials (IDS FunMat) joint doctoral program. IDS-FunMat program is funded by ERASMUS MUNDUS Program of the European Union. IDS FunMat PhD School offers PhD projects in Functional Material Science which have to be carried out in co-supervision between universities from different EU countries. In most PhD projects, an industrial partner is also involved. PhD candidates in this framework must spend at least 6 months in each Partner University. In total, PhD candidates have to spend at least 1.5 year in each of the university.

In this PhD project, two partner universities Université catholique de Louvain (IMCN, Belgium) and Université de Bordeaux (LCPO, France) and an industrial partner SERVIER company (David Lafarque, France) were collaborating.



*To my beloved parents*

## ACKNOWLEDGEMENT

I am deeply grateful to my both supervisors Prof. Charles-André Fustin and Prof. Sébastien Lecommandoux for their advices, endless help, and for encouraging my research during my PhD.

I would like to express my sincere thanks to my doctoral committee members Prof. Jean-François Gohy, Prof. Benjamin Elias, Prof. Christine Jérôme, Prof. Valérie Ravaine, Dr. Julien Nicolas and Dr. David Lafargue for agreeing to be in my thesis committee and evaluate my work.

I wish to acknowledge FSR (UCL) and F.R.S.-FNRS (FRIA) for financial support to my research project.

I would also like to express my gratitude to our collaborator Dr. Nathan D. McClenaghan from Institut des Sciences Moléculaires (UBx, ISM) and his group members Dr. Peter Verwilst for his valuable advices about the synthesis of aza-BODIPY dyes and Dr. Sergey Denisov for his help on photophysical characterization of my products, successions and friendship. I wish to express my sincere thanks to Prof. Véronique Prétat and Kevin Vanvarenberg for in vitro cellular investigations at Louvain Drug Research Institute (UCL). I would also thanks to Dr. Henri-François Renard from Institute of life sciences (UCL, ISV) to be very kind to provide us with HeLa cells.

I am also grateful to the entire MACRO group members especially Dr. Jérémy Brassinne, Dr. Nisar Ahmed, Roland Duchêne, Elio Poggi and Bruno Ernould for the sharing of their knowledge, kind friendship, encouragements and helps.

Heartiest thanks to all LCPO members for being such a friendly and joyful family and my colleagues Dr. Silvia Mazzaferro and Dr. Colin Bonduelle for their advices on polypeptide synthesis and also Julie, Edgar, Tuyen, An and Mathilde for all the good moments that I had with them in Bordeaux. I would like to also warmly thank to my friends Ozlem, Deniz and Mamatimin Abbas for being a family to me in France.

I must acknowledge the members of IDS-FunMat international doctoral school, Prof. Jean Etourneau, Prof. Laurent Servant, Audrey Sidobre, Christopher Niesen and Marianne Delmas, for giving me this great opportunity to gain international work experience in two countries and meet wonderful people from all around the world each year at training schools during my PhD.

Finally, I would like to express my sincere appreciation to my mam Kamila Mammadova and my dad Muslum Ibrahimov as well as my beloved sisters Celale, Saida and Mirana for their endless love, patience and support throughout my bitter- sweet journey. I am very grateful to my grandfather Asad Mammadov, who was a great teacher of chemistry, for passing me his “chemistry lover” genes.

## ABSTRACT

**In this work**, we developed photosensitizer (PTS) functionalized polypeptide-based theranostic nano-assemblies to be used in photodynamic therapy (PDT). The singlet oxygen generation and fluorescence properties of the PTS provide simultaneous diagnosis and therapy of the tumor.

An asymmetric and multifunctional derivative of the aza-dipyrromethene boron difluoride chelate (aza-BODIPY) fluorophore was synthesized to be used as a photosensitizer due to its nontoxic properties, insensitivity to external biological environment, high singlet oxygen generation and fluorescent quantum yield. To carry the photosensitizer to the tumor, four different (in terms of PTS localization and PEG chain length) amphiphilic block copolymers consisting of poly( $\gamma$ -benzyl-L-glutamate) (PBLG, DP~50) and poly(ethylene glycol) (PEG, DP=45 and 113) chains, able to self-assembled into micelles and vesicles, were synthesized. We developed a synthetic strategy allowing covalent linkage of PTS to the amphiphilic block copolymers, thus preventing PTS leakage before the nano-assembly reaches the tumor site. Moreover, we investigated PTS activity as a function of concentration, morphology of the nano-assemblies and PTS localization in the nano-assemblies. Finally, the efficacy of the nano-assemblies has been evaluated *in vitro* on HeLa and B16F1 cells.

**Keywords:** Polymer nanoparticles, polypeptides, amphiphilic block copolymer self-assembly, photosensitizers, aza-BODIPY, photodynamic therapy

Laboratoire de Chimie des Polymères  
Organiques (LCPO)  
16 avenue Pey Berland  
F-33607 Pessac  
France



Institute of Condensed Matter and  
Nanosciences (IMCN)  
Bio and soft matter division (BSMA)  
Place Louis Pasteur 1  
1348 Louvain-la-Neuve  
Belgium



## Resume

# Development of Polypeptide-Based Multifunctional Nano-Assemblies for a Theranostic Approach

IBRAHIMOVA Vusala

Supervisors: Prof. Charles-André FUSTIN (UCL)

Prof. Sébastien LECOMMANDOUX (UBx)

### 1.1 Introduction

La thérapie photodynamique (PDT) est une méthode non invasive qui a émergé comme l'une des options thérapeutiques les plus prometteuses dans le traitement des cancers et d'autres maladies. L'attractivité de la PDT vient principalement de sa spécificité et sélectivité, car en théorie, seuls les tissus qui sont irradiés par la lumière à une longueur d'onde appropriée seront exposés à des espèces toxiques, limitant de ce fait fortement les effets secondaires.

Bien que la thérapie photodynamique ait commencé à être utilisée en clinique pour le traitement du cancer depuis 1999, après l'approbation du premier agent PDT Photofrin®, [1,2] le concept lui-même a été observé dès le développement de la médecine antique. Il y a de cela 5000 ans, en Egypte, en Grèce ainsi que dans la médecine indienne, la combinaison de la lumière et des agents chimiques était utilisée pour traiter certains troubles.[3,4] Aujourd'hui, cette méthode thérapeutique non-invasive est la plupart du temps préférée pour traiter sélectivement le cancer à un stade précoce. La PDT peut être définie comme l'injection d'un colorant, connu comme photosensibilisateur (PTS), à un patient porteur d'une lésion, tel un cancer. Après un temps d'incubation suffisant, cette lésion est illuminée de manière sélective avec une lumière de longueur d'onde appropriée (laser ou LED) qui, en présence d'oxygène, conduit à la génération d'espèces oxygénées réactives cytotoxiques (ROS), et donc à la mort et la destruction des cellules et tissus de l'environnement tumorale (Figure 1).

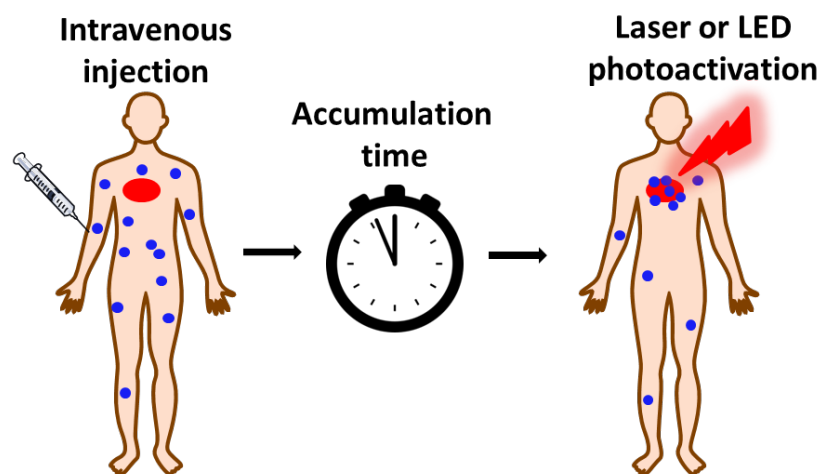


Figure 1: Illustration de la thérapie photodynamique (PDT). (Adapté de ref.3)



Comme les molécules de PTS sont intrinsèquement fluorescentes, cette fonctionnalité peut également être utilisée pour l'imagerie et de la localisation de pathologie, permettant ainsi une approche théranostic. Le terme théranostic signifie un nanodispositif multifonctionnel qui combine à la fois une modalité d'imagerie et une capacité thérapeutique [5]. Plus d'informations sur ce concept est prévu dans le chapitre 3.

Une grande variété de colorants fluorescents naturels et non-naturels sont en outre capables de générer des ROS sous activation de la lumière. Certains de ces photosensibilisants (porphyrines, chlorines, les phtalocyanines, les colorants BODIPY, etc.) [6,7] sont largement étudiés à des fins médicales et utilisées en thérapie photodynamique qui est discuté au chapitre 4. [8,9] La principale limitation dans la PDT est la complexité du tissus humain où seulement la lumière proche infrarouge (IR proche) peut pénétrer à travers et activer les PTS ciblées. Pour l'heure, le mode d'administration de l'agent photosensibilisant (PTS) n'est pas encore optimal et conduit à une accumulation non spécifique du PTS dans les tissus normaux, provoquant souvent une photosensibilisation générale du patient (en particulier la peau). Pour surmonter ce problème, l'utilisation de supports de distribution tels que des liposomes, des conjugués polymères, des nanoparticules polymères, ou des micelles de copolymères ont été proposée en raison des avantages précités des nanomedicines. Dans la grande majorité de ces cas, le PTS n'était pas lié de manière covalente à son porteur ce qui induit des problèmes de fuite. De plus, les faibles propriétés photophysiques (ie, faible longueur d'onde d'absorption, faible coefficient d'extinction, le rendement du ROS faible, le manque de contrôle sur la concentration PTS, etc.) des photosensibilisants cliniques existant nécessitent le développement de nouveaux systèmes pour augmenter l'efficacité du traitement et diminuer les effets secondaires.

## **1.2 Résumé du projet**

La thérapie photodynamique (PDT) est une méthode non invasive très prometteuse qui a émergé comme l'une des options thérapeutiques importantes dans la gestion du cancer et d'autres maladies. L'attractivité de la PDT provient principalement de sa spécificité fondamentale et de sa sélectivité, car en théorie seulement les tissus qui sont irradiés avec une lumière d'une longueur d'onde appropriée seront exposés à des espèces toxiques, limitant ainsi fortement les effets secondaires. Cependant, le mode d'administration du photosensibilisant (PTS) n'est pas encore optimale et conduit souvent à une accumulation non spécifique du PTS dans les tissus normaux, induisant une photosensibilité générale du patient (en particulier la peau). Pour surmonter ce problème, l'utilisation de supports de distribution tels que des liposomes, des conjugués polymères, des nanoparticules de polymères, ou des micelles de copolymères séquencés a été proposé. Dans la grande majorité de ces cas, le PTS n'était pas lié de manière covalente à son support, ce qui peut encore poser des problèmes de fuite. Par conséquent, dans ce projet, nous avons développé des systèmes de polypeptides à base de modèle (nanoparticules auto-assemblées) où le PTS est attaché de manière covalente aux blocs constituants les nano-particules. Ceci a pour but de résoudre les problèmes existants en PTD et de proposer de nouvelles pistes pour le développement de nouvelles thérapies PTD avec une toxicité minimale et une efficacité maximale.

Dans l'ensemble ce travail de thèse se compose de quatre étapes. Dans la première étape, les copolymères à blocs ont été synthétisés et caractérisés, dans la seconde partie les propriétés optiques et photo-physiques des produits et des nano-assemblages ont été étudiés, et en troisième partie, l'auto-assemblage de quatre polypeptides différents à base de copolymères à

blocs amphiphiles a été optimisé. Dans la dernière étape, nous avons effectué des tests *in vitro* sur deux lignées de cellules cancéreuses (HeLa et B16F1) pour étudier la toxicité dans l'obscurité des nanoparticules ainsi que leur localisation dans la cellule. En outre, au niveau cellulaire, l'efficacité de la PDT a été étudiée et une comparaison entre deux lignées cellulaires a été effectuée.

Dans la première partie du projet (chapitre 2) les différents blocs de construction: aza-BODIPY asymétrique, PBLG et PEG, ont été synthétisés et modifiés. En tant que photosensibilisateur, un aza-BODIPY portant les groupes fonctionnels appropriés pour l'incorporation dans les chaînes de copolymères (acide carboxylique et de l'azoture) a été synthétisée. Ces composés sont en effet connus pour être d'excellents photosensibilisants pour la génération d'oxygène singulet. De plus, ils possèdent des coefficients d'extinction molaires très élevés, sont photostables et ont des propriétés d'absorption et d'émission dans la gamme 650-750 nm. Deux blocs de poly( $\gamma$ -benzyl-L-glutamate) (PBLG, DP  $\sim$  50) ayant des extrémités de chaîne appropriées ont été synthétisés par polymérisation par ouverture de cycle N-carboxyanhydride (NCA) et couplés à l'aza-BODIPY par l'intermédiaire d'une réaction de couplage peptidique. Cette dernière a été optimisée pour obtenir une fonctionnalisation maximale. En outre, des PEGs ont été fonctionnalisés en bout de chaîne pour introduire les groupes réactifs nécessaires pour la cycloaddition azoture-alcyne catalysée au cuivre (I). Dans la dernière partie de la synthèse, des copolymères présentant deux types de structures ont été synthétisés par l'intermédiaire d'une stratégie de synthèse impliquant des réactions de couplages orthogonales. Ces systèmes sont les suivants : les copolymères portant le photosensibilisant à la fin du bloc de PBLG (PTS PBLG-*b*-PEG) et les copolymères portant le photosensibilisant à la jonction des PBLG et blocs PEG (PBLG-PTS-*b*-PEG). Des copolymères à base de polypeptides ont été utilisés dans ce projet, car ils sont particulièrement intéressants dans le cadre de la construction de micelles et de vésicules dans le but d'applications biologiques.

La deuxième étape du projet (chapitre 3) est axé sur l'auto-assemblage de copolymères PTS-PBLG-*b*-PEG / PBLG-PTS-*b*-PEG en solutions aqueuses en plusieurs nanostructures. Le bloc de PBLG est hydrophobe et forme ainsi le compartiment insoluble (cœur) de ces nanostructures. Le PEG est hydrophile et forme la couronne des nanostructures. En plus de la composition des copolymères (PEG de longueur différentes), des paramètres tels que la force ionique (auto-assemblage dans du PBS), la nature du solvant, la concentration, le débit, la vitesse d'agitation ... ont été modifiés pour obtenir des nanostructures bien définies et de taille contrôlée. Des tailles de quelques dizaines de nanomètres (20-200nm) ont été ciblées afin de bénéficier du ciblage passif des tumeurs grâce à l'effet EPR (perméabilité accrue et rétention lié au faible drainage lymphatique dans les tumeurs). Toutes les nanostructures ont été préparées par la technique de nano-précipitation en fixant le débit, la vitesse d'agitation et de la concentration. Cette technique nous a permis de contrôler facilement la formation des nano-assemblages. Après avoir optimisé le processus d'auto-assemblage de quatre copolymères fonctionnalisés contenant tous du PTS (PTS-PBLG<sub>49</sub>-*b*-PEG<sub>45</sub>, PTS-PBLG<sub>49</sub>-*b*-PEG<sub>45</sub>, PBLG<sub>53</sub>-PTS-*b*-PEG<sub>45</sub>, PBLG<sub>53</sub>-PTS-*b*-PEG<sub>113</sub>), ceux-ci ont été co-assemblés avec des copolymères non fonctionnalisés ayant la même composition (PBLG<sub>54</sub>-*b*-PEG<sub>45</sub>, PBLG<sub>54</sub>-*b*-PEG<sub>113</sub>) afin de diluer la concentration des PTS dans les nanostructures. En outre, la stabilité physico-chimique des nano-assemblages dans un environnement biologique simulé (sérum à 10% dans de l'eau Milli-Q) a été testée, et aucune formation d'agrégats n'a été observée. Les nano-assemblages obtenus ont été caractérisés par diffusion dynamique de lumière (DLS) et

par microscopie électronique à transmission (MET) après différents types de colorations ( $\text{RuO}_4$ ,  $\text{I}_2$  et au molybdate d'ammonium).

Le chapitre 4 est consacré à la caractérisation optique et photophysique (coefficient d'extinction molaire, rendement quantique de fluorescence, efficacité de la production d'oxygène singulet, vie de fluorescence ...) des conjugués PTS, PTS-PBLG et des nano-assemblages fonctionnalisés PTS. Ces caractérisations ont confirmé que le composé **24** bromé est adapté pour être utilisé pour de l'imagerie dans le proche infrarouge et comme photosensibilisateur (PTS) pour des applications biomédicales. L'Aza-BODIPYs bromé et non bromé présentait un coefficient d'extinction élevé respectivement de 71702 et de 83900  $\text{M}^{-1}\cdot\text{cm}^{-1}$  dans le THF. Bien que le rendement quantique de fluorescence soit passé de 0,36 à 0,08 après l'addition sur les positions 2,6 de deux groupements brome sur le noyau aza-BODIPY, le rendement de génération d'oxygène singulet a augmenté pour atteindre 0,66. Toutefois, les propriétés de fluorescence, même faibles, permettront la détection des signaux de fluorescence à partir des tissus ou de la peau et effectuer un traitement PDT sélectif. Nous avons observé des changements mineurs dans les propriétés optiques et photophysiques du PTS après conjugaison de celui-ci avec des chaînes de polymère. Cependant, dans l'eau, des propriétés différentes ont été observées en raison d'effets de localisation, de la morphologie et de la concentration. Dans les nano-assemblages, l'aza-BODIPY est situé dans le cœur des nano-ensembles lorsque des copolymères fonctionnalisés en fin de chaîne sont utilisés, ou à l'interface noyau / couronne si des copolymères portant le aza-BODIPY à la jonction des deux blocs sont utilisés. En particulier, l'influence de la localisation de l'aza-BODIPY dans les nano-assemblages et les effets de dilution (avec un copolymère non fonctionnalisé) sur les propriétés photophysiques de l'aza-BODIPY ont été étudiés par des techniques spectroscopiques. Cette différence dans la localisation et dans la morphologie a effectivement eu un impact sur le rendement de génération d'oxygène singulet et sur le rendement quantique de fluorescence, en considérant la différence dans le milieu et de concentration en oxygène. Les calculs de rendement quantique de génération d'oxygène singulet ont montré que les micelles présentent un rendement plus élevé par rapport à la structure vésiculaire. Par ailleurs, la dilution du PTS, par co-assemblage des copolymères fonctionnalisés avec les non fonctionnalisés, augmente l'activité du PTS en termes de génération d' $^1\text{O}_2$ . En outre, les nano-assemblages préparés à partir PBLG<sub>53</sub>-PTS-*b*-PEG<sub>45</sub> ont montré moins d'activité par rapport à ceux formés de PTS PBLG<sub>49</sub>-*b*-PEG<sub>45</sub>, probablement en raison d'interaction accrue avec des molécules d'eau.

Les quatre types de nanostructures multifonctionnelles obtenues ont été testées dans des expériences préliminaires *in vitro*; l'absorption par la lignée cellulaire d'adénocarcinome épithéliales humaines HeLa et la lignée cellulaire de cancer de la peau B16F1, des mesures de cytotoxicité et d'efficacité thérapeutique. Le temps et la concentration sur l'absorption cellulaire des nano-assemblages ont été quantifiés par cytométrie en flux où les micelles de PTS-PBLG<sub>49</sub>-*b*-PEG<sub>113</sub> (NAb 2) et PBLG<sub>53</sub>-PTS-*b*-PEG<sub>113</sub> (NAb 4) ont montré internalisation plus rapide par rapport aux nanoparticules de PTS -PBLG<sub>49</sub>-*b*-PEG<sub>45</sub> (NAb 1) et PBLG<sub>53</sub>-PTS-*b*-PEG<sub>45</sub> (NAb 3). Ils ont montré l'absorption maximale à 1 mg / mL après 24h d'incubation. Comme mentionné dans le chapitre 5, la différence morphologique de NAb1 et NAb2 (polymersomes) par rapport aux micelles est la principale raison de l'internalisation lente puisque toutes les nanostructures ont approximativement la même taille ( $R_h \sim 100\text{nm}$ ). La toxicité dans l'obscurité des nanostructures a été quantifiée par la mesure de la prolifération cellulaire

(test MTT) à différentes concentrations. Une faible toxicité dans l'obscurité à concentration élevée (1 mg / ml) a été observée. De plus, ce test a été répété après avoir effectué *in vitro* une activation PDT pour déterminer l'efficacité thérapeutique potentielle des nano-assemblages après photoactivation. Ainsi, nous avons observé une différence d'activité en fonction de la localisation de l'agent photosensibilisant entre 15 et 30 minutes d'irradiation (1,2 J / cm<sup>2</sup> et / dose de lumière 2,4 J/cm<sup>2</sup>). Le pourcentage plus élevé de mort cellulaire a été observée sur les nano-assemblages PBLG<sub>53</sub>-PTS-*b*-PEG<sub>113</sub> et PBLG<sub>53</sub>-PTS-*b*-PEG<sub>45</sub> où le PTS est localisé à l'interface. Parmi les deux nanostructures qui ont le PTS à l'interface, les nanoparticules de PBLG<sub>53</sub>-PTS-*b*-PEG<sub>45</sub> ont induit 100% d'apoptose sur les deux lignées cellulaires, même à faible concentration (0,125 mg / ml) (concentration du PTS de 3 pg / mL, 15pm) pour 15min (dose de lumière 1.2 J /cm<sup>2</sup>) de temps d'irradiation. En outre, après 1h d'irradiation par une LED, toutes les nanostructures ont également montré une toxicité élevée à 1 mg / ml.

Pour résumer, dans cette étude, nous avons développé une famille de quatre polypeptides et élaboré des nanoparticules modèles de différentes morphologies qui peuvent ouvrir une nouvelle porte pour le développement d'une nouvelle génération de produits thérapeutiques et repousser les limites existantes des agents cliniques actuels utilisés en PDT. Ces nano-assemblages offrent un contrôle sur la distribution de la taille, la morphologie, la concentration en agent photosensibilisant (PTS) et la localisation. En liant de manière covalente le PTS à des copolymères à blocs amphiphiles dans un ordre différent, nous pouvons quantitativement contrôler la concentration en nanoparticules et la localisation du PTS. De plus, la matrice de polymère hydrophobe protège le PTS de la dégradation dans les différents microenvironnements biologiques avant d'atteindre le site thérapeutique. En outre, en modifiant la localisation du PTS et la longueur de chaîne du PEG dans les copolymères séquences, nous avons démontré que le PTS montre une meilleure activité biologique sous activation LED lorsqu'il est situé à l'interface des nano-assemblages. L'activité biologique est encore meilleure pour des courtes chaînes de PEG formant la couronne des micelles. Cette stratégie permet aussi l'augmentation de l'efficacité thérapeutique en utilisant de très faibles quantités d'agent photosensibilisant. Avoir une plus grande efficacité à une concentration inférieure est également d'une grande importance dans l'industrie pharmaceutique afin de réduire à la fois les effets secondaires possibles et le coût des traitements anticancéreux.

## References

- (1) Awuah, S. G.; You, Y. RSC Advances 2012, 2, 11169.
- (2) Schweitzer, V. G. Lasers in Surgery and Medicine 2001, 29, 305.
- (3) Abdel-Kader, M. H., Ed.; Springer: Berlin, 2014.
- (4) Daniell, M. D.; Hill, J. S. Australian and New Zealand Journal of Surgery 1991, 61, 340.
- (5) Cabral, H.; Nishiyama, N.; Kataoka, K. Accounts of Chemical Research 2011, 44, 999.
- (6) Loudet, A.; Burgess, K. Chem Rev 2007, 107, 4891.
- (7) Lim, S. H.; Thivierge, C.; Nowak-Sliwinska, P.; Han, J.; van den Bergh, H.; Wagnieres, G.; Burgess, K.; Lee, H. B. J Med Chem 2010, 53, 2865.
- (9) Ding, H.; Yu, H.; Dong, Y.; Tian, R.; Huang, G.; Boothman, D. A.; Sumer, B. D.; Gao, J. J Control Release 2011, 156, 276.

## Résumé

Dans ce travail, nous avons développé des nanostructures théranostics à base de polypeptides fonctionnalisées avec un photosensibilisateur (PTS) dans le but d'être utilisées en thérapie photodynamique (PDT). La génération d'oxygène singulet et les propriétés de fluorescence du PTS peuvent ainsi à la fois diagnostiquer et traiter une tumeur.

Un dérivé asymétrique et multifonctionnel de l'aza-dipyrrrométhènes difluorure de bore chélate (aza-BODIPY) fluorogène a été synthétisé pour être utilisé comme photosensibilisateur en raison de ses propriétés non toxiques, son insensibilité à l'environnement biologique externe, sa production d'oxygène singulet élevée et son important rendement quantique de fluorescence. Pour permettre au photosensibilisant d'atteindre la tumeur, quatre copolymères à blocs amphiphiles différents en termes de localisation du PTS et de la longueur de la chaîne PEG ont été synthétisés. Les blocs amphiphiles sont constitués de segments poly( $\gamma$ -benzyl-L-glutamate) (PBLG, DP ~ 50) et poly(éthylène glycol) (PEG, DP = 45 et 113). Ces copolymères sont en outre capables de s'auto-assembler en micelles et en vésicules. Nous avons développé une stratégie de synthèse permettant la liaison covalente du PTS pour les copolymères à blocs amphiphiles, empêchant ainsi une fuite du PTS avant que les nanoparticules atteignent le site de la tumeur. En outre, nous avons étudié l'activité du PTS en fonction de la concentration, de la morphologie des nanoparticules et de la localisation du PTS dans les nanoparticules. Enfin, l'efficacité des nanoparticules a été évaluée *in vitro* sur des cellules HeLa et B16F1.

**Mots-clés:** nanoparticules polymériques, des polypeptides, amphiphile copolymère bloc d'auto-assemblage, photosensibilisateurs, aza-BODIPY, thérapie photodynamique

## TABLE OF CONTENT

PREAMBLE.....	i
ACKNOWLEDGEMENT .....	v
ABSTRACT .....	vii
TABLE OF CONTENT .....	ix
LIST OF SYMBOLS .....	xii
LIST OF ACRONYMS.....	xiii
CHAPTER 1	
1.1 GENERAL INTRODUCTION .....	3
1.1.1 Multifunctional polymeric nanoparticles' role in nanomedicine.....	4
1.1.2 Photodynamic therapy and its role in nanomedicine.....	5
1.2 Aim of the project .....	6
CHAPTER 2	
2. 1 INTRODUCTION.....	13
2.1.1 Boron dipyrin (BODIPY) dyes .....	14
2.1.2 Aza-BODIPYs, synthesis and applications .....	14
2.1.3 Polypeptide synthesis .....	17
2.1.4 Synthesis and application of poly( $\alpha$ -benzyl-L-glutamate).....	17
2.1.5 Poly(ethylene glycol) synthesis, properties and application .....	20
2.1.6 Peptidic coupling reaction .....	23
2.1.7 "Click chemistry" .....	25
2.1.8 Copper-catalyzed azide-alkyne cycloaddition reaction.....	25
2.1 Results and discussion.....	27
2.2.1 Synthesis of the building blocks.....	27
2.2.1.1 Synthesis of the photosensitizer.....	27
2.2.1.2 Synthesis of the polymer blocks .....	32
2.2.2 Block copolymer synthesis .....	34
2.2.2.1 Synthesis of PTS-PBLG conjugates .....	35
2.2.2.2 Functionalization of the PTS-PBLG <sub>53</sub> conjugate.....	36
2.2.2.3 Synthesis of PST-PBLG <sub>49</sub> - <i>b</i> -PEG block copolymers by CuAAC click reaction .	37
2.2.2.4 Synthesis of PBLG <sub>53</sub> -PTS- <i>b</i> -PEG type block copolymers by CuAAC click reaction.....	39
2.2.2.5 Synthesis of PBLG <sub>54</sub> - <i>b</i> -PEG type block copolymers .....	41
2.3 Conclusion.....	42

2.4 Experimental .....	42
Appendix 2: CHARACTERIZATION DATA FOR COMPOUNDS IN CHAPTER 2 .....	56
CHAPTER 3	
3.1 INTRODUCTION.....	73
3.1.1 Hydrophobic interactions and amphiphilic molecules .....	73
3.1.2 Hydrogen bonding .....	74
3.1.3 Polypeptide based block copolymers .....	75
3.1.4 Morphology control over the self-assembly of polypeptide based amphiphilic block copolymers.....	77
3.1.5 Self-assembly of PBLG- <i>b</i> -PEG block copolymers .....	79
3.2 Results and discussion.....	80
3.2.1 Self-assembly of the PTS bearing PBLG- <i>b</i> -PEG amphiphilic block copolymers in water .....	80
3.2.2 Characterization of the size and morphology of the nano-assemblies .....	82
3.2.3 Characterization of co-assembled particles and their physicochemical stability in cell-medium .....	85
3.3 Conclusion.....	92
3.4 Experimental .....	92
Appendix 3: CHARACTERIZATION DATA FOR CHAPTER 3 .....	95
CHAPTER 4	
4. 1 INTRODUCTION.....	103
4.1.1 Light - Matter Interactions.....	103
4.1.1.1 Fluorescence quantum yield measurement .....	104
4.1.1.2 Transient absorption.....	105
4.1.2 Photoactivation of photosensitizers (PTS) .....	106
4.1.3 Singlet oxygen .....	108
4.1.3.1 Detection of singlet oxygen in the solution .....	110
4.1.4 Photophysical properties of clinically used photosensitizers for photodynamic therapy .....	112
4.1.5 Photophysical properties of BODIPYs and heavy atom effect .....	114
4.2 Results .....	116
4.2.1 Overall photophysical properties of the PTS, PTS-PBLG conjugates and PTS functionalized block copolymers.....	116
4.2.2 Fluorescence quantum yield calculations .....	119
4.2.3 Time-resolved emission and transient absorption measurements .....	120
4.2.4 Singlet oxygen generation .....	121

4.3 Conclusion.....	125
4.4 Experimental .....	126
Appendix 4: CHARACTERIZATION DATA FOR CHAPTER 4 .....	129
CHAPTER 5	
5.1 INTRODUCTION.....	139
5.1.1 Application of aza-BODIPYs in fluorescence imaging .....	140
5.1.2 MTT assay test.....	144
5.1.3 Flow cytometry.....	145
5.2 Results .....	145
5.2.1 Cellular internalization test by flow cytometry .....	145
5.2.2 <i>In vitro</i> cytotoxicity .....	153
5.3 Conclusion.....	157
5.4 Experimental .....	158
CHAPTER 6	
6.1 GENERAL CONCLUSION AND PERSPECTIVES.....	163
CURRICULUM VITAE .....	167



## LIST OF SYMBOLS

$A$	absorbance
$D$	dispersity
$D$	diffusion coefficient
$C$	concentration
$M_n$	number average molecular weight
$M_w$	molecular weight
$R$	radius
$R_h$	hydrodynamic radius
$\Phi_F$	fluorescence quantum yield
$\Phi_\Delta$	singlet oxygen quantum yield
$\Phi_T$	triplet state quantum yield
$\lambda$	wavelength
$I_0$	intensity of the incident light
$I$	intensity of the transmitted light
$f\%$	weight fraction of the block copolymer
$\mathcal{F}$	decay rate
$q^2$	wave vector
$\lambda_{abs}$	maximum of absorption wavelength
$\lambda_{emiss}$	maximum of emission wavelength
$\varepsilon$	extinction coefficient
$a_0$	optimal interface
$l_c$	maximum length of insoluble chains
$l$	optical path length
$p$	packing parameter
$v$	volume occupied by insoluble chains
$K_d$	dissociation constant
$k_{nr}$	rate of non-radiative decay
$k$	rate constant
$S$	singlet state
$T$	triplet state
$\tau$	lifetime of the excited state
$\eta$	refractive index of the solvent
$E_{in}(\lambda)$	integrated luminescence in “IN”
$E_{out}(\lambda)$	integrated luminescence in “OUT”
$X_{empty}(\lambda)$	integrated excitation of empty sphere,
$X_{in}(\lambda)$	integrated excitation in “IN” configuration
$X_{out}(\lambda)$	integrated excitation in “OUT” configuration,
${}^3\Sigma_g^-$	triplet sigma oxygen
${}^1\Delta_g$	delta singlet oxygen
${}^1\Sigma_g^+$	singlet sigma oxygen
$m$	photobleaching rate
$F$	optical density

## LIST OF ACRONYMS

AVS	9,10-bis-(vinylsulfonate) anthracene
AP	9,10-bis(propionate)anthracene
AMM	activated monomer mechanism
aza-BODIPY	aza difluoroboron dipyrromethene
BLG-NCA	$\gamma$ -benzyl-L-glutamate N-carboxyanhydride
B16F1	skin cancer cell
BDP	4,4-difluoro-1,3,5,7-tetramethyl-4-bora-3a,4a-diaza-s-indacene
<sup>11</sup> B-NMR	boron (11)-nuclear magnetic resonance
BODIPY	difluoroboron dipyrromethene
BF <sub>3</sub> Et <sub>2</sub> O	diethyletherate
BuOH	butanol-1
CuAAC	copper(I)-catalyzed azide-alkyne cycloaddition
CD44	glycoproteins
CT	computerized tomography
CLSM	confocal laser scanning microscopy
CsF	cesium fluoride
DCM	dichloromethane
DPBF	1,3-Diphenylisobenzofuran
DEA	diethylamine
DAPI	4,6-diamidino-2-phenylindole
DIEA	diisopropylethylamine
DLS	dynamic light scattering
DMA	dimethylacetamide
DMF	dimethyl formamide
DP	degree of polymerization
DRI	differential refraction index
DIPA	diisopropylamine
DP	degree of polymerization
DHU	dicyclohexyl urea
Et <sub>3</sub> N	triethylamine
EPR	enhanced permeation and retention
EDCI	N-(3-dimethylaminopropyl)-N'-ethylcarbodiimide hydrochloride
EDTA	ethylenediaminetetraacetic acid
EtOH	Ethanol
EO	ethylene oxide
FDA	Food and Drug Administration
FTIR	Fourier transform infrared
FFA	furfuryl alcohol
FACS	flow cytometry
HPD	hematoporphyrin derivative

HeLa	human epithelial adenocarcinoma cell
HCl	hydrogen chloride
ISC	inter system crossing
IC	internal conversion
2I-BDP	4,4-difluoro-2,6-diiodo-1,3,5,7-tetramethyl-4-bora-3a,4a-diaza-sindacene
K <sub>x</sub> L <sub>y</sub>	poly(L-lysine)-b-poly(L-leucine)
QY	quantum yield
LED	light emitting diode
LROP	living anionic ring-opening polymerization
MB	methylene blue
MTT	3-(4,5-dimethylthiazol-2-yl)-2,5-diphenyltetrazolium bromide
mTHPC	m-Tetrahydroxyphenyl chlorin, Foscan <sup>®</sup>
mTHPP	5,10,15,20-tetrakis(meso-hydroxyphenyl)porphyrin
MeOH	Methanol
MRI	magnetic resonance imaging
MeOH	Methanol
NPs	Nanoparticles
NIR	near infrared
NAM	normal amine mechanism
NAbs	nano-assemblies
n/a	not applicable
NBS	n-bromosuccinimide
NCA	N-carboxyanhydride
ND	neutral density
nHOBt	1-hydroxybenzotriazole
OD	optical density
<sup>1</sup> O <sub>2</sub>	singlet oxygen
<sup>3</sup> O <sub>2</sub>	triplet oxygen
PDT	photodynamic therapy
PTS	Photosensitizer
PBD	poly(butadiene)
PBLG	poly(-benzyl-L-glutamate)
PDMAEMA	poly(2-(dimethylamino) ethyl methacrylate)
PBS	phosphate buffered saline
PB	phosphate buffer
PLys <sub>15</sub> -b-PLGA <sub>15</sub>	poly(L-lysine)-b-poly(L-glutamic acid)
PLGA	poly(L-glutamic acid)
PB-b-PLGA	polybutadiene-b-poly(L-glutamic acid)
PEG	poly(ethylene glycol)
PEO	poly(ethylene oxide)

POE	poly(oxyethylene)
PET	positron emission tomography
PeT	photoinduced electron transfer
PI	polyisoprene
PLA	poly(lactic acid)
PAA	polyacrylic acid
PLLys	poly(L-lysine)
PNIPAM	poly(Nisopropylacrylamide)
PTA	photothermal ablation
PDPA	poly(2-(diisopropylamino)ethyl methacrylate)
ROS	reactive oxygen species
RGD	arginylglycylaspartic acid
ROP	ring opening polymerization
ROP-NCA	ring-opening N-carboxyanhydride polymerization
RB	Rose Bengal
RT	room temperature
RES	reticuloendothelial system
SPECT	single-photon emission computed tomography
SEC	size exclusion chromatography
tBuOK	tert-butoxide
TFA-Lys	$\epsilon$ -trifluoroacetyl-L-Lysine
TBTA	tris(benzyltriazolylmethyl)amine
TEM	transmission electron microscopy
TBAF	tetrabutylammonium fluoride
TEM	transmission electron microscopy
TFA	trifluoroacetic acid
THF	tetrahydrofuran
TMSN <sub>3</sub>	trimethylsilyl azide
TX100	triton X100
TsCl	toluenesulfonyl chloride
UV/Vis	ultraviolet-visible
USPIO	superparamagnetic iron oxide
US	ultrasound imaging



---

# CHAPTER 1

---

## GENERAL INTRODUCTION

### *Abstract*

*Due to their small size, nanoparticles are utilized in a wide variety of areas like nanotechnology, bio-nanotechnology, nanomedicine etc. In this opening chapter, we will focus on the concept of nanomedicine and the role of multifunctional polymer based nanoparticles in medicine. In this context, the aim of this thesis is to develop polypeptide-based self-assemblies for nanomedicine applications*









## 1.1 GENERAL INTRODUCTION

Nanomedicine is the biomedical application of nanoscale materials for the diagnosis and/or therapy of disease. The use of ‘nanomedicine’ term in the publications can be seen from the year 2000, although the development of this area started a few years earlier in the field of nanotechnology.<sup>1,2</sup> The first examples of nanoparticles are even back to the 80’s when nanosize micelles have been proven to improve the intracellular delivery of drugs.<sup>3</sup> Nevertheless, it can be seen as a relatively new area of medicine which involves application of organic, inorganic<sup>4-7</sup> or hybrid<sup>4</sup> nanosized therapeutics in imaging, diagnosis, therapy and treatment that could not be achieved by micro or macro-systems.<sup>8-10</sup> The basis of the development of nanomedicine could be linked to the magical idea of Nobel Prize owner Paul Ehrlich in 1906 to create “magic bullets” (magische Kugel) that can be selectively targeted to the pathogenic site to treat the cancer.<sup>11</sup> During 100 years this idea has inspired scientists to develop selective targeting agents for cancer treatment including other life-threatening diseases.

Recent advances in nanotechnology and biotechnology have contributed to the development of multifunctional nanoparticles (NPs) for nanomedicine.<sup>12</sup> Due to their unique features including multifunctionality, large surface area or interior cargo volume, structural diversity, and long circulation lifetime in blood compared to small molecules, nanoparticles have emerged as attractive tools for optimized therapy through personalized medicine.<sup>8</sup> A wide variety of biocompatible, multifunctional,<sup>13,14</sup> remote controlled, stimuli responsive<sup>15</sup> and smart<sup>16</sup> theranostic<sup>17</sup> nanoparticles has been reported to be used in nanomedicine.<sup>18</sup> Multifunctional theranostic nanoparticles allow precise and fast diagnosis of the disease through synergetic imaging and treatment at the same time.

Thanks to the rapid and broad growth of nanomedicine, more than ~200 nanomedicine products have been approved or are under clinical trials.<sup>19</sup> However, the development of new therapeutics is a quite challenging process since it has to meet different requirements and pass through the three clinical phases to be approved by Food and Drug Administration (FDA) for medical use (Figure 1.1).<sup>2</sup> After the chemical examinations nanosized drugs should be tested *in vitro* and *in vivo* to test biocompatibility or toxicity of the new therapeutics. These steps are followed by evaluation of dose dependent toxicity in phase I clinical trial on a limited number of patients by using several techniques.<sup>20</sup> In the phase II step, if the drug exhibits a good efficacy, it can pass to the phase III trials which is more complex and requires long term studies since the new drug compounds are investigated on patients.<sup>21</sup>

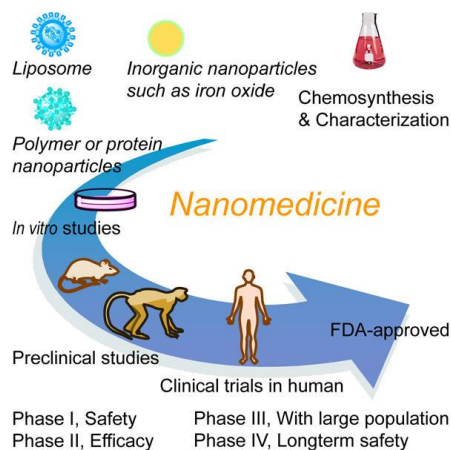


**Figure 1.1:** Schematic illustration of the drug development..<sup>2</sup>

### 1.1.1 Multifunctional polymeric nanoparticles' role in nanomedicine

Natural and synthetic polymers have an important role in medicine to carry the therapeutics as polymer-drug conjugates or by encapsulating or conjugating it into/to the polymeric nanoparticles (Figure 1.2).<sup>22</sup> The concept of using polymer-drug conjugates for cancer treatment was first introduced in 1970s and several types of conjugates have been studied in this context to increase the solubility of the drug and increase its circulation lifetime in the blood stream.<sup>23,24</sup> Polymer-protein conjugates were also studied for cancer treatment, where first one was approved in 1994.<sup>25</sup> However, due to the small size of the polymer chains (~1-10nm) very small amount of drugs can reach and accumulate in the tumor site, which decreases the efficacy of the treatment. Compared to polymer conjugates, monodispersed dendritic polymers have the advantage of encapsulating the small drug molecules, which decrease their toxicity and protect them from the various physiological conditions in the body before reaching the cancer site.<sup>26</sup> Despite these advantages, their syntheses are quite challenging. Moreover, they can easily lose water solubility after incorporation of hydrophobic drug molecules and form aggregates.

The cross-linked polymeric nanogels are another class of nanocarriers that offer a big volume and good dispensability in water. The large size (20-200nm) of the nanoparticles offers selective accumulation in tumor site due to the enhanced permeability and retention effect (EPR).<sup>27</sup> This effect occurs due to the vascular hyperpermeability near malignant tissues which permits the accumulation of the bigger particles as illustrated in Figure 1.3.

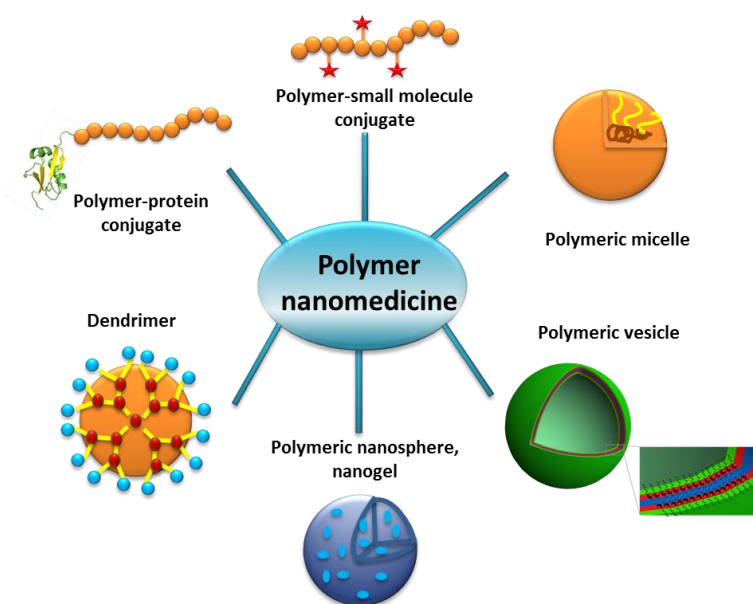


**Figure 1.2:** Schematic representation of polymeric drug-delivery vehicles. (adapted from ref.<sup>22</sup>)

The mostly preferred nanocarriers in the nanomedical applications are micelles<sup>28</sup> and vesicles which are formed through the self-assembly of amphiphilic block copolymers or lipids. In general, nanoparticles made from self-assembled block copolymers are particularly promising. Block copolymers are indeed interesting building blocks since their chemistry can be easily tuned, they can form stable nano-assemblies of various shapes and sizes with long circulation lifetimes, they can respond to many different stimuli, and they can easily encapsulate hydrophobic or hydrophilic drugs and therapeutic biomolecules (peptide, protein, DNA/RNA...) or contrasting agents (fluorophore, nanoparticle...).<sup>29</sup>

In general, polymeric nanocarriers reduce the toxicity of the drugs, protect them from degradation before reaching the targeted site and improve pharmacokinetic and pharmacological profiles of the treatment.<sup>9,30-32</sup>

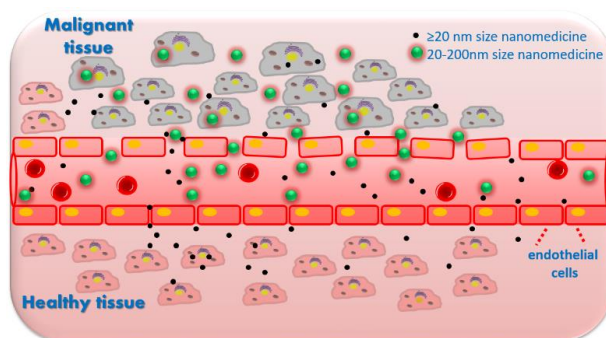


**Figure 1.3:** Schematic illustration of the enhanced permeability and retention effect (EPR). (adapted from ref.<sup>33</sup>)

### 1.1.2 Photodynamic therapy and its role in nanomedicine

Photodynamic therapy (PDT) is a very promising noninvasive method which has emerged as one of the important therapeutic options in management of cancers and other diseases. The attractiveness of PDT comes mainly from its fundamental specificity and selectivity, since in theory, only the tissues that are irradiated with light of an appropriate wavelength will be exposed to the toxic species, limiting therefore strongly side effects.

Although the photodynamic therapy has started to be used in clinics for cancer treatment since 1999, after the approval of first PDT agent Photofrin<sup>®</sup>,<sup>34,35</sup> the concept itself was seen in ancient medicine. In Egypt, Greek and Indian medicine the combination of light and chemical agents was used to treat some disorders 5000 years ago.<sup>36,37</sup> Nowadays, it is one of the mostly preferred non-invasive therapeutic method to selectively treat the cancer at early stage. Photodynamic therapy<sup>36</sup> is an externally triggered treatment for various diseases. PDT can be defined as the administration of a dye, known as a photosensitizer (PTS), to a patient bearing a lesion, which is frequently a cancer. After a sufficient incubation time with the PTS, this lesion is then selectively illuminated with light of appropriate wavelength (laser or LED), which, in the presence of oxygen, leads to the generation of cytotoxic reactive oxygen species (ROS) and consequently to cell death and tissue destruction (Figure 1.4).

A wide variety of natural and un-natural fluorescent dyes are moreover capable of generating ROS under light activation. Some of these photosensitizers (porphyrins, chlorins, phthalocyanines, BODIPY dyes,<sup>38,39</sup> etc.) are extensively investigated for medical purposes and used in photodynamic therapy which is discussed in Chapter 4.<sup>40,41</sup> The main limitation in PDT is the complexity of the human tissue where only near infrared (near-IR) light can penetrate through it and activate the targeted PTS. In addition, the administration mode of the photosensitizer (PTS) is not yet optimal and often leads to a nonspecific accumulation of the PTS in normal tissues, inducing a general photosensitivity of the patient (especially the skin). To overcome this problem, the use of delivery carriers such as liposomes, polymer conjugates, polymer nanoparticles, or block copolymer micelles has been proposed due to the aforementioned advantages of nanomedicine. In the great majority of these cases, the PTS was not covalently bond to its carrier which may still poses leakage problems. Moreover, the weak photophysical properties (i.e., low absorption wavelength, low extinction coefficient, low ROS

yield, lack of control on PTS concentration, etc.) of the existing clinical photosensitizers require the development of new systems to increase the efficacy of the treatment and decrease side effects.

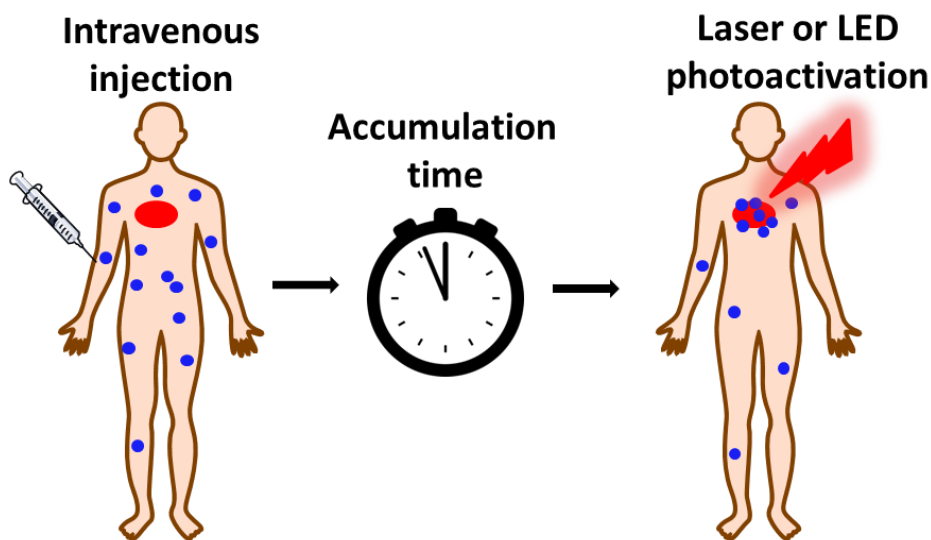


**Figure 1.4:** Illustration of the Photodynamic Therapy (PDT). (adapted from ref.<sup>36</sup>)

Since PTS molecules are inherently fluorescent, this feature can be also used for imaging and locating disease, allowing thus a theranostic approach. Theranostics are multifunctional nanodevices which combine one or multiple imaging and therapeutic techniques.<sup>27</sup> More information about this concept is provided in Chapter 3.

## 1.2 Aim of the project

The objective of this project is to develop polypeptide based, drug free, self-assembled theranostic particles which will be used in the diagnosis and therapy of cancer. These original multifunctional particles will allow fluorescence imaging and photodynamic therapy which will help to detect and treat the disease faster and efficiently without damaging healthy tissues.

In this project, asymmetric near-infrared dye, derivative of an aza-dipyromethene boron difluoride chelate (**Aza-BODIPY**)<sup>42</sup>, is synthesized to be used as a photosensitizer in PDT. To carry the photosensitizer (**PTS**) to the tumor it is covalently linked to amphiphilic block copolymers consisting of poly( $\gamma$ -benzyl-L-glutamate) and poly(ethylene glycol) chains with two different orders: **PTS-PBLG-*b*-PEG** and **PBLG-PTS-*b*-PEG**, and two different PEG chain length, by using peptidic coupling and Copper-catalyzed Azide-Alkyne Cycloaddition (CuAAC) click reactions as illustrated in Figure 1.5. The covalent attachment of the PTS to the block copolymer will prevent its leakage out of the nano-assemblies and provide quantitative characterization. These block copolymers will lead to different types of nano-assemblies due to the difference in hydrophilic/hydrophobic ratio and to the localization of the PTS in the block copolymer. Micelles or vesicles are expected and the PTS will concentrate either in the core (**PTS-PBLG-*b*-PEG**, Figure 1.6A) of the nano-assemblies or at the interface (**PBLG-PTS-*b*-PEG**, Figure 1.6B)

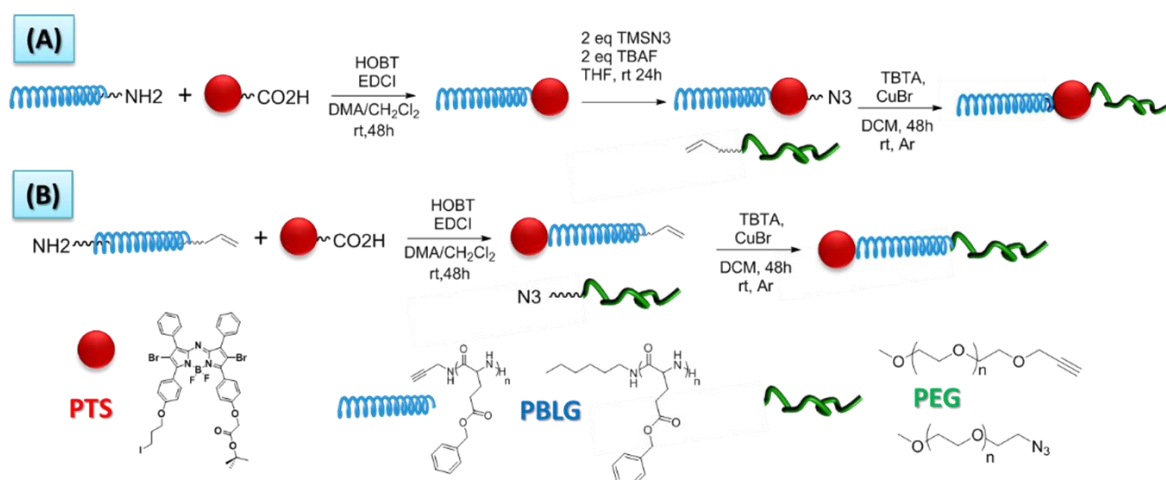


**Figure 1.5:** A) Carboxylic group bearing PTS conjugated to the PBLG by peptidic coupling and azide-functionalized PEG linked to the PBLG chain end via CuAAC click chemistry B) Carboxylic group bearing PTS conjugated to the PBLG by peptidic coupling, functionalized with an azide group and followed by CuAAC click reaction with alkyne functionalized PEG.

The largest part of the work was dedicated to the optimization of the synthesis of the copolymers, the study of their self-assembly behavior, and the photophysical characterization of the obtained photosensitizers (before and after introducing heavy atom and after deprotection of the carboxylic group), PTS-PBLG conjugate, PTS functionalized block copolymers and nano-assemblies. To this end, optimization of the synthesis of the aza-BODIPY dyes, polypeptides (PBLG) and four different types of block copolymers in term of PTS localization and chain length of the PEG was performed. Self-assembly behavior of these block copolymers (**PTS-PBLG-*b*-PEG/ PBLG-PTS-*b*-PEG**) was studied in aqueous solutions, and chain length and dilution effects on the morphology of the nano-assemblies were investigated. Singlet oxygen generation efficiency in different nano-assemblies was studied in terms of localization of PTS (in the core, in the interface of the corona, in the membrane of the vesicles, etc.). In the final step, concentration and time dependent cellular internalization and toxicity (dark and after irradiation) of the nano-assemblies were tested *in vitro* on HeLa and B16F1 cancer cell lines.

This strategy will thus be a fully "drug free" approach since it does not rely on the release of a drug for curing, circumventing therefore the often encountered problem of drug leakage out of the nanocarriers, and leading to unspecific release. The main advantages of this strategy are that the covalent linking provides quantitative control over PTS concentration and over its localization in the nano-assemblies, the large size of the nano-assemblies allows passive targeting through EPR effect, and the polymer shell prevents the degradation of PTS before it reaches the cancer site by playing a protective cage role.

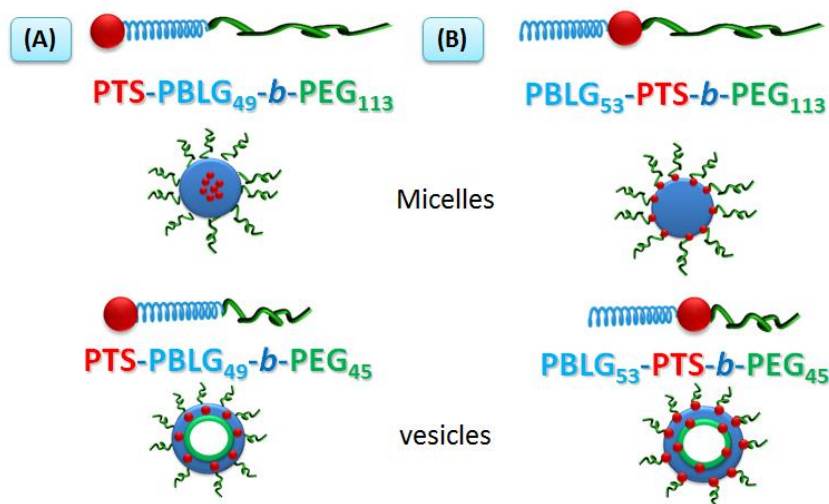


**Figure 1.6:** Self-assembly in aqueous environment. The numbers in subscript are the average degrees of polymerization.

## References

- (1) Wagner, V.; Dullaart, A.; Bock, A.-K.; Zweck, A. *Nat Biotech* **2006**, *24*, 1211.
- (2) Min, Y.; Caster, J. M.; Eblan, M. J.; Wang, A. Z. *Chemical Reviews* **2015**, *115*, 11147.
- (3) Couvreur, P.; Kante, B.; Roland, M.; Guiot, P.; Bauduin, P.; Speiser, P. *Journal of Pharmacy and Pharmacology* **1979**, *31*, 331
- (4) Epherre, R.; Duguet, E.; Mornet, S.; Pollert, E.; Louguet, S.; Lecommandoux, S.; Schatz, C.; Goglio, G. *Journal of Materials Chemistry* **2011**, *21*, 4393.
- (5) Hofmann-Antenbrink, M.; Grainger, D. W.; Hofmann, H. *Nanomedicine: Nanotechnology, Biology and Medicine* **2015**, *11*, 1689.
- (6) Cho, M. H.; Lee, E. J.; Son, M.; Lee, J.-H.; Yoo, D.; Kim, J.-w.; Park, S. W.; Shin, J.-S.; Cheon, J. *Nat Mater* **2012**, *11*, 1038.
- (7) Rai, M.; Ingle, A. P.; Birla, S.; Yadav, A.; Santos, C. A. *Critical reviews in microbiology* **2015**, *1*.
- (8) Paliwal, R.; Babu, R. J.; Palakurthi, S. *AAPS PharmSciTech* **2014**, *15*, 1527.
- (9) Duncan, R. *Current Opinion in Biotechnology* **2011**, *22*, 492.
- (10) Kievit, F. M.; Zhang, M. *Adv Mater* **2011**, *23*, H217.
- (11) Strebhardt, K.; Ullrich, A. *Nat Rev Cancer* **2008**, *8*, 473.
- (12) Rai, M.; Ingle, A. P.; Gaikwad, S.; Padovani, F. H.; Alves, M. *Critical Reviews in Biotechnology* **2015**, *1*.
- (13) Shi, D.; Bedford, N. M.; Cho, H.-S. *Small* **2011**, *7*, 2549.
- (14) Wang, H.; Li, F.; Du, C.; Wang, H.; Mahato, R. I.; Huang, Y. *Molecular Pharmaceutics* **2014**, *11*, 2600.
- (15) Mura, S.; Nicolas, J.; Couvreur, P. *Nat Mater* **2013**, *12*, 991.
- (16) Zhang, J.; Liang, Y.-C.; Lin, X.; Zhu, X.; Yan, L.; Li, S.; Yang, X.; Zhu, G.; Rogach, A. L.; Yu, P. K. N.; Shi, P.; Tu, L.-C.; Chang, C.-C.; Zhang, X.; Chen, X.; Zhang, W.; Lee, C.-S. *ACS Nano* **2015**, *9*, 9741.
- (17) Kunjachan, S.; Ehling, J.; Storm, G.; Kiessling, F.; Lammers, T. *Chemical Reviews* **2015**, *115*, 10907.
- (18) Hari Krishna, S.; Michael, P. E.; Hui, M.; Wang, Y. A.; Shuming, N.; Lily, Y. *Current Drug Discovery Technologies* **2009**, *6*, 43.
- (19) Etheridge, M. L.; Campbell, S. A.; Erdman, A. G.; Haynes, C. L.; Wolf, S. M.; McCullough, J. *Nanomedicine: Nanotechnology, Biology and Medicine* **2013**, *9*, 1.

- (20) Le Tourneau, C.; Lee, J. J.; Siu, L. L. *Journal of the National Cancer Institute* **2009**, *101*, 708.
- (21) Seymour, L.; Ivy, S. P.; Sargent, D.; Spriggs, D.; Baker, L.; Rubinstein, L.; Ratain, M. J.; Le Blanc, M.; Stewart, D.; Crowley, J.; Groshen, S.; Humphrey, J. S.; West, P.; Berry, D. *Clinical Cancer Research* **2010**, *16*, 1764.
- (22) Tong, R.; Cheng, J. *Polymer Reviews* **2007**, *47*, 345.
- (23) Ringsdorf, H. *Journal of Polymer Science: Polymer Symposia* **1975**, *51*, 135.
- (24) Duncan, R. *Nat Rev Drug Discov* **2003**, *2*, 347.
- (25) Duncan, R. *Nat Rev Cancer* **2006**, *6*, 688.
- (26) Krämer, M.; Stumbé, J.-F.; Türk, H.; Krause, S.; Komp, A.; Delineau, L.; Prokhorova, S.; Kautz, H.; Haag, R. *Angewandte Chemie International Edition* **2002**, *41*, 4252.
- (27) Cabral, H.; Nishiyama, N.; Kataoka, K. *Accounts of Chemical Research* **2011**, *44*, 999.
- (28) Oerlemans, C.; Bult, W.; Bos, M.; Storm, G.; Nijssen, J. F. W.; Hennink, W. E. *Pharmaceutical Research* **2010**, *27*, 2569.
- (29) Zhao, Y.; Sakai, F.; Su, L.; Liu, Y.; Wei, K.; Chen, G.; Jiang, M. *Advanced Materials* **2013**, *25*, 5215.
- (30) Lin, W. *Chemical Reviews* **2015**, *115*, 10407.
- (31) Wolfram, J.; Zhu, M.; Yang, Y.; Shen, J.; Gentile, E.; Paolino, D.; Fresta, M.; Nie, G.; Chen, C.; Shen, H.; Ferrari, M.; Zhao, Y. *Current drug targets* **2014**.
- (32) Thomas, B. G. *Recent Patents on Nanomedicine* **2012**, *2*, 52. (33) Sun, T.; Zhang, Y. S.; Pang, B.; Hyun, D. C.; Yang, M.; Xia, Y. *Angewandte Chemie International Edition* **2014**, *53*, 12320.
- (34) Awuah, S. G.; You, Y. *RSC Advances* **2012**, *2*, 11169.
- (35) Schweitzer, V. G. *Lasers in Surgery and Medicine* **2001**, *29*, 305.
- (36) Abdel-Kader, M. H., Ed.; Springer: Berlin :, 2014.
- (37) Daniell, M. D.; Hill, J. S. *Australian and New Zealand Journal of Surgery* **1991**, *61*, 340.
- (38) Loudet, A.; Burgess, K. *Chem Rev* **2007**, *107*, 4891.
- (39) Lim, S. H.; Thivierge, C.; Nowak-Sliwinska, P.; Han, J.; van den Bergh, H.; Wagnieres, G.; Burgess, K.; Lee, H. B. *J Med Chem* **2010**, *53*, 2865.
- (40) Ding, H.; Yu, H.; Dong, Y.; Tian, R.; Huang, G.; Boothman, D. A.; Sumer, B. D.; Gao, J. *J Control Release* **2011**, *156*, 276.
- (41) Sharman, W. M.; van Lier, J. E.; Allen, C. M. *Adv Drug Deliv Rev* **2004**, *56*, 53.
- (42) Murtagh, J.; Frimannsson, D. O.; O'Shea, D. F. *Org Lett* **2009**, *11*, 5386.







---

## CHAPTER 2

---

### SYNTHESIS OF BUILDING BLOCKS AND BLOCK COPOLYMERS

#### *Abstract*

*Literature examples of BODIPY dyes and aza-BODIPYs, polypeptides, properties of PEG and some synthetic strategies like peptidic coupling and “click” reaction are here described. In the first step of this work the building blocks, the original asymmetric aza-BODIPY (PTS) and poly( $\gamma$ -benzyl-L-glutamate) (PBLG) were synthesized. In the next step, aza-BODIPY was conjugated to two PBLG polymers bearing different functionality. In the final step, four different types of amphiphilic block copolymers in terms of PTS localization and PEG chain lengths, PTS-PBLG<sub>49</sub>-b-PEG<sub>45</sub>, PTS-PBLG<sub>49</sub>-b-PEG<sub>113</sub>, PBLG<sub>53</sub>-PTS-b-PEG<sub>45</sub> and PBLG<sub>53</sub>-PTS-b-PEG<sub>113</sub>, were synthesized and characterized.*

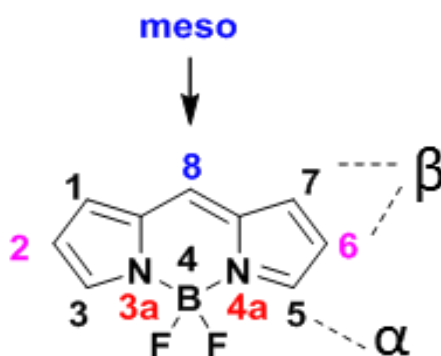




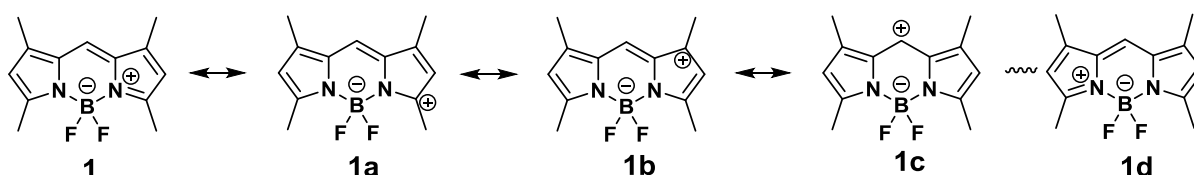
## 2. 1 INTRODUCTION

### 2.1.1 Boron dipyrin (BODIPY) dyes

BODIPY dyes are intensely fluorescent, color tunable and easily modified (from  $\alpha$ ,  $\beta$  and meso positions, Scheme 2.1) fluorophores that are formed usually by  $\text{BF}_2$  complexation of dipyrromethane ligand. These fluorophores are neutral but internally zwitterionic molecules. Moreover, they have high  $\pi$ -electron density in their backbone. Strong  $\pi$ -electron delocalization (see Scheme 2.2) in the BODIPY framework causes outstanding photophysical properties that can be tuned by further extending  $\pi$  conjugation (adding phenyl ring on 1, 2, 5, 7 positions or other electron donating groups) or introducing heavy atoms to the backbone or side groups.



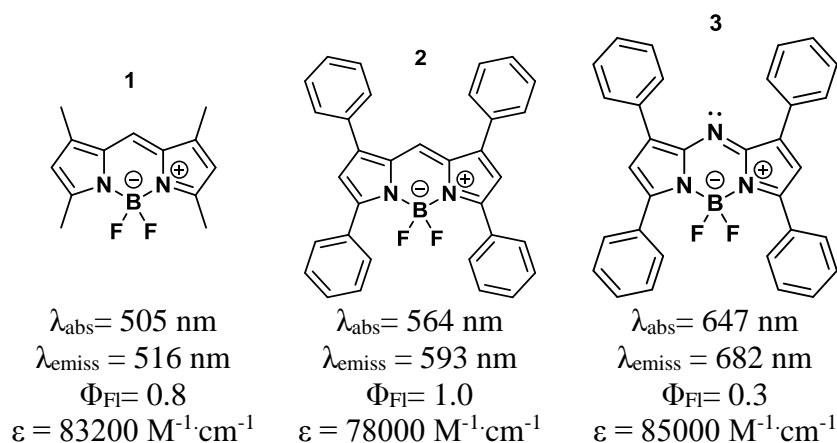
Scheme 2.1: BODIPY core and IUPAC numbering



Scheme 2.2: BODIPY delocalized structure

BODIPY core modification effect on optical properties can be seen from Scheme 2.3. The addition of the bulky phenyl groups increases the rigidity of the molecule and increases the electron density, consequently causing a 59 nm red shift in the absorption wavelength.<sup>1</sup> Moreover, the addition of electron donating nitrogen in meso-position causes a 142 nm red shift in absorption wavelength.<sup>2</sup> These new generation fluorophores are called aza-dipyrromethene boron difluoride (aza-BODIPY).

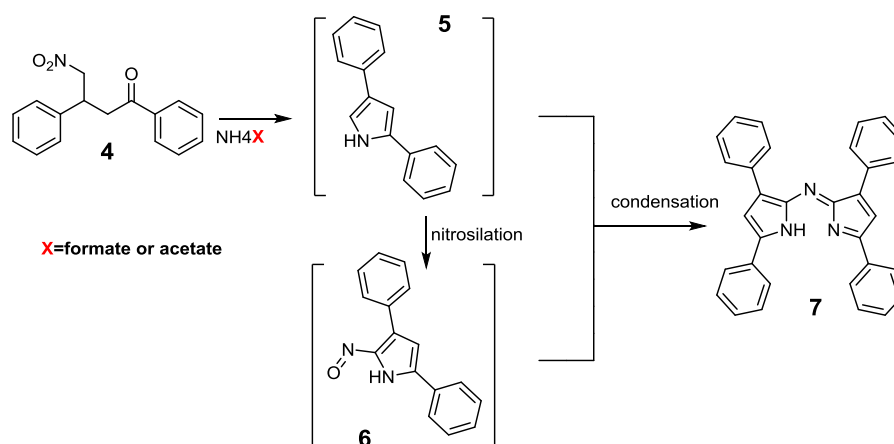
Conventional BODIPYs are extensively studied since 1968, after coincidentally discovery by Treibs and Kreuzer,<sup>3</sup> and applied in a wide variety of areas; solar cells<sup>4</sup>, biolabeling<sup>5,6</sup>, fluorescent probe<sup>7,8</sup> etc. Despite of their good optical properties, the limited wavelength range of absorption restricts their use in *in vivo* imaging and in photodynamic therapy (PDT) as a photosensitizer. However, the absorption of the aza-BODIPY fluorophores can be shifted above 740 nm<sup>9</sup> by core or side group modification.



**Scheme 2.3:** Chemical structures and optical properties of BODIPYs <sup>1,2</sup>

### 2.1.2 Aza-BODIPYs, synthesis and applications

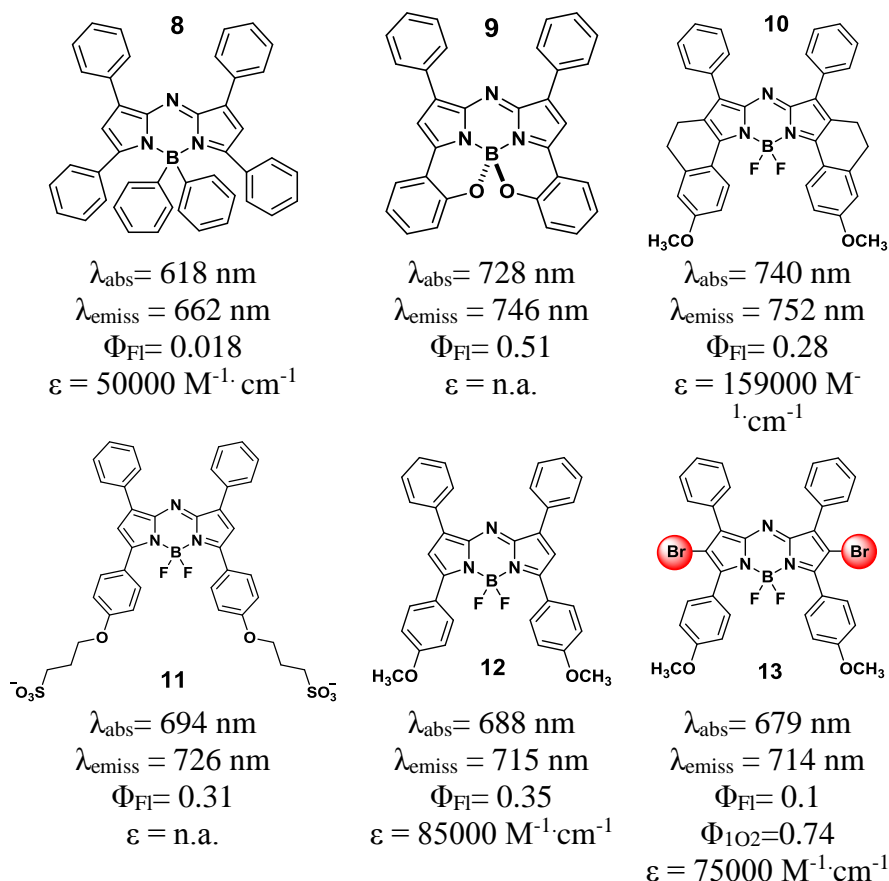
The synthesis of BF<sub>2</sub> chelates of the tetraphenyl aza-dipyrromethane **7** was first reported in 1990s as a laser dye by Govindarao and coworkers.<sup>10,11</sup> However, photophysical properties of the complex were not fully investigated. These compounds drew the attention of many scientists after Donald F. O'Shea<sup>12</sup> and coworkers reported about improved synthesis and detailed investigation of the photophysical properties of brominated and non-brominated aza-BODIPY dyes in 2002. Despite the fact that BF<sub>2</sub> complex of the aza-dipyrromethane ligand started to be explored in the last decade, the ligand itself was first reported in 1940s<sup>13,14</sup> by Roger M. A. T. It was used as an efficient blue coloring dye. Derivatives of aza-dipyrins were synthesized (see Scheme 2.4) by one pot condensation reaction of nitromethane adducts of chalcone **4** at elevated temperature in the presence of excess ammonium formate in solvent free conditions (34% yield).



**Scheme 2.4:** aza-dipyrromethane synthesis <sup>15</sup>

O'Shea and coworkers<sup>16</sup> further improved the aza-dipyrines' synthesis conditions by using ammonium acetate as an ammonium source and performed condensation reaction in nBuOH, EtOH and solvent free conditions. This study revealed that the reaction in nBuOH or in solvent free conditions gives higher isolated yield compared to EtOH. However, in terms of purification, the synthesis in alcohols is more favorable since a precipitation of pure deep blue aza-dipyrin crystals from the reaction mixture occurs, whereas solvent free conditions require a column chromatography.

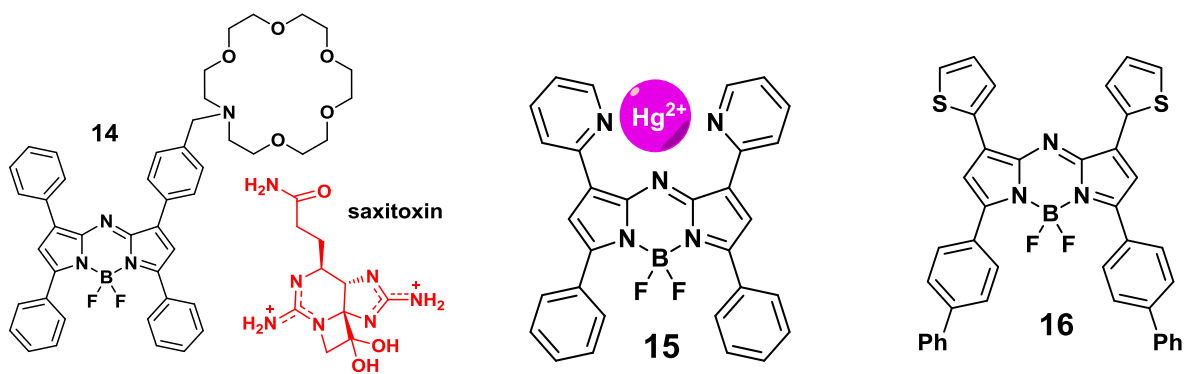
One of the outstanding properties of these dyes is a remarkable tunability of their optical properties. The core and side group functionalization of aza-BODIPYs tremendously affects their optical properties as shown in Scheme 2.5. The comparison of the optical and photophysical properties of aza-BODIPY derivatives that have been published up to now provides an opportunity to build new derivatives with desired properties.



**Scheme 2.5:** Chemical structures and optical properties of aza-BODIPYs: **8**<sup>17</sup>, **9**<sup>18</sup>, **10**<sup>9</sup>, **11**<sup>19</sup>, **12** and **13**<sup>16</sup> (n.a. not available)

The functionalization of the boron center<sup>17</sup> induces a blue shift and lower fluorescence quantum yield compared to BF<sub>2</sub> complex of the same ligand. The 47 nm blue shifting and remarkable decrease in fluorescence quantum yield were observed when the fluorine groups of the boron center were replaced with an aryl unit (compound **8**). The opposite phenomenon was observed when a B-O ring extended aza-BODIPYs<sup>18</sup> (**9**) was synthesized by forming benzi(1,3,2)oxozaborinine rings. Due to the restrictions caused by B-O bond on a chiral molecule, the red-shifting in absorption wavelength and increase in fluorescence quantum yield was observed compared to the conventional aza-BODIPY **3**. The cyclized aza-BODIPY **10**<sup>9</sup> with BF<sub>2</sub> complex also exhibits huge red shifting in absorbance wavelength but a slightly lower fluorescence quantum yield. Higher NIR emission and excellent photostability of these conformationally restricted aza-BODIPYs make them good candidates for bioimaging applications.





pH 7.1 (MeOH)  $K_d=1.6 \mu\text{M}$   
 $\lambda_{\text{abs}}=650 \text{ nm}$   
 $\lambda_{\text{emiss}}=680 \text{ nm}$   
 $\Phi_{\text{Fl}}= \text{n.a.}$   
 $\varepsilon = \text{n.a.}$

(AcCN)  $K_d=5.4 \mu\text{M}$   
 $\lambda_{\text{abs}}=696 \text{ nm}$   
 $\lambda_{\text{emiss}}=719 \text{ nm}$   
 $\Phi_{\text{Fl}}=0.17$   
 $\varepsilon = 77000 \text{ M}^{-1}.\text{cm}^{-1}$

$\lambda_{\text{abs}}=708 \text{ nm}$   
 $\lambda_{\text{emiss}}=738 \text{ nm}$   
 $\Phi_{\text{Fl}}=0.27$   
 $\varepsilon = 47000 \text{ M}^{-1}.\text{cm}^{-1}$

**Scheme 2.6:** Aza-BODIPYs in sensing and solar cell applications and optical properties ( $K_d$  - dissociation constant, n.a. -not available)<sup>20,21,22</sup>

Water soluble derivatives of aza-BODIPYs have been also synthesized<sup>23</sup> to be used in bio-imaging, chemosensing, biolabeling etc. The good NIR emission and photostability of these dyes decrease the auto-fluorescence of endogenous chromophores in the tissues and help to get efficient fluorescence signal with minimal cell damage. In order to make them water soluble, several hydrophilic side groups can be attached to aza-BODIPY scaffold.<sup>24-26</sup> In product **11**<sup>19</sup> addition of two sulfonyl groups increases the solubility of the dye in water and causes a slight red shift compared to **3**. The attachment of the electron donating groups also helps to push absorption and emission wavelength to the red region. Electron donating methylene substitution of the phenyl group in compound **12**<sup>16</sup> causes 40 nm red shifting but no change in fluorescence quantum yield was observed. Heavy atom addition from 2, 6 positions on aza-BODIPY core (**13**) causes huge decline in fluorescence quantum yield but increases the singlet oxygen generation efficiency.<sup>16</sup> The detailed information about heavy atom effect on photophysical properties is discussed in Chapter 4.

Owing to the higher and narrow absorption and fluorescence, higher extinction coefficient, photophysical and chemical stability of the derivatives of aza-BODIPY dyes has been applied in many areas like biology, medicine, optoelectronics etc.

Robert et al.<sup>20</sup> reported a highly sensitive biosensor **14** for sensing marine toxin saxitoxin, the paralytic shellfish poison. Mono 18-crown-6 substitution of aza-BODIPY caused fluorescence quenching due to the electron transfer from crown ether to the aza-BODIPY core. However, 100% fluorescence enhancement was detected in the presence of saxitoxin (1:1) due to the complexation with crown ether leading to the switching off the electron transfer process from the crown ether. Aza-BODIPYs have been also used as chemosensors.<sup>27-29</sup> Akkaya et al.<sup>21</sup> have designed aza-BODIPY **15** with 2-pyridyl substituents that shows great affinity toward cationic binding with mercury ions. The absorption and emission of the sensor in acetonitrile ( $\lambda_{\text{abs}}=655\text{nm}$ ,  $\lambda_{\text{emiss}}=682\text{nm}$  and  $\Phi_{\text{Fl}}=0.17$ ) are red shifted upon the  $\text{Hg}^{2+}$  ions detection in the solution, via complexing in 1:1 stoichiometry.

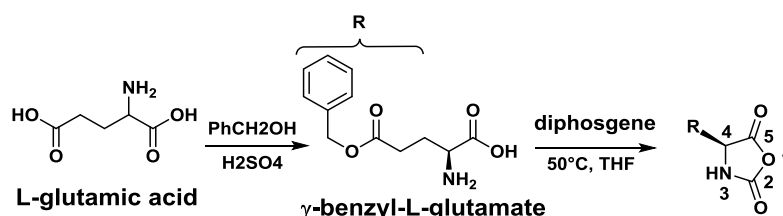
Besides good photophysical properties, aza-BODIPYs possess good electrochemical properties as well, which makes them good candidates for organic solar cell application.<sup>22,30-32</sup> Agarwal et al.<sup>22</sup> reported a new derivative of aza-BODIPYs with low band gaps and high electron affinity for solar cell application. Due to the long  $\pi$ -conjugated skeleton, compound **16**<sup>22</sup> exhibits longer absorption and fluorescence wavelength and has a lower optical band gap energy (1.28eV).

### 2.1.3 Polypeptide synthesis

Polypeptides are synthesized by ring opening polymerization of cyclic N-carboxyanhydride (NCA) monomers<sup>33</sup> (Leuch's anhydrides) which were coincidentally discovered by Hermann Leuchs et al.<sup>34-36</sup> in 1900s during the purification of N-methoxy or etoxycarbonyl amino acid chlorides *via* distillation.

Although, some derivatives are commercially available, NCA monomers could be synthesized by cyclization reaction of appropriate  $\alpha$ -amino acids. Wang and coworkers<sup>37</sup> synthesized  $\gamma$ -benzyl-L-glutamate N-carboxyanhydride (BLG-NCA) by the esterification reaction between benzyl alcohol and L-glutamic acid and followed by anhydride formation in the presence of diphosgene at elevated temperature as shown in Scheme 2.7. The main purification method for NCAs is recrystallization technique.

The polymerization of NCAs were first performed in 1920s by ring opening polymerization (ROP) initiated by water, primary amines and alcohols.<sup>38,39</sup> Nowadays, polypeptides of high molar mass can be synthesized on a large scale by conventional initiators (primary, secondary and tertiary amines, water and alcohols) as well as numerous other types of initiators like hexamethyldisilazanes, organometallic initiators, imidazoles, macroinitiators etc.<sup>40</sup>



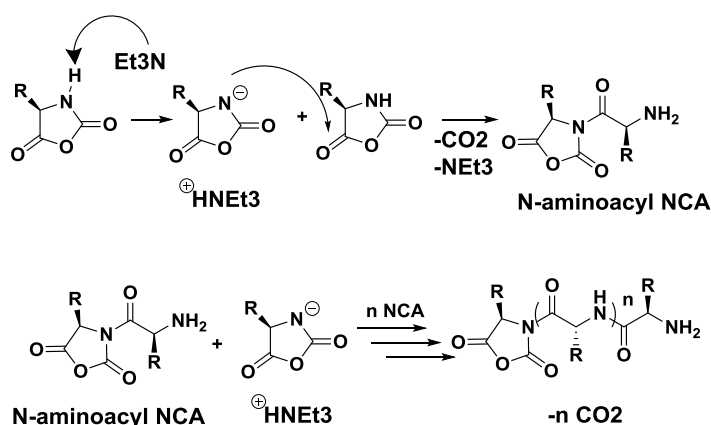
**Scheme 2.7:** Proposed synthesis of  $\gamma$ -benzyl-L-glutamate N-carboxyanhydride (BLG-NCA)<sup>37</sup>

### 2.1.4 Synthesis and application of poly( $\gamma$ -benzyl-L-glutamate)

The poly( $\gamma$ -benzyl-L-glutamate) (**PBLG**) is synthesized by ring-opening N-carboxyanhydride (**NCA-ROP**) polymerization<sup>40</sup> of NCA- $\gamma$ -benzyl-L-glutamate monomer initiated *via* nonionic initiators. Depending on the nature of the initiator and solvent, **ROP** polymerization can proceed by two pathways. Due to the basic nature of tertiary, secondary amines and alkoxides, polymerization takes place by activated monomer mechanism (**AMM**) (see Scheme 2.8). In this mechanism the initiator subtracts a proton from the NH group on NCAs to form an anion. This process is called preinitiation step and the main initiation step starts with anionic NCA's attack to the NCA monomers from 5-CO group. Propagation step starts by the attack of the newly formed NCA anion to the monomer or linear growing chain end at each step until all monomers are consumed.<sup>40</sup> The base initiated ring opening polymerization can only occur in N-unsubstituted NCAs and strongly depends on solvent polarity. Cosani et al.<sup>41</sup> conducted PBLG synthesis in DMF/Dioxane mixtures initiated with diisopropylamine (**DIPA**) and investigated the molecular weight (**Mw**) and polymerization rate dependence on the solvent composition.

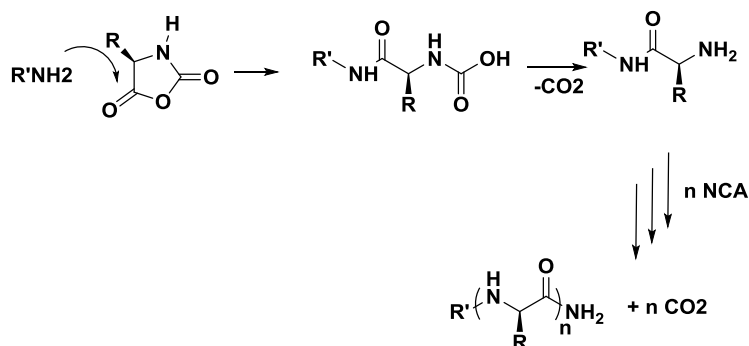
They found that when DMF concentration is increased  $M_w$  of the polymers decreased but reaction rate increased due to the increase of the basicity of DIPA in DMF. The disadvantage of this mechanism is the difficulties to control the average degree of polymerization (**DP**).

The second mechanism is called normal amine mechanism (**NAM**) which occurs with nucleophilic primary amine, alcohol and water initiated polymerizations. N-substituted and unsubstituted NCAs can be polymerized with this mechanism. The primary amine initiation is mostly preferred due to the easy control on average degree of polymerization (**DP**) by controlling initial monomer/initiator ratio ( $DP = [M_0/I_0]$ ). The advantage of primary amine initiated ROP is the faster initiation rate that yields narrow molecular weight distribution and easy controllable chain length.<sup>40,42</sup>



**Scheme 2.8:** Proposed activated monomer mechanism (**AMM**)<sup>43</sup>

The initiation process starts with a nucleophilic attack of the initiator on the 5-CO position which ends up by formation of unstable carbamic acid intermediate. The intermediate stabilizes by  $CO_2$  release and formation of new free primary amine group to initiate the next NCA monomer until all monomers are consumed as shown in Scheme 2.9.

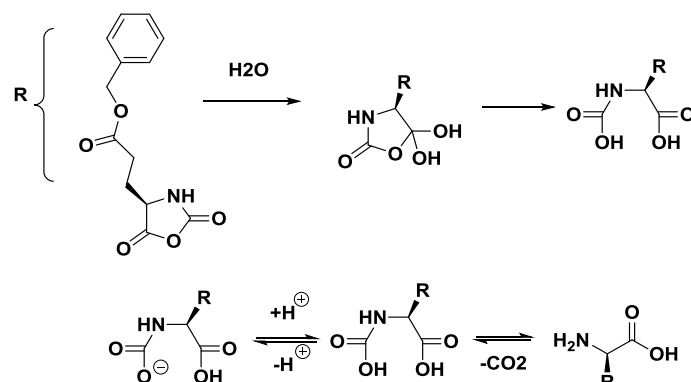


**Scheme 2.9:** Proposed normal amine mechanism (**NAM**)<sup>43</sup>

During polymerization, the chain growth pathway can switch back and forth between both mechanisms and lead to undesired side reactions.<sup>43</sup> However, these problems can be eliminated and controlled.

The primary amine initiated NCA-ROP is the mostly preferred method for polypeptide synthesis due to the easy control of the degree of polymerization, easy functionalization of

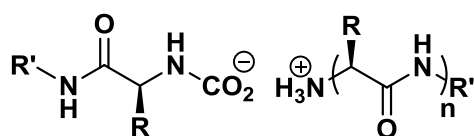
chain-ends and metal free nature. However, during primary amine initiated polymerization reaction, several side reactions may occur depending on the reaction conditions (temperature, solvent, etc.), initiators and nature of the NCA monomers.



**Scheme 2.10:** Hydrolysis of BLG-NCA <sup>40</sup>

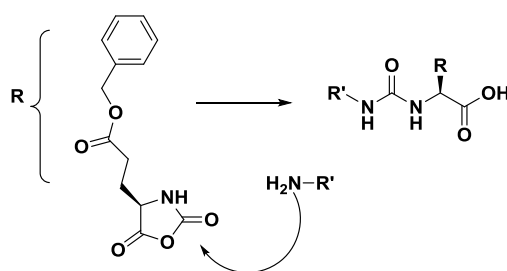
Impurities presented in NCA monomers (HCl, water, isocyanates, etc.) or in the initiator may cause several problems during polymerization. The water contamination influences the polymerization rate by acting as an initiator and leads to uncontrolled growth of the polymer chains or causes the hydrolysis of BLG-NCA monomer as shown in Scheme 2.10. <sup>40</sup>

The byproduct of NCA polymerization, carbon dioxide, can also cause side reactions when CO<sub>2</sub> removal is not performed. The intermediate compound in NAM can form carbamid acid salt with the propagating chain-end as shown in Scheme 2.11. <sup>40,44</sup> This salt causes uncontrolled chain grow by acting as catalyst in the propagating step. However, this process can be eliminated in DMF due to the acidic nature of the solvent and continuous removal of CO<sub>2</sub> during the polymerization process by static vacuum or nitrogen flow. <sup>44</sup>



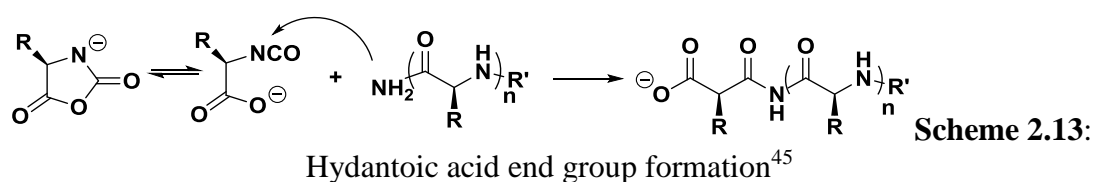
**Scheme 2.11:** Carbamid acid salt formation between two polypeptide chains <sup>40</sup>

One of the possible side reaction that causes termination of the propagation is a nucleophilic attack of the active primary amine chain-end to the 2-CO position of NCA as shown in Scheme 2.12.



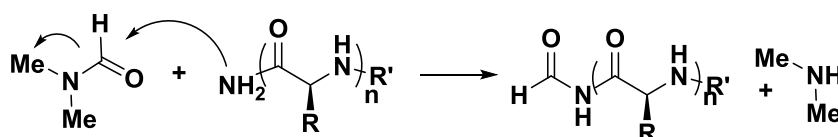
**Scheme 2.12:** Secondary reaction during BLG-NCA polymerization <sup>40</sup>

The primary amine chain-end may also subtract a proton from the NH group and create a NCA anion. Consequently, the NCA anion rearranges to an isocyanatocarboxylic acid that reacts with the propagating chain-end and forms dead hydantoic acid end groups (see Scheme 2.13).<sup>45</sup>

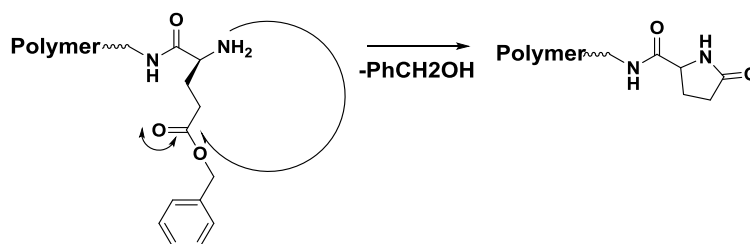


The active chain-end may also react with DMF<sup>43</sup> and causes dead chain formation as shown in Scheme 2.14.

Another unfavorable termination reaction is intramolecular “back biting” which is characteristic for primary amine initiated polyglutamates.<sup>42,46</sup> This process affects molecular weight distribution of the polymer due to the loss of primary amine functionality by intramolecular cyclization as represented in Scheme 2.15.



**Scheme 2.14:** Chain-end termination by DMF solvent.<sup>43</sup>



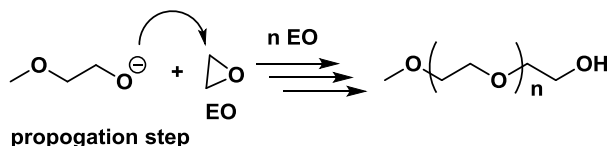
**Scheme 2.15:** Termination of the PBLG chain end by “back biting” reaction<sup>42</sup>

Most of these side reactions can be reduced or prevented by working in very cleaned and dried conditions and by decreasing the polymerization temperature to 0°C.<sup>47</sup> This enables controlled living polymerization with a high yield of active chain-ends and narrow dispersity. Francois and coworkers<sup>48</sup> investigated the temperature effect on ε-trifluoroacetyl-L-Lysine NCA (TFA-Lys NCA) polymerization in DMF. The results show uncontrolled behavior in n-hexylamine initiated polymerization at room temperature, which ends up with 78% dead chains. Increasing the reaction temperature up to 50°C did not change results. However, decreasing reaction temperature to 0°C yielded 99% living chain-ends. This can be explained by a higher activation energy of the side reactions at lower temperature.<sup>48</sup>

### 2.1.5 Poly(ethylene glycol) synthesis, properties and application

Poly(ethylene oxide) (PEO) also often referred as poly(ethylene glycol) (PEG) is synthesized by living anionic ring-opening polymerization (LROP) of ethylene oxide (EO)<sup>49</sup> (Scheme 2.16) which was first reported in early 1940s by P. J. Flory.<sup>50</sup>

A wide variety of PEGs or PEOs with different functionality (monofunctional, bifunctional, heterobifunctional etc.) and architecture (linear, branched, hyperbranched, star like, brush like etc.) is commercially available. Generally, the name PEG refers to polymers with  $M_w < 20$  kD and polymers with  $M_w > 20$  kD are called poly(ethylene oxide) (**PEO**), poly(oxyethylene) (**POE**) or poly(oxirane).<sup>51</sup>



**Scheme 2.16:** PEG synthesis<sup>49</sup>

These polymers have a broad application area due to the many attractive features like good solubility in water and in organic solvents, biocompatibility, easy modification, stealth properties (reduce enzyme immunogenicity) and metal complexation ability.<sup>52</sup> Moreover, PEG is a FDA approved nontoxic polymer and is extensively used in cosmetic products,<sup>53</sup> food industry and in pharmaceutical products.<sup>54</sup> However, the World Health Organization limited the molecular weight range of PEGs up to 10 kD for medical applications<sup>53</sup>, in order to make sure it can be properly excreted.

Due to the lower protein adsorption, lower cell adhesion and lower immunogenicity PEGs are conjugated to many biomolecules and to the surface of medical devices.<sup>54</sup> Such covalent attachment of PEG, also referred as “PEGylation”, stabilizes biomolecules, decreases toxicity, increases blood circulation lifetime, and increases the size of the molecule and accordingly reduces the renal clearance from the bloodstream.<sup>55</sup> There are many PEGylated drugs that are under clinical investigation or FDA approved for use in humans. Abuchowski and coworkers<sup>56</sup> have first reported the PEGylated protein (bovine serum albumin) and showed the loss of immunogenicity of the protein and increase the circulation lifetime after modification with sufficient amount of PEG chains in 1977. After this discovery many studies have been performed on different proteins and applied in medicine.<sup>55,57-59</sup> A list of some clinically used, FDA approved Protein-PEG conjugates is shown in Table 2.1.

The metabolism of the PEG in human and animal body takes place by oxidation of alcohol groups to carboxylic acids by the aldehyde dehydrogenase as illustrated in Figure 2.1.<sup>59</sup> Moreover, the clinical studies show that the metabolism depends on the molecular weight: the percentage of clearance by metabolism increases when the molecular weight decreases (PEG400 25%, PEG1000 15%, PEG6000 4%).<sup>59</sup> If not metabolized, PEG can also be cleared by renal filtration, especially when injected intravenously.

PEG is also used to coat a photosensitizer (m-Tetrahydroxyphenyl chlorin, **mTHPC**) encapsulated liposomal nanoparticles to prevent protein-liposome interaction and decrease the uptake by reticuloendothelial system (**RES**). This **PEG** coated liposomal drug is known as FosPeg<sup>®</sup> and is used in treatment of human prostate cancer and in vitro studied in human colon cancer cells.<sup>60</sup>

**Table 2.1:** The list of FDA approved Protein-PEG conjugates <sup>55</sup>

Commercial name	Protein	PEG size	Uses in the treatment of	Approved in
Adagen <sup>®</sup>	Adenosine deaminase	5 kDa	Severe combined immunodeficiency disease	1990
Oncaspar <sup>®</sup>	L-Asparagine	5 kDa	Acute lymphoblastic leukemia	1994
Krystexxa <sup>®</sup>	Mammalian urate oxidase (monomer)	10 kDa	Chronic gout	2010
Somavert <sup>®</sup>	hGH antagonist B2036	5 kDa	Acromegaly	2003

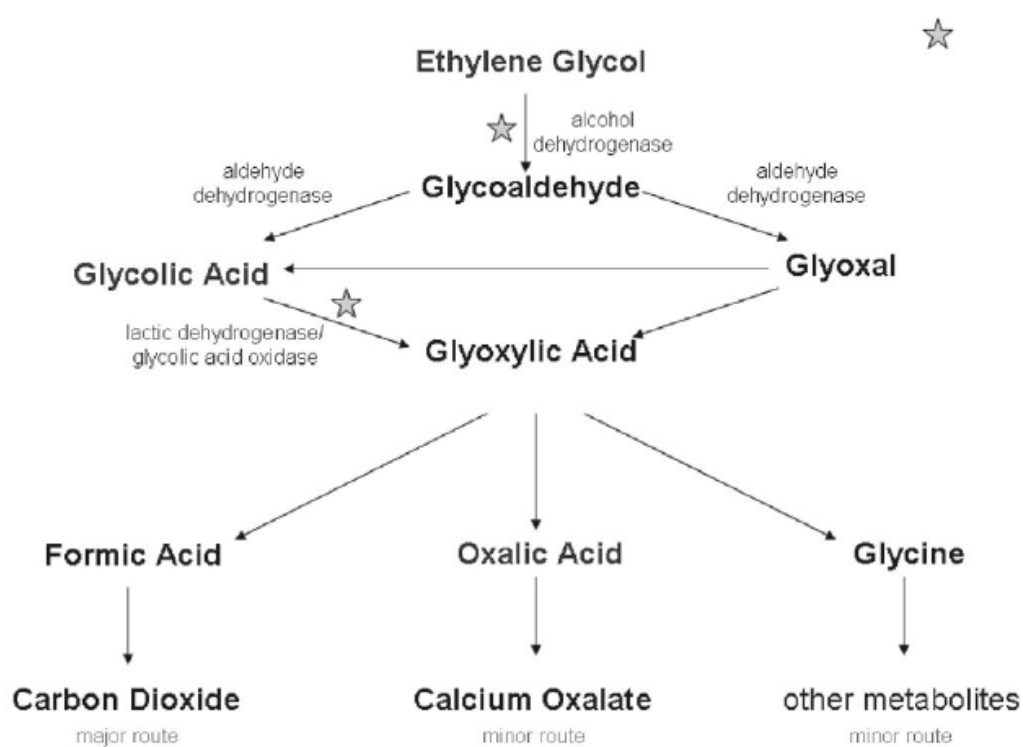
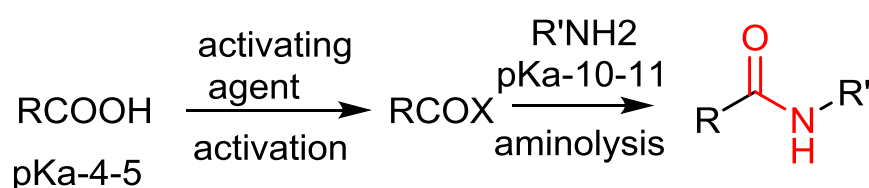


**Figure 2.1:** *In vivo* metabolism of PEG<sup>58</sup>

## 2.1.6 Peptidic coupling reaction

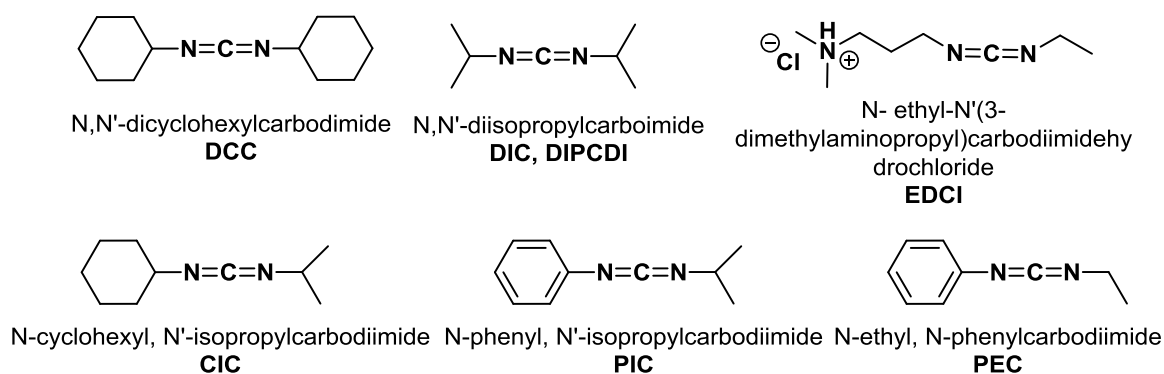
Peptide coupling reaction between carboxylic and amine groups plays an important role in nature and in chemistry. In nature, different peptides or proteins are formed *in vivo* by complex and selective peptidic coupling reactions between  $\alpha$ -amino acids or peptides. In chemistry, biochemistry or pharmaceutical industry it gives an opportunity to covalently bond different molecules, especially biomolecules, since majority of them (drugs, proteins, antibodies, peptides, etc.) bears an amine or a carboxylic functionality.<sup>61</sup>

Peptidic coupling reaction is a condensation reaction happening between amines and carboxylic acids with the help of activating agents that ends up with an amide bond formation. The reaction takes place by forming an active intermediate followed by the addition of an amine as shown in Scheme 2.17.



**Scheme 2.17:** Peptide bond formation<sup>61</sup>

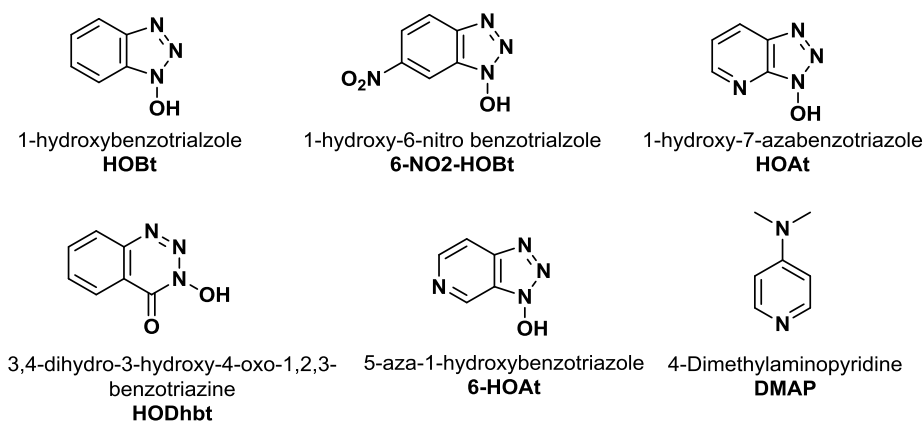
Although the condensation reaction can take place at very high temperature (160-180°C) without activation agent it is not suitable for many temperature sensitive molecules.<sup>62</sup> The peptidic coupling reaction in the presence of activation agents (most traditional ones are carbodiimides) takes place by reaction of the carboxylic acid with carbodiimide to form an O'acylisourea, which react with the amine at 0°C and form the desired product and urea as a byproduct (Scheme 2.20). Different carbodiimides<sup>63</sup> are commercially available but some commonly used ones like DCC, DIC, EDCI etc. are shown in Scheme 2.18.



**Scheme 2.18:** Commercially available carbodiimides for peptidic coupling reaction<sup>63</sup>

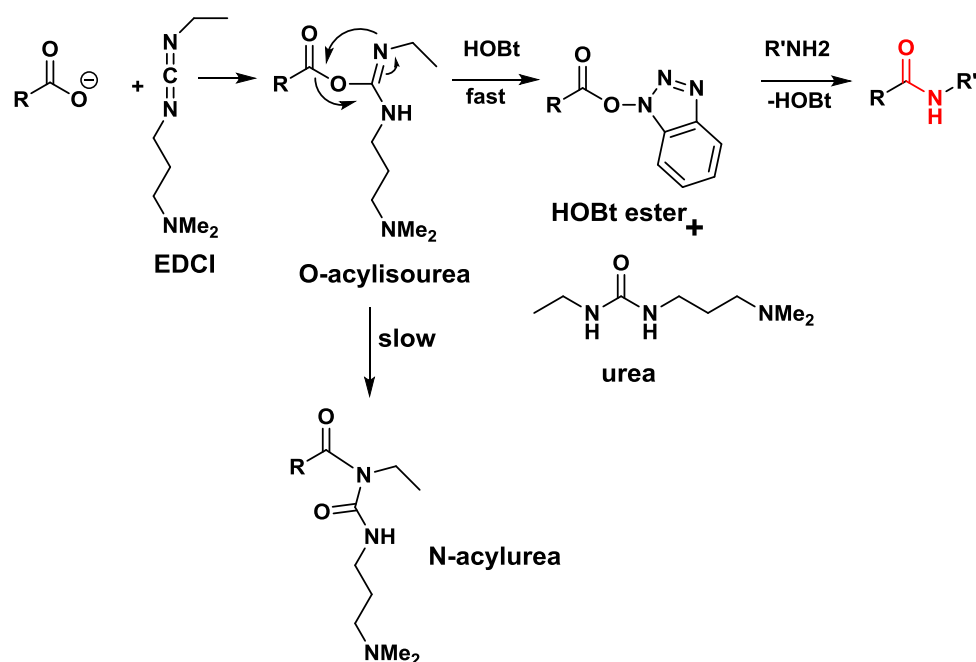
Moreover, during peptidic coupling reaction, undesired side products like unreactive N-acylurea may form due to the racemization and acetyl transfer reactions. Reducing the reaction temperature can reduce the formation of side products but is not enough to have efficient coupling yield. Adding selective nucleophiles<sup>63</sup> like DMAP, HOBT, HOAt, etc. (see Scheme 2.19), helps to form more active intermediates by reaction with an O'acylisourea.





**Scheme 2.19:** Additives for peptidic coupling<sup>63</sup>

Upon the addition of amine at 0°C, the aminolysis of the intermediate takes place faster compared to the competing acetyl transfer reaction, which helps to prevent side reaction and increase the coupling yield as shown in Scheme 2.20.



**Scheme 2.20:** Carbodiimide mediated coupling reaction<sup>63</sup>

The challenge of the chemists is finding an appropriate activator and additive that match the reaction condition of their compounds to get good coupling yield since the reactivity of each activator and additive are different in different conditions. This difference brings one more challenge, which is the purification of the resulting urea after the reaction. Dicyclohexyl urea DHU is rather insoluble<sup>61</sup> in dichloromethane which can be eliminated by filtration. The urea of DIC is highly soluble in DCM and can be eliminated by washing with DCM if the desired product is insoluble in it. Mostly preferred activator for carboxylic group is EDCI (with HOBT additive) due to the water solubility of its urea byproduct that provides an easy purification. Moreover, EDCI coupling reactions in the presence of HOBT is mostly preferred in biology due to the reactivity (>90% amide yield) in water as well.<sup>64</sup>

### 2.1.7 “Click chemistry”

The “click chemistry” concept was first introduced by Sharpless et al.<sup>65</sup> in 2001. They defined requirements for a click reaction like conditions should be simple, reagents should be readily available, easily purified and should give high yield. Moreover, the purification step should not require chromatographic techniques and should be done by simple methods like recrystallization, precipitation or distillation.<sup>65</sup> The overall requirements for both molecular and polymer click reaction are represented in Figure 2.2.<sup>66</sup> Click chemistry is a very useful tool especially for polymer chemistry by providing easy functionalization, linking of several polymer blocks, or to create dendritic macromolecules, etc.

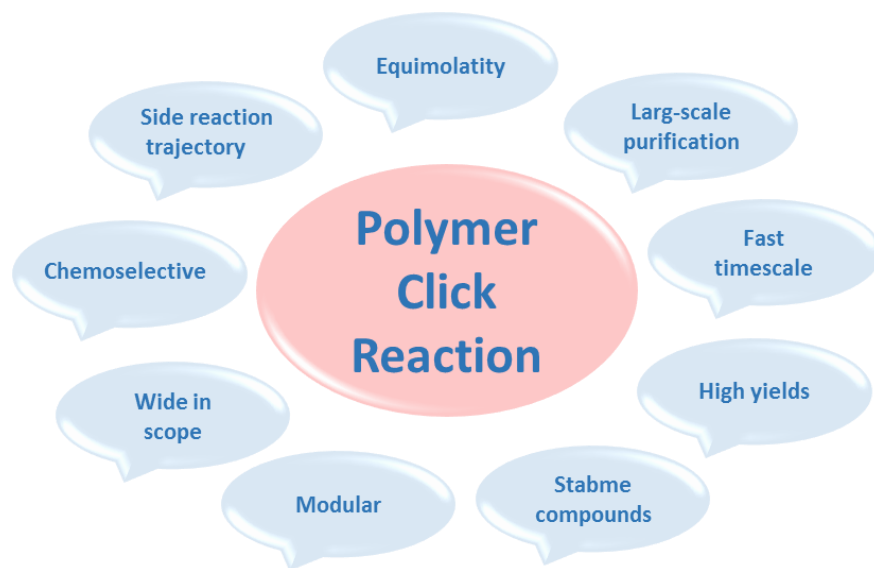
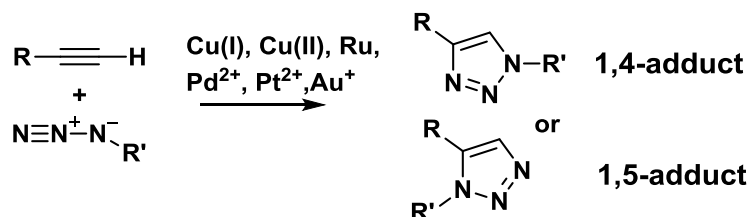


**Figure 2.2:** Requirement for click reaction (adapted from ref.<sup>66</sup>)

Some carbon-heteroatom bond formation reactions, Diels-Alder reaction, ring opening reactions, “non-aldol” type carbonyl chemistry, Michael addition, Huisgen’s reaction (copper assisted azide/alkyne cycloaddition) etc. are all good examples of click reaction.<sup>65</sup>

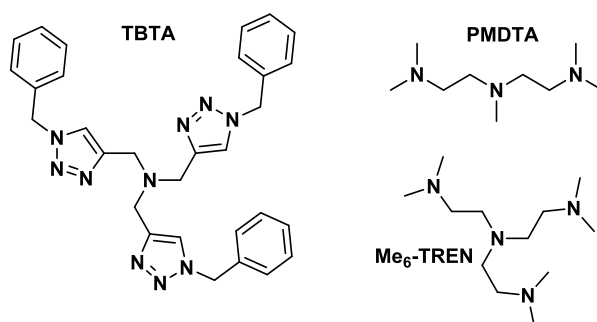
### 2.1.8 Copper-catalyzed azide-alkyne cycloaddition reaction

Copper-catalyzed azide-alkyne cycloaddition reaction (CuAAC), the catalyzed version of the Huisgen cycloaddition reaction, is the mostly used “click” reaction in polymer chemistry due to its regioselectivity, high tolerance to functional groups, mild conditions, easy purification etc.<sup>67</sup> Quantitative amount of polymer blocks, peptides, drugs, biomolecules etc. could be clicked together by a triazole ring.



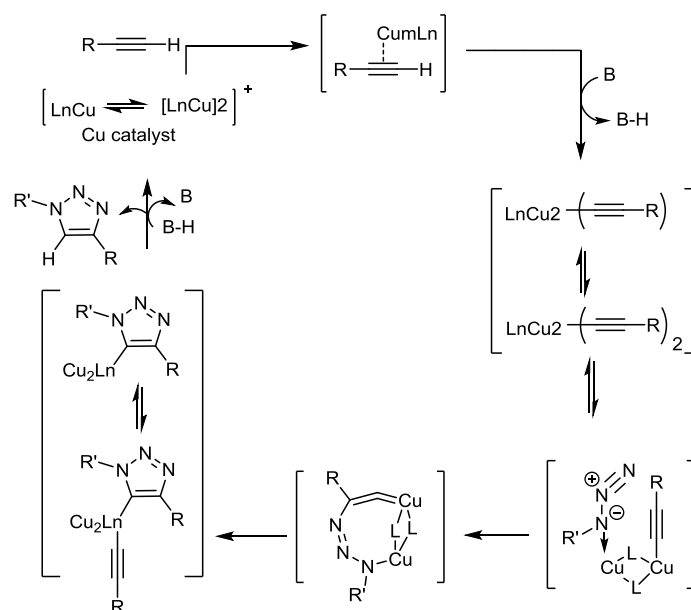
**Scheme 2.21:** Copper-catalyzed azide-alkyne cycloaddition reaction (CuAAC)

Reaction could be catalyzed by several metals like Ru complexes to yield 1,5-regioisomer<sup>68</sup>, Pd<sup>69</sup> and Au<sup>70</sup> salts that yield 1,4 adduct as well as 1.5 adduct. However, Cu(I) catalyzed reactions are milder and highly regioselective to yield 1,4-adduct. The copper(I)-catalyzed 1,3-dipolar cycloaddition reaction attracts more attention since 2002 after the introduction of Cu(I) as highly reactive catalyst for triazole formation by Tornøe and Meldal for peptide synthesis application.<sup>71</sup> Moreover, in the presence of appropriate ligands, Cu(I) catalyst shows high reactivity both in water and in organic solvent as well as on solid support.<sup>71,72</sup> In addition, CuSO<sub>4</sub> · 5H<sub>2</sub>O in the presence of excess reducing agent (sodium ascorbate) to reduce Cu(II) to Cu(I) oxidation state during the reaction is mostly preferred for aqueous reactions and even can be performed under open air conditions. In polymer chemistry, CuBr or CuI are used as a Cu(I) sources and require high temperature to facilitate Cu-alkyne complex formation or basic ligands (see Scheme 2.22) and inert atmosphere to prevent oxidation of the Cu(I) and a loss catalytic activity.



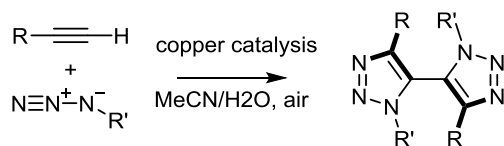
**Scheme 2.22:** Common ligands used in CuAAC reaction<sup>72</sup>

The proposed mechanism of the CuAAC reaction is shown in Scheme 2.23. First Cu coordinates with the  $\pi$ -electrons of the alkyne group and lower the pK<sub>a</sub> of the proton of the alkyne group. Cu-alkyne complex reacts with azide and forms a 6-membered metallocycle. This cycle then rearranges itself and protonation of the obtained Cu-triazole complex gives the desired product.<sup>72</sup>



**Scheme 2.23:** Proposed mechanism of the azide/alkyne click reaction<sup>67</sup>

Despite of the fact that CuAAC reaction plays an important role in polymer and organic chemistry, some minor side reactions may also presented.



**Scheme 2.24:** Dimerization of the triazole<sup>73</sup>

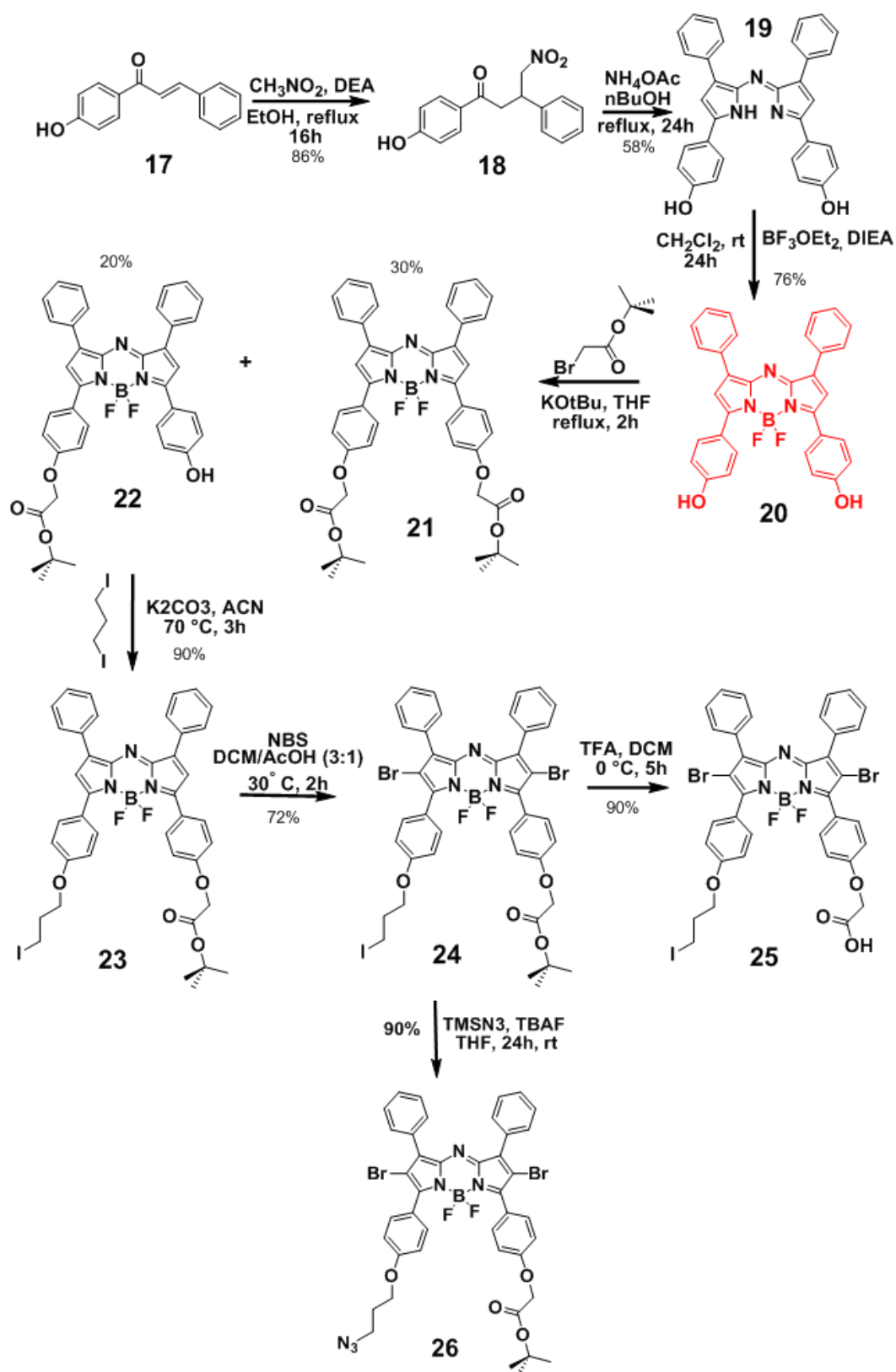
For example, Yu and Kevin<sup>73</sup> reported that during CuAAC reaction triazol rings can dimerize and even oxidative dimers can become the main product under basic conditions ( $K_2CO_3$ , LiOH,  $Na_2CO_3$ , etc.) as shown in Scheme 2.24.

## 2.1 Results and discussion

### 2.2.1 Synthesis of the building blocks

#### 2.2.1.1 Synthesis of the photosensitizer

Novel photosensitizers (**25**) and (**26**) from the aza-BODIPY family, bearing the appropriate functional groups for the coupling of the polymer chains were synthesized and characterized. To this end the multistep reaction shown in Scheme 2.25 was developed and optimized. Although the synthesis of compound **20** was reported by O'Shea and coworkers<sup>74</sup>, we further functionalized and brominated it to increase singlet oxygen generation yield and to obtain the multifunctional photosensitizers as shown in Scheme 2.25.

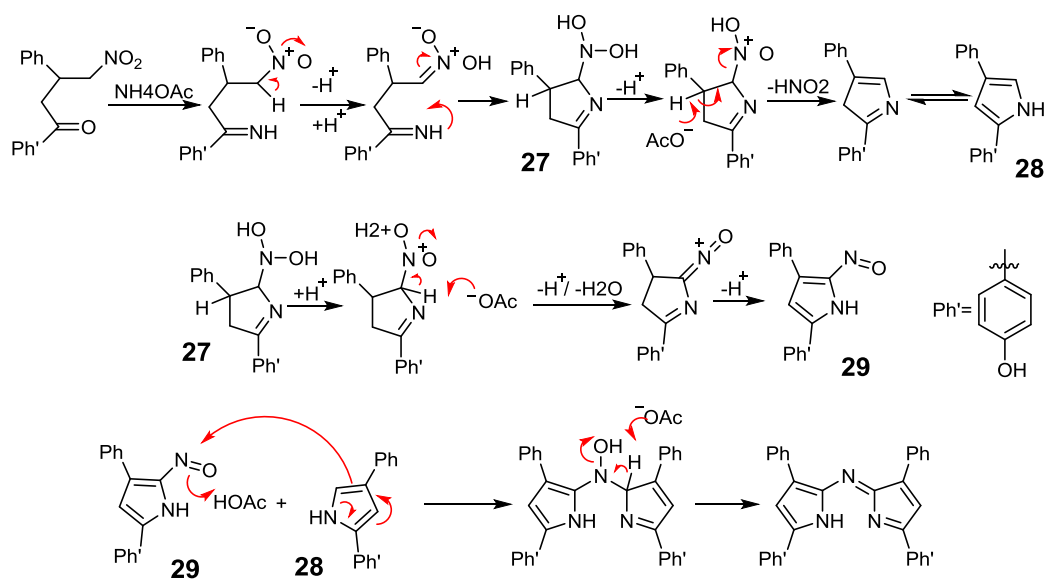


**Scheme 2.25:** Synthesis scheme of the dye 2,8-dibromo-3-(4-(carboxymethoxy)phenyl)-5,5-difluoro-7-(4-(3-iodopropoxy)phenyl)-1,9-diphenyl-5H-dipyrrolo[1,2-c:2',1'-f][1,3,5,2]triazaborinin-4-ium-5-uide (**25**) and 7-(4-(3-azidopropoxy)phenyl)-2,8-dibromo-3-(4-(2-(tert-butoxy)-2-oxoethoxy)phenyl)-5,5-difluoro-1,9-diphenyl-5H-dipyrrolo[1,2-c:2',1'-f][1,3,5,2]triazaborinin-4-ium-5-uide (**26**)

Compound **18**<sup>74</sup> was obtained by a Michael addition reaction of the 4'-hydroxy chalcone with nitromethane in the presence of diethylamine (DEA).

The 1-(4-hydroxyphenyl)-4-nitro-3-phenylbutan-1-one **18** was then refluxed with excess amount of ammonium acetate (35eq.) in n-butanol for 24h to end up with dark blue crystals of bis-phenol-substituted azadipyrromethene (product **19**). The pure product crystallized inside the reaction flask while the solvent cooled down with 58% isolation yield.

During the condensation process, the first pyrroles are formed and then nitrosilated in the reaction mixture. The second condensation reaction takes place with the pyrrole and nitrosopyrroles ring to form aza-dipyrin ligands through the following complex mechanism (see Scheme 2.26).

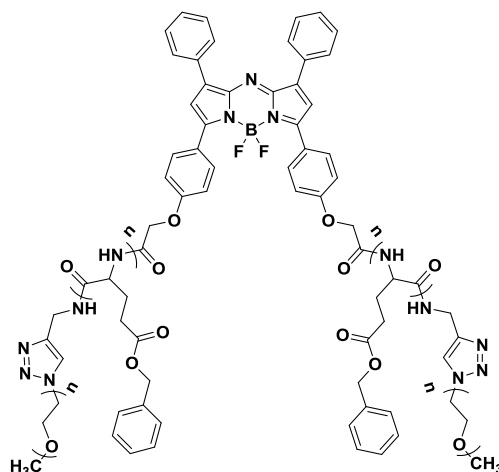


**Scheme 2.26:** Condensation of nitromethane adduct of chalcone <sup>75</sup>

BF<sub>2</sub> chelate of compound **19**, was obtained by treating it with boron trifluoride diethyl etherate (BF<sub>3</sub> Et<sub>2</sub>O) and diisopropylethylamine (DIEA) in dry dichloromethane and purified by column chromatography on silica gel.

The BF<sub>2</sub> chelate of bis-phenol-substituted azadipyrromethene **20** was monofunctionalized with tert-butyl bromoacetate by using the bulky base, potassium tert-butoxide (tBuOK), in dry tetrahydrofuran (THF) and easily purified by column chromatography on silica gel due to polarity difference with bi-functionalized product. Although the desired product yield was low in this condition (20%), O'Shea and coworkers<sup>76</sup> recently have reported the synthesis of product **22** as an intermediate compound with 75% yield. They carried out the reaction in 20min in anhydrous DMSO and used cesium fluoride (CsF) instead of tBuOK.

The side product of the reaction, the difunctional product **21** was used in the master thesis of Mathie Najberg<sup>77</sup> "Development of Triblock Copolymers for Nanomedicine Applications" under the supervision of Prof. Charles-André Fustin. She synthesized PBLG based triblock copolymers shown in Scheme 2.27.



**Scheme 2.27:** Aza-BODIPY functionalized PBLG based triblock copolymer

A second alkylation reaction with 1,3-diiodo propane was performed on product **22** to obtain the desired asymmetric product **23** which was easily purified by column chromatography on silica gel.

We found out that performing the bromination on product **23**, i.e. after both alkylation reactions, gives more stable products compared to when bromination is performed on product **20** or **22**. Ionic bromination reaction was performed at room temperature with *n*-bromosuccinimide (NBS) in acidic environment (CHCl<sub>3</sub>: Acetic acid, 3:1, v/v). Purification by column chromatography on silica gel yielded the dark red metallic solid product **24** with 72% yield. Heavy atom addition to 2 and 6 positions of the aza-BODIPY core was confirmed by disappearance of two protons peak at 7ppm in <sup>1</sup>H-NMR spectrum (see Figure A2.9). Moreover, the modification on the backbone caused a 0.81 ppm shift of the BF<sub>2</sub> triplet peak in <sup>11</sup>B-NMR and can be easily visualized from Figure 2.3.

Product **24** was treated with trifluoroacetic acid (TFA) in DCM to obtain the carboxylic group bearing product **25**. Pure crystals of the **25** were obtained with high yield (92%) by recrystallization method and dried under high vacuum. <sup>11</sup>B-NMR confirmed the presence of the BF<sub>2</sub> complex after the deprotection in these highly acidic conditions (see Figure A2.17).

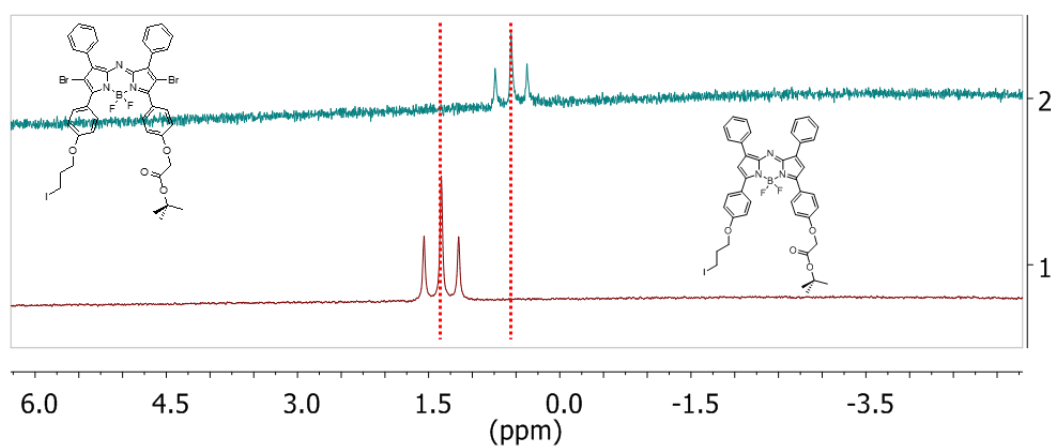


**Figure 2.3:** <sup>11</sup>B-NMR spectrum of (1) compound **23**, (2) compound **24** (500 MHz, CDCl<sub>3</sub>)

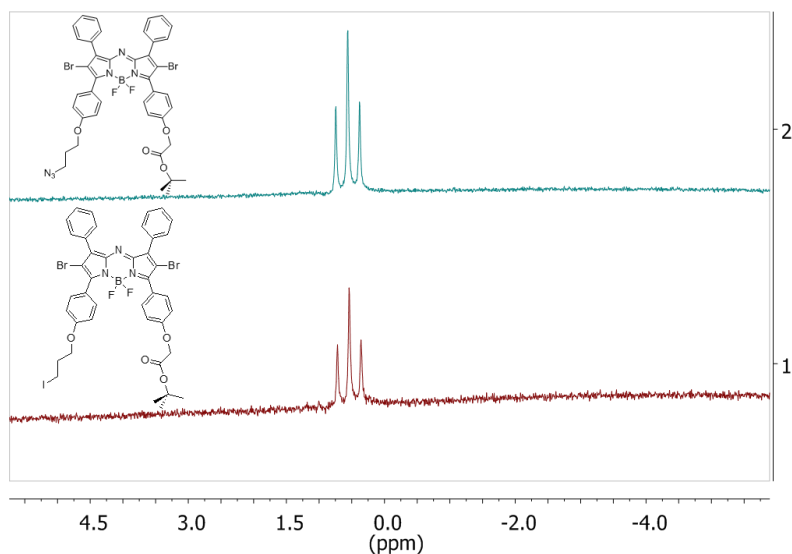


**Figure 2.4:**  $^{11}\text{B}$ -NMR spectrum of (1) compound **24** (2) compound **26** (500 MHz,  $\text{CDCl}_3$ )

In the last step, the iodine group of **24** was converted into an azide group under mild conditions by using trimethylsilyl azide ( $\text{TMSN}_3$ ) and tetrabutylammonium fluoride (TBAF) and purified via recrystallization in a petroleum ether and DCM mixture. It is worthwhile to note that after using several azide conversion reactions we observed that aza-BODIPY possesses high sensitivity to basic/nucleophilic conditions and DMF solvent, it can thus be easily degraded during the reaction and forms several side products. Due to the mild conditions of this reaction we could obtain the pure azide functionalized **26** with high yield (90%).

No shifting or new peak formation was observed in  $^{11}\text{B}$ -NMR (Figure 2.4) which confirms that there was no modification on the F or Br groups of the molecule. Moreover, an azide functionalization can be proved by the presence of the characteristic sharp peak at  $2096\text{ cm}^{-1}$  wavenumber on the FTIR spectrum (Figure 2.5).

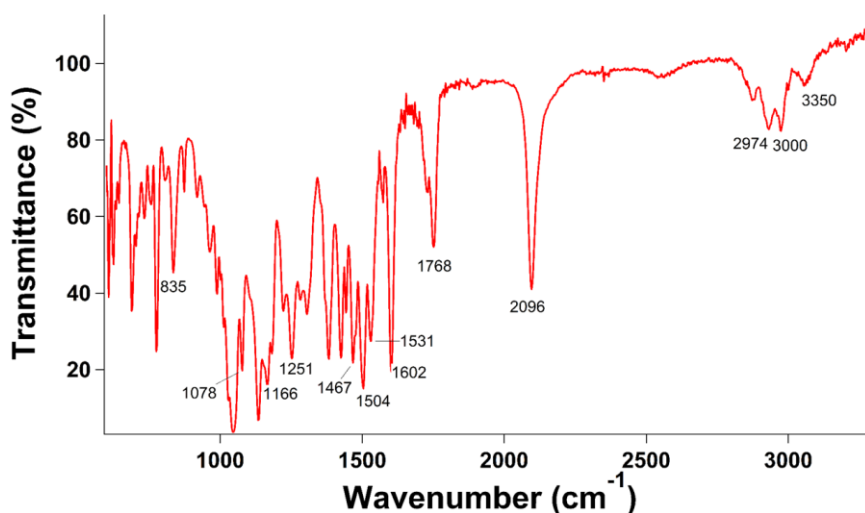


**Figure 2.5:** FTIR transmittance spectrum of compound **26** (ATR)

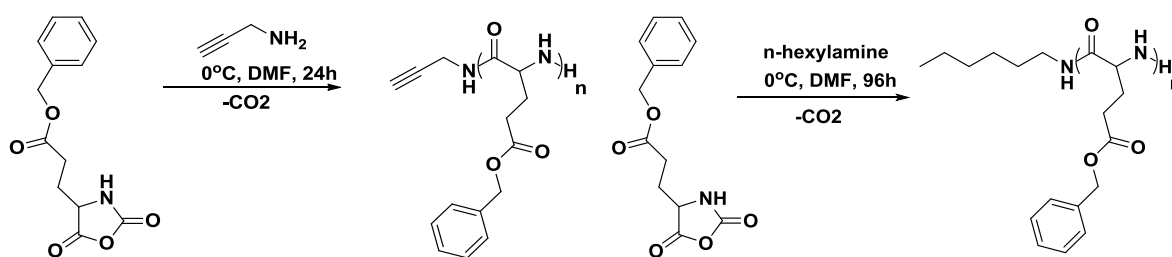
After each functionalization, absorption and emission spectra were recorded. No big shifts were observed depending on the functional groups (Figure A4.1, Chapter 4). The detailed optical characterizations of the aza-BODIPY dyes are shown in Chapter 4.



### 2.2.1.2 Synthesis of the polymer blocks

The poly ( $\gamma$ -benzyl-L-glutamate) (PBLG) was chosen as hydrophobic block and synthesized by ring-opening N-carboxyanhydride (NCA) polymerization.<sup>78</sup> To increase the primary amine yield at the chain-end of the polymer, reactions need to be performed at 0°C (to avoid the previously described chain-end cyclisation side reaction). In the first step, we performed the polymerization of the BLG-NCA in dry DCM at 0°C due to the easy removal of the solvent. However, we obtained PBLG with high dispersity and observed the formation of a second population with small molecular weight. This could be due to the termination of polymerization of some propagating chains due to the low polymer solubility in DCM, decreasing thereby the accessibility of the active chain-end at low temperature. However, when we repeated the reaction in DMF at 0°C we obtained polymers with narrow weight distribution and with high primary amine functionality.

Three PBLG with similar degrees of polymerization were synthesized at 0°C in DMF as shown in Table 2.2 and characterized by <sup>1</sup>H-NMR spectroscopy and size exclusion chromatography (SEC). To obtain different functionalities at the chain-end two different, carefully purified initiators, n-hexylamine and propargylamine, were reacted with NCA- $\gamma$ -benzyl-L-glutamate (NCA-BLG) monomer to obtain the desired polymers (Scheme 2.28).



**Scheme 2.28:** NCA polymerization of  $\gamma$ -benzyl-L-glutamate

**Table 2.2.** Synthesis conditions of the heterobifunctional and monofunctional PBLG polymers and their analytical data from NMR and SEC.

PBLG	Initiator, T <sup>a</sup> , t <sup>b</sup>	Feed ratio [M <sub>0</sub> /I <sub>0</sub> ]	DP <sup>c</sup>	Đ <sup>d</sup>	M <sub>n</sub> <sup>d</sup> [g/mol]	f%	y%
PBLG <sub>49</sub>	propargylamine 0 °C, 24h	50/1	49	1.14	2500	95	93
PBLG <sub>54</sub>	propargylamine 0 °C, 24h	50/1	54	1.14	3240	92	-
PBLG <sub>53</sub>	n-hexylamine 0 °C, 96h	50/1	53	1.14	2860	87	98

<sup>a</sup> temperature, <sup>b</sup> time, <sup>c</sup> degree of polymerization obtained from <sup>1</sup>H-NMR (400MHz, CDCl<sub>3</sub>/TFA 85/15%), <sup>d</sup> determined by SEC (DMF 2.5 M of NH<sub>4</sub>PF<sub>6</sub>, PEO calibration), <sup>f</sup> isolated yield and <sup>y</sup> primary amine yield on the chain end of the PBLG (calculated by acid titration)

The degree of polymerization of alkyne functionalized PBLGs was calculated by comparing the proton ratio between the two protons on the propargyl group located near the amine group (position **a**) and one proton in position **b** on the polymer backbone as can be seen from Figure 2.6.

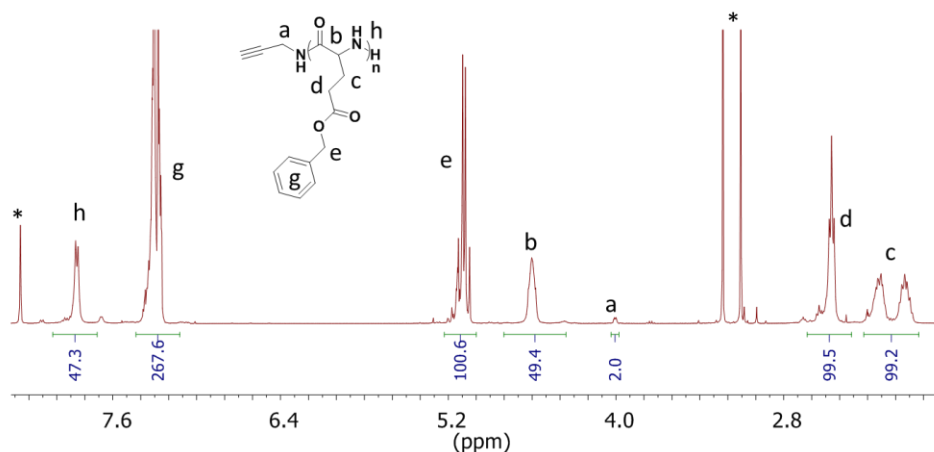


**Figure 2.6:**  $^1\text{H-NMR}$  spectrum of bi-functionalized PBLG<sub>49</sub> (400 MHz, TFA/ $\text{CDCl}_3$ , \*DMF)

The degree of polymerization of hexyl functionalized PBLG was calculated according to the  $\text{CH}_3$  proton ratio of the initiator (hexylamine) and CH protons (position **c**) on the polymer backbone as shown in Figure 2.7.

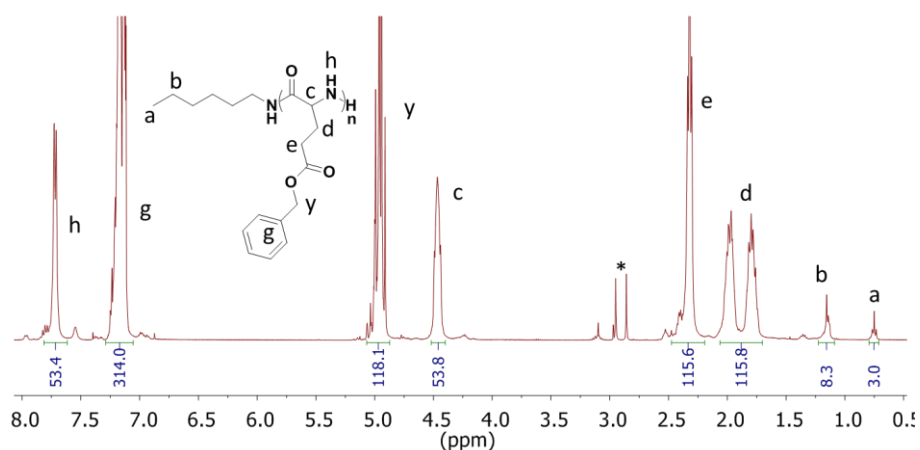
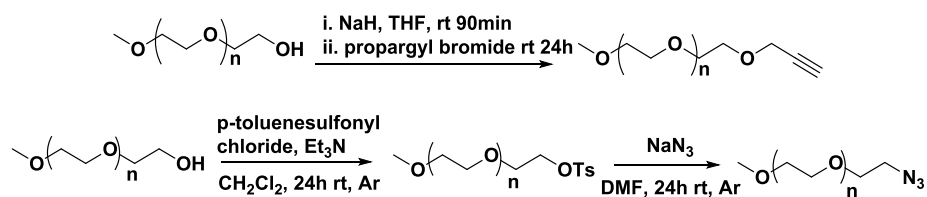


**Figure 2.7:**  $^1\text{H-NMR}$  spectrum of mono-functionalized PBLG<sub>53</sub> (400 MHz, TFA/ $\text{CDCl}_3$ , \*DMF)

As hydrophilic block, commercially available PEG (Mn: 5000g/mol and 2000g/mol) were functionalized with a propargyl or an azide group (see Scheme 2.29) to be able to further conjugate them to the photosensitizer or PBLG by the copper-catalyzed azide-alkyne cycloaddition (CuAAC) reaction.



**Scheme 2.29:** PEG functionalization

Functionalization of the PEG chain-end was followed by  $^1\text{H-NMR}$  spectroscopy. From the integration of the appropriate peaks (Figure A2.19) the alkyne group functionalization was

calculated as 90% for PEG<sub>45</sub> and 91% for PEG<sub>113</sub> and the azide functionalization yield was calculated as 93% PEG<sub>45</sub> for and 100% for PEG<sub>113</sub> (Figure A2.20 and A2.21).

## 2.2.2 Block copolymer synthesis

A library of block copolymers, PTS functionalized (with two different strategy) and non-functionalized, with different PEG chain length (2000, 5000) were synthesized. To this aim, the PTS was first conjugated to the PBLG (DP49 and DP53) via peptidic coupling between the carboxylic acid of the PTS and the primary amine chain-end of the two different PBLG. Click reactions were then performed to attach a PEG chain either on the PTS side or on the propargyl chain-end of the PBLG, to obtain PTS-PBLG-*b*-PEG, PBLG-PTS-*b*-PEG type amphiphilic block copolymers. PBLG-*b*-PEG block copolymers without PTS were also synthesized.

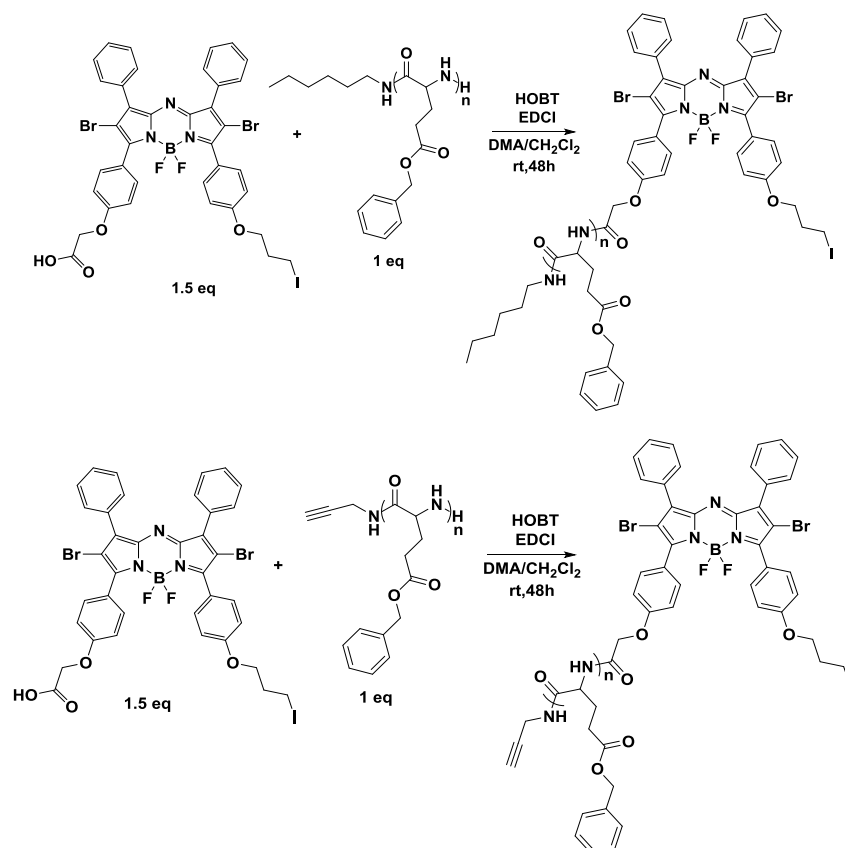
**Table 2.3:** The library of polymers

Library of polymers	$\bar{D}^a$	$\bar{M}_n$ -SEC <sup>a</sup> [g/mol]	$\bar{M}_n$ - <sup>1</sup> H NMR <sup>b</sup> [g/mol]
PBLG <sub>49</sub>	1.14	2500	10730
PTS-PBLG <sub>49</sub>	1.16	2740	11640
PTS-PBLG <sub>49</sub> - <i>b</i> -PEG <sub>45</sub>	1.19	3930	13640
PTS-PBLG <sub>49</sub> - <i>b</i> -PEG <sub>113</sub>	1.19	7540	16640
PBLG <sub>53</sub>	1.14	2860	11610
PBLG <sub>53</sub> -PTS	1.18	3230	12435
PBLG <sub>53</sub> -PTS- <i>b</i> -PEG <sub>45</sub>	1.22	4940	14435
PBLG <sub>53</sub> -PTS- <i>b</i> -PEG <sub>113</sub>	1.22	8360	17435
PBLG <sub>54</sub>	1.14	3240	11830
PBLG <sub>54</sub> - <i>b</i> -PEG <sub>45</sub>	1.15	5520	13830
PBLG <sub>54</sub> - <i>b</i> -PEG <sub>113</sub>	1.16	8910	16830

<sup>a</sup> determined by SEC (DMF 2.5 M of NH<sub>4</sub>PF<sub>6</sub>, PEO calibration), <sup>b</sup> calculated from <sup>1</sup>H-NMR (400MHz, CDCl<sub>3</sub>/TFA 85/15%)

### 2.2.2.1 Synthesis of PTS-PBLG conjugates

Photosensitizer **25** (1.5 equivalent) was grafted to the chain end of PBLG (DP49 and 53, 1eq.) by EDC (1-Ethyl-3-(3-dimethylaminopropyl) carbodiimide, 3eq.) coupling reaction in the presence of hydroxybenzotriazole (HOBT, 2 eq.) and purified by preparative size exclusion chromatography (SEC) on Bio-Beads and precipitation into cold diethyl ether. The degree of functionalization was calculated as 100% in PBLG<sub>53</sub>-PTS and 92% in PBLG<sub>49</sub>-PTS conjugates according to the <sup>1</sup>H-NMR (see Figure 2.8).



**Scheme 2.30:** The synthesis of PBLG-PTS conjugates by peptidic coupling reaction

Moreover, the functionalization of PBLG with photosensitizer was followed by SEC. PTS distribution throughout the polymer chains was monitored by the UV detector of SEC set at a wavelength of 630 nm, and compared with the signal from the DRI detector. The chromatograms obtained from both UV and DRI detectors for PBLG<sub>49</sub>-PTS and PBLG<sub>53</sub>-PTS conjugates are very similar, which confirms the successful functionalization as can be seen from Figure 2.9. However, the distribution of the PBLG<sub>49</sub>-PTS conjugate from the UV detector is slightly narrower. This may be correlated to the presence of small amount of PBLG without PTS, in agreement with <sup>1</sup>H NMR results (92% functionalization).

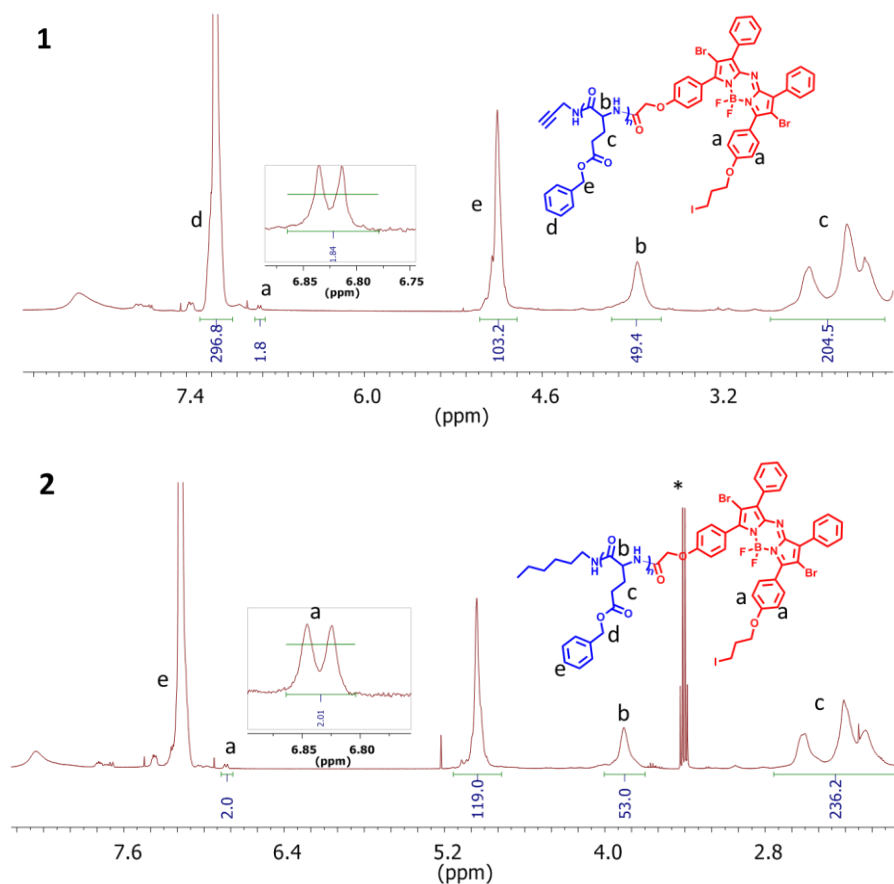


**Figure 2.8:**  $^1\text{H-NMR}$  spectra of (1) PBLG<sub>49</sub>-PTS conjugate, (2) PBLG<sub>53</sub>-PTS conjugate (400 MHz,  $\text{CDCl}_3$ , \* $\text{Et}_2\text{O}$ )

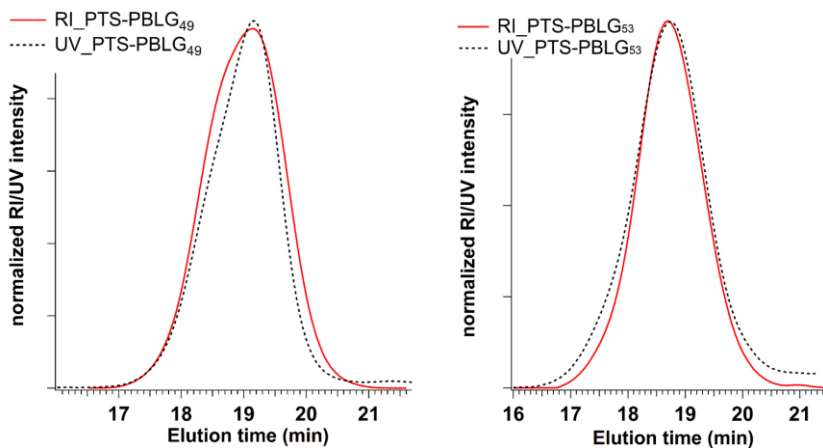
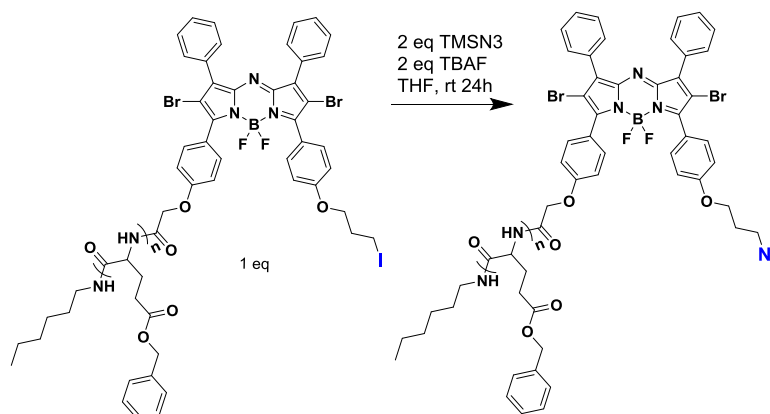


**Figure 2.9:** SEC chromatograms for PBLG<sub>49</sub>-PTS and PBLG<sub>53</sub>-PTS conjugates (DMF 2.5 M of  $\text{NH}_4\text{PF}_6$ , PEO standards)

### 2.2.2.2 Functionalization of the PTS-PBLG<sub>53</sub> conjugate

Since an azide functionalized **26** showed instability under acidic condition, we wouldn't perform deprotection of carboxylic group and conjugate it directly to the PBLG<sub>53</sub> by peptidic coupling reaction. Instead product **25** was conjugated first to the PBLG<sub>53</sub> as depicted in Scheme 2.30 and modified after.

The iodine group on the side chain of PTS was converted into an azide group under mild conditions, by using the conditions that were optimized for **26** (see Scheme 2.25). The conversion takes place in the presence of trimethylsilyl azide (TMSN<sub>3</sub>) (2 eq.) and tetrabutylammonium fluoride (TBAF) (2 eq.) as shown in Scheme 2.31. The purification of the polymer was performed *via* extraction between water and DCM and followed by precipitation into cold diethyl ether. The presence of the azide group was confirmed by FTIR spectroscopy due to the appearance of a small peak at 2190 cm<sup>-1</sup> wavenumber as shown in Figure 2.10. However, it is not possible to quantitatively control the azide conversion yield.



**Scheme 2.31:** Azide group functionalization of PBLG<sub>53</sub>-PTS conjugate

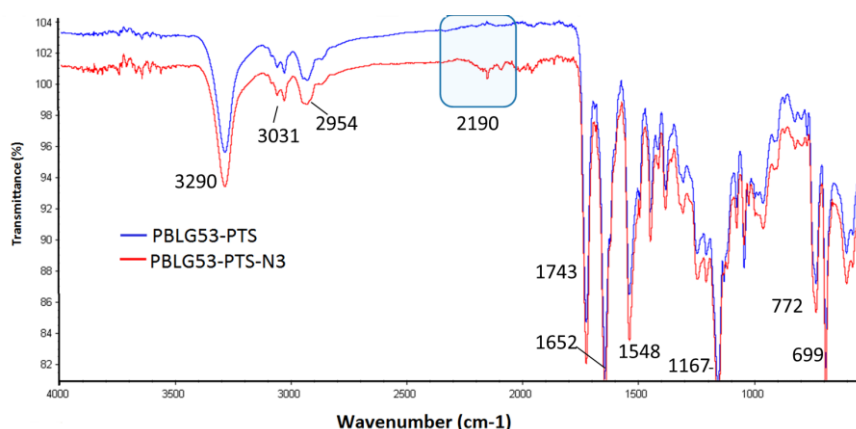
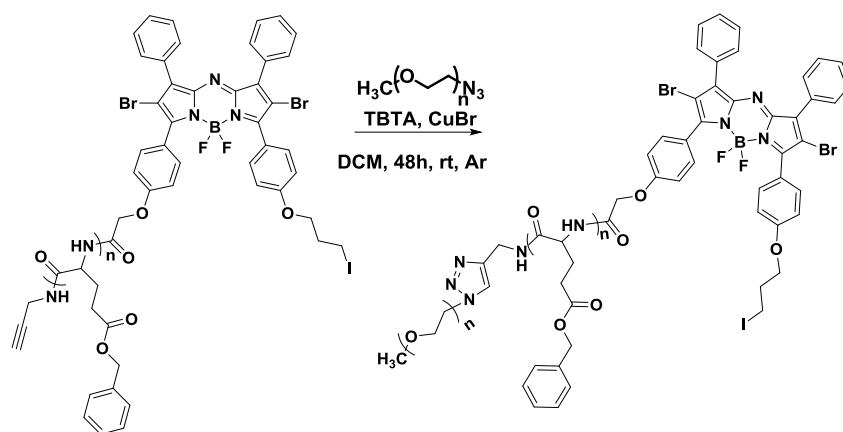


**Figure 2.10:** FTIR spectrum of the azide functionalized PBLG<sub>53</sub>-PTS conjugate

### 2.2.2.3 Synthesis of PST-PBLG<sub>49</sub>-*b*-PEG block copolymers by CuAAC click reaction

PTS-PBLG<sub>49</sub> (1 eq.) conjugate was clicked to the PEG-N<sub>3</sub> (M<sub>n</sub> 5000 (DP113) and 2000 (DP45), 1.5 eq.) via the CuAAC reaction as shown in Scheme 2.32. The excess of catalyst and PEG was removed by dialyzing (dialysis tube MWCO-15000) the reaction mixture in ethylenediaminetetraacetic acid (EDTA) solution in Milli-Q water (400 mg/L) and pure Milli-Q water, respectively, for 3 days. However, we still observed some excess amount of PEG after the dialysis process, which was completely removed by washing several times the precipitate with Milli-Q water and recovered by centrifugation. Finally, the water was removed by lyophilization and the final yield of the product was calculated as 94% for PTS-PBLG<sub>49</sub>-*b*-PEG<sub>45</sub> and 80% for PTS-PBLG<sub>49</sub>-*b*-PEG<sub>113</sub>. The block copolymers were characterized by <sup>1</sup>H NMR (conjugation yield *via* click reaction is 100% for both block copolymers) and SEC (see Figure 2.11 and 2.12).



**Scheme 2.32:** Synthesis of PTS-PBLG<sub>49</sub>-*b*-PEG<sub>45</sub> and PTS-PBLG<sub>49</sub>-*b*-PEG<sub>113</sub> block copolymers by copper-catalyzed azide-alkyne cycloaddition (CuAAC) reaction

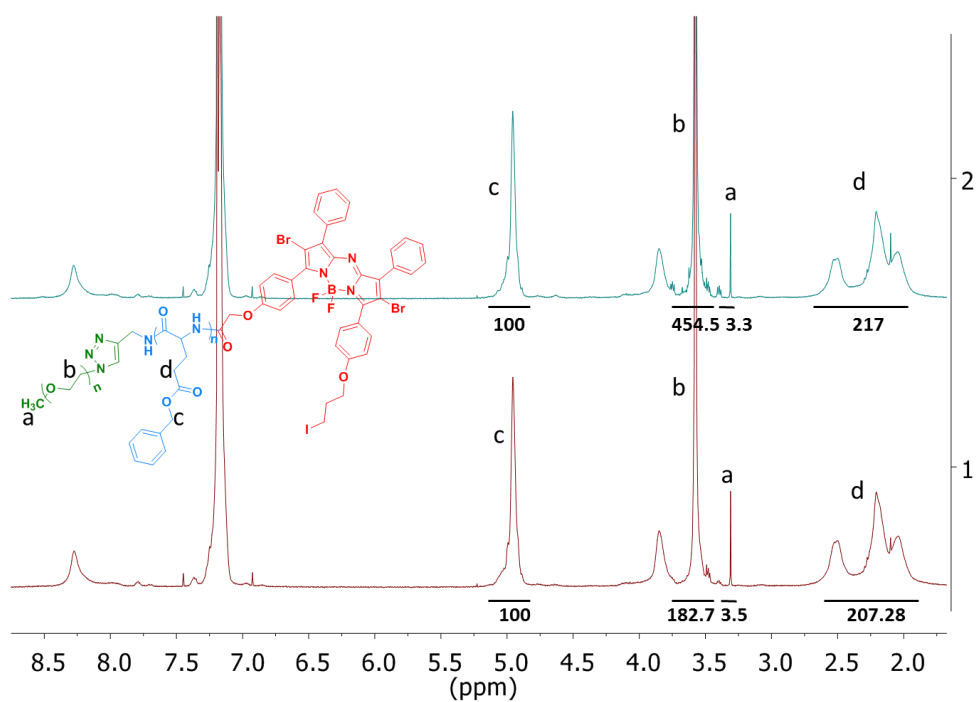


**Figure 2.11:** <sup>1</sup>H NMR spectra of (1) PTS-PBLG<sub>49</sub>-*b*-PEG<sub>45</sub>, (2) PTS-PBLG<sub>49</sub>-*b*-PEG<sub>113</sub> block copolymers (400 MHz, CDCl<sub>3</sub>)

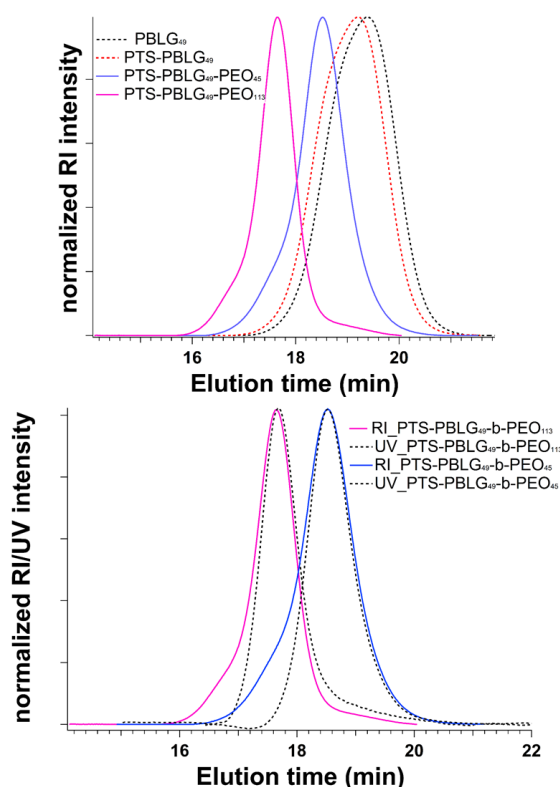
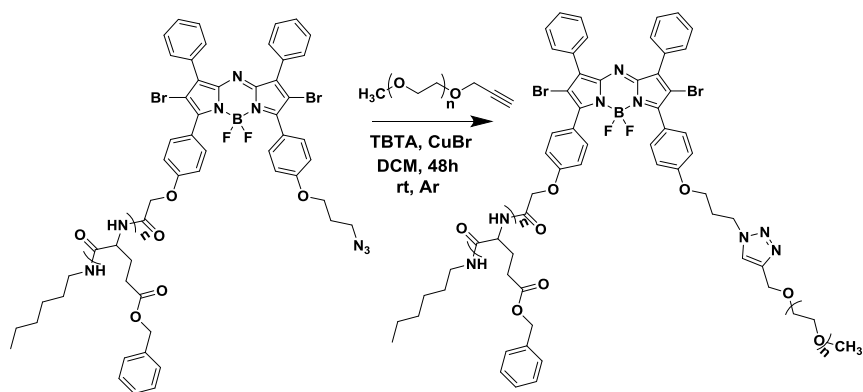


**Figure 2.12:** SEC chromatograms of PBLG<sub>49</sub>, PBLG<sub>49</sub>-PTS, PTS-PBLG<sub>49</sub>-*b*-PEG<sub>45</sub> and PTS-PBLG<sub>49</sub>-*b*-PEG<sub>113</sub> polymers (DMF 2.5 M of NH<sub>4</sub>PF<sub>6</sub>, standard PEO)

#### 2.2.2.4 Synthesis of PBLG<sub>53</sub>-PTS-*b*-PEG type block copolymers by CuAAC click reaction

Azide functionalized PTS-PBLG<sub>53</sub> (1 eq.) was clicked to an excess PEG-alkyne (1.2 eq.) (Mn 5000 (DP113) and 2000 (DP 45), 1.5 eq.) *via* CuAAC reaction as shown in Scheme 2.33. The excess of catalyst, PEG, and unreacted PBLG was removed by column chromatography on a small pad of silica gel by using a DCM:MeOH (9:1) mixture. After removing the first fraction (unreacted PBLG), the pure block copolymer was collected, concentrated under reduced pressure and precipitated into cold diethyl ether. To remove traces of Cu, the block copolymers were dialyzed (dialysis tube MWCO-15000) in EDTA solution in Milli-Q water (400mg/L) and pure Milli-Q water for 2 days each.



**Scheme 2.33:** Synthesis of PBLG<sub>53</sub>-PTS-*b*-PEG<sub>45</sub> and PBLG<sub>53</sub>-PTS-*b*-PEG<sub>113</sub> block copolymers by CuAAC reaction



Finally, water was removed by lyophilization and the block copolymers were characterized by  $^1\text{H-NMR}$  and SEC (see Figure 2.14 and 2.15). Integration results obtained from the  $^1\text{H-NMR}$  spectrum and the single peak in the SEC trace confirmed the successful removal of the excess  $\text{PBLG}_{53}\text{-PTS}$ . The final yields of the pure block copolymers have been calculated as 61% for  $\text{PBLG}_{53}\text{-PTS-}b\text{-PEG}_{45}$  and 58% for  $\text{PBLG}_{53}\text{-PTS-}b\text{-PEG}_{113}$ . The reason of lower conjugation yield is due to the uncontrolled azide functionalization yield of  $\text{PBLG}_{53}\text{-PTS}$  as mentioned in Section 2.2.2.2.

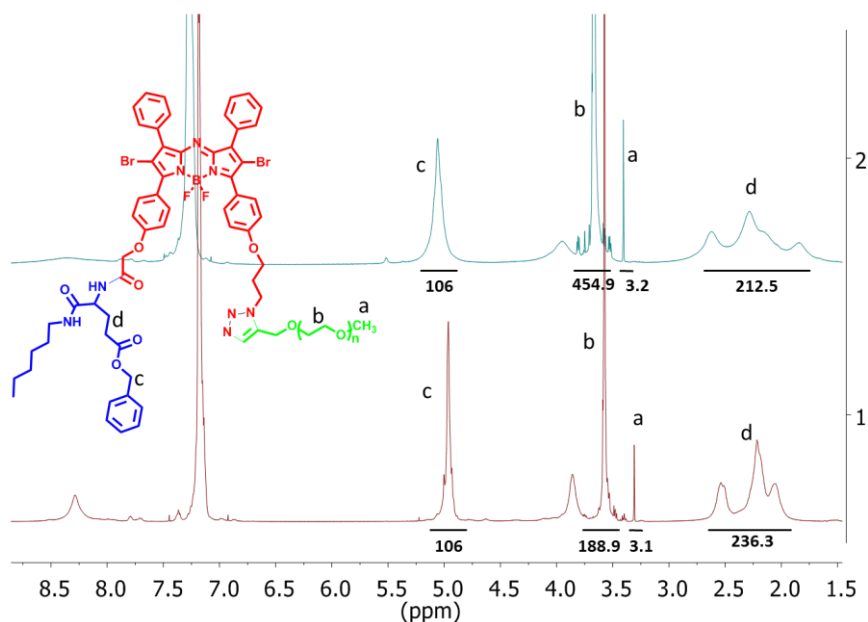


**Figure 2.13:**  $^1\text{H NMR}$  spectra of (1)  $\text{PBLG}_{53}\text{-PTS-}b\text{-PEG}_{45}$  (400 MHz,  $\text{CDCl}_3$ ), (2)  $\text{PBLG}_{53}\text{-PTS-}b\text{-PEG}_{113}$  block copolymers (500 MHz,  $\text{CDCl}_3$ )

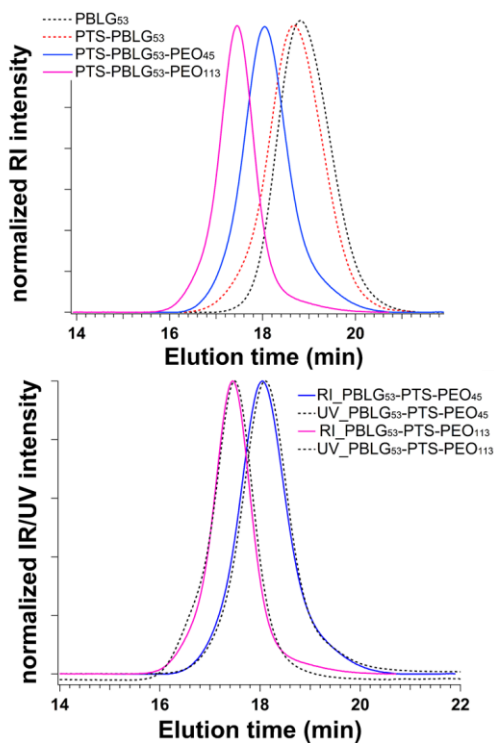
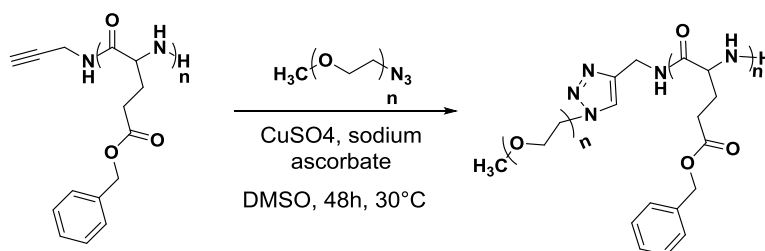


**Figure 2.14:** SEC chromatogram of  $\text{PBLG}_{53}$ ,  $\text{PBLG}_{53}\text{-PTS}$ ,  $\text{PBLG}_{53}\text{-PTS-}b\text{-PEG}_{45}$  and  $\text{PBLG}_{53}\text{-PTS-}b\text{-PEG}_{113}$  polymers ( $\text{DMF}$  2.5 M of  $\text{NH}_4\text{PF}_6$ , PEO standard)

### 2.2.2.5 Synthesis of PBLG<sub>54</sub>-*b*-PEG type block copolymers

To prevent possible quenching of the PTS fluorescence due to their packing ( $\pi$ - $\pi$  stacking) in the nano-assemblies, PTS free block copolymers with the same degree of polymerization were synthesized to be mixed with PTS bearing block copolymers. The synthesis of the block copolymers was performed by clicking PBLG<sub>54</sub> to PEG<sub>45</sub> and PEG<sub>113</sub> in DMSO by using Cu<sub>2</sub>SO<sub>4</sub> as a catalyst. The purification of the polymers was done by extraction between DCM and EDTA solution in Milli-Q water (400mg/L) and then pure Milli-Q water. In a final step, the polymer solution was concentrated under reduced pressure and precipitated into cold diethyl ether and characterized via <sup>1</sup>H-NMR and SEC (see Figure 2.15 and 2.16). No excess amount or unreacted polymer was observed in both characterization techniques, which confirms the successful click reaction.



**Scheme 2.34:** Synthesis of PBLG<sub>54</sub>-*b*-PEG<sub>45</sub> and PBLG<sub>54</sub>-*b*-PEG<sub>113</sub> block copolymers by copper-catalyzed azide-alkyne cycloaddition (CuAAC) reaction

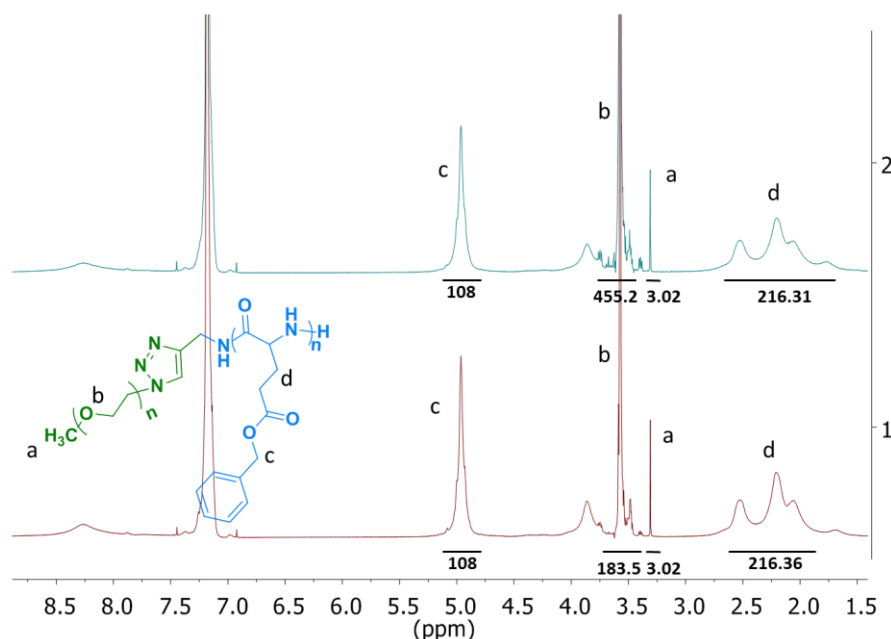


**Figure 2.15:** <sup>1</sup>H NMR spectra of (1) PBLG<sub>54</sub>-*b*-PEG<sub>45</sub>, (2) PBLG<sub>54</sub>-*b*-PEG<sub>113</sub> block copolymers (400 MHz, CDCl<sub>3</sub>)

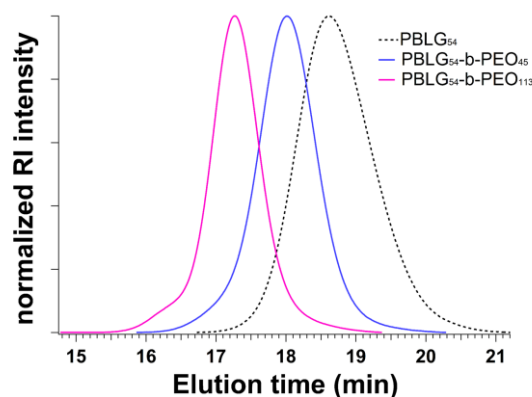


**Figure 2.16:** SEC chromatogram of PBLG<sub>54</sub>, PBLG<sub>54</sub>-*b*-PEG<sub>45</sub> and PBLG<sub>54</sub>-*b*-PEG<sub>113</sub> polymers (DMF 2.5 M of NH<sub>4</sub>PF<sub>6</sub>, PEO standard)

### 2.3 Conclusion

In the first part of the project we developed three brominated asymmetric aza-BODIPY derivatives with different functional groups. The polypeptide chain (PBLG homopolymers) were synthesized by NCA-ROP polymerization technique. In order to synthesize polypeptide-based hybrid amphiphilic block copolymers the hydrophilic PEG chains (DP 45 and 113) were functionalized with azide or alkyne groups. Finally, all building blocks were assembled together in different order by using peptidic coupling and CuAAC click reaction in order to obtain PTS-PBLG<sub>49</sub>-*b*-PEG<sub>45</sub>, PTS-PBLG<sub>49</sub>-*b*-PEG<sub>113</sub>, PBLG<sub>53</sub>-PTS-*b*-PEG<sub>45</sub>, PBLG<sub>53</sub>-PTS-*b*-PEG<sub>113</sub>, PBLG<sub>54</sub>-*b*-PEG<sub>45</sub> and PBLG<sub>54</sub>-*b*-PEG<sub>113</sub> hybrid block copolymers that will be self-assembled into different nanostructures and used in PDT application.

### 2.4 Experimental

#### Materials and methods

##### Materials

The following reagents have been used without further purifications: diethyl amine ((C<sub>2</sub>H<sub>5</sub>)<sub>2</sub>NH, Sigma-Aldrich, 99.5%), nitromethane (CH<sub>3</sub>CN, Sigma-Aldrich, HPLC grade, 96%), 4'-hydroxychalcone (C<sub>15</sub>H<sub>12</sub>O<sub>2</sub>, TCI chemicals, 95%), sodium chloride (NaCl, VWR, 100%), 1,3-diiodopropane (I(CH<sub>2</sub>)<sub>3</sub>I, Sigma-Aldrich, purum 97.0%), ammonium acetate (C<sub>2</sub>H<sub>3</sub>O<sub>2</sub>NH<sub>4</sub>, Sigma-Aldrich, BioXtra 98%), potassium tert-butoxide (KOtBu, Fluka, purum 99%), tert-Butyl bromoacetate (BrCH<sub>2</sub>COOC(CH<sub>3</sub>)<sub>3</sub>, Sigma-Aldrich, 98%), propargyl bromide (Acros Organics, 80wt% solution in toluene, stabilized), N,N-diisopropylethylamine (DIPEA, Sigma-Aldrich, 99%), boron trifluoride etherate (BF<sub>3</sub>·OEt<sub>2</sub>, TCI, 98%), trifluoroacetic acid (C<sub>2</sub>HF<sub>3</sub>O<sub>2</sub>, TCI, 99%), n-bromosuccinimide (NBS, Sigma-Aldrich, 99%), sodium bicarbonate (NaHCO<sub>3</sub>, ACS reagent, 99.7+%), 1-hydroxybenzotriazole hydrate (HOBT, Sigma-Aldrich, 97%), 1-(3-dimethylaminopropyl)-3-ethylcarbodiimide hydrochloride (EDCI, Acros Organics, 98+%), poly(ethylen oxyde) methyl ether (Mn = 2000, 5000 g/mol, Aldrich), sodium sulfate (Na<sub>2</sub>SO<sub>4</sub>, VWR, 98%), potassium carbonate (K<sub>2</sub>SO<sub>4</sub>, VWR), magnesium sulphate (MgSO<sub>4</sub>, VWR), sodium hydride (NaH, Sigma-Aldrich, 60% in mineral oil), p-toluene-sulfonyl chloride (C<sub>7</sub>H<sub>7</sub>ClO<sub>2</sub>S, Acros Organics, 99+%), sodium azide (NaN<sub>3</sub>, Acros Organics, 99% extra pure), tris(benzyltriazolylmethyl)amine (TBTA, TCI, 97%), ethylenediaminetetraacetic acid disodium salt dihydrate (EDTA, ACS reagent, 99%), triethylamine (TEA, Merck Schuchardt

OHG, pharma grade), acetic acid glacial ( $\text{CH}_3\text{CO}_2\text{H}$ , Chem-Labs Limited), hydrogen chloride (HCl, VWR, 37%), tetrabutylammonium fluoride (TBAF, 1M solution in THF, TCI chemicals), azidotrimethylsilane ( $\text{TMSN}_3$ , Alfa Aser, 94%), copper(I) sulfate ( $\text{Cu}_2\text{SO}_4$ , Acros Organics, 98%), copper(I) bromide (CuBr, Acros Organics, 98%), L-Ascorbic acid sodium salt ( $\text{C}_6\text{H}_7\text{NaO}_6$ , Acros Organics, 99%), bio-beads TM S-X1 (BIO-RAD, 200-400 mesh), silica gel 60A ( $\text{SiO}_2$ , 230-400 mesh ASTM, ROCC, 99.5%),  $\gamma$ -benzyl-L-glutamate N-carboxyl anhydride (NCA-BLG, Isochem France).

The following solvents have been used without further purification: ethanol (EtOH, VWR chemicals, analytical grade, 100%), dichloromethane (DCM, Sigma-Aldrich, analytical grade, 99.9%), n-hexane ( $\text{C}_6\text{H}_{12}$ , Sigma-Aldrich, analytical grade, 97%), 1-butanol (n-BuOH, Acros Organics, extra pure 99+%), N, N - dimethylformamide (DMF, Fluka, 99.8%), acetonitrile (AcCN, VWR chemicals, HPLC grade, 99.9%), tetrahydrofuran (THF, Fluka, 99.8%), ethyl acetate (EtOAc, Sigma-Aldrich, 99.5%), acetone ( $(\text{CH}_3)_2\text{CO}$ , Sigma-Aldrich, 99.5%), diethyl ether ( $\text{Et}_2\text{O}$ , VWR chemicals, 97%), dimethyl sulfoxide (DMSO, Sigma-Aldrich, 99.9%).

## Methods

**Nuclear Magnetic Resonance (NMR):**  $^1\text{H}$ ,  $^{13}\text{C}$  and  $^{11}\text{B}$  NMR 500 MHz spectra have been taken with a Bruker 500 MHz Avance.  $^1\text{H}$  NMR 300 MHz spectra have been taken with a Bruker 300 MHz Avance II.  $^1\text{H}$  NMR 400 MHz spectra have been taken with a Bruker Avance DPX 400. Deuterated chloroform ( $\text{CDCl}_3$ , Euriso-top, 99.8%), deuterated dimethylsulfoxide ( $d\text{-DMSO}$ , Euriso-top, 99.8%), deuterated methanol ( $\text{CD}_4\text{O}$ , Euriso-top, 99.8%) and deuterated acetone ( $(\text{CD}_3)_2\text{O}$ , Euriso-top, 99.8%), have been used as solvent and reference for the lock.

**Size Exclusion Chromatography (SEC):** Analyses by SEC have been performed on a Agilent gel permeation chromatography system and on Varian system. Agilent SEC was equipped with RI and UV detectors, an Agilent 1100/1200 pump (35°C; eluent: DMF 2.5 M of  $\text{NH}_4\text{PF}_6$ ; flow rate of 1 mL/min), an Agilent differential refractometer and two PSS GRAM columns (beads 10  $\mu\text{m}$ ; porosity of column 1, 1000 Å; porosity of column 2, 100 Å). The calibration was performed using PEO standards. Varian, PL-SEC 50 Plus integrated, equipped with a RI and UV detectors, a guard column (Polymer Laboratories, PL gel 5 $\mu\text{M}$ , 7.5 mm ID x 5.0 cm.L) followed by two columns (Polymer Laboratories, PL gel Mixed-D columns, 5  $\mu\text{m}$ , 7.5mm ID x 30 cm.L) and eluent was DMF 1M LiBr (flow rate 0.8 mL. min<sup>-1</sup>, 80°C, standard PS).

**Mass Spectrometry (MS):** The high accuracy mass spectrometry analyses were performed on a ThermoScientific Q-Exactive mass spectrometer. The analyte solutions (1 mg/mL) were delivered to the ESI source by a Harvard Apparatus syringe pump at a flow rate of 5 mL/min. Typical ESI conditions were: capillary voltage, 3.5 kV; cone voltage, 30 V; source temperature, 80°C; desolvation temperature, 120°C, capillary temperature 320°C.

**Attenuated total reflection Fourier transform infrared spectroscopy (ATR FTIR):** Fourier transform infrared transmission spectra were recorded directly on a powder samples at 400-4000  $\text{cm}^{-1}$  (resolution of 4 wavenumber) range by using attenuated total reflection mode.

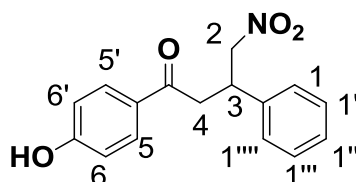
**Titration:** The primary amine yields in the polypeptides chain-end were calculated with basic acid-base titration method. 100mg of polymer samples were dissolved in DCM/Acetic acid mixture (1ml DCM/ 2ml Acetic acid), a few drops of crystal violet was added and followed by acid titration (0.005M perchloric acid in acetic acid 100%).

Analytical thin-layer chromatography (TLC) was performed on alumina plates coated with silica gel GF254 (Merck, 0.22 mm thick)

## Synthesis

### Synthesis of 1-(4-Hydroxyphenyl)-4-nitro-3-phenylbutan-1-one (**18**)<sup>74</sup>

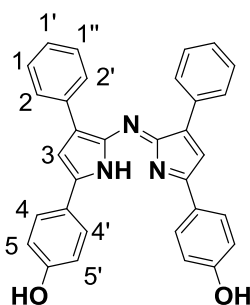
Diethyl amine (23.1 ml, 0.223 mol, 5eq) and nitro methane (24 ml, 0.446 mol, 10eq) were added into the solution of the 4'-hydroxychalcone (10 g, 0.0446 mol, 1eq) in ethanol (70 ml) and refluxed for 24 h. The reaction mixture cooled down to room temperature and neutralized by 4M HCl solution. Products were separated from aqueous phase by extracting with ethyl acetate (100 ml). The organic layer was washed with deionized water (2x 50 ml), dried over Na<sub>2</sub>SO<sub>4</sub>, filtrated and evaporated under reduced pressure. Resulted brown solid was washed with small amount of cold diethyl ether and filtrated to obtain desired white product compound **18** (12.75 g, 100 %)



<sup>1</sup>H NMR (400 MHz, CDCl<sub>3</sub>) δ 7.78 (d, *J* = 8.8 Hz, 2H<sub>5,5'</sub>), 7.28-7.21 (m, 5H<sub>1,1',1''</sub>), 6.80 (d, *J* = 8.8 Hz, 2H<sub>6,6'</sub>), 5.53 (s, 1H, OH), 4.78-4.73 (m, 1H<sub>2</sub>), 4.64-4.59 (m, 1H<sub>2</sub>), 4.17-4.10 (m, 1H<sub>3</sub>), 3.38-3.26 (m, 2H<sub>4</sub>).

### Synthesis of [5-(4-hydroxyphenyl)-3-phenyl-1H-pyrrol-2-yl]-[5-(4-hydroxyphenyl)-3-phenylpyrrol-2-ylidene] amine (**19**)<sup>74</sup>

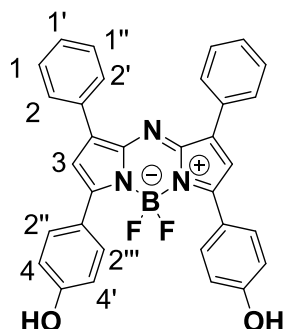
Ammonium acetate (93.9 g, 1.219 mol, 35eq) and compound **18** (9.93 g, 0.035 mol, 1eq) were dissolved in 1-butanol (400 ml) and heated under reflux for 48h. The solution was cooled down and kept for 24 h at room temperature for dark blue crystals formation in the reaction mixture. The solution filtrated, washed with cold ethanol and dried under reduced pressure to have pure dark blue shiny crystals (compound **19**) (4.815g, 58%).



<sup>1</sup>H NMR (300 MHz, MeOD) δ 8.02 (d, *J* = 8.0 Hz, 4H<sub>4,4'</sub>), 7.83 (d, *J* = 8.8 Hz, 4H<sub>2,2'</sub>), 7.32 (m, 6H<sub>1,1'</sub>), 7.20 (s, 2H<sub>3</sub>), 6.94 (d, *J* = 8.8 Hz, 4H<sub>5,5'</sub>), 1.95 (s, 3H, excess NH<sub>3</sub>Ac) (NH, OH not observed).

### Synthesis of BF<sub>2</sub> Chelate of [5-(4-hydroxyphenyl)-3-phenyl-1H-pyrrol-2-yl]-[5-(4-hydroxyphenyl)-3-phenylpyrrol-2-ylidene]amine (**20**)<sup>74</sup>

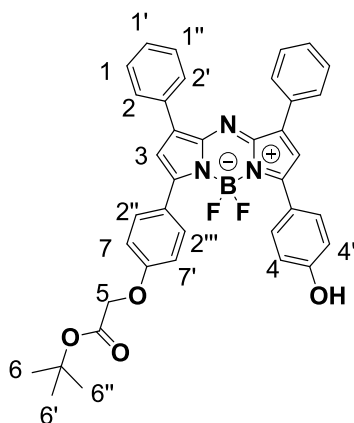
The ligand (compound **19**) 400mg, 0.82 mmol, 1eq) was dissolved in dry DCM (50ml), N,N-diisopropylethylamine (DIPEA, 1.42 ml, 8.2 mmol, 10eq) was slowly added under stirring and followed by BF<sub>3</sub> diethyletherate (1.48ml, 12 mmol, 14eq) addition, respectively and stirred under nitrogen for 24h. The reaction solution was diluted with EtOAc (50ml) and partitioned with deionized water (2x 50ml). The organic layer was separated and dried under reduced pressure. Column chromatography on silica gel (eluent DCM: EtOAc: hexane (3:1:1)) yields dark red metallic solid (product **20**, 336mg, 76%).



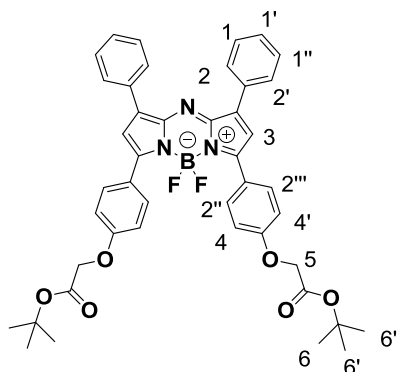
<sup>1</sup>H NMR (300 MHz, MeOD)  $\delta$  8.04 (m, 8H<sub>2,2'''</sub>), 7.33 (m, 6H<sub>1,1''</sub>), 7.15 (s, 2H<sub>3</sub>), 6.88 (m, 4H<sub>4,4'</sub>) (OH not observed). <sup>11</sup>B NMR (500 MHz, Acetone-d<sub>6</sub>)  $\delta$  1.47 (t, *J* = 100 Hz, 1B). <sup>19</sup>F NMR (300 MHz, Acetone-d<sub>6</sub>)  $\delta$  -170.57 (dd, *J* = 36, 33 Hz, 2F).

**Synthesis of BF<sub>2</sub> Chelate of tert-butyl 2-(4-(5-(5-(4-hydroxyphenyl)-3-phenyl-2H-pyrrol-2-ylideneamino)-4-phenyl-1H-pyrrol-2-yl)phenoxy)acetate and tert-butyl (Z)-2-(4-(2-((5-(4-(2-(tert-butoxy)-2-oxoethoxy)phenyl)-3-phenyl-1H-pyrrol-2-yl)imino)-3-phenyl-2H-pyrrol-5-yl)phenoxy)acetate (**22** and **22**)**

Compound **20** (500mg, 0.944 mmol, 1eq) was dissolved in dry THF (40 ml) and KOtBu (127 mg, 1.133 mmol, 1.2 eq) was added to the solution at 0°C under N<sub>2</sub> atmosphere and followed by slow addition of the tert-buthyl bromoacetate (0.181 ml, 1.22 mmol, 1.3 eq). The reaction mixture was warmed up to room temperature then heated under reflux (75-80°C) for 2h. The reaction cooled down to the room temperature and partitioned between EtOAc (50ml) and brine solution (30ml). The organic layer was separated, dried over sodium sulfate, filtrated and the solvent evaporated under reduced pressure. Products were purified by column chromatography on silica gel (60 Å, 200-400 mesh) by eluting with hexane: EtOAc (3:1) mixture. After collecting the first eluted pure compound **22** (144 mg, 24%, dark red metallic crystals) the ration of eluent is changed to hexane: EtOAc (3:1.5) and pure compound **21** were collected (214 mg, 30%, dark red metallic crystals). By increasing EtOAc ratio (hexane: EtOAc (1:1)) starting material compound **20** was recovered.



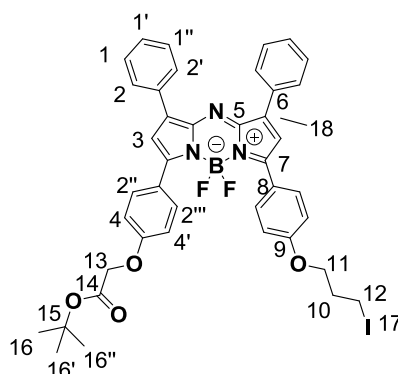
Analysis for **22**:  $^1\text{H}$  NMR (300 MHz, Acetone- $d_6$ )  $\delta$  8.29 – 8.17 (m,  $8\text{H}_{2-2''}$ ), 7.60 – 7.41 (m,  $6\text{H}_{1-1''}$ ), 7.10 (d,  $J = 9.1$  Hz,  $2\text{H}_{7,7'}$ ), 7.03 (d,  $J = 8.9$  Hz,  $2\text{H}_{4,4'}$ ), 4.77 (s,  $2\text{H}_5$ ), 1.50 (s,  $9\text{H}_{6-6''}$ ).



Analysis for **21**:  $^1\text{H}$  NMR (500 MHz,  $\text{CDCl}_3$ )  $\delta$  8.09-8.05 (dd,  $J = 10.4, 8.0$  Hz,  $8\text{H}_{2-2''}$ ), 7.50 – 7.39 (m,  $6\text{H}_{1-1''}$ ), 7.04 (s,  $2\text{H}_3$ ), 7.00 (d,  $J = 9.0$  Hz,  $4\text{H}_{4,4'}$ ), 4.59 (s,  $4\text{H}_5$ ), 1.51 (s,  $18\text{H}_{6-6''}$ ).  $^{11}\text{B}$  (500 MHz,  $\text{CDCl}_3$ ):  $\delta$  1.34 (t,  $J = 100$  Hz, 1B).

### Synthesis of tert-butyl 2-(4-(5,5-difluoro-7-(4-(3-iodopropoxy)phenyl)-1,9-diphenyl-5H-4,4,5,14-dipyrrolo[1,2-c:2',1'-f][1,3,5,2]triazaborinin-3-yl)phenoxy)acetate (**23**)

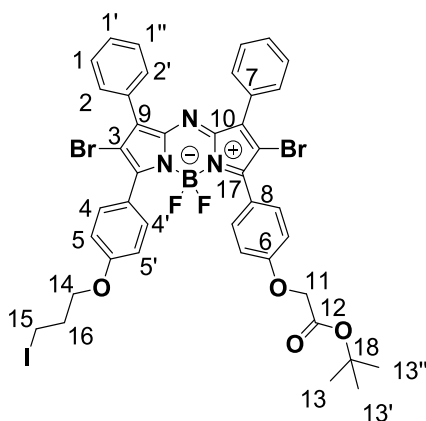
Dry acetonitrile (15 ml) was added into the mixture of compound **22** (2.19 g, 4.04 mmol, 1eq) and  $\text{K}_2\text{CO}_3$  was added (5.58 g, 40.4 mmol, 10eq) under vigorous stirring and placed in ice bath, followed by 1,3- diiodopropane (2.32 ml, 20.2 mmol, 5eq) dropwise addition and refluxed at  $70^\circ\text{C}$  for 3h. The reaction solution was cooled down, filtrated and partitioned between DCM (50ml) and deionized water (3x 50ml). The organic layer was separated and dried over  $\text{Na}_2\text{SO}_4$ , filtrated and the solvent was evaporated under reduced pressure. In final step, recrystallization in DCM: petroleum ether (1:9) mixture yield dark red metallic crystals of product **23** (2.38mg, 73%).



$^1\text{H}$  NMR (300 MHz,  $\text{CDCl}_3$ )  $\delta$  8.14 – 8.01 (m,  $8\text{H}_{2-2''}$ ), 7.51 – 7.38 (m,  $6\text{H}_{1-1''}$ ), 7.08 – 6.96 (m,  $6\text{H}_{4,4',3}$ ), 4.59 (s,  $2\text{H}_{13}$ ), 4.13 (t,  $J = 5.8$  Hz,  $2\text{H}_{11}$ ), 3.39 (t,  $J = 6.7$  Hz,  $2\text{H}_{12}$ ), 2.37 – 2.25 (m,  $2\text{H}_{10}$ ), 1.52 (s,  $9\text{H}_{16-16'}$ ).  $^{11}\text{B}$  (500 MHz,  $\text{CDCl}_3$ ):  $\delta$  1.36 (t,  $J = 100$  Hz, 1B).  $^{13}\text{C}$  NMR (500 MHz,  $\text{CDCl}_3$ ):  $\delta$  168 ( $\text{C}_{17}$ ), 161.6 ( $\text{C}_7$ ), 160 ( $\text{C}_9$ ), 132.5 ( $\text{C}_{18}$ ), 129.8 ( $\text{C}_5$ ), 125.3 ( $\text{C}_6$ ), 115 ( $\text{C}_4$ ), 83.4 ( $\text{C}_{15}$ ), 67.9 ( $\text{C}_{11}$ ), 66.2 ( $\text{C}_{13}$ ), 33.2 ( $\text{C}_{10}$ ), 28.4 ( $\text{C}_{16}$ ), 2.69 ( $\text{C}_{12}$ ). Mass (ESI):  $m/z$  [ $\text{M}^+$ ] calculated for  $\text{C}_{41}\text{H}_{37}\text{BF}_2\text{IN}_3\text{O}_4$ , 811,189; found 811,188.

**Synthesis of tert-butyl 2-(4-(2,8-dibromo-5,5-difluoro-7-(4-(3-iodopropoxy)phenyl)-1,9-diphenyl-5H-4l4,5l4-dipyrrolo[1,2-c:2',1'-f][1,3,5,2]triazaborinin-3-yl)phenoxy)acetate (24)**

Compound **23** (1.133g, 6.36 mmol, 1 eq) was dissolved in a chloroform CHCl<sub>3</sub>:acetic acid (100ml, 3:1) mixture and n-bromosuccinimide (2.066g, 2.54 mmol, 2.5 eq) was added under vigorous stirring in inert atmosphere (N<sub>2</sub>) for 2-3h, at 30°C. The reaction mixture was quenched by sodium bicarbonate (10%) solution and organic layer diluted with DCM and washed with deionized water (2x 100ml). The organic layer dried over Na<sub>2</sub>SO<sub>4</sub>, filtrated and concentrated under reduced pressure. Column chromatography was performed on silica gel (60 Å, 200-400 mesh) by using pure DCM as an eluent without applying any pressure to obtain pure dark red metallic crystals (compound **24**, 1.77 g, 72%).

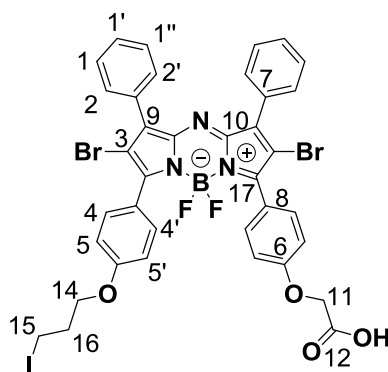


<sup>1</sup>H NMR (500 MHz, CDCl<sub>3</sub>) δ 7.90 (dd, *J* = 7.4, 2.2 Hz, 4H<sub>2,2'</sub>), 7.81 (d, *J* = 8.8 Hz, 4H<sub>4,4'</sub>), 7.50 – 7.42 (m, 6H<sub>1-1''</sub>), 7.00 (dd, *J* = 9.0, 2.7 Hz, 4H<sub>5,5'</sub>), 4.58 (s, 2H<sub>11</sub>), 4.08 (t, *J* = 5.7 Hz, 2H<sub>14</sub>), 3.37 (t, *J* = 6.7 Hz, 2H<sub>15</sub>), 2.29 (m, 2H<sub>16</sub>), 1.53 (s, 9H<sub>13-13''</sub>). <sup>11</sup>B (500 MHz, CDCl<sub>3</sub>): δ 0.55 (t, *J* = 85 Hz). <sup>13</sup>C NMR (500 MHz, CDCl<sub>3</sub>) δ 168.11 (C<sub>12</sub>), 161.31 (C<sub>17</sub>), 160.46 (C<sub>17</sub>), 158.14 (C<sub>6</sub>), 157.57 (C<sub>6</sub>), 144.73 (C<sub>9</sub>), 142.89 (C<sub>9</sub>), 133.00 (C<sub>10</sub>), 131.23 (C<sub>4</sub>), 130.01 (C<sub>4'</sub>), 128.46 (C<sub>1-1'</sub>), 123.08 (C<sub>7</sub>), 122.36 (C<sub>8</sub>), 114.48 (C<sub>5</sub>), 83.09 (C<sub>18</sub>), 67.73 (C<sub>14</sub>), 66.14 (C<sub>11</sub>), 33.31 (C<sub>3</sub>), 28.53 (C<sub>13</sub>), 2.9 (C<sub>15</sub>). APCI. Calculated for C<sub>41</sub>H<sub>36</sub>BB<sub>2</sub>F<sub>2</sub>IN<sub>3</sub>O<sub>4</sub> [M+H]<sup>+</sup>: *m/z* 970,26; found *m/z* 970,01.

**Synthesis of 2-(4-(2,8-dibromo-5,5-difluoro-7-(4-(3-iodopropoxy)phenyl)-1,9-diphenyl-5H-4l4,5l4-dipyrrolo[1,2-c:2',1'-f][1,3,5,2]triazaborinin-3-yl)phenoxy)acetic acid (25)**

Compound **24** (470 mg, 0.484 mmol) was dissolved in dichloromethane and TFA (3ml, DCM:TFA 5:1) mixture at 0°C and stirred for 3h at room temperature. Deprotection reaction was followed by TLC on DCM. The solvent was evaporated under reduced pressure and resulted dark red product recrystallized in DCM: petroleum ether mixture (1:9), obtained pure crystals were filtrated and dried under reduced pressure (compound **25**, 407 mg, 92%).

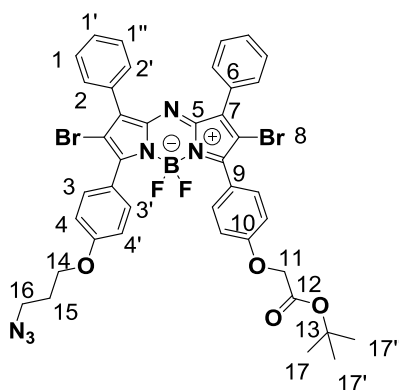




$^1\text{H}$  NMR (500 MHz, Acetone- $d_6$ )  $\delta$  7.92 (d,  $J$  = 8.3 Hz, 2H), 7.76 (d,  $J$  = 8.9 Hz, 2H), 7.54–7.48 (m, 6H), 7.10 (d,  $J$  = 9.0 Hz, 2H), 4.19 (t,  $J$  = 5.8 Hz, 2H), 3.47 (t,  $J$  = 6.9 Hz, 2H), 2.36 – 2.28 (m, 2H).  $^{11}\text{B}$  NMR (500 MHz, acetone- $d_6$ )  $\delta$  0.54 (t,  $J$  = 90 Hz).  $^{13}\text{C}$  NMR (500 MHz, acetone- $d_6$ )  $\delta$  205.62 ( $\text{C}_{12}$ ), 132.87 ( $\text{C}_{10}$ ), 130.98 ( $\text{C}_{4,4'}$ ), 130.08 ( $\text{C}_{2,2'}$ ), 128.55 ( $\text{C}_{1-1''}$ ), 115.79 ( $\text{C}_7$ ), 114.61 ( $\text{C}_8$ ), 114.44 ( $\text{C}_5$ ), 114.36 ( $\text{C}_{5'}$ ), 67.87 ( $\text{C}_{14}$ ), 64.71 ( $\text{C}_{11}$ ), 33.45 ( $\text{C}_{16}$ ), 2.51 ( $\text{C}_{15}$ ). APCI. Calculated for  $\text{C}_{37}\text{H}_{26}\text{BBr}_2\text{F}_2\text{N}_3\text{O}_4$  [ $\text{M}-\text{H}$ ] $^-$ :  $m/z$  912.15; found  $m/z$  912.94.

### Synthesis of tert-butyl 2-(4-(7-(4-(3-azidopropoxy)phenyl)-2,8-dibromo-5,5-difluoro-1,9-diphenyl-5H-4l4,5l4-dipyrrolo[1,2-c:2',1'-f][1,3,5,2]triazaborinin-3-yl)phenoxy)acetate (26)

Compound **24** (100 mg, 0.103 mmol, 1eq) dissolved in THF (5ml), azidotrimethylsilane ( $\text{TMSN}_3$ , 0.162 ml, 0.123 mmol, 1.2eq) and tetrabutylammonium fluoride (TBAF, 0.029 ml, 0.103 mmol, 1eq) were added to the reaction solution at  $0^\circ\text{C}$ , respectively, and stirred at room temperature for 24h under nitrogen. Reaction mixture diluted with THF and partitioned between DCM (30ml) and deionized water (4x 20ml). The organic layer were separated dried over  $\text{Na}_2\text{SO}_4$ , filtrated and the solvent was evaporated under reduced temperature. The resulted dark red shiny crystals were washed with petroleum ether and dried under reduced pressure (82mg, 90%)

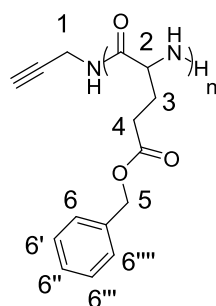


$^1\text{H}$  NMR (300 MHz,  $\text{CDCl}_3$ )  $\delta$  7.91 – 7.81 (m,  $4\text{H}_{3,3'}$ ), 7.77 (dd,  $J$  = 8.8, 1.8 Hz,  $4\text{H}_{2,2'}$ ), 7.47–7.42 (m,  $6\text{H}_{1-1''}$ ), 6.98 (dd,  $J$  = 8.9, 1.5 Hz,  $4\text{H}_{4,4'}$ ), 4.57 (s,  $2\text{H}_{11}$ ), 4.11 (t,  $J$  = 5.8 Hz,  $2\text{H}_{14}$ ), 3.54 (t,  $J$  = 6.6 Hz,  $2\text{H}_{16}$ ), 2.16 – 2.00 (m,  $2\text{H}_{15}$ ), 1.49 (s,  $9\text{H}_{17-17''}$ ).  $^{11}\text{B}$  NMR (500 MHz,  $\text{CDCl}_3$ )  $\delta$  0.56 (t,  $J$  = 90 Hz).  $^{13}\text{C}$  NMR (300 MHz,  $\text{CDCl}_3$ )  $\delta$  132.63 ( $\text{C}_{2,2'}$ ), 130.88 ( $\text{C}_3$ ), 129.68 ( $\text{C}_{3'}$ ), 128.14 ( $\text{C}_{1-1''}$ ), 114.35 ( $\text{C}_{4,4'}$ ), 65.81 ( $\text{C}_{11}$ ), 64.63 ( $\text{C}_{14}$ ), 48.30 ( $\text{C}_{16}$ ), 28.81 ( $\text{C}_{15}$ ), 28.16 ( $\text{C}_{17-17''}$ ). IR (ATR-FTIR)  $\nu_{\text{max}}$  853, 1029, 1045, 1078, 1134, 1166, 1251, 1305, 1382, 1425, 1467, 1504, 1531, 1602, 1768, 2096, 2974, 3000, 3350  $\text{cm}^{-1}$ .

## Synthesis of heterobifunctional and monofunctional poly( $\gamma$ -benzyl-L-glutamate) (PBLG) polypeptides

### Heterobifunctional poly( $\gamma$ -benzyl-L-glutamate) synthesis by ring-opening N-carboxyanhydride polymerization (ROP-NCA)

The cyclic monomer, N-carboxyl- $\alpha$ -amino acid anhydride of  $\gamma$ -benzyl-L-glutamate (NCA-BLG) (2 g, 7.6 mmol), was weighted in a glove box under argon and placed in Schlenk flask, equipped with magnetic stirrer. The white NCA-BLG crystals were dissolved in 15 ml anhydrous DMF under argon and placed in a cooling chamber. The initiator, double distilled propargylamine (cryogenic distillation) (9.6  $\mu$ L, 0.15 mmol), was added dropwise and stirred under static vacuum for 48h at 0°C. The reaction mixture was concentrated by evaporating the solvent under reduced pressure and precipitated into cold diethylether. White precipitate was filtered and dried under high vacuum to afford desired polymer.

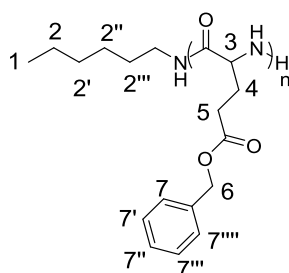


Analysis for PBLG<sub>49</sub>: (DP<sub>49</sub>, 1.58g, product yield 95%, primary amine yield  $\approx$ 93%), SEC (DMF 2.5 M of  $\text{NH}_4\text{PF}_6$ , standard PEO)  $M_n = 2.36\text{kDa}$ ,  $M_w/M_n = 1.16$ .  $^1\text{H NMR}$  (400MHz,  $\text{CDCl}_3/\text{TFA}$  85/15%)  $\delta$  7.87–7.85 (d,  $J = 6.7$  Hz, 49H, N-H), 7.37–7.27 (m, 250H<sub>6-6'''</sub>), 5.17–5.05 (m, 100H<sub>5</sub>), 4.60 (br s, 49H<sub>2</sub>), 4 (m, 2H<sub>1</sub>), 2.47–2.44 (t,  $J = 7.0$ Hz, 100H<sub>4</sub>), 2.20–1.90 (br m, 100H<sub>3</sub>).

Analysis for PBLG<sub>54</sub>: (DP<sub>54</sub>, 1.52g, isolated yield 92%), SEC (DMF 2.5 M of  $\text{NH}_4\text{PF}_6$ , standard PEO)  $M_n = 3.237\text{kDa}$ ,  $M_w/M_n = 1.14$ .  $^1\text{H NMR}$  (400MHz,  $\text{CF}_3\text{COOD}$  (15%)/ $\text{CDCl}_3$ )  $\delta$  7.69 (d,  $J = 6.9$  Hz, 54H, N-H), 7.08–7.17 (m, 270 H<sub>6-6'''</sub>), 4.88 – 4.98 (m, 108H<sub>5</sub>), 4.45 (br s, 54H<sub>2</sub>), 3.83 (m, 2H<sub>1</sub>), 2.29 (t,  $J = 7.0$  Hz, 108H<sub>4</sub>), 1.94–1.77 (br, 108H<sub>3</sub>).

### Monofunctional poly( $\gamma$ -benzyl-L-glutamate) synthesis by ring-opening N-carboxyanhydride polymerization (ROP-NCA)

N-carboxyl- $\alpha$ -amino acid anhydride of  $\gamma$ -benzyl-L-glutamate (NCA-BLG) (2 g, 7.604 mmol), was weighted in a glove box under argon and placed in Schlenk flask, equipped with magnetic stirrer. The white NCA-BLG crystals were dissolved in 10 ml anhydrous DMF under argon and placed in a cooling chamber (0°C). The initiator, double distilled n-hexylamine (cryogenic distillation) (20  $\mu$ L, 0.152 mmol), was added dropwise and stirred under static vacuum for 96h at 0°C. The reaction mixture was concentrated by evaporating the solvent under reduced pressure and precipitated into cold diethylether. The white precipitate was filtered and dried under high vacuum. (DP<sub>53</sub>, 1.44g, 87%, primary amine yield 98%).

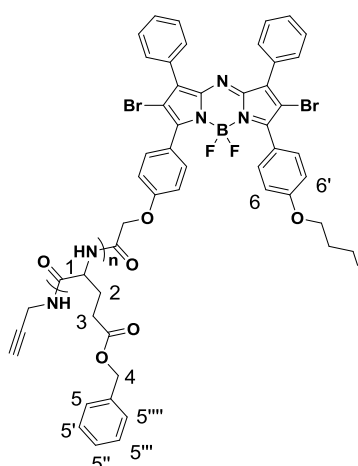


SEC (DMF 2.5M of  $\text{NH}_4\text{PF}_6$ , standard PEO)  $M_n = 2.855\text{kDa}$ ,  $M_w/M_n = 1.14$ .  $^1\text{H}$  NMR (400MHz,  $\text{CDCl}_3$ )  $\delta$  7.72 (d,  $J = 7.0$  Hz, 53H, N-H), 7.12 – 7.22 (m, 265H<sub>7-7''''</sub>), 5.03 – 4.91 (m, 106H<sub>6</sub>), 4.47 (br t,  $J = 10.4$  Hz, 53H<sub>3</sub>), 2.32 (t,  $J = 7.0$  Hz, 106H<sub>5</sub>), 1.76-2 (m, 106H<sub>4</sub>), 1.15 (br, 8H<sub>2-2''''</sub>), 0.75 (t,  $J = 6.8$  Hz, 3H<sub>1</sub>).

### Peptidic coupling between brominated aza-BODIPY (compound 8) and poly( $\gamma$ -benzyl-L-glutamate)

#### Synthesis of PTS-PBLG<sub>49</sub> conjugate

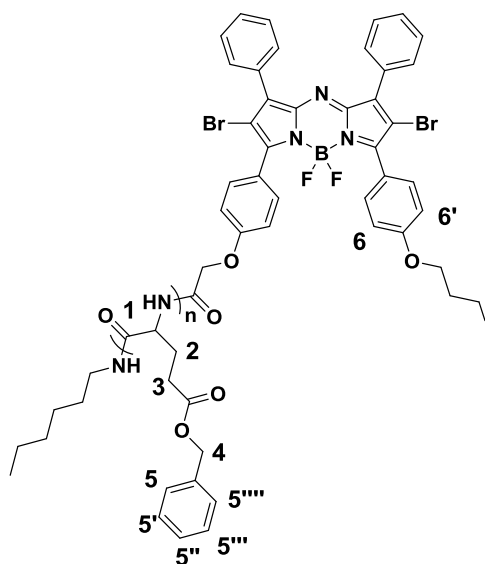
Compound **25** (43 mg, 0.05 mmol, 1.5 eq), PBLG<sub>49</sub> (340mg, 0.032mmol) and hydroxybenzotriazole (HOBT, 11 mg, 0.08 mmol, 2.5 eq) were placed in a flask and kept under vacuum for 1h. 3 mL DCM and 2 mL dimethylacetamide (DMA) were added, added while vigorous stirring in ice bath. The reaction solution was degassed by frizz-thaw cycle and coupling agent, (1-Ethyl-3-(3-dimethylaminopropyl) carbodiimide (EDCI, 18 mg, 0.1 mmol, 3 eq) was added, stirred for 3h in ice bath and 48h at room temperature, under nitrogen. The solution was diluted with DCM and washed with water (3x). The organic layer was dried over  $\text{Na}_2\text{SO}_4$ , filtrated and concentrated under reduced pressure. The purification of the conjugate performed by preparative size exclusion chromatography (SEC, in DCM) on Bio-Beads. Pure conjugate PTS-PBLG<sub>49</sub> phase collected, concentrated under reduced pressure and precipitated into cold diethyl ether. Dark green product filtrated and dried under high vacuum to afford 325mg (88%) pure product. Degree of functionalization was calculated as 92% according to the  $^1\text{H}$ -NMR peak integration.



SEC (DMF 2.5M of  $\text{NH}_4\text{PF}_6$ , standard PEO)  $M_n = 2.763\text{kDa}$ ,  $M_w/M_n = 1.16$ .  $^1\text{H}$  NMR (400MHz,  $\text{CDCl}_3$ )  $\delta$  8.25 (br, NH), 7.67-7.81 (m, Ph, BODIPY), 7.17-7.20 (br, 245H<sub>5-5''''</sub>), 6.82 (d,  $J = 8.6$  Hz, 2H<sub>6,6'</sub>), 4.95 (s, 100H<sub>4</sub>), 3.86 (s, 49H<sub>1</sub>), 2.07-2.51 (br, 200H<sub>2,3</sub>).

## Synthesis of PTS-PBLG<sub>53</sub> conjugate

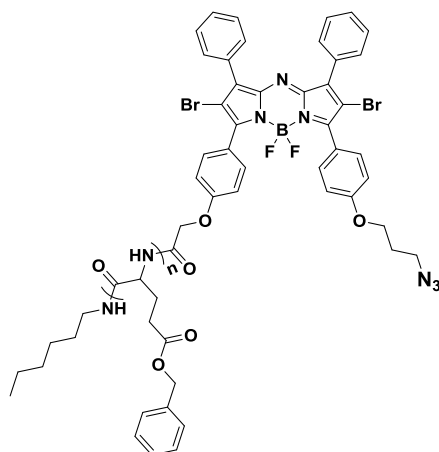
Compound **25** (71 mg, 0.08 mmol, 1.5 eq), PBLG<sub>49</sub> (600mg, 0.052mmol) and hydroxybenzotriazole (HOBT, 17 mg, 0.13 mmol, 2.5 eq) were placed in a flask and dried under vacuum for 1h. 3 mL DCM and 2 mL dimethylacetamide (DMA) were added, added while vigorous stirring in ice bath. The reaction solution was degassed by frizz-vacuum-thaw cycle and coupling agent, (1-Ethyl-3-(3-dimethylaminopropyl) carbodiimide (EDCI, 30 mg, 0.15 mmol, 3 eq) was added, stirred for 3h in ice bath and 48h at room temperature, under nitrogen. The solution was diluted with DCM and washed with water (3x). The organic layer was dried over Na<sub>2</sub>SO<sub>4</sub>, filtrated and concentrated under reduced pressure. The purification of the conjugate performed by preparative size exclusion chromatography (SEC, in DCM) on Bio-Beads. Pure conjugate PTS-PBLG<sub>53</sub> phase collected, concentrated under reduced pressure and precipitated into cold diethyl ether. Dark green product filtrated and dried under high vacuum to afford 630mg (97%) pure product. Degree of functionalization was calculated as 100% according to the <sup>1</sup>H-NMR.



SEC (DMF 2.5M of NH<sub>4</sub>PF<sub>6</sub>, standard PEO) Mn = 3.23kDa, Mw/Mn = 1.18. <sup>1</sup>H NMR (400MHz, CDCl<sub>3</sub>) δ 8.26 (br s, NH), 7.68-7.80 (m, Ph, aza-BODIPY), 7.32 – 7.05 (br m, 265H<sub>5-5''''</sub>), 6.84 (d, *J* = 8.6Hz, 2H<sub>6,6'</sub>), 4.96 (br s, 106H<sub>4</sub>), 3.86 (br s, 53H<sub>1</sub>), 2.05-2.50 (br, 212H<sub>2,3</sub>).

## Azide functionalization of the chain end of PTS-PBLG<sub>53</sub> conjugate

PTS-PBLG<sub>53</sub> (659mg, 0.057mmol, 1eq) dissolved in THF (5ml), azidotrimethylsilane (TMSN<sub>3</sub>, 22μL, 0.17mmol, 3eq) and tetrabutylammonium fluoride (TBAF, 33μL, 0.13mmol, 2eq) were added at 0°C, respectively, and stirred at room temperature for 24h under nitrogen. The reaction mixture diluted with THF and partitioned between DCM (50ml) and deionized water (4x 50ml). The organic layer were separated and dried over Na<sub>2</sub>SO<sub>4</sub>, filtrated, concentrated under reduced pressure and precipitated into cold diethyl ether, respectively. The resulted dark green precipitate were filtrated and dried under high vacuum (574mg, 87%).



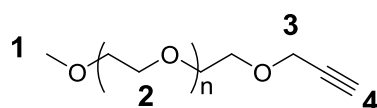
IR (ATR-FTIR)  $\nu_{\text{max}}$  3290, 3031, 2954, 2190, 1734, 1652, 1548, 1167, 772, 699  $\text{cm}^{-1}$

## End group functionalization of $\alpha$ -methoxyethyl- $\omega$ -propargyloxypoly(ethylene glycol) (PEG)

### Alkyne end group functionalization of m-PEG

#### General synthetic procedure for PEG<sub>113</sub>-alkyne synthesis

Prior to synthesis, poly(ethylene glycol) methyl ether (PEG,  $M_n = 5000 \text{ g/mol}$  or  $2000 \text{ g/mol}$ , 1eq) was dried by azeotropic cycles by dissolving it in dry toluene and removing the solvent by evaporating it under reduced pressure (3x). Then dissolved in dry THF, under nitrogen atmosphere. Sodium hydride (60% in mineral oil, 3eq) was added at  $0^\circ\text{C}$  and the mixture stirred at room temperature for 1 hour. Propargyl bromide (80wt% solution in toluene, 3eq) was slowly added at  $0^\circ\text{C}$  and the resulting solution stirred for 24 hours at room temperature. The reaction mixture was filtered and concentrated under reduced pressure. The crude product was precipitated into cold  $\text{Et}_2\text{O}$  and filtrated. The white powder of PEG-alkyne washed with excess  $\text{Et}_2\text{O}$  and dried under high vacuum.



Analysis for **PEG<sub>45</sub>-alkyne** (Starting PEG<sub>45</sub> 2g, yield 1.8g, 88% (functionalization yield calculated from  $^1\text{H NMR}$  90%)):  $^1\text{H NMR}$  (500 MHz,  $\text{CDCl}_3$ )  $\delta$  4.19 (d,  $J = 2.4 \text{ Hz}$ ,  $2\text{H}_3$ ), 3.81 – 3.44 (m,  $182\text{H}_2$ ), 3.36 (s,  $3\text{H}_1$ ), 2.43 (t,  $J = 2.4 \text{ Hz}$ ,  $1\text{H}_4$ ).

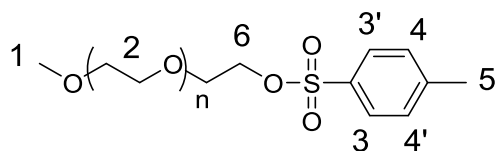
Analysis for **PEG<sub>113</sub>-alkyne** (Starting PEG<sub>113</sub> 2g, yield 1.9g, 94% (functionalization yield calculated from  $^1\text{H NMR}$  91%)):  $^1\text{H NMR}$  (500MHz,  $\text{CDCl}_3$ )  $\delta$  4.18 (d,  $J = 2.4 \text{ Hz}$ ,  $2\text{H}_3$ ), 3.81 – 3.45 (m,  $454 \text{ H}_2$ ), 3.36 (s,  $3 \text{ H}_1$ ), 2.43 (t,  $J = 2.4 \text{ Hz}$ ,  $1\text{H}_4$ ).

### Azide end group functionalization of PEG

#### General synthetic procedure of PEG- $\text{N}_3$ synthesis

Poly(ethylene glycol) methyl ether (PEG,  $M_n = 5000 \text{ g/mol}$  or  $2000 \text{ g/mol}$ , 1eq) and *p*-toluenesulfonyl chloride (TsCl, 9eq) were dried under high vacuum and flushed with argon.

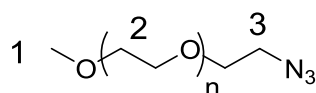
The mixture dissolved in dry DCM, placed in ice bath and triethylamine (10eq) was added, respectively. The solution was stirred at room temperature for 24h under argon atmosphere. The product was then partitioned between water and DCM. The organic phase was separated dried over Na<sub>2</sub>SO<sub>4</sub>, filtrated, concentrated under reduced pressure and precipitated into cold Et<sub>2</sub>O/i-PrOH mixture (4:1). The resulting precipitates were filtrated, washed with excess diethyl ether and dried under high vacuum to obtain white powder of PEG-Ts.



Analysis for **PEG<sub>45</sub>-Ts** (Starting PEG<sub>45</sub> 2g, final product yield 1.68mg (78%) (Functionalization yield calculated from <sup>1</sup>H NMR 100%)): <sup>1</sup>H NMR (500MHz, CDCl<sub>3</sub>) δ 7.78 (d, *J* = 8.3Hz, 2H<sub>4,4'</sub>), 7.33 (d, *J* = 8.6Hz, 2H<sub>3,3'</sub>), 4.16 – 4.10 (m, 2H<sub>6</sub>), 3.79 – 3.45 (m, 181H<sub>2</sub>), 3.36 (s, 3H<sub>1</sub>), 2.43 (s, 2H<sub>5</sub>).

Analysis for **PEG<sub>113</sub>-Ts** (Starting PEG<sub>113</sub> 2 g, final product yield 1.708 g (82%) (Functionalization yield calculated from <sup>1</sup>H-NMR 100%): <sup>1</sup>H NMR (400MHz, CDCl<sub>3</sub>) δ 7.73 (d, *J* = 8.3Hz, 2H<sub>4,4'</sub>), 7.28 (d, *J* = 8.1Hz, 2H<sub>3,3'</sub>), 4.09-4.10 (m, 2H<sub>6</sub>), 3.82 – 3.37 (m, 454H<sub>2</sub>), 3.31 (s, 3H<sub>1</sub>), 2.38 (s, 2H<sub>5</sub>).

PEG-Ts (Mn = 5158g/mol or 2158g/mol, 1eq) was dissolved in anhydrous DMF and NaN<sub>3</sub> (21eq) was added. The reaction flask was flushed with argon and the solution was stirred at RT for 24h. To quench the reaction deionized water was added and diluted with DCM. The water phase was three times washed with DCM. The organic phase was dried over Na<sub>2</sub>SO<sub>4</sub>, filtrated, concentrated and precipitated into cold Et<sub>2</sub>O. The white powder of final product PEG-N<sub>3</sub> was filtrated and dried under high vacuum.



Analysis for **PEG<sub>45</sub>-N<sub>3</sub>** (Starting m-PEG<sub>45</sub>-Ts 1.68g, isolated yield 1.36g, 86% (functionalization yield calculated from <sup>1</sup>H NMR 93%)): <sup>1</sup>H NMR (500 MHz, CDCl<sub>3</sub>) δ 3.81 – 3.46 (m, 181H<sub>2</sub>), 3.43 – 3.32 (m, 5H; fused t –CH<sub>2</sub>N<sub>3</sub> and s –CH<sub>3</sub> terminals).

Analysis for **PEG<sub>113</sub>-N<sub>3</sub>** (Starting m-PEG<sub>113</sub>-Ts 405mg, yield 332mg, 84% (functionalization yield calculated from <sup>1</sup>H NMR 100%)): <sup>1</sup>H NMR (400 MHz, CDCl<sub>3</sub>) δ 3.79 – 3.37 (m, 454H<sub>2</sub>), 3.36 – 3.29 (m, 5H; fused t –CH<sub>2</sub>N<sub>3</sub> and s –CH<sub>3</sub> terminals).

## Amphiphilic PTS-PBLG-*b*-PEG type block copolymer synthesis by

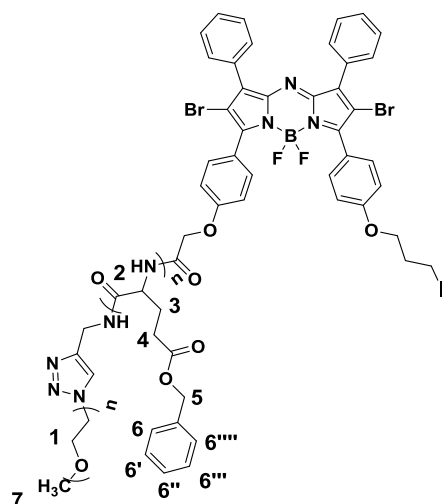
### CuAAC click reaction

#### General procedure for Cu(I) catalyzed click reaction

PEG-N<sub>3</sub> (Mn = 5041g/mol or 2041g/mol, 1.5 eq), PBLG (1 eq) and tris(benzyltriazolylmethyl)amine (TBTA, 1eq) were dissolved in excess of dry DCM under nitrogen and degassed via frizz-thaw cycle. CuBr (1eq) was then added and the solution was

degassed one more time with frizz-vacuum-thaw cycle and stirred at ambient temperature for 24h, under nitrogen.

The solution was filtrated and partitioned between EDTA (400mg/L) solution and DCM. The organic phase was separated and dried over  $\text{MgSO}_4$  and concentrated. Crude product was purified by column chromatography on silica gel (60 Å, 200-400 mesh) by using DCM:MeOH (9:1) mixture as an eluent. Pure block copolymer fraction were concentrated under reduced pressure, precipitated into cold  $\text{Et}_2\text{O}$  and filtrated. The green precipitate dried and washed with deionized water several times and lyophilized.



Analysis for **PTS-PBLG<sub>49</sub>-b-PEG<sub>45</sub>** (Starting PTS-PBLG<sub>49</sub> 150 mg, yield of the block copolymer 168 mg, 94% (click reaction yield calculated from  $^1\text{H}$  NMR 100%)): SEC (DMF 2.5M of  $\text{NH}_4\text{PF}_6$ , standard PEO)  $M_n = 3.926$  kDa,  $M_w/M_n = 1.19$ .  $^1\text{H}$  NMR (400 MHz,  $\text{CDCl}_3$ )  $\delta$  8.26 (br, NH), 7.21 (br, 245H<sub>6-6'''</sub>), 4.96 (br, 100H<sub>5</sub>), 3.85 (br, 49H<sub>2</sub>), 3.70 – 3.37 (m, 182H<sub>1</sub>), 3.31 (s, 3H<sub>7</sub>), 2.25 (br, 196H<sub>3,4</sub>).

Analysis for **PTS-PBLG<sub>49</sub>-b-PEG<sub>113</sub>** (Starting PTS-PBLG<sub>49</sub> 150 mg, yield of the block copolymer 175 mg, 80% (click reaction yield calculated from  $^1\text{H}$  NMR is 100%)): SEC (DMF 2.5M of  $\text{NH}_4\text{PF}_6$ , standard PEO)  $M_n = 7.537$  kDa,  $M_w/M_n = 1.19$ .  $^1\text{H}$  NMR (400MHz,  $\text{CDCl}_3$ )  $\delta$  8.28 (br, NH), 7.34 – 7.03 (m, 245H<sub>6-6'''</sub>), 4.96 (br, 100H<sub>5</sub>), 3.85 (br, 49H<sub>2</sub>), 3.78 – 3.37 (m, 454H<sub>1</sub>), 3.31 (s, 3H<sub>7</sub>), 2.25 (br, 196H<sub>3,4</sub>).

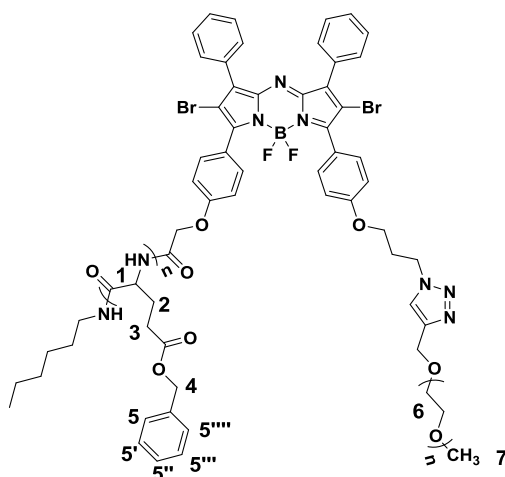
## Amphiphilic PBLG-PTS-*b*-PEG type block copolymer synthesis

### General procedure

PEG-alkyne ( $M_n = 5039$ g/mol or 2039g/mol, 1 eq), PBLG (1 eq) and tris(benzyltriazolylmethyl) amine (TBTA, 1eq) were dissolved in excess of dry DCM under nitrogen and degassed via frizz-thaw cycle.  $\text{CuBr}$  (1eq) was then added and the solution was degassed one more time with frizz-vacuum-thaw cycle and stirred at ambient temperature for 24h, under nitrogen.

The solution was filtrated and partitioned between EDTA (400mg/L) solution and DCM. The organic phase was separated and dried over  $\text{MgSO}_4$  and concentrated. Crude product was purified by column chromatography on silica gel (60 Å, 200-400 mesh) by using DCM:MeOH

(9:1) mixture as an eluent. Pure block copolymer fraction were concentrated under reduced pressure, precipitated into cold Et<sub>2</sub>O and filtrated. The green precipitate dried and washed several times with deionized water and lyophilized.



Analysis for **PBLG<sub>53</sub>-PTS-*b*-PEG<sub>45</sub>** (Starting PBLG<sub>53</sub>-PTS 280mg, isolated yield of the block copolymer 198mg, 61% (click reaction yield calculated from <sup>1</sup>H NMR 72%)): SEC (DMF 2.5M of NH<sub>4</sub>PF<sub>6</sub>, standard PEO) Mn = 4.938 kDa, Mw/Mn = 1.22. <sup>1</sup>H NMR (400 MHz, CDCl<sub>3</sub>) δ 8.28 (br, NH), 7.18 (br, 265H<sub>5-5''''</sub>), 4.96 (br, 106H<sub>4</sub>), 3.86 (br, 53H<sub>1</sub>), 3.57 (m, 182H<sub>6</sub>), 3.31 (s, 3H<sub>7</sub>), 2.27 (br, 212H<sub>2,3</sub>).

Analysis for **PBLG<sub>53</sub>-PTS-*b*-PEG<sub>113</sub>** (Starting PBLG<sub>53</sub>-PTS 240mg, isolated yield of the block copolymer 195mg, 58% (click reaction yield calculated from <sup>1</sup>H NMR 88%)): SEC (DMF 2.5 M of NH<sub>4</sub>PF<sub>6</sub>, standard PEO) Mn = 8.36kDa, Mw/Mn = 1.22. <sup>1</sup>H NMR (500MHz, CDCl<sub>3</sub>) δ 8.35 (br, NH), 7.60 – 7.00 (br m, 265H<sub>5-5''''</sub>), 5.06 (br, 106H<sub>4</sub>), 3.93 (br, 53H<sub>1</sub>), 3.85 – 3.45 (m, 454H<sub>6</sub>), 3.41 (s, 3H<sub>7</sub>), 1.84-2.62 (br, 212H<sub>2,3</sub>).

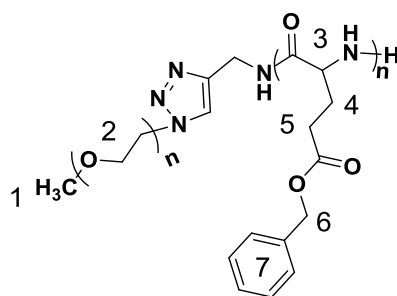
## PTS free PBLG-*b*-PEG type block copolymer synthesis by Cu(II) catalysed click reaction

### General Procedure

PEG-N<sub>3</sub> (Mn = 5041g/mol or 2041g/mol, 1.5 eq) and PBLG<sub>54</sub> (1 eq) were dissolved in DMSO at 30°C. Sodium ascorbate (3.5eq) was added under vigorous stirring and followed by CuSO<sub>4</sub> (2eq) addition. The solution was stirred at 30°C for 48h, under nitrogen.

The solution was partitioned between EDTA (400 mg/L, 5x) solution, deionized water (2x) and DCM, respectively. The organic phase was separated, dried over MgSO<sub>4</sub> and concentrated under reduced pressure. Concentrated polymer solution in DCM was precipitated into cold diethyl ether and filtrated. The white precipitate dried, washed with deionized water and centrifuged several times to remove excess PEG and finally dried by lyophilization.





Analysis for **PBLG<sub>54</sub>-*b*-PEG<sub>45</sub>** (Starting PBLG<sub>54</sub> 500 mg, yield of the block copolymer 531mg, 91% (click reaction yield calculated from <sup>1</sup>H NMR is 100%)): SEC (DMF 2.5M of NH<sub>4</sub>PF<sub>6</sub>, standard PEO) Mn = 5.517 kDa, Mw/Mn = 1.15. <sup>1</sup>H NMR (400 MHz, CDCl<sub>3</sub>) δ 8.26 (br, NH), 7.18 (br, 270H<sub>7</sub>), 4.96 (br, 108H<sub>6</sub>), 3.86 (br, 54H<sub>3</sub>), 3.57 (m, 182H<sub>2</sub>), 3.31 (s, 3H<sub>1</sub>), 2.05-2.53 (br, 216H<sub>4,5</sub>).

Analysis for **PBLG<sub>54</sub>-*b*-PEG<sub>113</sub>** (Starting PBLG<sub>54</sub> 500mg, yield of the block copolymer 562mg, 79% (click reaction yield calculated from <sup>1</sup>H NMR is 100%)): SEC (DMF 2.5M of NH<sub>4</sub>PF<sub>6</sub>, standard PEO) Mn = 8.913 kDa, Mw/Mn = 1.18. <sup>1</sup>H NMR (400 MHz, CDCl<sub>3</sub>) δ 8.26 (br s, NH), 7.18 (br, 270H<sub>7</sub>), 4.96 (br, 108H<sub>6</sub>), 3.87 (br, 54H<sub>3</sub>), 3.57 (m, 454H<sub>2</sub>), 3.31 (s, 3H<sub>1</sub>), 2.05-2.53 (br, 216H<sub>4,5</sub>).

## Appendix 2: CHARACTERIZATION DATA FOR COMPOUNDS IN CHAPTER 2

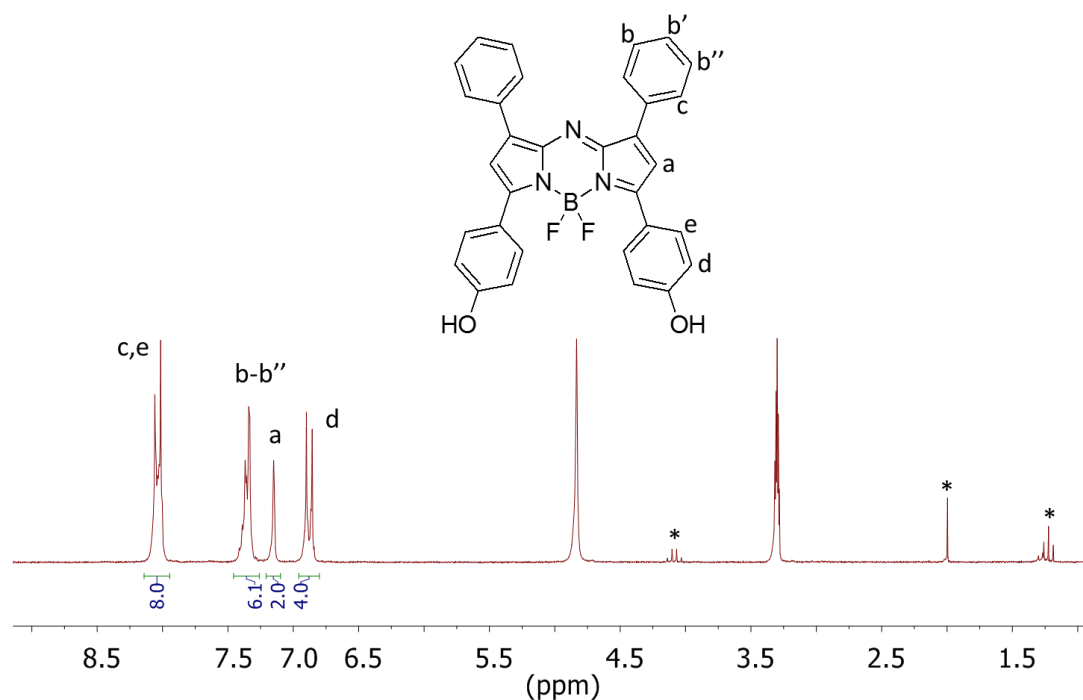


**Figure A2.1:** <sup>1</sup>H-NMR of BF<sub>2</sub> chelate of compound **20** (MeOD, 300 MHz, \*AcOEt)

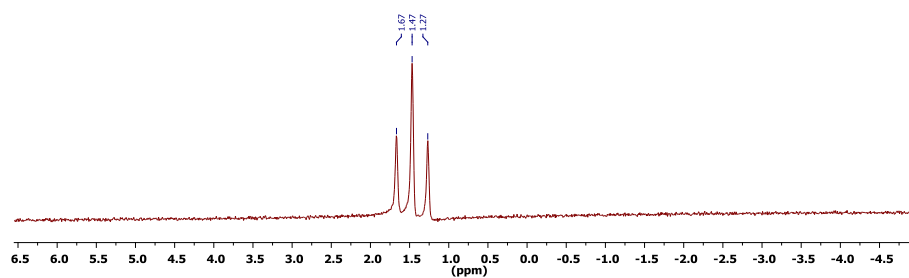


**Figure A2.2:**  $^{11}\text{B}$ -NMR of  $\text{BF}_2$  chelate of compound **20** ( $\text{MeOD}$ , 300 MHz)

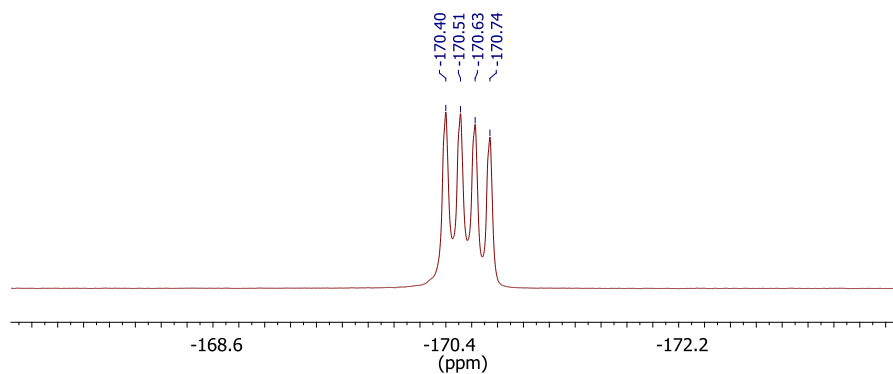


**Figure A2.3:**  $^{19}\text{F}$ -NMR of  $\text{BF}_2$  chelate of compound **20** ( $\text{Acetone-d}_6$ , 300 MHz)

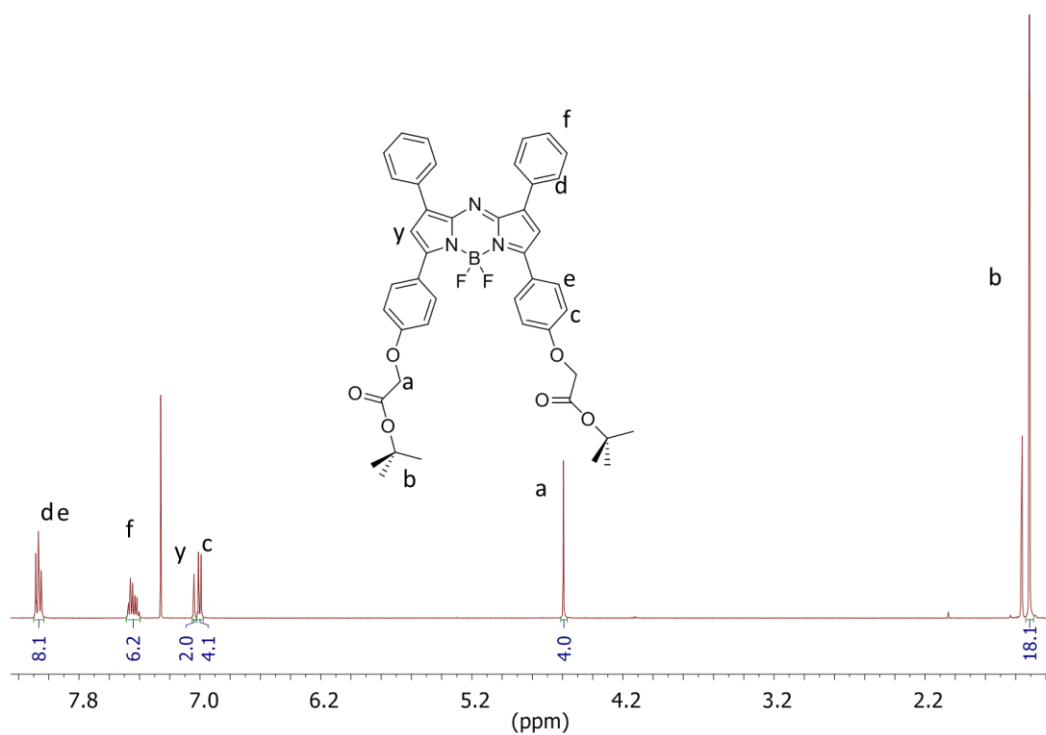


**Figure A2.4:**  $^1\text{H}$ -NMR spectrum of **21** ( $\text{CDCl}_3$ , 300 MHz)

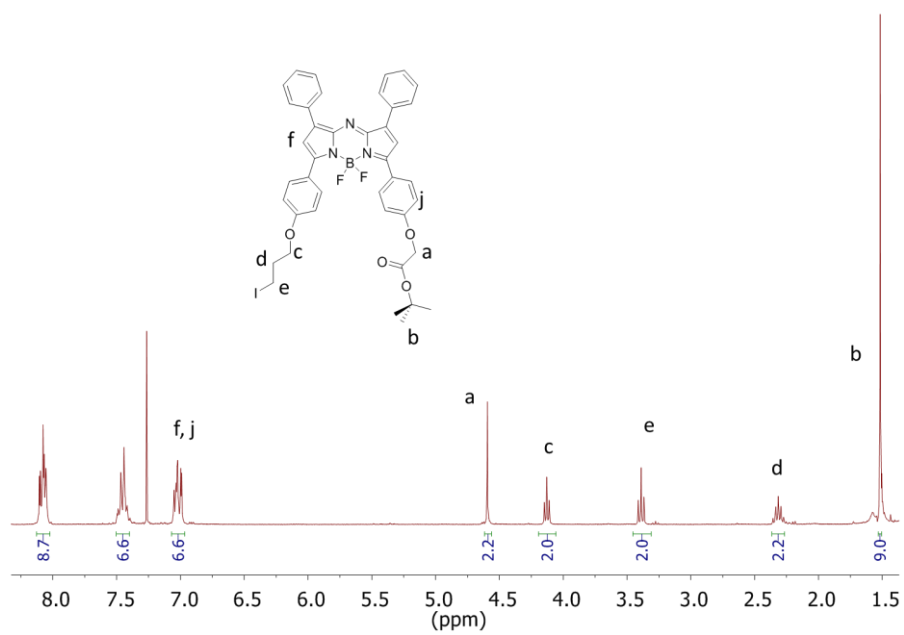


**Figure A2.5:** <sup>1</sup>H-NMR spectrum of compound **23** (300 MHz, CDCl<sub>3</sub>)

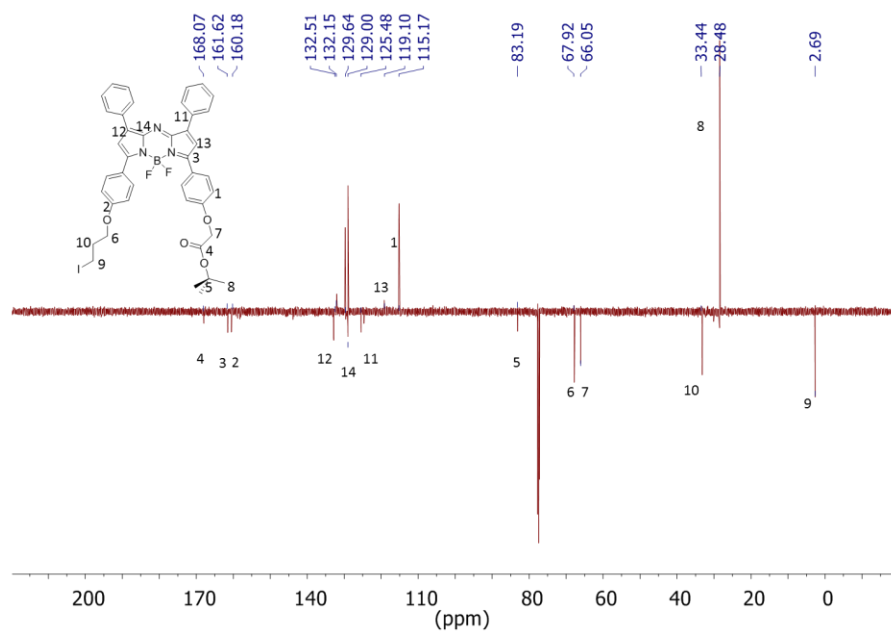


**Figure A2.6:** <sup>13</sup>C-NMR spectrum of compound **23** (500 MHz, CDCl<sub>3</sub>)

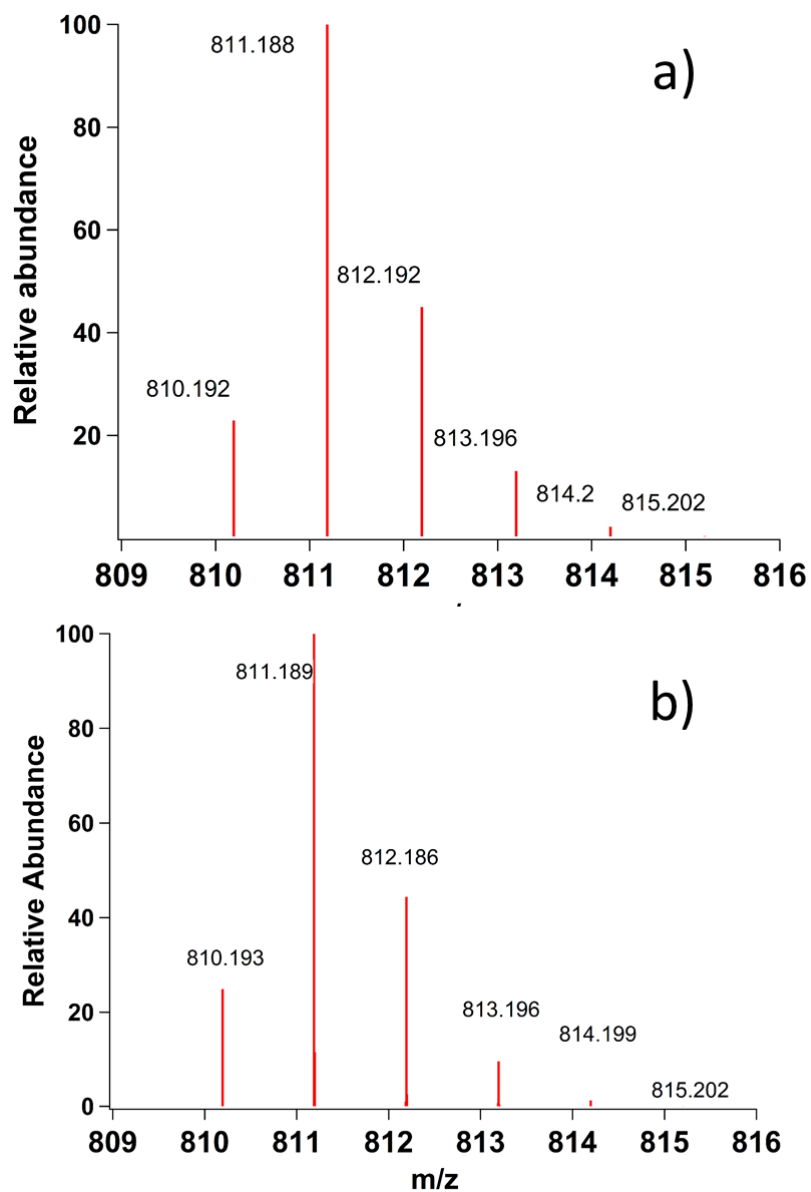


**Figure A2.7:** Mass spectroscopy result of compound **23** a) experimental isotopic mass distribution obtained from ESI mass spectroscopy measurement b) theoretical result obtained from mmass simulator.

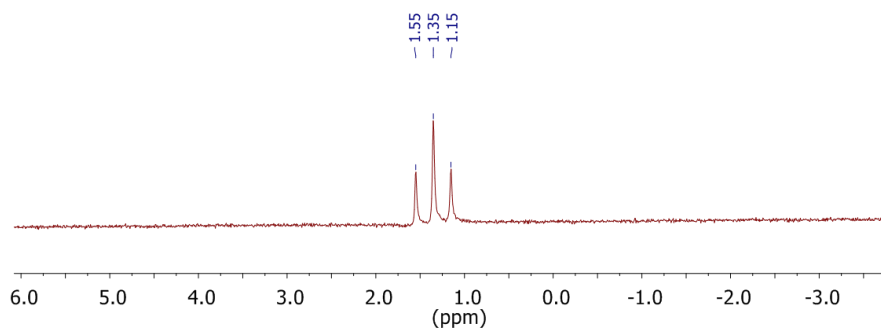


**Figure A2.8:**  $^{11}\text{B}$ -NMR spectrum of compound **23** (500 MHz,  $\text{CDCl}_3$ )

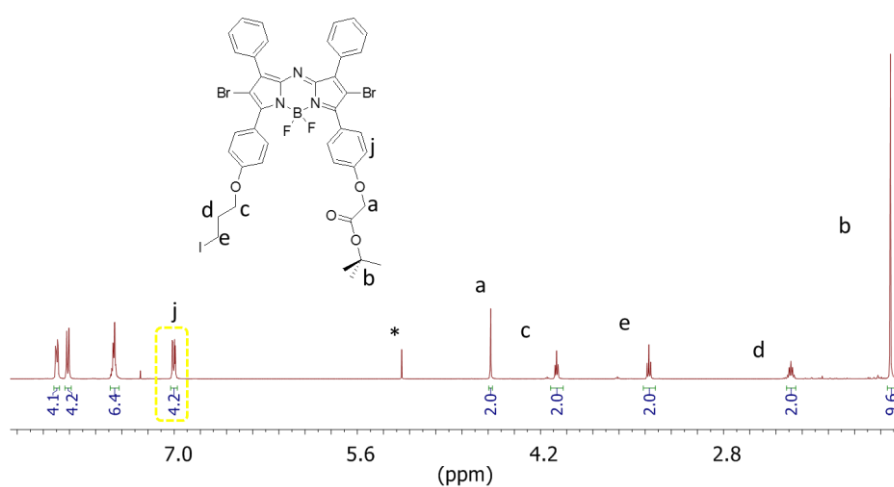


**Figure A2.9:**  $^1\text{H}$ -NMR spectrum of compound **24** (500 MHz,  $\text{CDCl}_3$ )

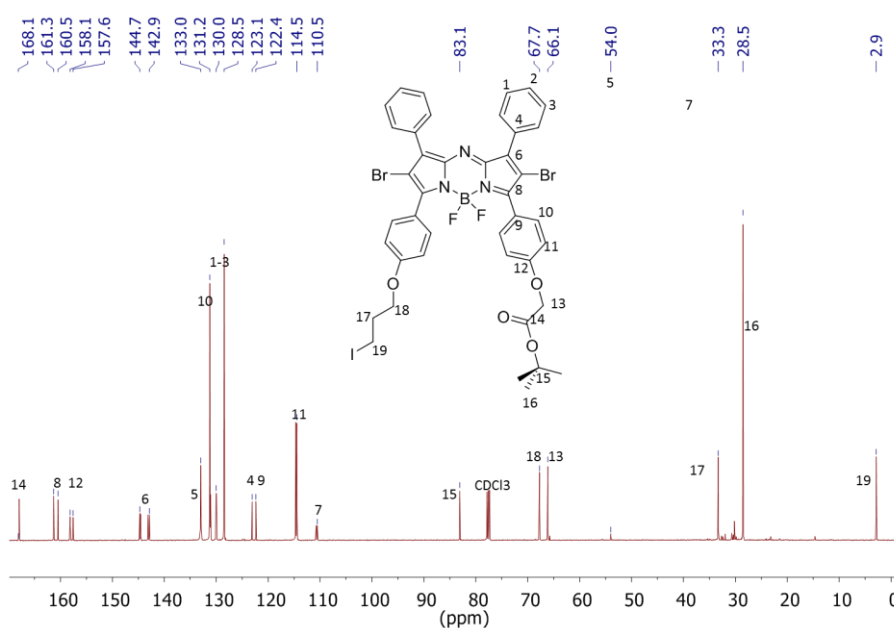


**Figure A2.10:**  $^{13}\text{C}$ -NMR spectrum of compound **24** (500 MHz,  $\text{CDCl}_3$ )

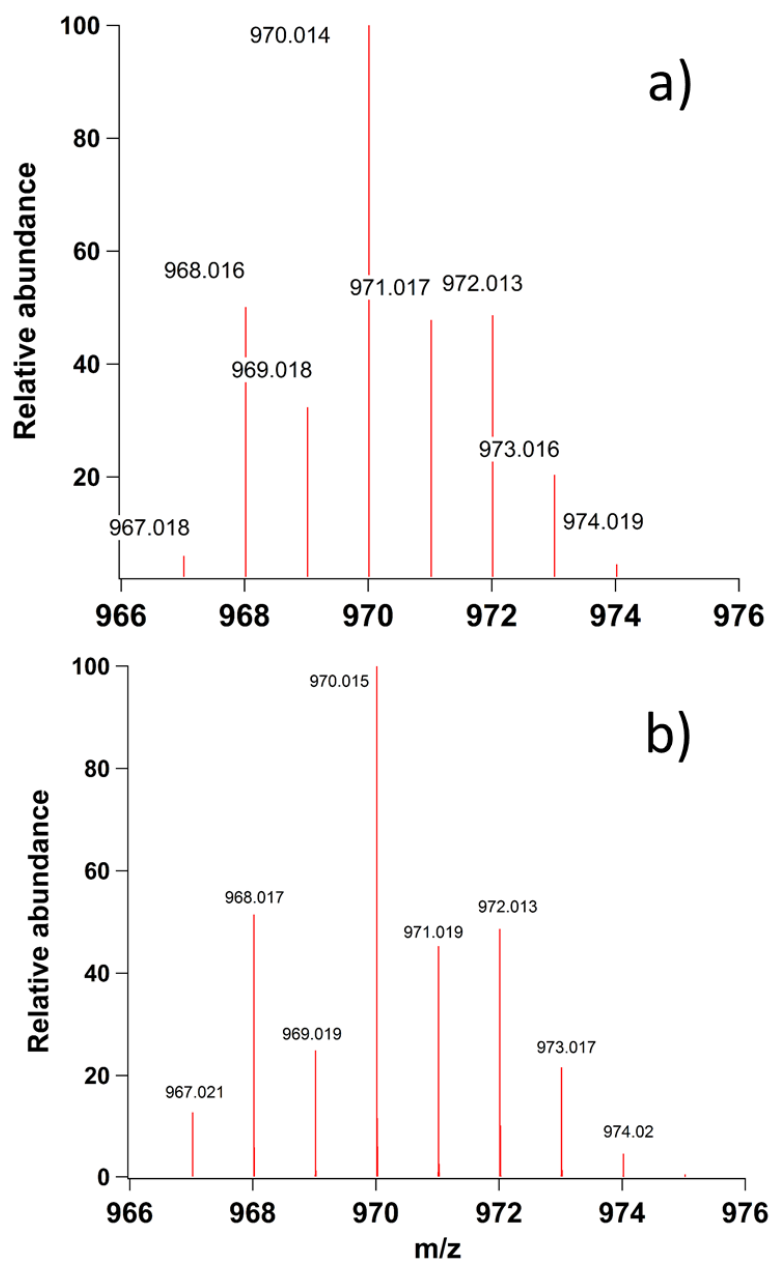


**Figure A2.11:** Mass spectroscopy result of compound **24** a) experimental isotopic mass distribution obtained from APCI  $[M+H]^+$  mass spectroscopy measurement b) theoretical result obtained from mmass simulator.

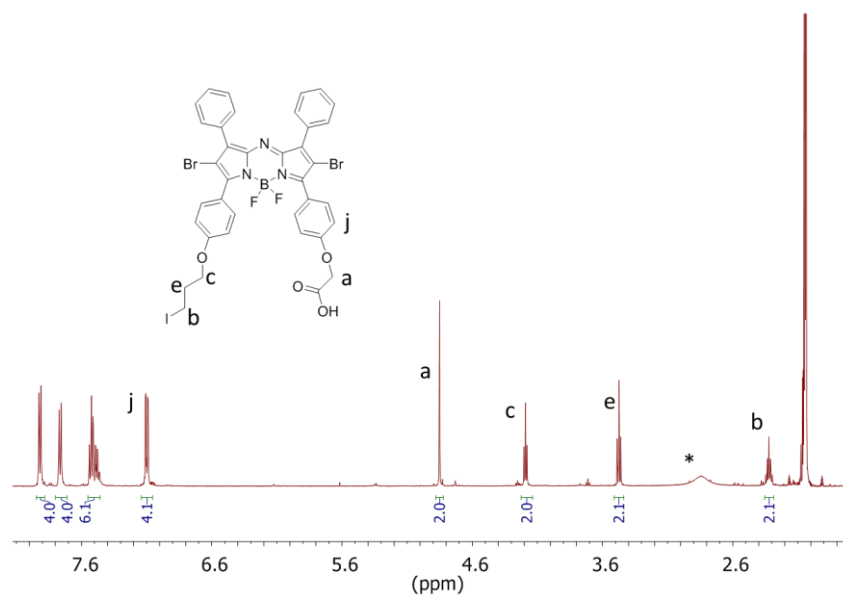


**Figure A3.12:**  $^1\text{H-NMR}$  spectrum of compound **25** (500 MHz, acetone- $d_6$ )

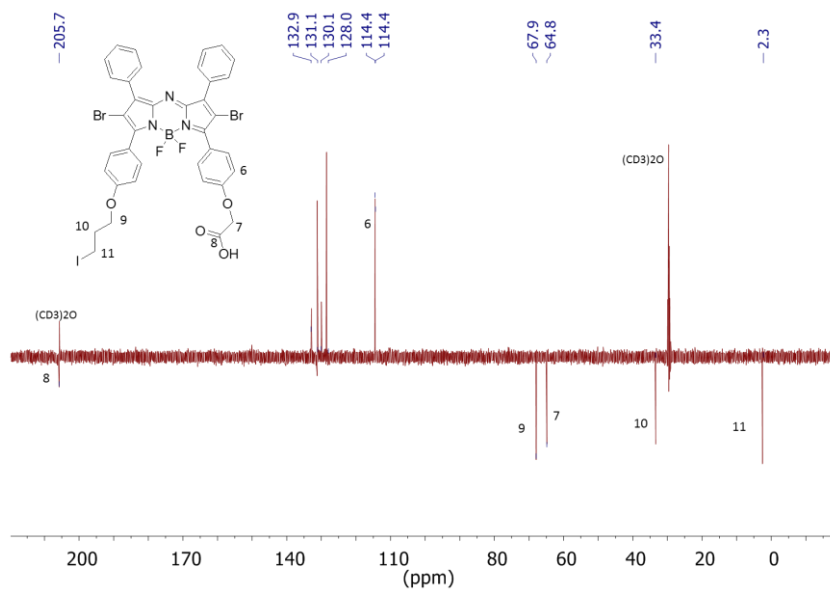


**Figure A2.13:**  $^{13}\text{C-NMR}$  spectrum of compound **25** (500 MHz, acetone- $d_6$ )

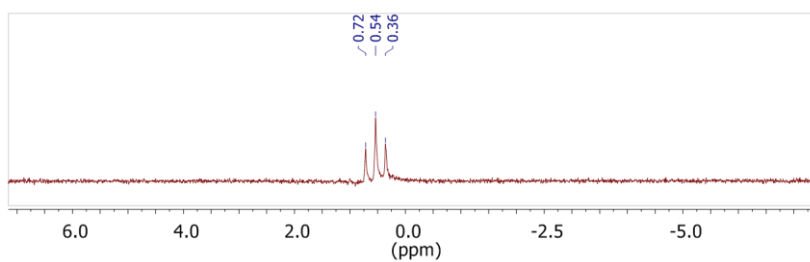


**Figure A2.14:**  $^{11}\text{B}$ -NMR spectrum of compound **25** (500 MHz, acetone- $d_6$ )

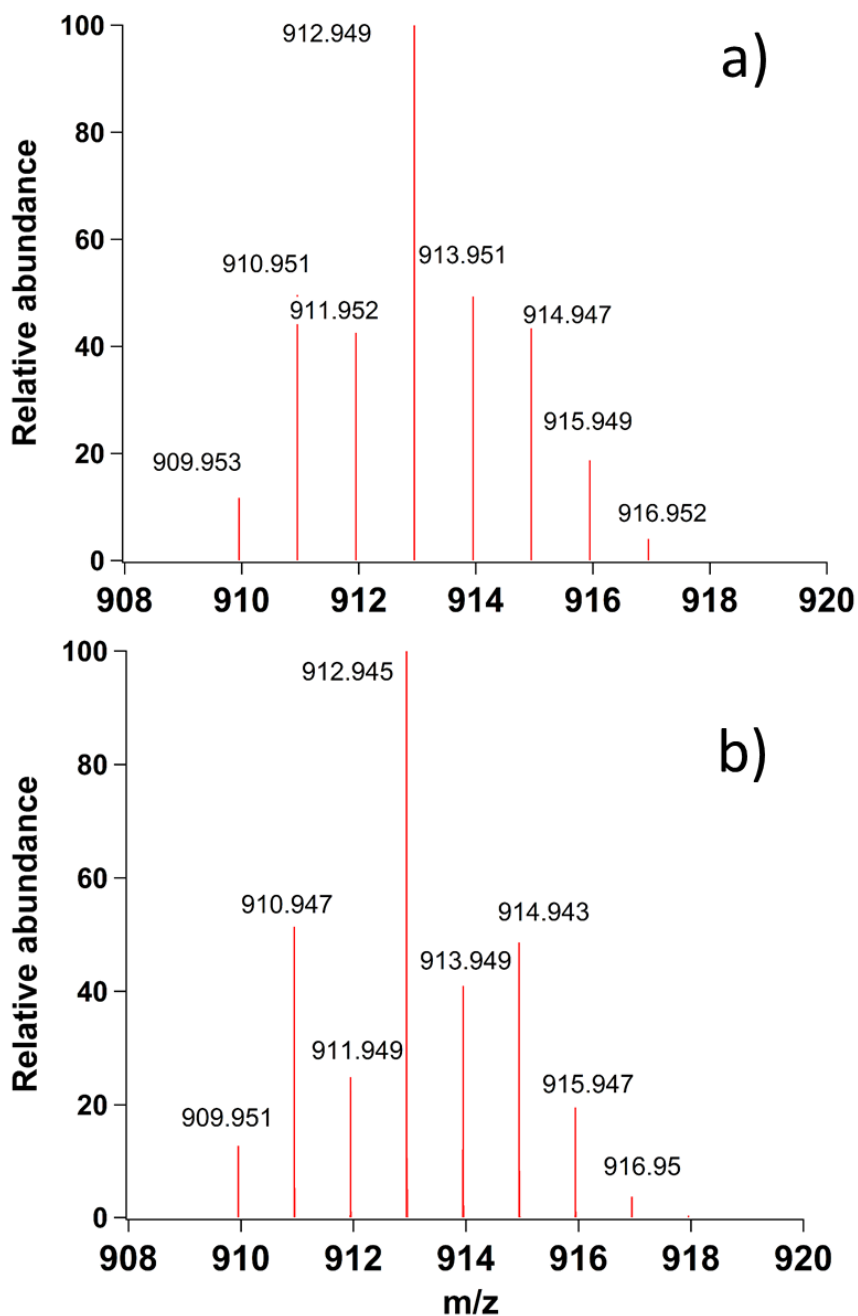


**Figure A2.15:** Mass spectroscopy result of compound **25** a) experimental isotopic mass distribution obtained from APCI  $[\text{M}-\text{H}]^+$  mass spectroscopy measurement b) theoretical result obtained from mmass simulator.



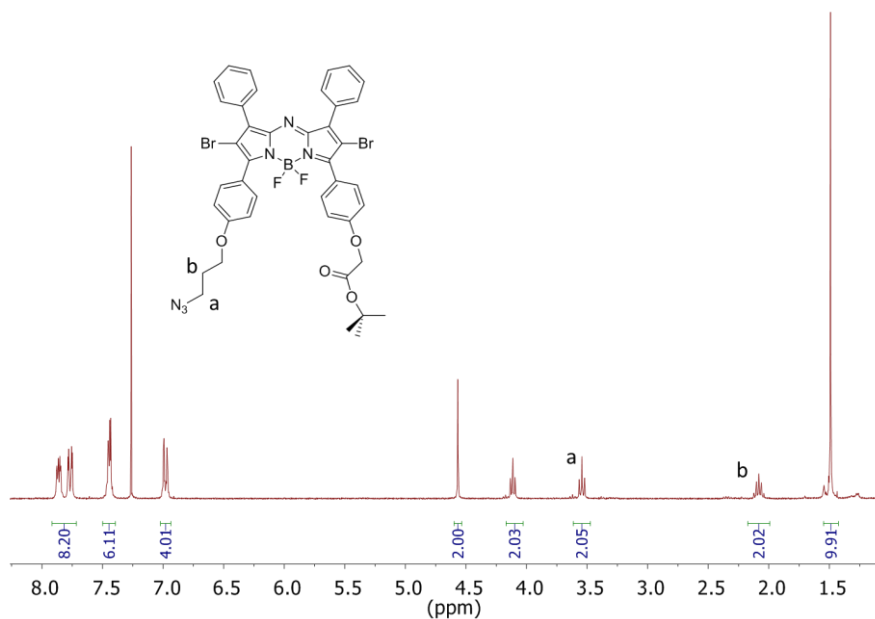


**Figure A2.16:**  $^1\text{H}$  NMR spectrum of compound **26** (300 MHz,  $\text{CDCl}_3$ )

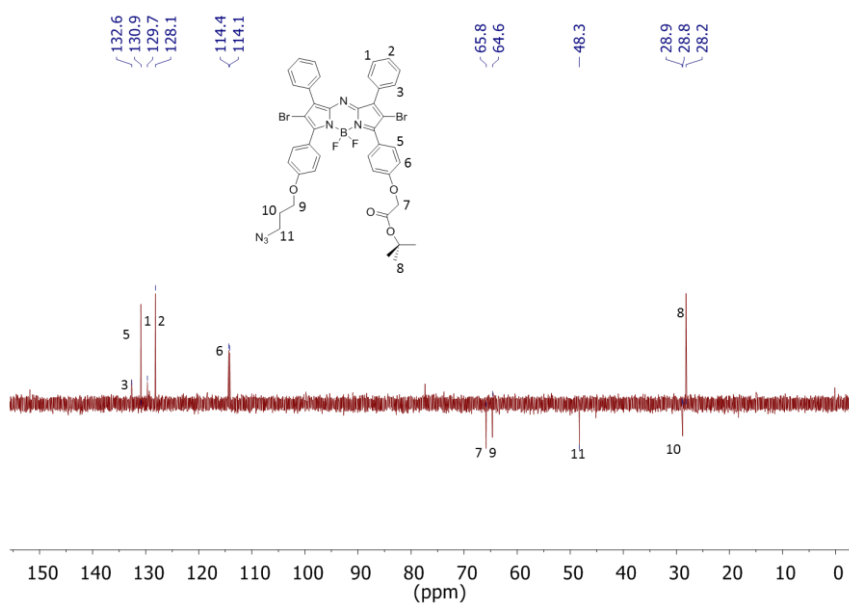


**Figure A2.17:**  $^{13}\text{C}$ -NMR spectrum of compound **26** (300 MHz,  $\text{CDCl}_3$ )

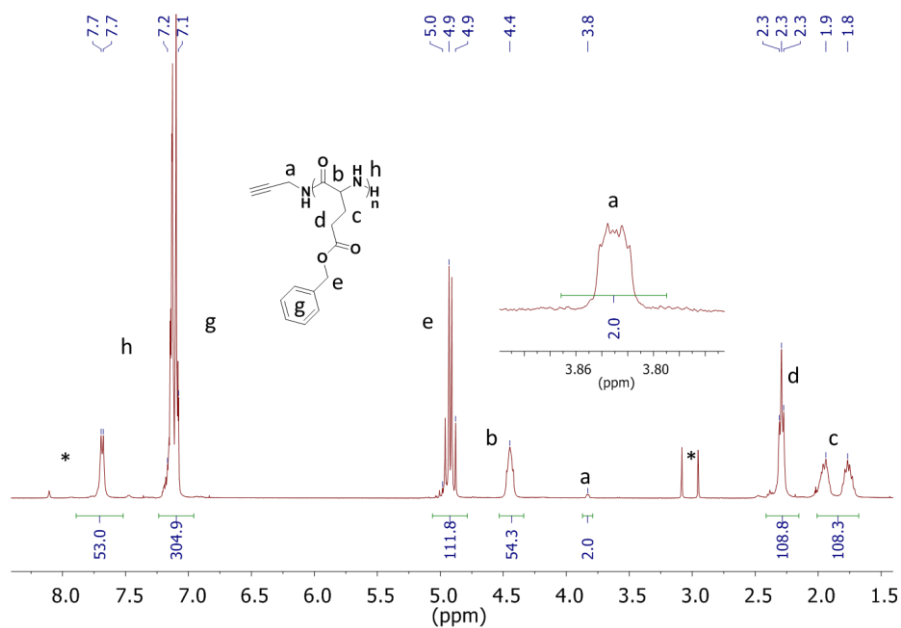


**Figure A2.18:**  $^1\text{H}$  NMR spectrum of PBLG<sub>54</sub> (400 MHz, TFA/ $\text{CDCl}_3$ , \*DMF)

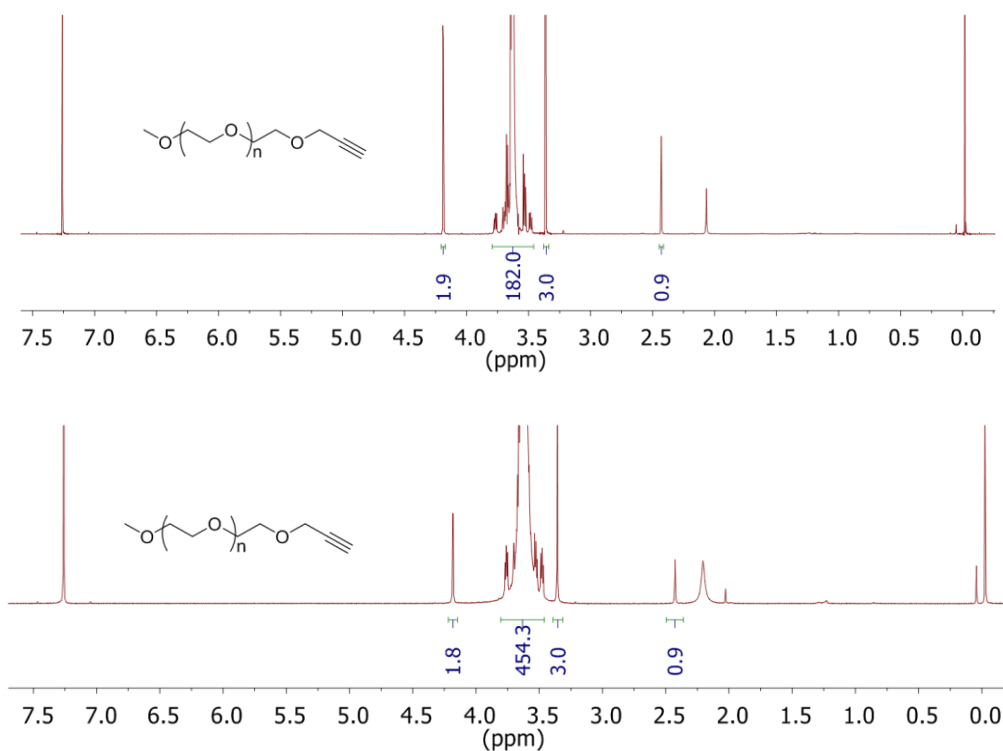


**Figure A2.19:**  $^1\text{H}$  NMR spectrum of (1) PEG<sub>45</sub>-alkyne, (2) PEG<sub>113</sub>-alkyne polymers (500 MHz,  $\text{CDCl}_3$ )

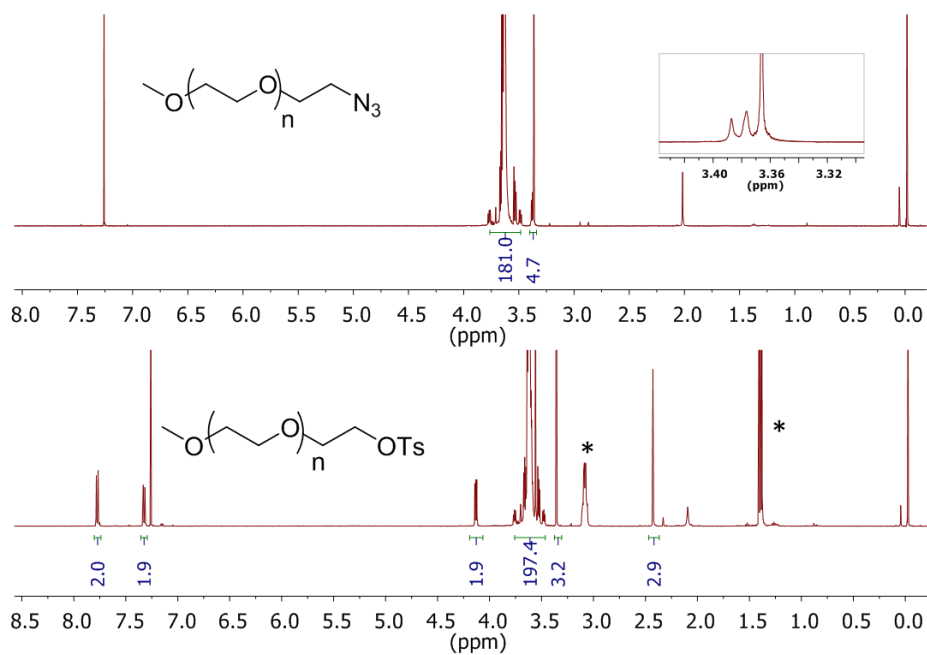


**Figure A2.20:**  $^1\text{H}$  NMR spectrum of PEG<sub>45</sub>-Ts and PEG<sub>45</sub>-N<sub>3</sub> polymers (500 MHz, CDCl<sub>3</sub>, \*Et<sub>2</sub>O)

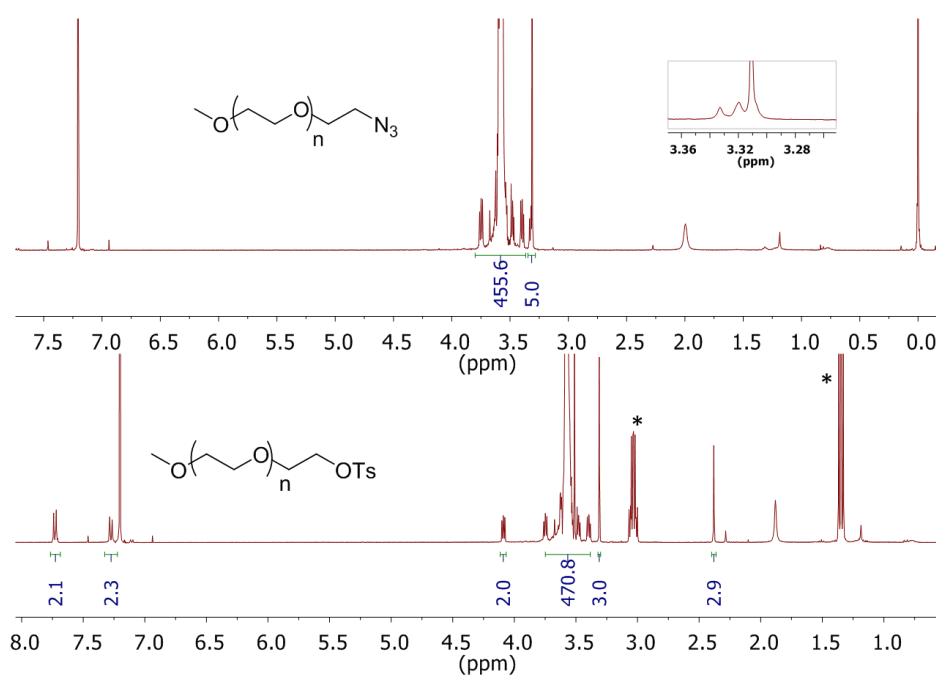


**Figure A2.21:**  $^1\text{H}$  NMR spectrum of PEG<sub>113</sub>-Ts and PEG<sub>113</sub>-N<sub>3</sub> polymers (400 MHz, CDCl<sub>3</sub>, \*Et<sub>2</sub>O)

## References

- (1) Wu, L.; Burgess, K. *Chemical Communications* **2008**, 4933.
- (2) Nepomnyashchii, A. B.; Bröring, M.; Ahrens, J.; Bard, A. J. *Journal of the American Chemical Society* **2011**, *133*, 8633.
- (3) Treibs, A.; Kreuzer, F.-H. *Justus Liebigs Annalen der Chemie* **1968**, 718, 208.
- (4) Kolemen, S.; Cakmak, Y.; Ozdemir, T.; Erten-Ela, S.; Buyuktemiz, M.; Dede, Y.; Akkaya, E. U. *Tetrahedron* **2014**, *70*, 6229.
- (5) Wang, D.; Fan, J.; Gao, X.; Wang, B.; Sun, S.; Peng, X. *The Journal of Organic Chemistry* **2009**, *74*, 7675.
- (6) Li, Z.; Mintzer, E.; Bittman, R. *The Journal of Organic Chemistry* **2006**, *71*, 1718.
- (7) Michel, B. W.; Lippert, A. R.; Chang, C. J. *Journal of the American Chemical Society* **2012**, *134*, 15668.
- (8) Sozmen, F.; Kolemen, S.; Kumada, H.-O.; Ono, M.; Saji, H.; Akkaya, E. U. *RSC Advances* **2014**, *4*, 51032.
- (9) Zhao, W.; Carreira, E. M. *Angewandte Chemie International Edition* **2005**, *44*, 1677.
- (10) Sathyamoorthi, G.; Soong, M. L.; Ross, T. W.; Boyer, J. H. *Heteroat. Chem.* **1993**, *4*, 603.
- (11) Toomas H. Allik, R. E. H., Govindarao Sathyamoorthi, Joseph H. Boyer *Proc. SPIE-Int. Soc. Opt. Eng.* **1994**, *2115*, 9.
- (12) Killoran, J.; Allen, L.; Gallagher, J. F.; Gallagher, W. M.; O'Shea, D. F. *Chem Commun (Camb)* **2002**, 1862.
- (13) Rogers, M. A. T. *Journal of the Chemical Society (Resumed)* **1943**, 590.
- (14) Rogers, M. T.; Roberts, J. D. *Journal of the American Chemical Society* **1946**, *68*, 843.
- (15) Boens, N.; Leen, V.; Dehaen, W. *Chemical Society Reviews* **2012**, *41*, 1130.
- (16) Gorman, A.; Killoran, J.; O'Shea, C.; Kenna, T.; Gallagher, W. M.; O'Shea, D. F. *J Am Chem Soc* **2004**, *126*, 10619.
- (17) Jiang, X.-D.; Fu, Y.; Zhang, T.; Zhao, W. *Tetrahedron Letters* **2012**, *53*, 5703.
- (18) Loudet, A.; Bandichhor, R.; Burgess, K.; Palma, A.; McDonnell, S. O.; Hall, M. J.; O'Shea, D. F. *Org Lett* **2008**, *10*, 4771.
- (19) Tasior, M.; Murtagh, J.; Frimannsson, D. O.; McDonnell, S. O.; O'Shea, D. F. *Organic & Biomolecular Chemistry* **2010**, *8*, 522.
- (20) Gawley, R. E.; Mao, H.; Haque, M. M.; Thorne, J. B.; Pharr, J. S. *The Journal of Organic Chemistry* **2007**, *72*, 2187.
- (21) Coskun, A.; Yilmaz, M. D.; Akkaya, E. U. *Organic Letters* **2007**, *9*, 607.
- (22) Khan, T. K.; Sheokand, P.; Agarwal, N. *European Journal of Organic Chemistry* **2014**, *2014*, 1416.
- (23) Fan, G.; Yang, L.; Chen, Z. *Front. Chem. Sci. Eng.* **2014**, *8*, 405.
- (24) Kamkaew, A.; Burgess, K. *Chemical Communications* **2015**, *51*, 10664.
- (25) Collado, D.; Vida, Y.; Najera, F.; Perez-Inestrosa, E. *RSC Advances* **2014**, *4*, 2306.
- (26) Wu, D.; O'Shea, D. F. *Org Lett* **2013**, *15*, 3392.
- (27) Zhang, X.-X.; Wang, Z.; Yue, X.; Ma, Y.; Kiesewetter, D. O.; Chen, X. *Molecular Pharmaceutics* **2013**, *10*, 1910.
- (28) Adarsh, N.; Krishnan, M. S.; Ramaiah, D. *Analytical Chemistry* **2014**, *86*, 9335.
- (29) Adarsh, N.; Shanmugasundaram, M.; Ramaiah, D. *Anal Chem* **2013**, *85*, 10008.

- (30) Kraner, S.; Widmer, J.; Benduhn, J.; Hieckmann, E.; Jägeler-Hoheisel, T.; Ullbrich, S.; Schütze, D.; Sebastian Radke, K.; Cuniberti, G.; Ortmann, F.; Lorenz-Rothe, M.; Meerheim, R.; Spoltore, D.; Vandewal, K.; Koerner, C.; Leo, K. *physica status solidi (a)* **2015**, n/a.
- (31) Shimizu, S.; Iino, T.; Saeki, A.; Seki, S.; Kobayashi, N. *Chemistry – A European Journal* **2015**, *21*, 2893.
- (32) Min, J.; Ameri, T.; Gresser, R.; Lorenz-Rothe, M.; Baran, D.; Troeger, A.; Sgobba, V.; Leo, K.; Riede, M.; Guldi, D. M.; Brabec, C. J. *ACS Applied Materials & Interfaces* **2013**, *5*, 5609.
- (33) Kricheldorf, H. In  *$\alpha$ -Aminoacid-N-Carboxy-Anhydrides and Related Heterocycles*; Kricheldorf, H., Ed.; Springer Berlin Heidelberg: 1987, p 3.
- (34) Leuchs, H. *Berichte der deutschen chemischen Gesellschaft* **1906**, *39*, 857.
- (35) Leuchs, H.; Manasse, W. *Berichte der deutschen chemischen Gesellschaft* **1907**, *40*, 3235.
- (36) Leuchs, H.; Geiger, W. *Berichte der deutschen chemischen Gesellschaft* **1908**, *41*, 1721.
- (37) Wang, L.-l.; Wu, Y.-x.; Xu, R.-w.; Wu, G.-y.; Yang, W.-t. *Chinese Journal of Polymer Science* **2008**, *26*, 381.
- (38) Curtius, T.; Sieber, W. *Berichte der deutschen chemischen Gesellschaft (A and B Series)* **1921**, *54*, 1430.
- (39) F., W. *Z. Physiol. Chem.* **1925**, *146*, 72
- (40) Hadjichristidis, N.; Iatrou, H.; Pitsikalis, M.; Sakellariou, G. *Chemical Reviews* **2009**, *109*, 5528.
- (41) Cosani, A.; D'Este, G.; Peggion, E.; Scoefone, E. *Biopolymers* **1966**, *4*, 595.
- (42) Kricheldorf, H. R. *Angewandte Chemie International Edition* **2006**, *45*, 5752.
- (43) Deming, T. In *Peptide Hybrid Polymers*; Klok, H.-A., Schlaad, H., Eds.; Springer Berlin Heidelberg: 2006; Vol. 202, p 1.
- (44) Ballard, D. G. H.; Bamford, C. H. *Proceedings of the Royal Society of London A: Mathematical, Physical and Engineering Sciences* **1954**, *223*, 495.
- (45) Kricheldorf, H. R.; v. Lossow, C.; Schwarz, G. *Macromolecular Chemistry and Physics* **2005**, *206*, 282.
- (46) Kricheldorf, H. In  *$\alpha$ -Aminoacid-N-Carboxy-Anhydrides and Related Heterocycles*; Kricheldorf, H., Ed.; Springer Berlin Heidelberg: 1987, p 158.
- (47) Aliferis, T.; Iatrou, H.; Hadjichristidis, N. *Biomacromolecules* **2004**, *5*, 1653.
- (48) Vayaboury, W.; Giani, O.; Cottet, H.; Deratani, A.; Schué, F. *Macromolecular Rapid Communications* **2004**, *25*, 1221.
- (49) Penczek, S.; Cypriak, M.; Duda, A.; Kubisa, P.; Słomkowski, S. In *Controlled and Living Polymerizations*; Wiley-VCH Verlag GmbH & Co. KGaA: 2010, p 241.
- (50) Flory, P. J. *Journal of the American Chemical Society* **1940**, *62*, 1561.
- (51) Harris, J. M. *Poly (ethylene glycol) chemistry: biotechnical and biomedical applications*; Springer Science & Business Media, 2013.
- (52) Harris, J. M.; Struck, E. C.; Case, M. G.; Paley, M. S.; Yalpani, M.; Van Alstine, J. M.; Brooks, D. E. *Journal of Polymer Science Polymer Chemistry Edition* **1984**, *22*, 341.
- (53) Fruijtier-Pölloth, C. *Toxicology* **2005**, *214*, 1.
- (54) Gombotz, W. R.; Guanghui, W.; Horbett, T. A.; Hoffman, A. S. *Journal of Biomedical Materials Research* **1991**, *25*, 1547.
- (55) Alconcel, S. N. S.; Baas, A. S.; Maynard, H. D. *Polymer Chemistry* **2011**, *2*, 1442.
- (56) Abuchowski, A.; Van Es, T.; Palczuk, N.; Davis, F. *Journal of Biological Chemistry* **1977**, *252*, 3578.

- (57) Veronese, F. M.; Pasut, G. *Drug Discovery Today* **2005**, *10*, 1451.
- (58) Veronese, F. M.; Birkhäuser Verlag/ Springer: Berlin, Germany, 2009.
- (59) Rob Webster, E. D., Philip Harris, Ned Siegel, Jeanne Stadler, Lorraine Tilbury and Dennis Smith *Drug Metab Dispos.* **2007**, *35*, 9.
- (60) Wu, R. W. K.; Chu, E. S. M.; Huang, Z.; Olivo, M. C.; Ip, D. C. W.; Yow, C. M. N. *Journal of Innovative Optical Health Sciences* **2015**, *08*, 1550027.
- (61) Montalbetti, C. A. G. N.; Falque, V. *Tetrahedron* **2005**, *61*, 10827.
- (62) Jursic, B. S.; Zdravkovski, Z. *Synthetic Communications* **1993**, *23*, 2761.
- (63) El-Faham, A.; Albericio, F. *Chemical Reviews* **2011**, *111*, 6557.
- (64) Chan, L. C.; Cox, B. G. *The Journal of Organic Chemistry* **2007**, *72*, 8863.
- (65) Kolb, H. C.; Finn, M. G.; Sharpless, K. B. *Angewandte Chemie International Edition* **2001**, *40*, 2004.
- (66) Barner-Kowollik, C.; Du Prez, F. E.; Espeel, P.; Hawker, C. J.; Junkers, T.; Schlaad, H.; Van Camp, W. *Angew Chem Int Ed Engl* **2011**, *50*, 60.
- (67) Binder, W. H.; Sachsenhofer, R. *Macromolecular Rapid Communications* **2007**, *28*, 15.
- (68) Zhang, L.; Chen, X.; Xue, P.; Sun, H. H. Y.; Williams, I. D.; Sharpless, K. B.; Fokin, V. V.; Jia, G. *Journal of the American Chemical Society* **2005**, *127*, 15998.
- (69) Chowdhury, C.; Mandal, S. B.; Achari, B. *Tetrahedron Letters* **2005**, *46*, 8531.
- (70) Robilotto, T. J.; Alt, D. S.; von Recum, H. A.; Gray, T. G. *Dalton Transactions* **2011**, *40*, 8083.
- (71) Tornøe, C. W.; Christensen, C.; Meldal, M. *The Journal of Organic Chemistry* **2002**, *67*, 3057.
- (72) Meldal, M.; Tornøe, C. W. *Chemical Reviews* **2008**, *108*, 2952.
- (73) Angell, Y.; Burgess, K. *Angewandte Chemie International Edition* **2007**, *46*, 3649.
- (74) Murtagh, J.; Frimannsson, D. O.; O'Shea, D. F. *Org Lett* **2009**, *11*, 5386.
- (75) Loudet, A.; Burgess, K. *Chem Rev* **2007**, *107*, 4891.
- (76) Wu, D.; Cheung, S.; Daly, R.; Burke, H.; Scanlan, E. M.; O'Shea, D. F. *European Journal of Organic Chemistry* **2014**, *2014*, 6841.
- (77) Najberg, M., Université catholique de Louvain, 2015.
- (78) Hadjichristidis, N.; Iatrou, H.; Pitsikalis, M.; Sakellariou, G. *Chem Rev* **2009**, *109*, 5528.







---

## CHAPTER 3

---

### **SELF-ASSEMBLY OF THE PHOTSENSITIZER BEARING AMPHIPHILIC BLOCK COPOLYMERS**

*Abstract*

*By using non-covalent interactions as a tool it is possible to mimic Nature and engineer a wide variety of self-assembled nanostructures. In this chapter, some non-covalent interactions and their role in the self-assembly behavior of the polypeptide based amphiphilic block copolymers are discussed by reviewing literature examples. Finally, the self-assembly of four different PTS functionalized block copolymers, in terms of PTS localization and PEG chain length, was optimized in Milli-Q water and analyzed in detail.*





### 3.1 INTRODUCTION

The concept of self-organization was originated by Erwin Schrödinger when he described order in the living systems in 1944.<sup>1</sup> The self-organization corresponds to the spontaneous assembly of molecules driven by non-covalent interactions to form highly ordered structures.<sup>2</sup> To apply this concept to molecular chemistry or polymer chemistry, scientists have developed a wide variety of materials with distinctive sides to facilitate their self-assembly in a selective environment for one side. In the following sections some fundamental non-covalent interactions for the self-assembly of amphiphilic materials and literature examples of the self-assembled polypeptide based block-copolymers are described.

#### 3.1.1 Hydrophobic interactions and amphiphilic molecules

Polar and ionic compounds have good solubility in polar protic solvents. Due to the water loving nature of those molecules, they are called hydrophilic (*hydro*, water; *philic*, loving) compounds.<sup>3</sup> On the other hand, non-polar compounds have very poor solubility in polar protic solvents. The water avoiding property of non-polar compounds is caused by the so-called hydrophobic (*phobic*, avoiding or hating) interactions. In water, it initiates the association of the hydrophobic molecules together in order to minimize the contact area with the water molecules.

The hydrophilic and hydrophobic interactions are essential, especially for the biological molecules to fulfill important functions in aqueous cellular environments. For example, hydrophobic interactions contribute to the protein folding in aqueous environments which is essential for its biological activity.<sup>4,5</sup> Moreover, some (biological) molecules can bear both hydrophilic and hydrophobic units. These so-called amphiphilic molecules can adopt different structures depending on the environment. A natural example of amphiphilic compounds is phospholipids. Due to an appropriate hydrophilic to hydrophobic balance and molecule shape, they can assemble together in perfect order by hydrophobic interactions and form bilayer cell membranes (see Figure 3.2).<sup>6</sup>

This unique property attracts attention of many scientists to investigate the origin of life, understand the complex structures (cell membrane, protein folding or aggregation, etc.) in living systems by mimicking them *via* synthetic amphiphilic block copolymers or lipids.<sup>7-9</sup> The synthetic amphiphilic block copolymers are also used to build a variety of nanostructures (micelles, nanoworms, nanocylinders, vesicles, etc.) for drug delivery applications.<sup>10-13</sup>

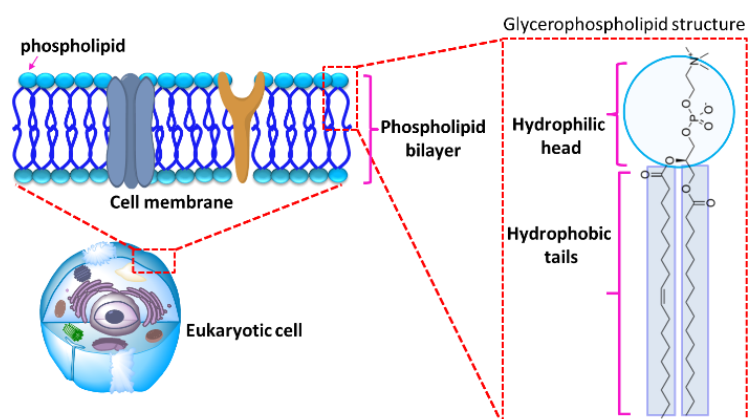


**Figure 3.1:** Illustration of the structure of the cell membrane (adapted from ref<sup>14</sup>)

### 3.1.2 Hydrogen bonding

Hydrogen bonds occur between the hydrogen atom of one molecule and electronegative atoms (nitrogen, oxygen, fluorine, etc.) of the same or different molecules.<sup>15,16</sup> At the macromolecular level, repeated intermolecular and intramolecular H-bonds can form different structures; helices,  $\beta$ -sheets, tubes, fibers, rod-like structures, etc. The double helix DNA molecule is formed by intermolecular H-bonds between two strands running in the opposite directions. However, hydrophobic interactions,  $\pi$ - $\pi$  stacking and electrostatic interactions are also involved in the stabilization of the DNA structure.<sup>17</sup>

Moreover, the secondary, tertiary and quaternary conformations in the peptides and polypeptides are formed as a result of the repeated intramolecular H-bondings.<sup>18-20</sup> The secondary conformations; random coil,  $\alpha$ -helix, and  $\beta$ -sheet (Figure 3.2), are formed by H-bond formation between N-H and C=O groups of the amino acid sequences on the backbone and can be destroyed by addition of strong acids like trifluoroacetic acid.

Secondary structures are characteristic for both natural and synthetic polypeptides. Several non-covalent interactions are also involved in the stabilization of the secondary conformations. For example, a synthetic polypeptide poly( $\gamma$ -benzyl-L-glutamate) (PBLG)<sup>21</sup> can adopt  $\alpha$ -helical or  $\beta$ -sheet conformations depending on the chain length. It has been reported that the  $\beta$ -sheet conformation is characteristic for shorter PBLG chains, up to about 40 repeating units, and  $\alpha$ -helical conformation dominates for longer chains.<sup>22</sup> This could be easily monitored by FT-IR spectroscopy by following the amide I and amide II bands at  $\sim 1655$  and  $\sim 1550$   $\text{cm}^{-1}$  which are distinctive for  $\alpha$ -helical conformation, and the band at  $\sim 1630$   $\text{cm}^{-1}$  belongs to the amide I in  $\beta$ -sheet conformation (Figure 3.3).<sup>22,23</sup>

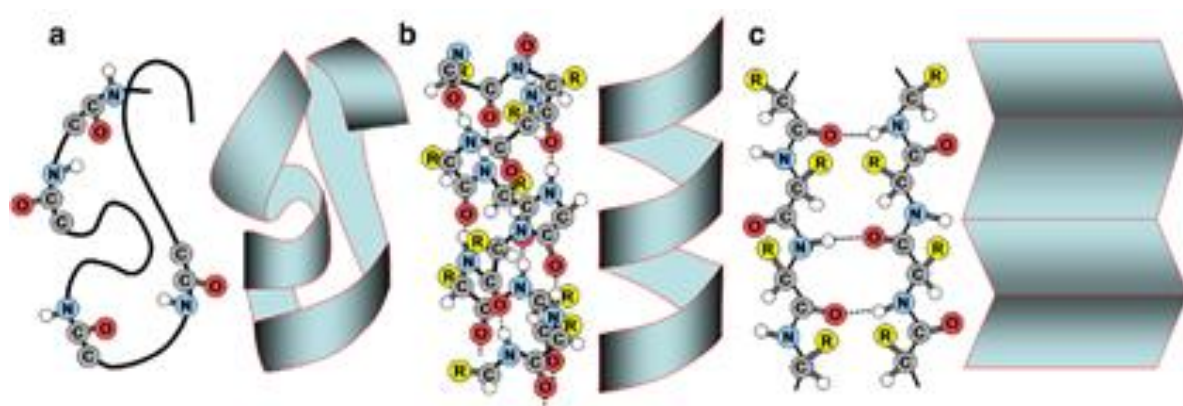


**Figure 3.2:** Schematic diagram of the secondary structures commonly adopted by polypeptides: a) random coil, b)  $\alpha$ -helix, and c) anti-parallel  $\beta$ -sheet.<sup>24</sup>

The tertiary and quaternary structures can be seen in folded proteins that are built by the assembly of the different polypeptide chains with various secondary conformations. However, the formation of these self-assemblies are initiated by mainly H-bonding and hydrophobic interactions.<sup>25</sup> The presence of the other non-covalent interactions further strengthened the H-bonds and stabilizes the complex structure of biological molecules in the intracellular environment.

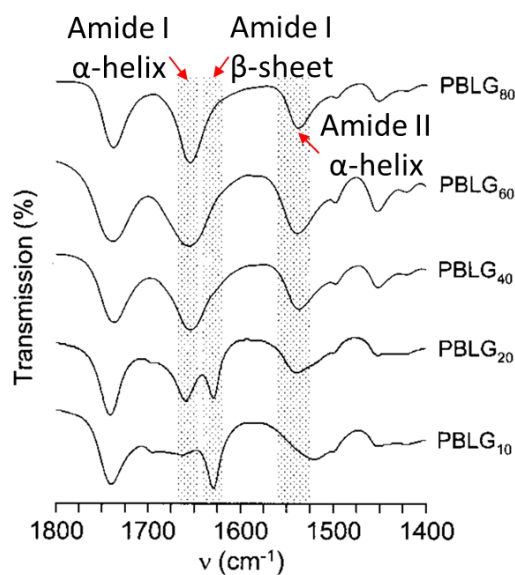


**Figure 3.3:** FT-IR spectra of poly( $\gamma$ -benzyl-L-glutamates) (PBLG<sub>n</sub>, n = 10, 20, 40, 60, 80) <sup>22</sup>

### 3.1.3 Polypeptide based block copolymers

Bioinspired materials like lipids, amphiphilic block copolymers, etc. have great interest in drug delivery applications due to their self-assembly properties into different nanostructures. Vesicles such as liposomes that are formed by the self-assembly of lipids, have been extensively studied for drug delivery applications.<sup>26</sup> However, their application is limited, mainly due to the lack of mechanical and chemical stability, and low functionality.<sup>27</sup> The amphiphilic block copolymers instead have more functionality and chemical diversity. Moreover, they can self-assemble into stable polymersomes, micelles or other nanostructures. On the other hand, some block copolymers face biodegradability and biocompatibility issues for biomedical applications.

In 1996 the first idea of self-assembly of helical oligopeptides into the vesicle structure was suggested,<sup>28</sup> which led to the development of various oligopeptides, polypeptides, block copolypeptides which could self-assemble into various nanostructures.<sup>29</sup> Block copolypeptides are synthesized to bring together two different properties of two different polypeptides. Holowka and coworkers<sup>30</sup> have reported the self-assembly behavior of rod-coil like amphiphilic block copolypeptides, poly(L-lysine)-*b*-poly(L-leucine) (K<sub>x</sub>L<sub>y</sub>). In aqueous medium, by varying the lengths of the blocks, they could obtain stable vesicle formation from K<sub>60</sub>L<sub>20</sub> (Figure 3.4).<sup>30</sup> Poly(L-lysine) is a hydrophilic positively charged polypeptide with coil like conformation, and poly(L-leucine) is a hydrophobic polypeptide that adopts an  $\alpha$ -helical conformation.

At the same time, Lecommandoux's group<sup>31</sup> reported the formation of schizophrenic vesicles from the rod-coil like amphiphilic block copolypeptide poly(L-lysine)-*b*-poly(L-glutamic acid) (PLys<sub>15</sub>-*b*- PLGA<sub>15</sub>). This zwitterionic block copolypeptide has a coil-coil structure in neutral pH due to the positive charges on the lysine domain and negative charges on the glutamic acid domain. However, they can reversibly self-assemble in acidic (pH < 4) and basic (pH > 10) conditions due to the conformation change of one of the block of the copolypeptide (Figure 3.5). At low pH, the solubility of PLGA unit decreases due to its neutralization, and it changes its conformation from coil to  $\alpha$ -helical structure. This conformation change initiates the self-

assembly of the block copolyptide by forming the core of the assemblies. In basic conditions the reverse assembly takes place where the coil like PLGA forms the corona of the vesicles. <sup>31</sup>

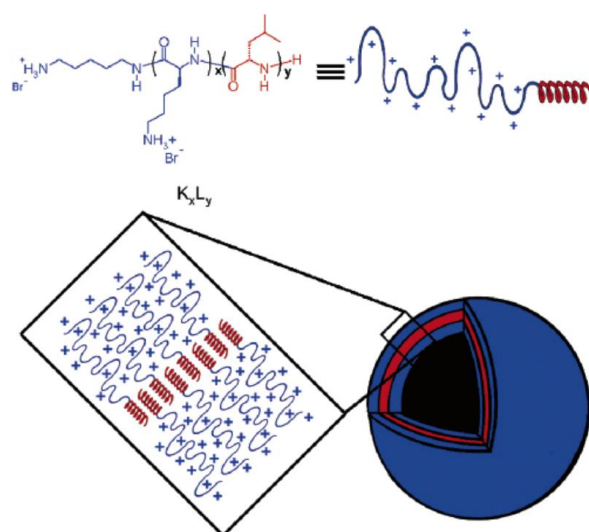


**Figure 3.4:** Illustration of the self-assembly of poly(L-lysine)-*b*-poly(L-leucine) ( $K_{60}L_{20}$ ) block copolyptides into vesicle structure <sup>30</sup>

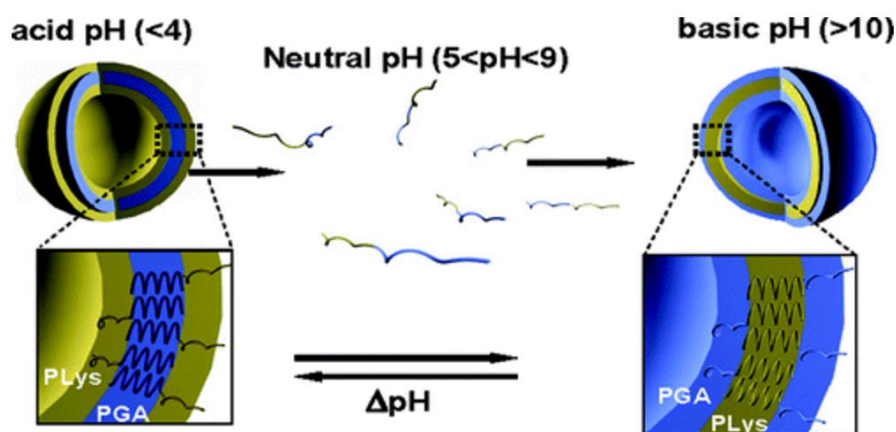


**Figure 3.5:** Schematic representation of the self-assembly of the poly(L-lysine)-*b*-poly(L-glutamic acid) ( $PLys_{15}-b-PLGA_{15}$ ) block copolyptides into vesicle structure. <sup>31</sup>

There are also polypeptide hybrid systems that are synthesized by conjugating a polypeptide to a synthetic polymer block. This enables to combine the attractive features of the synthetic polymers (processability, multifunctionality, good solubility, etc.) with the ones of polypeptides (biocompatibility, biodegradability, secondary conformation, etc.) and enhance the control over self-assembly.<sup>24</sup> Lecommandoux's <sup>32</sup> and Schlaad's <sup>33</sup> groups first and independently reported the self-assembly of the pH responsive hybrid copolymer polybutadiene-*b*-poly(L-glutamic acid) (PB-*b*-PLGA). The size of these peptosomes can be reversibly manipulated by pH and ionic strength in aqueous solutions due to the conformation change in PLGA domain. Many other stimuli responsive block copolyptides<sup>34,35</sup> and hybrid polypeptides<sup>36,37</sup> have been reported in literature to architect 'smart' nanostructures that have broad application areas like sensors,<sup>38</sup> tissue engineering,<sup>39-41</sup> drug delivery,<sup>42</sup> etc.

### 3.1.4 Morphology control over the self-assembly of polypeptide based amphiphilic block copolymers

Well defined amphiphilic copolypeptides and polypeptide based hybrid block copolymers can spontaneously self-assemble into different nanostructures in an aqueous solvent (block selective solvent) in order to minimize the energetically unfavorable water-hydrophobic group interactions.<sup>43</sup> As a result of the comparison of various published experimental data, it has been proposed that the relative fraction of hydrophilic-hydrophobic block volume dictates the morphology, and the overall molecular weight of the amphiphilic block copolymer dictates the membrane thickness of the nano-assemblies.<sup>44</sup>

Israelachvili and coworkers<sup>45</sup> hypothesized that the morphology of nano-assemblies can be predicted by taking geometric properties into account (Figure 3.6). According to them the morphology can be predicted from the “packing parameter”,  $p$  (Equation 3.1), which is also called shape factor and is defined as:

$$p = \frac{v}{a_0 l_c} \quad (3.1)$$

where  $v$  is the volume of the hydrophobic chain,  $l_c$  is the length of the hydrophilic chain and  $a_0$  is the optimal area of the head group.<sup>43,46,47</sup>

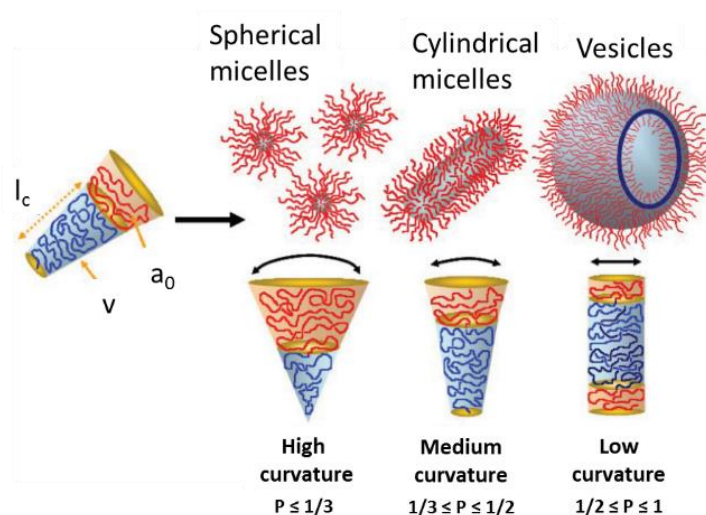


**Figure 3.6:** Illustration of different self-assembled nanostructures formed by amphiphilic block copolymers<sup>43</sup>

In addition, Disher and Eisenberg have proposed that the morphology of the nano-assemblies can be predicted according to the hydrophilic weight fraction of the block copolymer ( $f\%$ ).<sup>48</sup> By unifying the rules they proposed that when hydrophilic weight is  $f \sim 25-40\%$  amphiphilic block copolymers tend to form polymersomes, in the case of  $f > 45\%$  the formation of micelles can be expected. Finally, when the hydrophilic volume fraction is smaller than 25% the formation of the inverted structures can be expected.<sup>44,47,48</sup> Such empirical laws however present some limitations and cannot be used in predictive manner. The morphology shifting could also be observed during the degradation of one unit on the block copolymer which consequently changes the volume fractions of hydrophobic and hydrophilic units. Fariyal and coworkers have prepared polylactide-based biodegradable paclitaxel and doxorubicin loaded



polymersomes for human breast tumors.<sup>49</sup> The polymersomes were prepared from the co-assembly of the amphiphilic PEG-*b*-(polylactic acid, PLA) block copolymer with inert PEG-*b*-(polybutadiene, PBD) block copolymer in 25/75mol% ratio, and change their morphology from vesicle to micelles during the degradation process of PLA block. This transition takes from an hour to one day and includes the release of the hydrophilic and hydrophobic drug content during this process. The reason of morphology shift is explained by the hydrolysis of PLA block in acidic tumor microenvironment, thus the gradual increases in hydrophilic block volume fraction changes the morphology (see Figure 3.7).

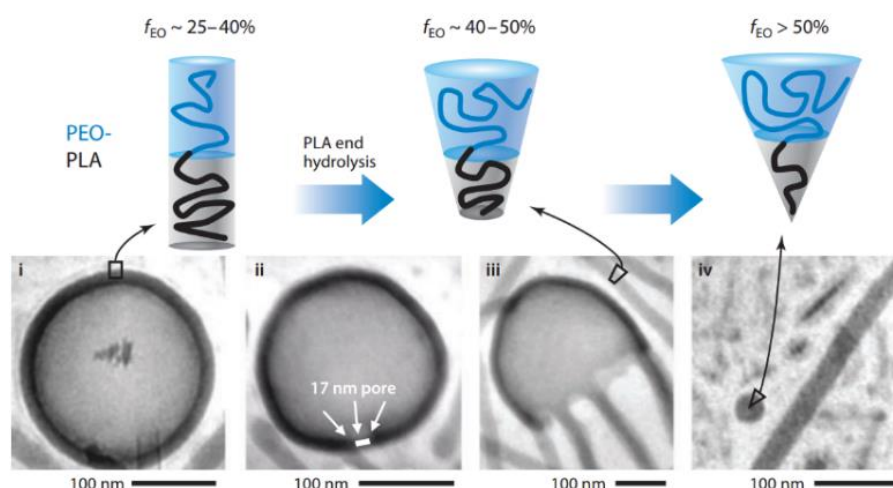


**Figure 3.7:** Degradation of PEG-*b*-PLA polymersome inducing a morphology change<sup>49</sup>

The morphology of the nano-assemblies can be affected also by the secondary conformation of the polypeptide chains.<sup>22,23,46</sup> First, Deming<sup>29</sup> and Lecommandoux<sup>30</sup> proposed that vesicular structure could be favored and stabilized by the  $\alpha$ -helical confirmation of polypeptides. Later, Ding et al.<sup>50</sup> experimentally showed that changing the conformation of PBLG-*b*-PEG block copolymers from rod-coil structure<sup>23,51</sup> to coil-coil structure, changes the morphology of the nano-assembly from cylinder-like micelles to spherical structure (Figure 3.8A). The conformation change of PBLG block, triggered by trifluoroacetic acid (TFA), was caused by a chain transformation of PBLG from a  $\alpha$ -helix to a random coil structure by breaking the H-bonds. Moreover, co-assembling small nanoparticles with amphiphilic polypeptides can also modify the morphology of the self-assembly. Chunhua et al.<sup>52</sup> showed that the co-assembly of 25 nm spherical gold nanoparticles (AuNP) with PBLG-*b*-PEG causes the formation of spherical micelles whereas the pure copolymer self-assembled into long cylindrical micelles (Figure 3.9B). This transformation is explained by a distortion of the ordered packing of rod-coil polymer by the large hydrophobic volume of the nanoparticles during the co-micellization process.

Agut et al.<sup>53</sup> also observed similar behavior while co-assembling hydrophobic ultra-small superparamagnetic iron oxide (USPIO, 6.3nm) nanoparticles with rod-coil like PBLG-*b*-PDMAEMA (poly(2-(dimethylamino) ethyl methacrylate)) block copolymer. They reported that the pure PBLG-*b*-PDMAEMA block copolymer forms a vesicle structure in water. However, after incorporation of USPIO nanoparticles, a phase transition from vesicle to spherical micelle was observed. This morphology shift is explained by a complex phase behavior that is caused by depletion forces between spherical nanoparticles and PBLG rods.

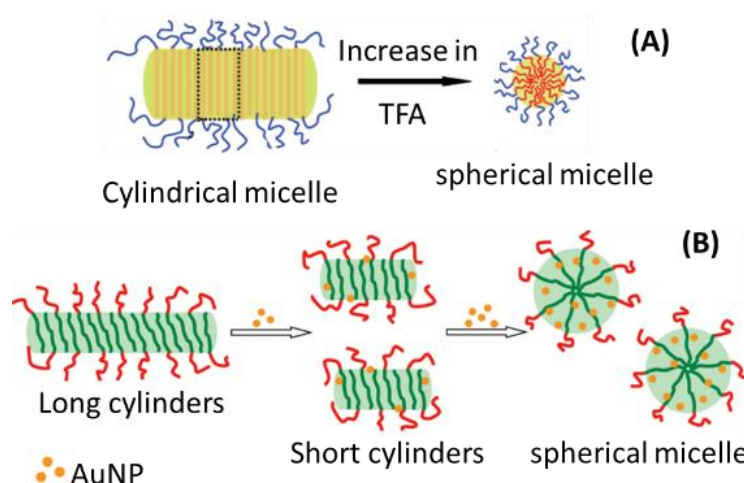


**Figure 3.8:** Morphology change due to the (A) chain conformation change<sup>50</sup> and (B) incorporation of nanoparticles into self-assembly (PBLG-*b*-PEG concentration 0.25g/L, AuNP from  $2.5 \times 10^{-5}$  to  $2.5 \times 10^{-2}$  g/L)<sup>52</sup>

The polypeptide based amphiphilic block copolymers have an important role in drug delivery applications<sup>54,55</sup> due to the biocompatibility and biodegradable nature.<sup>56,57</sup> In addition, they are extensively studied due to their stimuli responsiveness<sup>31,58,59</sup> and secondary conformation which makes them ideal building blocks to fabricate a wide variety of supramolecular nanostructures.<sup>23,46</sup>

### 3.1.5 Self-assembly of PBLG-*b*-PEG block copolymers

In the literature, PBLG-*b*-PEG systems have been extensively studied in different application areas due to their good self-assembly properties in solution and in solid state.<sup>60-64</sup> The self-assembly behavior of PBLG-*g*-PEG and morphology modifications by co-assembling it with PBLG homopolymers,<sup>65</sup> and of PBLG-*b*-PEG block copolymers<sup>66</sup> have been reported. The self-assembly of PBLG-*b*-PEG with different chain length was also reported in several studies.<sup>52,66,67</sup> By combining the literature examples we can clearly see that the morphology of PBLG-*b*-PEG self-assemblies is not only affected by environmental factors (solvent, ionic strength, temperature, concentration etc.) but also the chain length of the each unit in the block copolymer has a high impact (Figure 3.9).

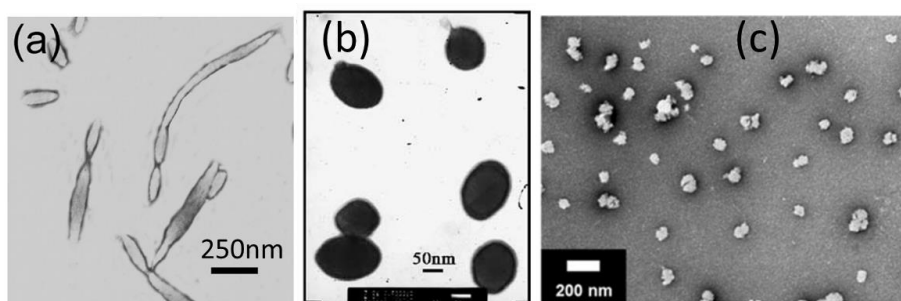


**Figure 3.9:** Literature examples of TEM images of pure PBLG-*b*-PEG self-assemblies in water (a) PBLG<sub>630</sub>-*b*-PEG<sub>454</sub> (138000-*b*-20000 g/mol)<sup>52</sup> long cylindrical micelles (b) PBLG<sub>273</sub>-*b*-PEG<sub>113</sub> (60000-*b*-5000 g/mol)<sup>66</sup> spherical micelles (c) PBLG<sub>13</sub>-*b*-PEG<sub>45</sub> (2850-*b*-2000 g/mol) particulate morphology<sup>67</sup>

Lecommandoux's group<sup>54</sup> has reported the formation of vesicle like nano-assemblies from PBLG<sub>29</sub>-*b*-PEG<sub>115</sub>, PBLG<sub>29</sub>-*b*-PEG<sub>510</sub>, PBLG<sub>29</sub>-*b*-PEG<sub>115</sub>-*b*-PBLG<sub>29</sub> copolymers which were used as a cargo to load the doxorubicin for cancer treatment application. Differently from other studies, this was the first time that PBLG was conjugated to the PEG chain via the CuAAC "click" reaction. In previous studies PBLG chains were indeed directly polymerized from a PEG-NH<sub>2</sub> macro-initiator. Moreover, Felipe and coworkers<sup>67</sup> performed a detailed biocompatibility study on PBLG-*b*-PEG copolymer nanoparticles where they experimentally confirmed their use for in nanomedicine.

### 3.2 Results and discussion

In this work, by designing four different polypeptide based rod-coil like amphiphilic block copolymers, in which the PTS localization in the structure and PEG chain length are varied, we aimed at designing nanoparticles with different morphologies and establish proper structures and properties relationships. These model systems will especially help us to quantitatively control the PTS concentration and its localization in the nano-assemblies and find the best system suited to Photodynamic Therapy to find new clues for development of new therapeutics with low dark toxicity and high activity. In this context, self-assembly behavior of these polymers in water were first evaluated and also repeated in PBS solution. Moreover, the co-assembly of those polymers with non-functionalized PBLG-*b*-PEG block copolymers was optimized to modulate and possibly increase the efficacy of PTS. Finally, the physicochemical stability of the co-assembled particles was tested in the presence of 10% of MEM alpha serum to evaluate their stability and suitability for *in vitro* and *in vivo* applications.

#### 3.2.1 Self-assembly of the PTS bearing PBLG-*b*-PEG amphiphilic block copolymers in water

In our project, four different linear rod-coil like amphiphilic block copolymers in terms of photosensitizer (PTS, aza-BODIPY) localization and PEG chain length, PTS-PBLG<sub>49</sub>-*b*-PEG<sub>113</sub>, PBLG<sub>53</sub>-PTS-*b*-PEG<sub>113</sub>, PTS-PBLG<sub>49</sub>-*b*-PEG<sub>45</sub> and PBLG<sub>53</sub>-PTS-*b*-PEG<sub>45</sub>, were used to prepare nano-assemblies with different morphologies. These amphiphilic block copolymers consist of the rigid  $\alpha$ -helical hydrophobic PBLG block (DP~50) and coil-like flexible hydrophilic PEG (DP=45,113) chain with weight fraction of  $f \sim 15\%$  and  $f \sim 30\%$ . PTS is covalently bounded either to the chain-end of PBLG or in the middle of two blocks, in order to control its localization in the nano-assemblies. The PEG length is varied in order to control the morphology of the nano-assemblies (Figure 3.10). By increasing the PEG length we expect to obtain spherical micelles and with shorter chains the formation of vesicles was targeted.

To optimize the condition of self-assembly several methods have been utilized and after several trials well-defined spherical particles with low polydispersity were obtained by the "nano-precipitation", also named solvent displacement" technique<sup>68</sup>. In this technique the block copolymers were dissolved in THF, which is a good solvent for both blocks (PBLG and PEG), and the selective solvent (H<sub>2</sub>O) was added in a controlled manner as depicted in Figure 3.11. THF is then removed by dialysis.

Since the self-assembly of these polymers is strongly dependent on the external factors (solvent, concentration, stirring speed and flow rate) it requires to find the best condition for the self-assembly of each block copolymer. In our study, we optimized the conditions for pure PTS functionalized block copolymers at 1g/L concentration by adjusting the stirring rate to 500RPM and flow rate of water addition to 0.37mL/min.

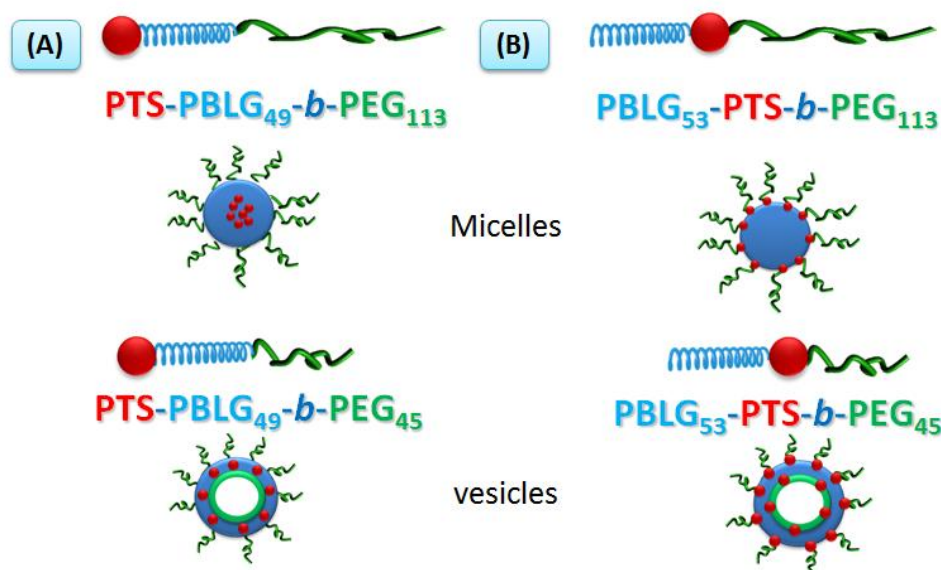


**Figure 3.10:** Schematic illustration of rod-coil block copolymers and the expected morphology after self-assembly in water

The same procedure was repeated in a phosphate buffered saline (PBS, 10mM) solution. The self-assembly in PBS has been performed in order to verify the stability of the nano-assemblies in physiological conditions. Although we obtained stable nano-assemblies in the PBS solutions, they showed different characteristics compared to the self-assembly in pure water due to the rather high salt content (137mM NaCl, 2.7mM KCl, 10mM Na<sub>2</sub>HPO<sub>4</sub> and 2mM KH<sub>2</sub>PO<sub>4</sub>). It is known that a small amount of salt in the solution can prevent (decrease) the aggregation of particles with a PEG corona. PEG chains can be complexed with salt ions and form polyelectrolyte like corona which causes a better solubilization by pulling them away from each other by electrostatic interactions and swelling of the corona. However, an excess amount of salt can decrease the solubility of PEG chains.<sup>69,70</sup>

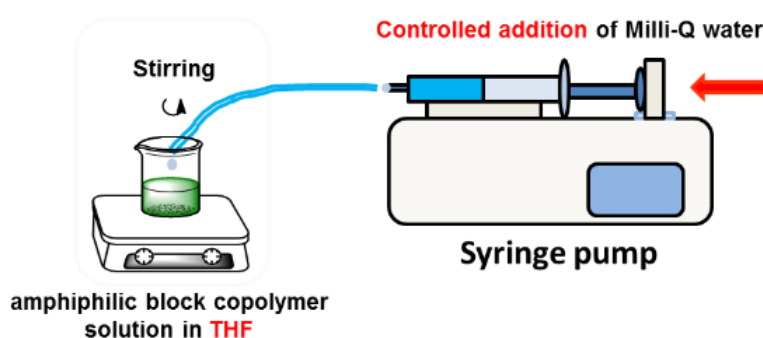


**Figure 3.10:** Schematic representation of the nanoprecipitation method

To optimize the best PTS concentration for the photodynamic therapy (PTD), we co-assembled these block copolymers with PTS free PBLG<sub>54</sub>-b-PEG<sub>45</sub> and PBLG<sub>54</sub>-b-PEG<sub>113</sub> block copolymers in different weight ratio and chose the best ratio as 1:1 where the higher singlet oxygen generation was obtained. The details about the dilution effect on photophysical properties will be discussed in Chapter 4.

### 3.2.2 Characterization of the size and morphology of the nano-assemblies

The hydrodynamic radii ( $R_h$ ) and size dispersity (PDI) of the nano-assemblies were first measured by dynamic light scattering at 90°. The measurements were performed at 25°C and at a concentration of about 1g/L without filtration. According to the obtained size distributions, the block copolymers with longer PEG chains form bigger particles compared to the block copolymers with smaller PEG unit. However, the size of all nano-assemblies fits the required size range (20-200nm) for enhanced permeability and retention effect (EPR)<sup>71</sup> to have an efficient targeting.

**Table 3.1:** Parameters of self-assembled block copolymers

Names	$f$ (%)	Non-selective solvent	Selective solvents			
			H <sub>2</sub> O		PBS	
			<sup>b</sup> $R_h$	<sup>b</sup> PDI	<sup>b</sup> $R_h$	<sup>b</sup> PDI
PTS-PBLG <sub>49</sub> - <i>b</i> -PEG <sub>45</sub>	16	THF	31	0.105	40	0.118
PBLG <sub>53</sub> -PTS- <i>b</i> -PEG <sub>45</sub>	15	THF	33	0.093	83	0.159
PTS-PBLG <sub>49</sub> - <i>b</i> -PEG <sub>113</sub>	32	THF	95	0.151	49	0.320
PBLG <sub>53</sub> -PTS- <i>b</i> -PEG <sub>113</sub>	29	THF	105	0.053	17; 158*	0.369

$f$ - hydrophilic volume fraction in the block copolymers,  $b$ - hydrodynamic radius ( $R_h$ ) and polydispersity index (PDI) obtained by DLS, \*- two populations in the size distribution were observed for this sample.

As can be seen from the results in Table 3.1 both types of block copolymers, PTS-PBLG-*b*-PEG and PBLG-PTS-*b*-PEG, formed nano-assemblies characterized by a single population in the size distribution histogram, and low polydispersity index (Figure 3.12). In the case of the self-assembly in PBS (Figure 3.13 and Table 3.1) we used the conditions that were optimized for the self-assembly in Milli-Q water. As a result, we observed an increase in polydispersity index of the nano-assemblies (except in PTS-PBLG<sub>49</sub>-*b*-PEG<sub>45</sub>) and changes in sizes distribution compared to pure water. These behaviors could be due to the high salt (10mM) concentration in PBS solution and their interaction with PEG chains during the self-assembly process as mentioned above. We didn't optimize the conditions of self-assembly in PBS to obtain better size distribution since all our studies were performed in water.

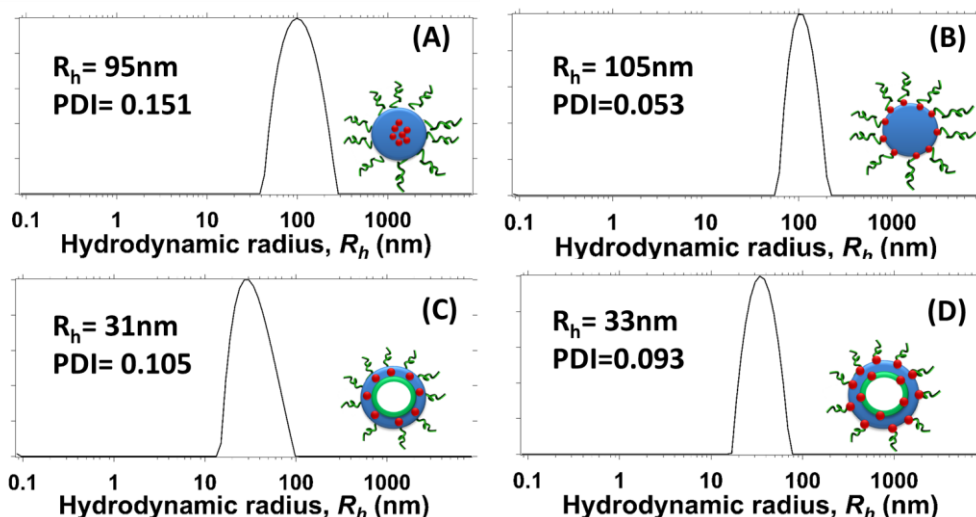


**Figure 3.12:** The size distribution of the nano-assemblies of (A) PTS-PBLG<sub>49</sub>-*b*-PEG<sub>113</sub> (B) PBLG<sub>53</sub>-PTS-*b*-PEG<sub>113</sub> (C) PTS-PBLG<sub>49</sub>-*b*-PEG<sub>45</sub> (D) PBLG<sub>53</sub>-PTS-*b*-PEG<sub>45</sub> prepared in Milli-Q water (T= 25°C, C= 1g/L, 90° angle)

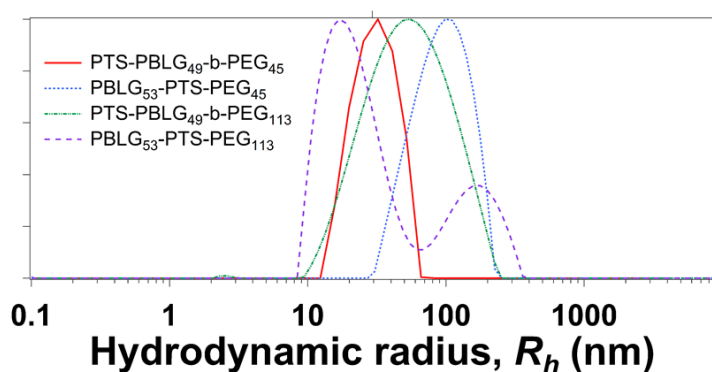


**Figure 3.13:** Overlaid size distribution of the nano-assemblies prepared in PBS solution (T= 25°C, C= 1mg/mL, pH= 7.4, 90° angle)

The morphology of the nano-assemblies in water was characterized by transmission electron microscopy (TEM). Although PBLG has higher electronic density than PEG, it wasn't enough to reveal the morphology of the vesicles. To increase the contrast, two staining agents; RuO<sub>4</sub> and I<sub>2</sub>, were used. The staining with RuO<sub>4</sub> vapors should reveal the aromatic groups in the copolymer.<sup>72</sup> However, due to the high reactivity of RuO<sub>4</sub> it could also contrast the PEG corona by deposition of heavy atoms with a high electronic density. The staining with I<sub>2</sub> was also performed which is used usually to stain the materials with amine groups. TEM images of the micelle solutions prepared from PTS-PBLG<sub>49</sub>-*b*-PEG<sub>113</sub> and PBLG<sub>53</sub>-PTS-*b*-PEG<sub>113</sub> block copolymers showed spherical black objects with ~200nm in diameter for both types of polymer nano-assemblies. We did not observe any contrast difference between the RuO<sub>4</sub> and I<sub>2</sub> stained samples, which confirms the formation of spherical micellar structures (Figure 3.14).

The images of the nano-assemblies prepared from PTS-PBLG<sub>49</sub>-*b*-PEG<sub>45</sub> show clear contrast difference between RuO<sub>4</sub> and I<sub>2</sub> stained samples (Figure 3.15). For the RuO<sub>4</sub> stained sample, we observed spherical black objects, whereas for the I<sub>2</sub> stained sample we clearly observed roughly spherical nanostructures with a kind of "membrane". Although staining is

inhomogeneous it is enough to see the contrast difference in the nanostructures. As a result of this study, we confirm that the block copolymers with shorter PEG chain form vesicle structures as expected. Eventually, we can say  $I_2$  staining is the better staining agent for PEG-*b*-PBLG block copolymers to reveal the real morphology.

From  $I_2$  stained TEM images (C) and (D) (Figure 3.15) we observed that PBLG<sub>53</sub>-PTS-*b*-PEG<sub>45</sub> form similar nano-assemblies as PTS-PBLG<sub>49</sub>-*b*-PEG<sub>45</sub>: spherical vesicle like particles with ~60nm in diameter can be clearly seen.

Overall, we can come to the conclusion that the self-assembly of all four types of block copolymers is not affected by the localization difference of PTS in the chain. Both types of block copolymers with longer PEG chains tend to form a micellar structure with similar size (diameter ~200 nm) and block copolymers with shorter PEG chains, and consequently with lower hydrophilic ratio, tend to form vesicle structure (diameter ~60 nm). The micellar structure is certainly not at the thermodynamic equilibrium and probably does not correspond to a simple core-shell morphology, as the diameter is rather large compared to the copolymer molar mass. The formed structures are probably more micellar aggregates or nano-spheres resulting from the out of equilibrium nanoprecipitation process.

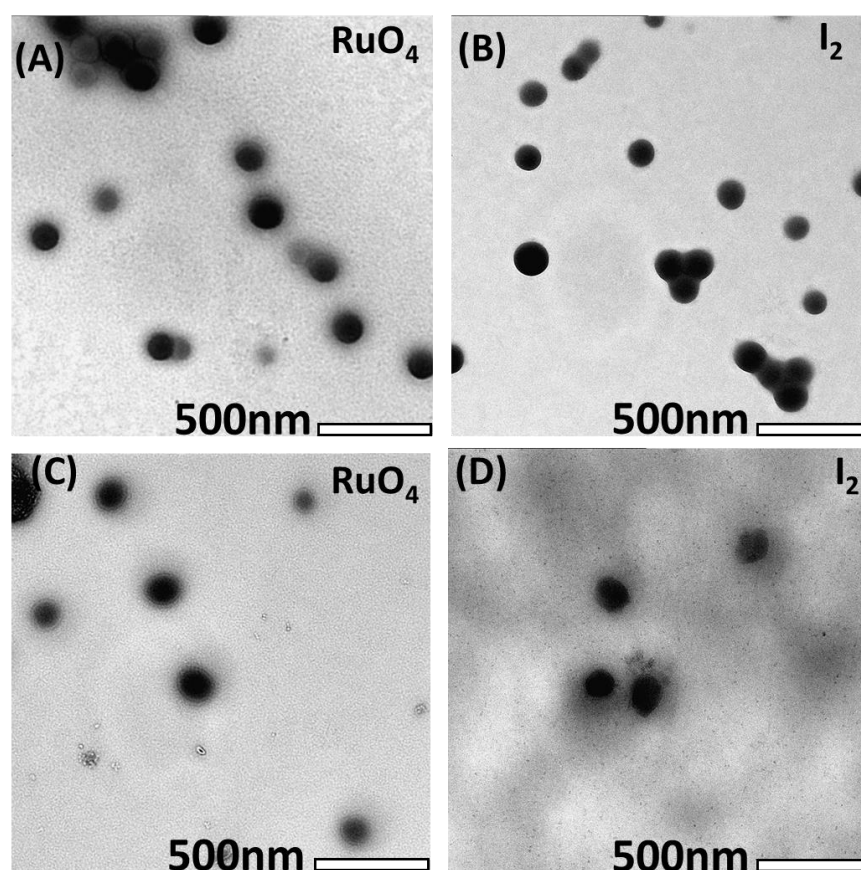


**Figure 3.14:** TEM images of the micelles prepared from PTS-PBLG<sub>49</sub>-*b*-PEG<sub>113</sub> (A) stained with RuO<sub>4</sub> vapors (B) stained with I<sub>2</sub> vapors; and from PBLG<sub>53</sub>-PTS-*b*-PEG<sub>113</sub> (C) stained with RuO<sub>4</sub> vapors (D) stained with I<sub>2</sub> vapors.

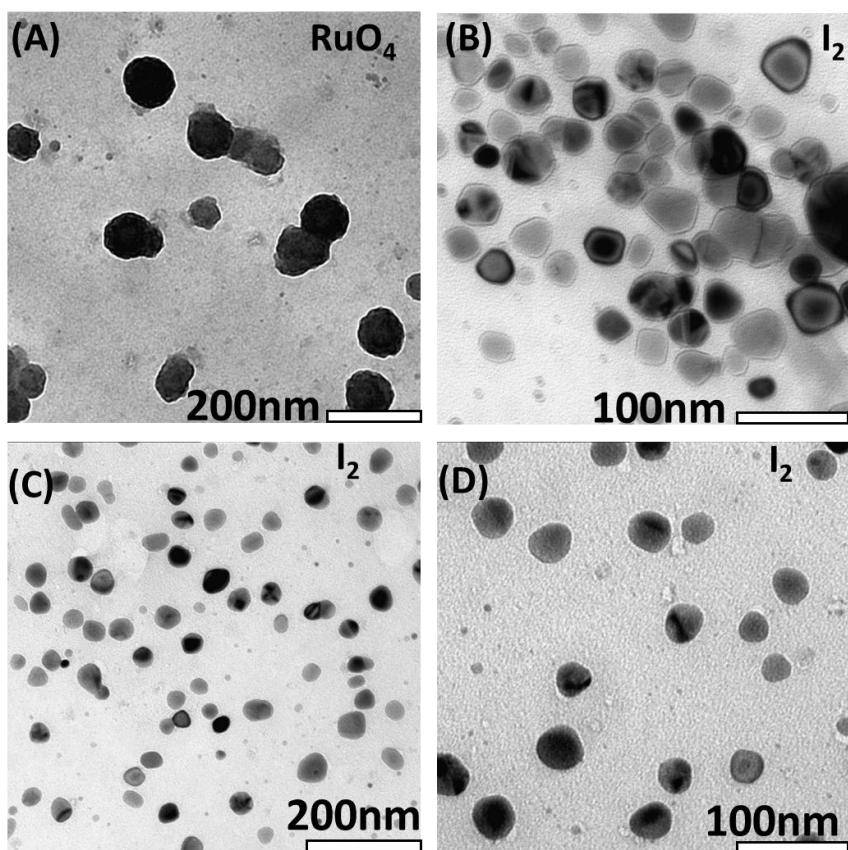


**Figure 3.15:** TEM images of the vesicles prepared from PTS-PBLG<sub>49</sub>-*b*-PEG<sub>45</sub> (A) stained with RuO<sub>4</sub> vapors (B) stained with I<sub>2</sub> vapors; (C) and (D) I<sub>2</sub> stained vesicles prepared from PBLG<sub>53</sub>-PTS-*b*-PEG<sub>45</sub> block copolymers.

### 3.2.3 Characterization of co-assembled particles and their physicochemical stability in cell-medium

In order to decrease the concentration of PTS in the nano-assemblies we diluted the PTS bearing block copolymers with non-functionalized PBLG<sub>54</sub>-*b*-PEG<sub>45</sub> and PBLG<sub>54</sub>-*b*-PEG<sub>113</sub> copolymers. We investigated the dilution effect on the self-assembly behavior on both types of block copolymer, PTS-PBLG-*b*-PEG and PBLG-PTS-*b*-PEG, with longer PEG chain and co-assembled them with PBLG<sub>54</sub>-*b*-PEG<sub>113</sub> in three different weight ratios. Although the block copolymers consist of the same PBLG and PEG chain length, DLS measurements show that increasing the content of PBLG<sub>54</sub>-*b*-PEG<sub>113</sub> to more than 50% (w/w) increases the polydispersity of the nano-assemblies by forming particles of multiple sizes (see Table 3.2 and Figure 3.16).

Since the photophysical analysis of the dilution effect on <sup>1</sup>O<sub>2</sub> generation (Chapter 4) showed that higher yields are obtained for co-assembled particles in a 1:1 weight ratio we continued our studies with this mixing ratio.

PTS-PBLG<sub>49</sub>-*b*-PEG<sub>45</sub> and PBLG<sub>53</sub>-PTS-*b*-PEG<sub>45</sub> were also co-assembled with PBLG<sub>54</sub>-*b*-PEG<sub>45</sub> in 1:1 weight ratio, and nano-assemblies with low polydispersity were observed (Figure 3.17). After mixing, we observed a rather large increase in the size of both nano-assembly solutions, which indicate the clear influence of the addition of the unfunctionalized polymer chains. Many reasons can explain these differences but this is rather difficult to provide a clear



one without significant additional experiments. Indeed, the functionalized and unfunctionalized copolymers may have difference in interactions, critical solubility in the solvent mixture, diffusion properties...

**Table 3.2:** DLS results of co-assembled micelles.

Nano-assemblies	Mixing ratio of (w/w)							
	PTS functionalized/ non-functionalized polymers							
	No mixing		4:1		1:1		1:4	
	R <sub>h</sub>	PDI	R <sub>h</sub>	PDI	R <sub>h</sub>	PDI	R <sub>h</sub>	PDI
*PTS-PBLG <sub>49</sub> - <i>b</i> -PEG <sub>113</sub>	95	0.151	89	0.214	107	0.078	a	0.512
*PBLG <sub>53</sub> -PTS- <i>b</i> -PEG <sub>113</sub>	105	0.053	65	0.103	93	0.171	a	0.508

\* Polymers co-assembled with non-PTS functionalized PBLG<sub>54</sub>-*b*-PEG<sub>113</sub>, *a*- multiple size

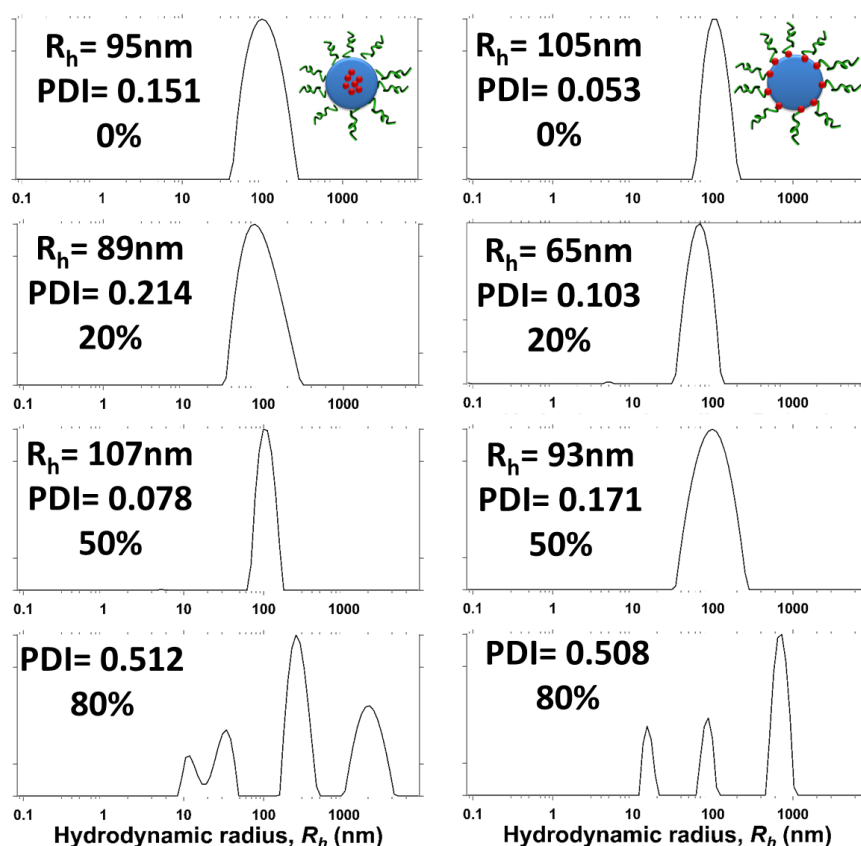


**Figure 3.16:** The dilution effect on micellization. The micelles prepared from PTS-PBLG<sub>49</sub>-*b*-PEG<sub>113</sub> and PBLG<sub>53</sub>-PTS-*b*-PEG<sub>113</sub> block copolymers and their co-assembly with PBLG<sub>54</sub>-*b*-PEG<sub>113</sub> in different ratios (the percentages show the content of non-functionalized block copolymers by weight, in the micelles).

The size distributions of the 1:1 weight ratio mixed nano-assemblies, prepared from PTS-PBLG<sub>49</sub>-*b*-PEG<sub>113</sub>, PBLG<sub>53</sub>-PTS-*b*-PEG<sub>113</sub>, PTS-PBLG<sub>49</sub>-*b*-PEG<sub>45</sub> and PBLG<sub>53</sub>-PTS-*b*-PEG<sub>45</sub>

block copolymers, at different angles (60-140°) and concentrations (see Figure A3.1) confirmed the formation of well-defined homogeneous nano-assemblies in water.

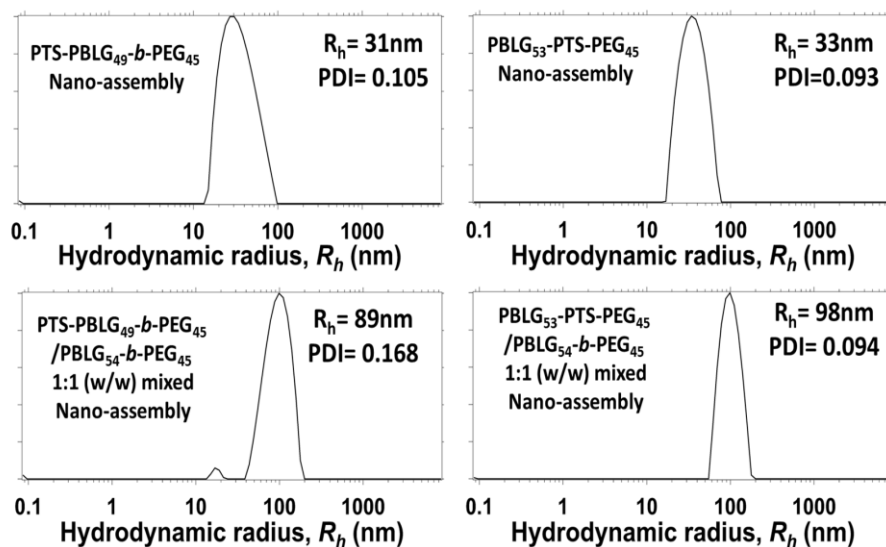


**Figure 3.17:** The dilution effect on the size of the PTS-PBLG<sub>49</sub>-*b*-PEG<sub>113</sub> and PBLG<sub>53</sub>-PTS-*b*-PEG<sub>113</sub> block copolymers nano-assemblies by co-assembling them with PBLG<sub>54</sub>-*b*-PEG<sub>113</sub> in 1:1 weight ratio.

Finally, the dilution effect on morphology was visualized by TEM imaging via I<sub>2</sub> and ammonium molybdate staining. No visible change was observed in the TEM images of 1:1 mixed nano-assemblies of PTS-PBLG<sub>49</sub>-*b*-PEG<sub>113</sub> and PBLG<sub>53</sub>-PTS-*b*-PEG<sub>113</sub> (Figure 3.18) compared to the results obtained from pure PTS functionalized block copolymers. Even the sizes of the nano-assemblies were not much affected by the incorporation of PTS free block copolymer chains. The comparison of two different staining methods showed that ammonium molybdate staining could better reveal the corona of the particles, even the PEG corona could be identified. From I<sub>2</sub> stained TEM images of co-assembled PTS-PBLG<sub>49</sub>-*b*-PEG<sub>45</sub> (A) and PBLG<sub>53</sub>-PTS-*b*-PEG<sub>45</sub> (C) (Figure 3.19) we observed spherical disc-like particles similar to the morphology of pure PTS functionalized block copolymers assemblies (Figure 3.15) but with larger size. However, despite the I<sub>2</sub> staining it is difficult to verify the existence of the vesicle like morphology from these images. Thus staining with ammonium molybdate solution, which is used to stain osmotically sensitive organelles in biology, was applied and a better contrast difference was observed. From images (B) and (D) in Figure 3.19 we can confirm the existence of vesicle structures despite of the inhomogeneous staining. Since ammonium molybdate stained samples were prepared by drop casting method we observed aggregates of vesicles compared to I<sub>2</sub> stained samples which were prepared by spin-coating technique.

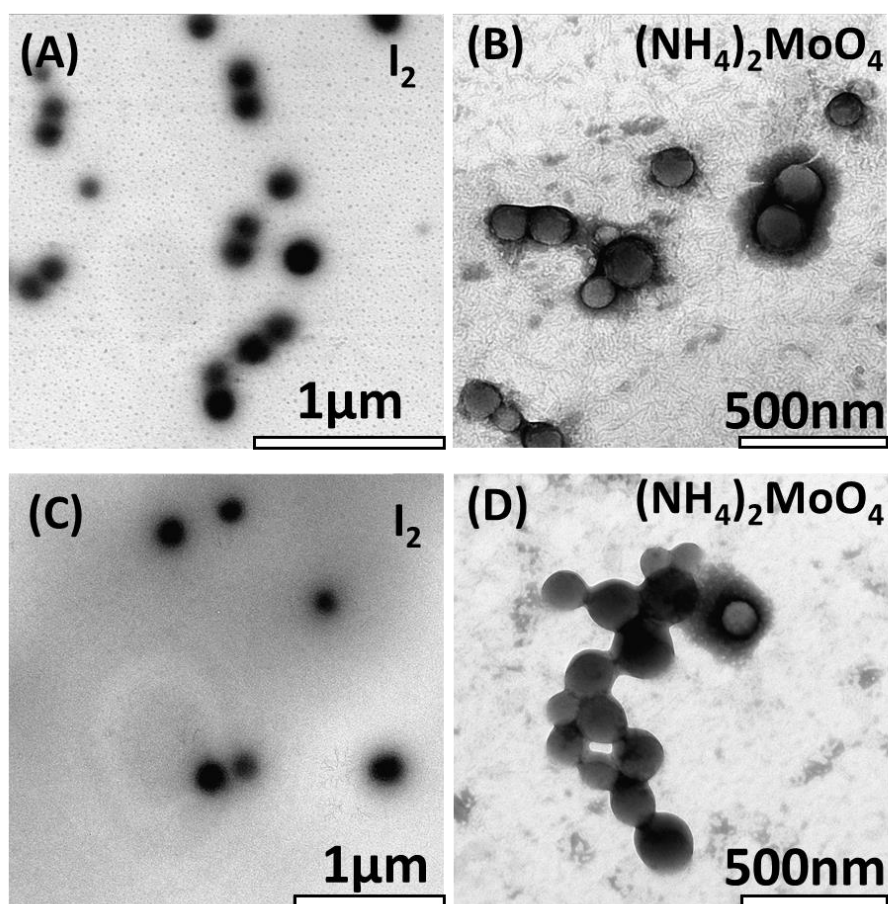


**Figure 3.18:** TEM images of the micelles prepared from PTS-PBLG<sub>49</sub>-*b*-PEG<sub>113</sub> (1:1 mixed with PBLG<sub>54</sub>-*b*-PEG<sub>113</sub>) (A) stained with I<sub>2</sub> vapors (spin coated) (B) stained with ammonium molybdate solution (2%) (drop casted); and from PBLG<sub>53</sub>-PTS-*b*-PEG<sub>113</sub> (1:1 mixed with PBLG<sub>54</sub>-*b*-PEG<sub>113</sub>) (C) stained with I<sub>2</sub> vapors (spin coated) (D) stained with ammonium molybdate solution (2%) (drop casted)

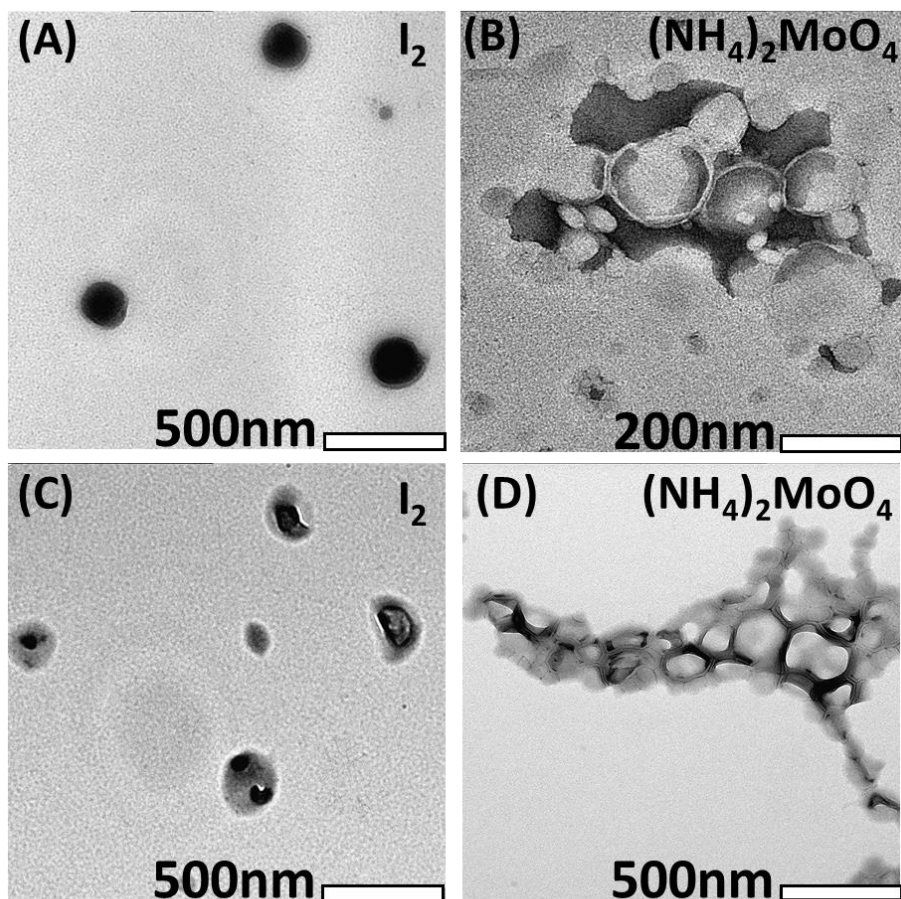


**Figure 3.19:** TEM images of the vesicles prepared from PTS-PBLG<sub>49</sub>-*b*-PEG<sub>45</sub> (1:1 mixed with PBLG<sub>54</sub>-*b*-PEG<sub>45</sub>) (A) stained with I<sub>2</sub> vapors (spin coated) (B) stained with ammonium molybdate solution (2%) (drop casted); and from PBLG<sub>53</sub>-PTS-*b*-PEG<sub>45</sub> (1:1 mixed with PBLG<sub>54</sub>-*b*-PEG<sub>45</sub>) (C) stained with I<sub>2</sub> vapors (spin coated) (D) stained with ammonium molybdate solution (2%) (drop casted).

After choosing the best mixing ratio for the self-assembly and for the photophysical properties, we evaluated the stability of the nano-assemblies in the presence of cell medium (MEM alpha, GlutaMAX(TM)). It is known that a long circulation lifetime of the particles in blood stream is important for EPR effect, to have internalization of a sufficient amount of particles in the tumor site.<sup>71</sup> However, the nanoparticles may form aggregates in the blood stream due to the protein adsorption, which will eventually decrease the efficacy of targeting and of the therapy. Many experimental results from the literature proved that nanomaterials with PEG corona have stealth property. They can thus escape from macrophage recognition and protein or cell adsorption.<sup>73</sup> To test this phenomenon for our nano-assemblies we added 10% (v/v) of cell medium (MEM alpha, GlutaMAX(TM)) into 1g/L nano-assembly solutions and the size was measured at 25°C with time. We did not observe any aggregate formation under those conditions or visible precipitate formation. Only a second population at small sizes was observed in the size distribution histogram, which could be due to the proteins in the cell medium. To check this we measured the size distribution of proteins in the cell medium by mixing 10% of it with pure Milli-Q water and indeed observed 12nm size particles that correspond to the small size population in the copolymer MEM solutions (see Figure 3.21). Moreover, to evaluate the stability of the nano-assemblies at body temperature we heated the solution up to 37°C and kept it for 12h. Even after high temperature and longer incubation time no visible aggregate formation was observed in the nano-assembly solutions (see Figure 3.20) which confirms the stability of nano-assemblies in the presence of proteins.

To sum up, we obtained four different stable nano-assemblies with similar sizes but with different morphologies and different PTS localization to evaluate their photophysical behaviors and efficacy in in vitro application to find the best system for PDT application.

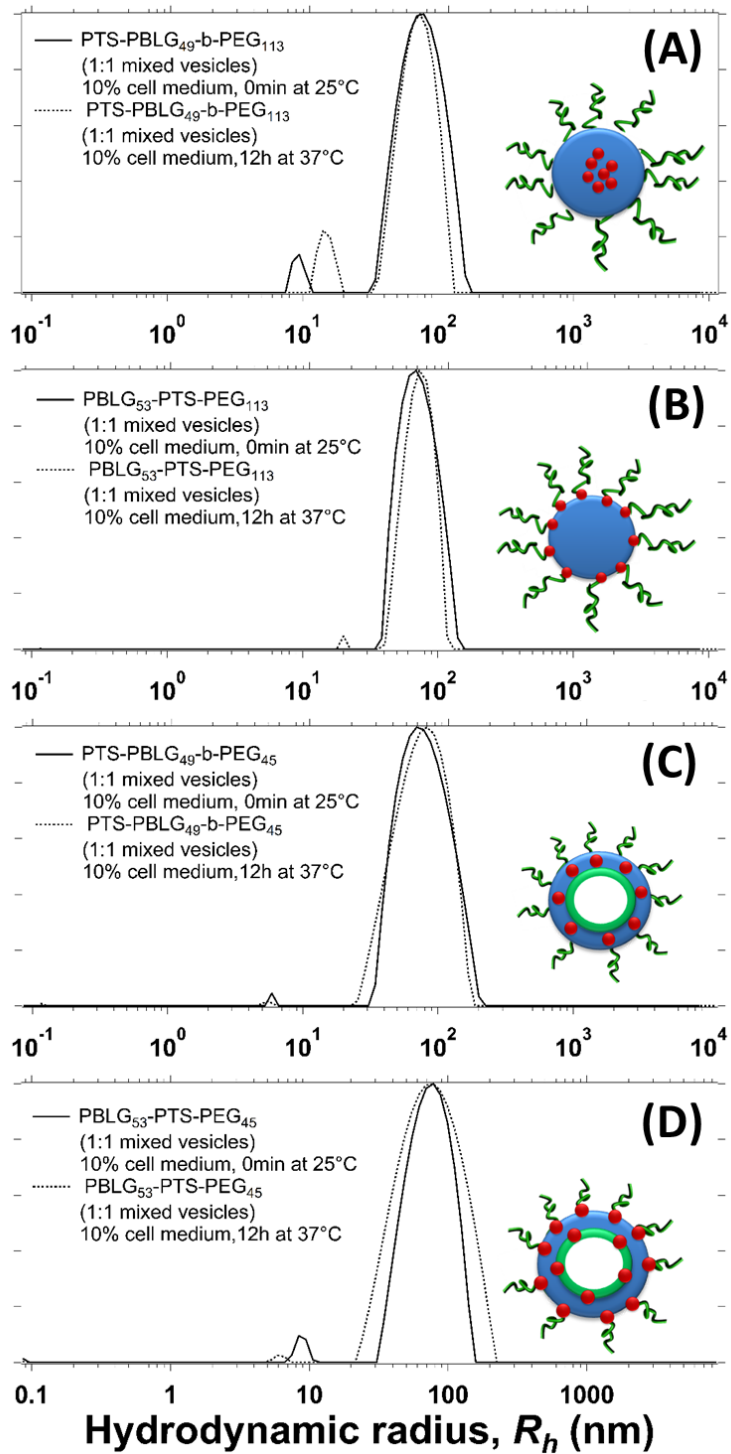


**Figure 3.20:** Size distribution of the nano-assemblies in the presence of 10% (v/v) cell medium (MEM alpha, GlutaMAX(TM)) at 25°C and 37°C, 90°

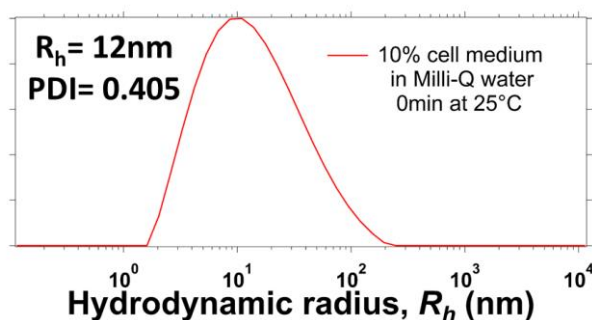


**Figure 3.21:** Size distribution diagram of the 10% (v/v) cell medium (MEM alpha, GlutaMAX(TM)) mixed Milli-Q water at 25°C, 90° angle

### 3.3 Conclusion

In this work, we studied the self-assembly behavior of aza-BODIPY conjugated PTS-PBLG<sub>49</sub>-*b*-PEG<sub>113</sub>, PBLG<sub>53</sub>-PTS-*b*-PEG<sub>113</sub>, PTS-PBLG<sub>49</sub>-*b*-PEG<sub>45</sub> and PBLG<sub>53</sub>-PTS-*b*-PEG<sub>45</sub> block copolymers. Self-assembly of block copolymers with a longer PEG chain formed spherical micelle-like morphology, whereas the copolymers with a shorter PEG chain formed vesicle like structures. In addition, the co-assembly of those block copolymers with non-functionalized PBLG<sub>54</sub>-*b*-PEG<sub>113</sub> and PBLG<sub>54</sub>-*b*-PEG<sub>45</sub> was optimized and repeated in PBS solution. The size and morphology of the nano-assemblies were carefully analyzed by DLS and TEM techniques by using three different staining agents. In a final step, physicochemical stability of the nano-assemblies was tested in the presence of 10% of serum which confirmed the stability of the nano-assemblies in biological environment. As a result of this study, we obtained four different nano-assemblies to further investigate their photophysical behaviors in water (Chapter 4) and test *in vitro* on HeLa and B16F1 cells (Chapter 5).

### 3.4 Experimental

#### Materials and methods

##### Materials

The following reagents have been used without further purifications: ruthenium (III) chloride (RuCl<sub>3</sub> · xH<sub>2</sub>O, Sigma-Aldrich, >99.8%), sodium hypochlorite (NaClO, Sigma-Aldrich, 10-15% solution), iodine (I<sub>2</sub>, Sigma-Aldrich, >99.8%).

##### Methods

**Dynamic light scattering:** Hydrodynamic radius ( $R_h$ ) of the nano-assemblies were measured by dynamic light scattering (DLS) which have been carried out with a ALV/ CGS3 device with a He-Ne laser at a wavelength of 632.8 nm and a thermostat at 25°C. The measures have been taken at angles of 90° and 60-140° (step 10°) with an acquisition time of 30s. Results were analyzed using the CONTIN algorithm. The hydrodynamic radius is determined from Stokes-Einstein equation (3.1)

$$R_h = \frac{k_B T}{6\pi\eta D} \quad (3.1)$$

where  $k_B$  is a Boltzmann's constant,  $T^\circ$  is the absolute temperature and  $\eta$  is the viscosity of the solvent. The self-diffusion coefficients ( $D$ ), which can be obtained from several measurements, have been taken at different concentrations and angles *via* the equation (3.2)

$$D = \frac{\Gamma}{q^2} \quad (3.2)$$

where  $\Gamma$  is the decay rate and  $q^2$  is the square of the wave vector which are obtained from DLS measurement. Finally, the "true"  $R_h$  value could be calculated from equation (3.1) by extrapolating the self-diffusion coefficient to zero concentration ( $C=0$ ).

**Transmission Electron Microscopy:** TEM images have been recorded with a transmission electron microscope LEO 922, with an acceleration voltage of 200 kV with radial field mode. TEM grids were carbon coated 200 Mesh Cu PK/100 purchased from SPI supplies.

### TEM sample preparation

Samples prepared for transmission electron microscopy have been deposited on the TEM grids by spin-coating. The grids have been washed with distilled water and dried thanks to the spin-coater with a speed of 2000 revolutions per minutes. A 20  $\mu$ L drop of nano-assemblies solution is then deposited on the grid and it is finally spin-coated with the same program.

The grids are stained by three staining agents,

1. A  $\text{RuO}_4$  vapor has been produced in situ by reacting ruthenium (III) chloride ( $\text{RuCl}_3 \cdot x\text{H}_2\text{O}$ ) with a 15% solution of sodium hydrochlorite ( $\text{NaClO}$ ) in water.

A drop of the solution is added in a closed petri dish containing the TEM grids for 5 min to stain the nano-assemblies with ruthenium oxide vapors.

2. The staining with iodine vapor was performed over 1h in a closed petri dish containing iodine crystals.

3. The negative staining was performed with 2 wt % of ammonium molybdate solution in water. First, equal amounts of sample and staining solution are mixed and 20 $\mu$ L of the mixture was deposited on the grid and the water was removed by filter paper after  $\sim$ 20 sec.

### General procedure of Self-assembly

All self-assembled nanoparticle solutions were prepared at 4mg/mL concentration in Milli-Q water. Amphiphilic block copolymers bearing photosensitizer, PTS-PBLG<sub>49</sub>-*b*-PEG<sub>113</sub>, PBLG<sub>53</sub>-PTS-*b*-PEG<sub>113</sub>, PTS-PBLG<sub>49</sub>-*b*-PEG<sub>45</sub> and PBLG<sub>53</sub>-PTS-*b*-PEG<sub>45</sub>, were co-assembled with PTS free amphiphilic block copolymers PBLG<sub>54</sub>-*b*-PEG<sub>113</sub> and PBLG<sub>54</sub>-*b*-PEG<sub>45</sub> in 1:1 weight ratio, respectively.

4mg of PTS functionalized and non-functionalized polymer mixtures (1:1 w/w) were dissolved in 200 $\mu$ L THF and stirred for 30min. 1mL of Milli-Q water was added by fixing the flow rate with syringe pump and stirring speed. The nano-assembly solution was stirred for 5 min, transferred to dialyses bag (cut-off MWCO 12-14 kDa) and dialyzed for 24h.



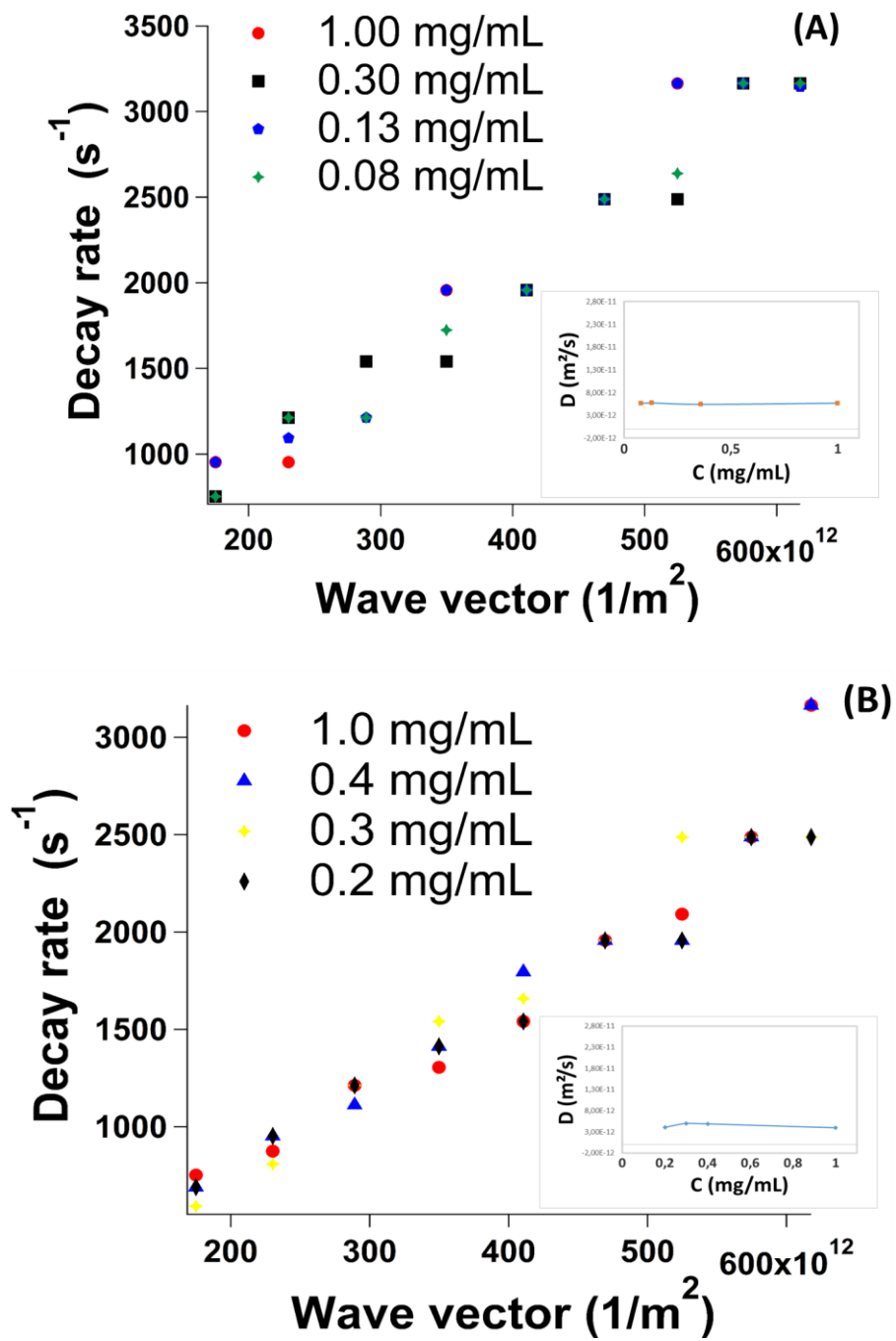
**Table 3.3:** Optimized conditions for self-assembly of the block copolymers in Milli-Q water at ambient temperature

<b>Nano-assemblies</b>	<b>Mixing ratio w/w</b>	<b>Stirring speed (RPM)</b>	<b>Flow rate (mL/min)</b>
PTS-PBLG <sub>49</sub> - <i>b</i> -PEG <sub>45</sub> / PBLG <sub>54</sub> - <i>b</i> -PEG <sub>45</sub>	1:1	500	0.37
PBLG <sub>53</sub> -PTS- <i>b</i> -PEG <sub>45</sub> / PBLG <sub>54</sub> - <i>b</i> -PEG <sub>45</sub>	1:1	500	0.37
PTS-PBLG <sub>49</sub> - <i>b</i> -PEG <sub>113</sub> / PBLG <sub>54</sub> - <i>b</i> -PEG <sub>113</sub>	1:1	500	0.37
PBLG <sub>53</sub> -PTS- <i>b</i> -PEG <sub>113</sub> / PBLG <sub>54</sub> - <i>b</i> -PEG <sub>113</sub>	1:1	1000	0.74

### **Dialysis of nanoparticles**

The dialyses were performed using a dialysis membrane Spectra/Por with molecular weight cut-off MWCO 12-14 kDa in a pure Milli-Q water to remove the traces of THF and stabilize the nano-assemblies. The bath is changed every 3 to 12h for 24h. The final concentration is evaluated from the quantity of copolymer used and the final volume of the solution

Appendix 3: CHARACTERIZATION DATA FOR CHAPTER 3



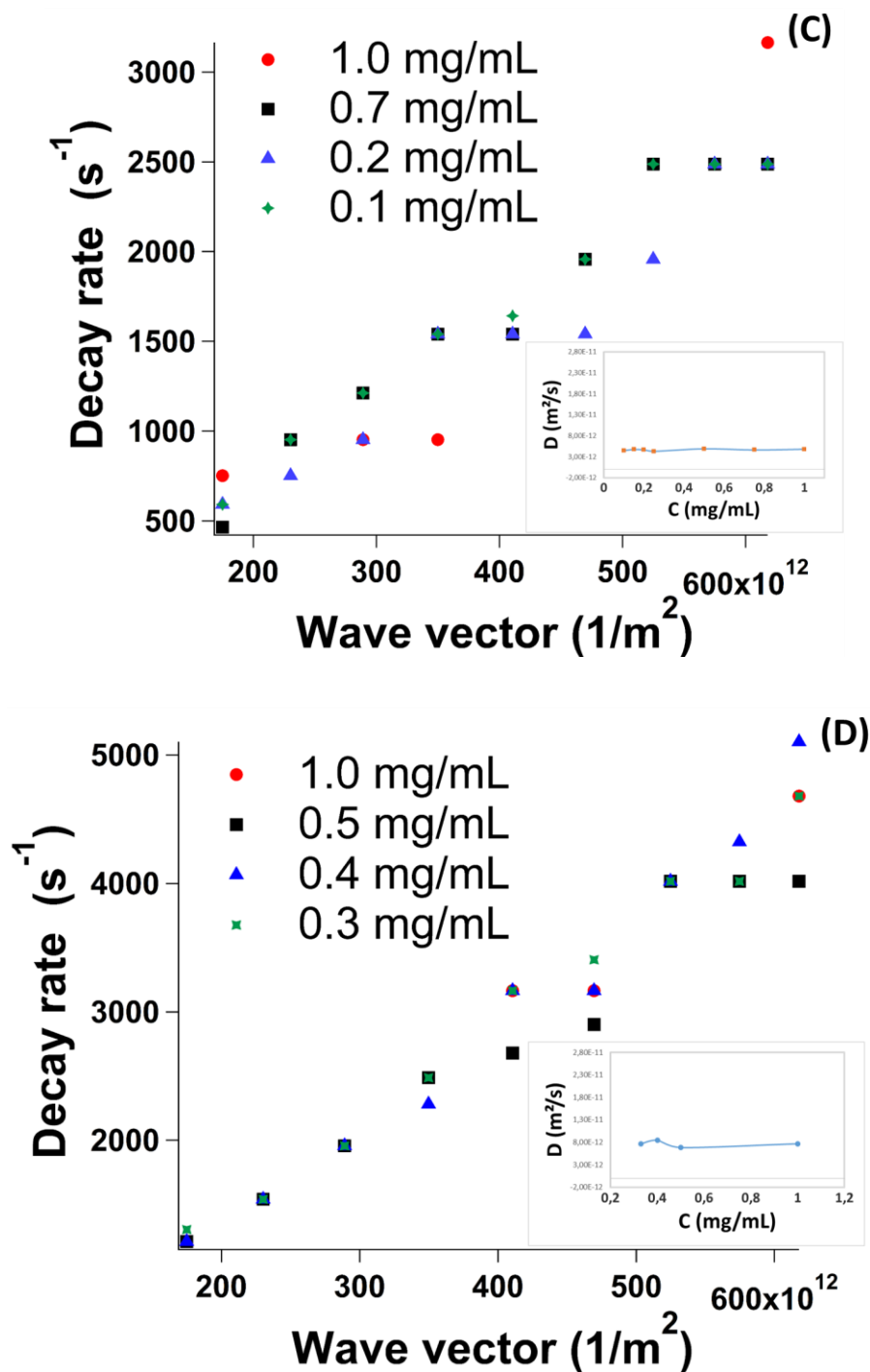


**Figure A3.1:** Overlaid plot of the decay rate ( $\Gamma$ ) obtained by DLS (ALV) as a function of wave vector ( $q^2$ ) at angles 60-140° (step 10°) for four different concentrations of the (A) PTS-PBLG<sub>49</sub>-*b*-PEG<sub>113</sub> (B) PTS-PBLG<sub>49</sub>-*b*-PEG<sub>45</sub> (C) PBLG<sub>53</sub>-PTS-*b*-PEG<sub>113</sub> (D) PBLG<sub>53</sub>-PTS-*b*-PEG<sub>45</sub> nano-assemblies in water ( $\Gamma = q^2D$ , where  $D$  is the diffusion coefficient and  $C$  is the concentration of the solution; the nano-assemblies are prepared by co-assembling them with PBLG<sub>54</sub>-*b*-PEG<sub>113</sub> and PBLG<sub>54</sub>-*b*-PEG<sub>45</sub> in 1:1 weight ratio)

## References

- (1) SCHRODINGER, E. *WHAT IS LIFE?*; Cambridge University Press: United Kingdom, 1944.
- (2) Stefan C. Muller, J. P.; Stefan C. Muller, J. P., Ed.; Springer Series in Material Science: Switzerland, 2015; Vol. 217.
- (3) Solomons, T. W. G.; Fryhle, C. *Organic Chemistry, Binder Ready Version*; John Wiley & Sons Canada, Limited, 2007.
- (4) Matthews, B. W. In *eLS*; John Wiley & Sons, Ltd: 2001.
- (5) Baldwin, R. L. *Proceedings of the National Academy of Sciences* **1986**, *83*, 8069.
- (6) Armstrong, C. L.; Hau, Seydel, T.; Katsaras, J.; Rheinstadter, M. C. *Soft Matter* **2014**, *10*, 2600.
- (7) Zhang, X.; Tanner, P.; Graff, A.; Palivan, C. G.; Meier, W. *Journal of Polymer Science Part A: Polymer Chemistry* **2012**, *50*, 2293.
- (8) Bhowmik, D.; Mote, K. R.; MacLaughlin, C. M.; Biswas, N.; Chandra, B.; Basu, J. K.; Walker, G. C.; Madhu, P. K.; Maiti, S. *ACS Nano* **2015**, *9*, 9070.
- (9) Fang, R. H.; Luk, B. T.; Hu, C.-M. J.; Zhang, L. *Advanced Drug Delivery Reviews* **2015**, *90*, 69.
- (10) Adams, M. L.; Lavasanifar, A.; Kwon, G. S. *Journal of Pharmaceutical Sciences* **2003**, *92*, 1343.
- (11) Wang, J.; Yao, K.; Wang, C.; Tang, C.; Jiang, X. *Journal of Materials Chemistry B* **2013**, *1*, 2324.
- (12) Kelley, E. G.; Murphy, R. P.; Seppala, J. E.; Smart, T. P.; Hann, S. D.; Sullivan, M. O.; Epps, T. H. *Nat Commun* **2014**, *5*.
- (13) Wang, Y.-X.; Guo, D.-S.; Duan, Y.-C.; Wang, Y.-J.; Liu, Y. *Scientific Reports* **2015**, *5*, 9019.
- (14) [https://www.tes.com/lessons/w6jYj0K0o\\_gDhw/cell-membranes](https://www.tes.com/lessons/w6jYj0K0o_gDhw/cell-membranes).
- (15) Zhan-Ting Li, L.-Z. W. 2015; Vol. 87, p 350.
- (16) Seiffert, S. *Supramolecular Polymer Networks and Gels*; 2015 ed.; Springer International Publishing, 2015.
- (17) Fonseca Guerra, C.; Bickelhaupt, F. M.; Snijders, J. G.; Baerends, E. J. *Journal of the American Chemical Society* **2000**, *122*, 4117.
- (18) Jahn, T. R.; Radford, S. E. *Archives of biochemistry and biophysics* **2008**, *469*, 100.
- (19) Benedetti, E.; Palumbo, M.; Bonora, G. M.; Toniolo, C. *Macromolecules* **1976**, *9*, 417
- (20) Keiderling, T. A. *Current Opinion in Chemical Biology* **2002**, *6*, 682.
- (21) T. W. Graham Dolomons, C. B. F.; 9th ed.; John Wiley & Sons, Inc.: Unites States of America, 2007, p 1191.
- (22) Lecommandoux, S.; Achard, M.-F.; Langenwalter, J. F.; Klok, H.-A. *Macromolecules* **2001**, *34*, 9100.
- (23) Klok, H. A.; Lecommandoux, S. *Advanced Materials* **2001**, *13*, 1217.
- (24) Carlsen, A.; Lecommandoux, S. *Current Opinion in Colloid & Interface Science* **2009**, *14*, 329.
- (25) Aggeli, A.; Boden, N.; Zhang, S. *Self-assembling peptide systems in biology, medicine, and engineering*; Springer, 2001.
- (26) Pattni, B. S.; Chupin, V. V.; Torchilin, V. P. *Chemical Reviews* **2015**, *115*, 10938.
- (27) Sercombe, L.; Veerati, T.; Mohemani, F.; Wu, S. Y.; Sood, A.; Hua, S. *Frontiers in Pharmacology* **2015**, *6*.

- (28) Imanishi, Y.; Fujita, K.; Miura, Y.; Kimura, S. *Supramolecular Science* **1996**, *3*, 13.
- (29) Choe, U.-J.; Sun, V. Z.; Tan, J.-K. Y.; Kamei, D. T. In *Peptide-Based Materials*; Deming, T., Ed.; Springer Berlin Heidelberg: Berlin, Heidelberg, 2012, p 117.
- (30) Holowka, E. P.; Pochan, D. J.; Deming, T. J. *Journal of the American Chemical Society* **2005**, *127*, 12423.
- (31) Rodríguez-Hernández, J.; Lecommandoux, S. *Journal of the American Chemical Society* **2005**, *127*, 2026.
- (32) Checot, F.; Lecommandoux, S.; Klok, H.-A.; Gnanou, Y. *The European Physical Journal E* **2003**, *10*, 25.
- (33) Kukula, H.; Schlaad, H.; Antonietti, M.; Förster, S. *Journal of the American Chemical Society* **2002**, *124*, 1658.
- (34) Iatrou, H.; Frielinghaus, H.; Hanski, S.; Ferderigos, N.; Ruokolainen, J.; Ikkala, O.; Richter, D.; Mays, J.; Hadjichristidis, N. *Biomacromolecules* **2007**, *8*, 2173.
- (35) Deming, T. J. *Wiley Interdisciplinary Reviews: Nanomedicine and Nanobiotechnology* **2014**, *6*, 283.
- (36) Vandermeulen, G. W. M.; Klok, H.-A. *Macromolecular Bioscience* **2004**, *4*, 383.
- (37) Gebhardt, K. E.; Ahn, S.; Venkatachalam, G.; Savin, D. A. *Journal of Colloid and Interface Science* **2008**, *317*, 70.
- (38) Maeda, M.; Tsuzaki, Y.; Nakano, K.; Takagi, M. *Journal of the Chemical Society, Chemical Communications* **1990**, 1529
- (39) Nettles, D. L.; Chilkoti, A.; Setton, L. A. *Advanced Drug Delivery Reviews* **2010**, *62*, 1479.
- (40) Hirano, Y.; Mooney, D. J. *Advanced Materials* **2004**, *16*, 17.
- (41) Kutikov, A. B.; Song, J. *ACS Biomaterials Science & Engineering* **2015**, *1*, 463.
- (42) Deming, T. J. *Advanced Drug Delivery Reviews* **2002**, *54*, 1145.
- (43) Blanazs, A.; Armes, S. P.; Ryan, A. J. *Macromolecular Rapid Communications* **2009**, *30*, 267.
- (44) van Rijn, P.; Tutus, M.; Kathrein, C.; Zhu, L.; Wessling, M.; Schwaneberg, U.; Boker, A. *Chemical Society Reviews* **2013**, *42*, 6578.
- (45) Israelachvili, J. N. In *Intermolecular and Surface Forces (Third Edition)*; Academic Press: San Diego, 2011, p 503.
- (46) Lim, Y.-b.; Moon, K.-S.; Lee, M. *Journal of Materials Chemistry* **2008**, *18*, 2909.
- (47) Rodríguez-Hernández, J.; Chécot, F.; Gnanou, Y.; Lecommandoux, S. *Progress in Polymer Science* **2005**, *30*, 691.
- (48) Discher, D. E.; Eisenberg, A. *Science* **2002**, *297*, 967. (49) Ahmed, F.; Pakunlu, R. I.; Brannan, A.; Bates, F.; Minko, T.; Discher, D. E. *Journal of Controlled Release* **2006**, *116*, 150.
- (50) Ding, W.; Lin, S.; Lin, J.; Zhang, L. *The Journal of Physical Chemistry B* **2008**, *112*, 776.
- (51) Lee, M.; Cho, B.-K.; Zin, W.-C. *Chemical Reviews* **2001**, *101*, 3869.
- (52) Cai, C.; Wang, L.; Lin, J.; Zhang, X. *Langmuir* **2012**, *28*, 4515.
- (53) Agut, W.; Taton, D.; Brûlet, A.; Sandre, O.; Lecommandoux, S. *Soft Matter* **2011**, *7*, 9744.
- (54) Kakkar, D.; Mazzaferro, S.; Thevenot, J.; Schatz, C.; Bhatt, A.; Dwarakanath, B. S.; Singh, H.; Mishra, A. K.; Lecommandoux, S. *Macromolecular Bioscience* **2015**, *15*, 124.
- (55) Huang, W.; Wang, W.; Wang, P.; Tian, Q.; Zhang, C.; Wang, C.; Yuan, Z.; Liu, M.; Wan, H.; Tang, H. *Acta Biomaterialia* **2010**, *6*, 3927.

- (56) Sanson, C.; Schatz, C.; Le Meins, J.-F.; Brûlet, A.; Soum, A.; Lecommandoux, S. *Langmuir* **2010**, *26*, 2751.
- (57) Huang, J.; Bonduelle, C.; Thévenot, J.; Lecommandoux, S.; Heise, A. *Journal of the American Chemical Society* **2012**, *134*, 119.
- (58) Agut, W.; Brûlet, A.; Schatz, C.; Taton, D.; Lecommandoux, S. *Langmuir* **2010**, *26*, 10546.
- (59) Ray, J. G.; Johnson, A. J.; Savin, D. A. *Journal of Polymer Science Part B: Polymer Physics* **2013**, *51*, 508.
- (60) Marsden, H. R.; Handgraaf, J.-W.; Nudelman, F.; Sommerdijk, N. A. J. M.; Kros, A. *Journal of the American Chemical Society* **2010**, *132*, 2370.
- (61) Marsden, H. R.; Quer, C. B.; Sanchez, E. Y.; Gabrielli, L.; Jiskoot, W.; Kros, A. *Biomacromolecules* **2010**, *11*, 833.
- (62) Cai, C.; Lin, J.; Chen, T.; Tian, X. *Langmuir* **2010**, *26*, 2791.
- (63) Parras, P.; Castelletto, V.; Hamley, I. W.; Klok, H. A. *Soft Matter* **2005**, *1*, 284.
- (64) Cho, C.-S.; Nagata, R.; Yagawa, A.; Takahashi, S.; Kunou, M.; Akaike, T. *Journal of Polymer Science Part C: Polymer Letters* **1990**, *28*, 89.
- (65) Tang, D.; Lin, J.; Lin, S.; Zhang, S.; Chen, T.; Tian, X. *Macromolecular Rapid Communications* **2004**, *25*, 1241.
- (66) Li, T.; Lin, J.; Chen, T.; Zhang, S. *Polymer* **2006**, *47*, 4485.
- (67) Goñi-de-Cerio, F.; Mariani, V.; Cohen, D.; Madi, L.; Thevenot, J.; Oliveira, H.; Uboldi, C.; Giudetti, G.; Coradeghini, R.; Garanger, E.; Rossi, F.; Portugal-Cohen, M.; Oron, M.; Korenstein, R.; Lecommandoux, S.; Ponti, J.; Suárez-Merino, B.; Heredia, P. *J Nanopart Res* **2013**, *15*, 1.
- (68) Paliwal, R.; Babu, R. J.; Palakurthi, S. *AAPS PharmSciTech* **2014**, *15*, 1527.
- (69) Gohy, J.-F.; Lohmeijer, B. G. G.; Varshney, S. K.; Schubert, U. S. *Macromolecules* **2002**, *35*, 7427.
- (70) Zhuang, Z.; Cai, C.; Jiang, T.; Lin, J.; Yang, C. *Polymer* **2014**, *55*, 602.
- (71) Greish, K. In *Cancer Nanotechnology: Methods and Protocols*; Grobmyer, R. S., Moudgil, M. B., Eds.; Humana Press: Totowa, NJ, 2010, p 25.
- (72) Agarwal, S. **2016**.
- (73) Schöttler, S.; Becker, G.; Winzen, S.; Steinbach, T.; Mohr, K.; Landfester, K.; Mailänder, V.; Wurm, F. R. *Nat Nano* **2016**, *11*, 372.



---

# CHAPTER 4

---

## **PHOTOPHYSICAL PROPERTIES OF AZA-BODIPY DYES, PBLG CONJUGATES AND BLOCK COPOLYMERS**

*Abstract*

*In this chapter, matter - light interaction and some photophysical characterization methods are briefly introduced. Moreover, the activation mechanisms of the photosensitizers and quantification of singlet oxygen generation are discussed. Some examples from the literature on photophysical properties of clinically used PTSs and Aza-BODIPYs are highlighted. Finally, the photophysical properties of PTS, PTS-PBLG conjugates, PTS-PBLG-b-PEG and PBLG-PTS-b-PEG type block copolymers as well as those of the nano-assemblies are investigated in detail. The aim of this study is to evaluate the optical and photophysical behaviour of the PTS after conjugation to the block copolymers from two different positions, and photoactivity of PTS in 4 different nano-assemblies (in terms of PTS localization and morphology), to find the best PDT conditions*





## 4. 1 INTRODUCTION

### 4.1.1 Light - Matter Interactions

Light and matter interactions result in a range of photophysical processes. When incident light ( $I_0$ ) interacts with matter the intensity of transmitted light ( $I$ ) is reduced due to absorption, scattering or emission of absorbed light as illustrated in Figure 4.1.<sup>1</sup>

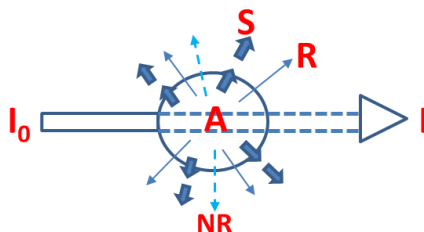


**Figure 4.1:** Photophysical processes resulting from light - matter interactions: (A) absorption, (S) scattering, (R) radiative emission and (NR) non-radiative processes.<sup>1</sup>

The absorption of a photon by a photoactive molecule (rate constant,  $k=10^{15}$ - $10^{16}$ s<sup>-1</sup>)<sup>2</sup> is explained by Beer-Lambert-Bouguer law. It is expressed by equation 4.1:

$$A = -\log(I/I_0) = \epsilon c l \quad (4.1)$$

Where  $A$  is the absorption or optical density,  $\epsilon$  is the molar excitation coefficient ( $M^{-1}cm^{-1}$ ),  $c$  is a molar concentration of the molecule ( $mol L^{-1}$ ), and  $l$  is the optical path length (cm).<sup>3</sup>

Different photophysical processes can be initiated by light absorption.<sup>2</sup> When the molecule absorbs a photon, an electron is promoted to an energetically higher-lying orbital. The excited molecule is thermodynamically unstable, and subsequently returns back to the ground state by radiative (luminescence) and non-radiative processes.<sup>1</sup> Depending on the nature of the molecule, radiative relaxation process can happen through the “emissive passage between two levels of the same multiplicity”<sup>2</sup> ( $S_n \rightarrow S_0$ ,  $S_n \rightarrow S_i$  or  $T_n \rightarrow T_i$ ) which is called fluorescence (lifetime 10 ns)<sup>4</sup> and “emissive passage between two states of the same molecule which are of different multiplicity”<sup>2</sup> ( $S_n \rightarrow T_i$  or  $T_n \rightarrow S_i$ ) which is called phosphorescence (lifetime  $10^2$ - $10^4$  s) as illustrated in Figure 4.2.

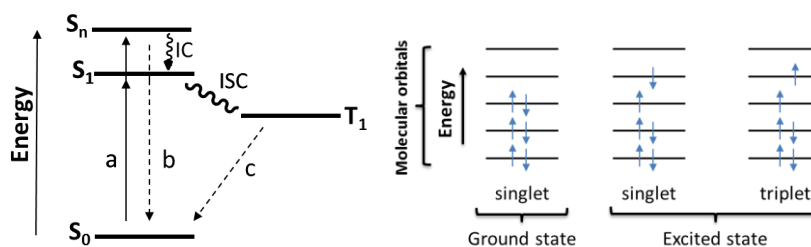


**Figure 4.2:** Simplified Perrin-Jablonski diagram ( $a$  photon absorption,  $b$  fluorescence ( $k=10^6$ - $10^9$ s<sup>-1</sup>),  $c$  phosphorescence ( $k=10^2$ - $10^4$ s<sup>-1</sup>),  $IC$  internal conversion ( $k=10^6$ - $10^{12}$ s<sup>-1</sup>) and  $ISC$  intersystem crossing ( $k=10^4$ - $10^{12}$ s<sup>-1</sup>) and illustration of spin arrangement in ground and excited state molecular orbitals<sup>2,5</sup>

The efficiency of fluorescence or phosphorescence emission process is quantitatively characterized by the emission quantum yield ( $\Phi$ ). It depends on the temperature, solvent and other parameters as well as on the number of photons absorbed, and is quantified by spectroscopic techniques. It is defined as: <sup>2</sup>

$$\phi = \frac{\text{Number of emitted photons}}{\text{Number of photons absorbed}} \quad (4.2)$$

Another parameter to characterize the luminescence emission is the lifetime of the excited state ( $\tau$ ). It is the average time that an excited molecule spends in excited state before it returns to ground state and is defined as:<sup>4</sup>

$$\tau = \frac{1}{\Gamma + k_{nr}} \quad (4.3)$$

When there is no non-radiative decay it is given by:

$$\tau = \frac{1}{\Gamma} \quad (4.4)$$

Where  $\Gamma$  is an emissive rate of luminescence and  $k_{nr}$  is a rate of non-radiative decay. The lifetime of the excited state is measured by time-resolved spectroscopy that is based on the measurement of the luminescence intensity decay by high-speed detection system in wide range of timescale.

#### 4.1.1.1 Fluorescence quantum yield measurement

The fluorescence quantum yield ( $\Phi_F$ ) calculation is one of the important parameters required in evaluation of the photophysical properties of molecules. There are two methods to calculate this parameter. The first one is the comparative method (or relative) where the emission of the optically matched standard compound is compared with the sample and calculated following the equation (4.5).<sup>6,7</sup>

$$\Phi_x = \Phi_{st} \times \left(\frac{I_x}{I_{st}}\right) \times \left(\frac{F_{st}}{F_x}\right) \times \left(\frac{\eta_x^2}{\eta_{st}^2}\right) \quad (4.5)$$

Where  $\Phi_x$  is the fluorescence quantum yield of the sample,  $\Phi_{st}$  is the fluorescence quantum yield of the reference compound,  $I$  is the integrated emission intensity,  $F$  is the optical density at the irradiation wavelength and  $\eta$  is the refractive index of the solvent.

The second method  $\Phi_F$  calculation is the absolute method which is performed using an integration sphere, as shown in Figure 4.3. It consists of a Teflon sample holder and sphere with exit port and entrance port which fits in a spectrofluorimeter sample chamber. This method is applicable for a wide variety of materials, mostly highly emissive samples like nanomaterials, metal complexes<sup>7</sup> etc. It can collect all the emission from the sample and does not require a reference sample.<sup>6</sup>

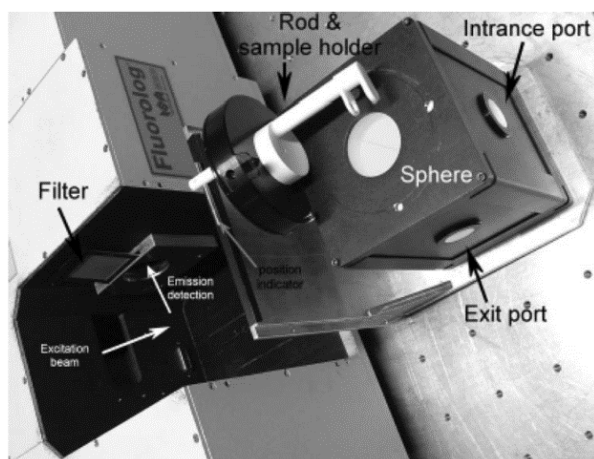


**Figure 4.3:** Integration Sphere<sup>6</sup>

The absolute fluorescence quantum yield is calculated after performing measurements in two configurations. First one is the “IN” configuration where incident beam hits the sample directly and emission signals is collected from exit port. In “OUT” configuration the sample holder is rotated by different degree of angel to collect excitation and emission signals without direct hitting the sample with light source as shown in Figure 5.4.<sup>6</sup> To decrease the light intensity without changing spectral profile gauze neutral density (ND) filters are used during the excitation. Finally,  $\Phi_F$  is calculated by equations 4.6 and 4.7 which were developed by Mello and coworkers.<sup>8</sup>

$$\Phi_F = \frac{E_{in}(\lambda) - (1 - \alpha)E_{out}(\lambda)}{X_{empty}(\lambda)\alpha} ND \quad (4.6)$$

$$\alpha = \frac{X_{out}(\lambda) - X_{in}(\lambda)}{X_{out}(\lambda)} \quad (4.7)$$

Where,  $E_{in}(\lambda)$  and  $E_{out}(\lambda)$  are the integrated luminescence in “IN” and “Out” configuration and  $\alpha$  is an absorption of the sample.  $X_{empty}(\lambda)$ ,  $X_{in}(\lambda)$ ,  $X_{out}(\lambda)$ , integrated excitation of empty sphere, with sample in “IN” configuration and in “OUT” configuration, respectively.

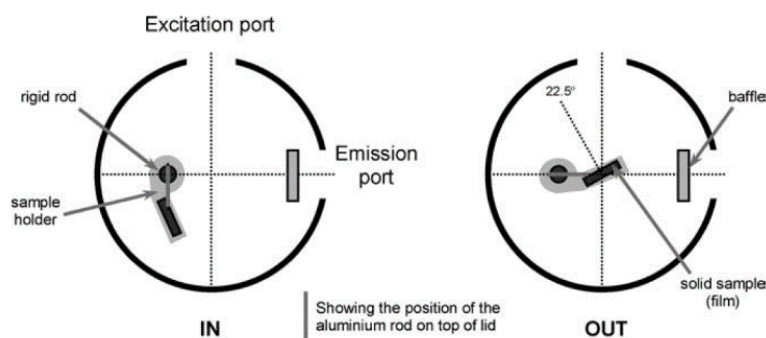


**Figure 4.4:** Illustration of the position of the sample IN and OUT of the beam<sup>6</sup>

#### 4.1.1.2 Transient absorption

Transient absorption spectroscopy characterizes the electronic properties of photoactive molecules in the excited state by pump-probe techniques. In this method a fraction of the molecules (within the pump, approximately 0.1-20%) are excited by a pump pulse, and a time delay probe pulse is sent through the sample as it can be seen from Figure 4.5. The difference between the absorption of excited states and the absorption of the ground state helps to

characterize different photophysical and photochemical processes like electron transfer, proton transfer, energy migration, intersystem crossing etc.<sup>9,10</sup>

Transient absorption spectra can be constructed via equation 4.8 by measuring the intensity of a probe beam which passes through the sample ( $I_0(\lambda)$ ) at different time delays by multichannel detectors (PDA or CCD) and after passing through the sample ( $I(\lambda, \tau)$ ).<sup>11</sup>

$$A_{(\lambda, \tau)} = \log_{10} \frac{I_0(\lambda)}{I(\lambda, \tau)} \quad (4.8)$$

Finally, the absorption of the unexcited sample is subtracted from the measured transient absorption as shown in the following equation<sup>11</sup>

$$A = \log_{10} \frac{I_0(\lambda)}{I(\lambda, \tau)} - \log_{10} \frac{I_0(\lambda)}{I(\lambda, \infty)} = \log_{10} \frac{I(\lambda, \infty)}{I(\lambda, \tau)} \quad (4.9)$$

Where  $I(\lambda, \infty)$  is the intensity of probe pulse after passing through the sample without excitation.

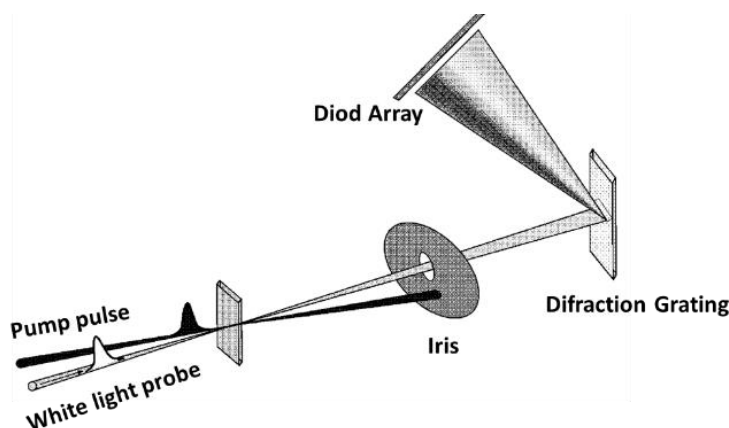


**Figure 4.5:** The schematic representation of transient absorption spectroscopy principle.<sup>9</sup>

#### 4.1.2 Photoactivation of photosensitizers (PTS)

Upon light exposure at an appropriate wavelength, PTS absorbs the photon and an excited state is reached. The excited PTS\* may be converted to a long-lived triplet state by ISC process in certain cases. In the triplet state,  $^3\text{PTS}^*$  can create reactive oxygen species (**ROS**) through intermolecular electron transfer or energy transfer to molecular oxygen (see Table 4.1).<sup>12</sup>

Type I photosensitizers can cause several chemical reactions under photodynamic action by electron transfer or hydrogen abstraction. These photosensitizers can generate several ROS like superoxide anion ( $\text{O}_2^-$ ), hydroxyl radical ( $\text{OH}^\cdot$ ) and hydrogen peroxide ( $\text{H}_2\text{O}_2$ ). The drawback of this process is the consumption of the PTS during photodynamic action due to the irreversible reactions.<sup>13</sup>

Type II process takes place by electronic energy transfer from the photosensitizer in the excited triplet state ( $^3\text{PTS}^*$ ) to the ground state oxygen ( $^3\text{O}_2$ ) and generates highly reactive singlet oxygen ( $^1\text{O}_2$ ) as illustrated in the simplified Perrin-Jablonski diagram (Figure 4.6).

**Table 4.1:** Reactions occurring upon PTS activation<sup>13</sup>

Excitation	${}^1\text{PTS} + h\nu \rightarrow {}^1\text{PTS}^* \rightarrow {}^3\text{PTS}^*$	
	Reaction	Product
<b>Type I</b>	${}^3\text{PTS}^* + {}^1\text{PTS} \rightarrow$	$\text{PTS}^{\cdot-} + \text{PTS}^{\cdot+}$
	${}^3\text{PTS}^* + D \rightarrow$	$\text{PTS}^{\cdot-} + D^+$
	$\text{PTS}^{\cdot-} + \text{O}_2 \rightarrow$	${}^1\text{PTS} + \text{O}_2^{\cdot-}$
	${}^3\text{PTS}^* + \text{O}_2 \rightarrow$	$\text{PTS}^{\cdot+} + \text{O}_2^{\cdot-}$
	$2\text{O}_2^{\cdot-} + 2\text{H}^+ \rightarrow$	$\text{O}_2 + \text{H}_2\text{O}_2$
	$\text{Fe}^{3+} + \text{O}_2^{\cdot-} \rightarrow$	$\text{Fe}^{2+} + \text{O}_2$
	$\text{Fe}^{2+} + \text{H}_2\text{O}_2 \rightarrow$	$\text{O}_2 + \text{OH}^- + \text{OH}^{\cdot}$
<b>Type II</b>	${}^3\text{PTS}^* + {}^3\text{O}_2 \rightarrow$	${}^1\text{PTS} + {}^1\text{O}_2$

Superscript *1* represents a singlet state, *3* triplet state, \* excited state and *D* is an electron donor molecule.

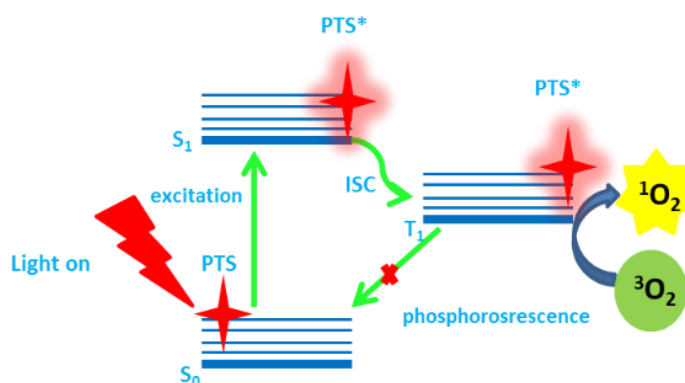


**Figure 4.6:** Simplified Perrin-Jablonski diagram of type II photoactivation process

This cyclic process can continue until the oxygen is consumed or the light source is removed. However, it also depends on the oxidation potential of the PTS since small quantities of generated singlet oxygen can react with PTS itself. There are only a limited number of PTSs that can be activated by Type II processes since not many photoactive molecules are capable to transfer their energy in their excited state to molecular oxygen.<sup>12,13</sup>

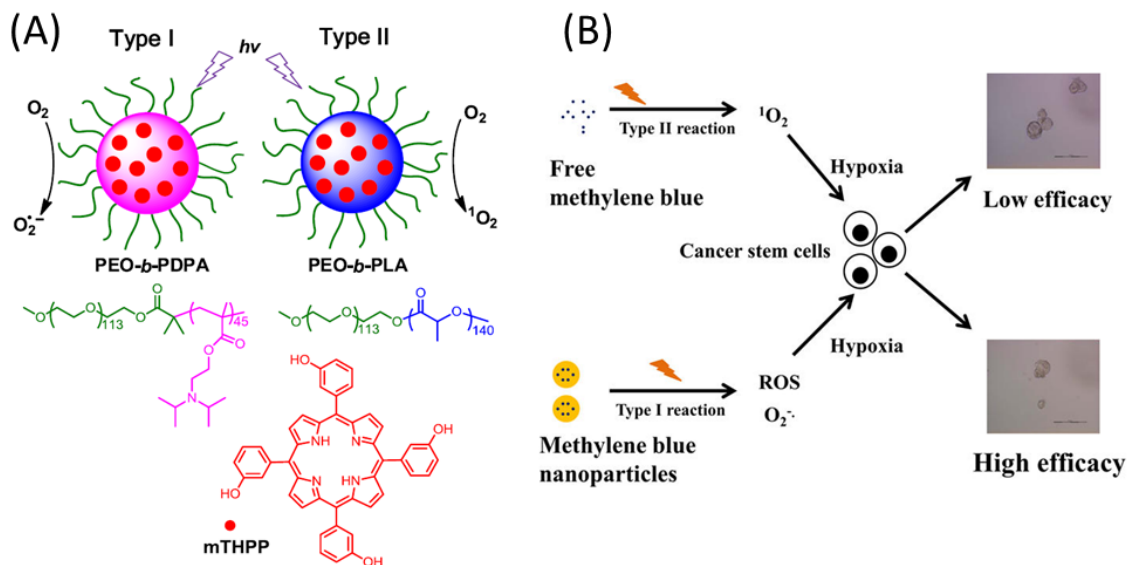


**Figure 4.7:** Schematic illustration of (A) mTHPP photoactivation pathway shift in different polymer matrix<sup>14</sup> (B) photoactivation reaction shift in free and encapsulated MB<sup>15</sup>

Due to some environmental factors the same photosensitizer may also switch between type I and type II photoreaction pathways. Ding et al<sup>14</sup> have prepared 5,10,15,20-tetrakis(meso-hydroxyphenyl) porphyrin (mTHPP) loaded micelles by using PEG-*b*-poly(D,L-lactide) (PEG-*b*-PLA) and poly(ethylene glycol)-*b*-poly(2-(diisopropylamino)ethyl methacrylate) (PEG-*b*-PDPA) block copolymers, where mTHPP photosensitizer promotes different activation reactions in each block copolymer (Figure 4.7a). Although the mTHPP is a type II agent, it switches to the type I mechanism and shows enhanced superoxide anion (O<sub>2</sub><sup>•-</sup>) generation due to the electron rich nature of PEG-*b*-PDPA block copolymer, whereas no change was observed in electron deficient PEG-*b*-PLA block copolymer encapsulated mTHPP. The same phenomenon was observed in methylene blue (MB) encapsulated polymer nanoparticles. Usacheva and co-workers<sup>15</sup> have prepared MB encapsulated alginate polymer nanoparticles for efficient elimination of cancer stem cells (Figure 4.7b). The anionic polymer enhances the encapsulation of higher amount of cationic MB by electrostatic interaction and also causes switching of the photoactivation reaction from type II to type I mechanism. This process is explained by the dimerization of MB due to the polymer-PTS interaction. This interaction enhances the charge transfer process which facilitates the radical formation.

### 4.1.3 Singlet oxygen

The singlet oxygen is the lowest excited electronic level of molecular oxygen in singlet state that has characteristic NIR emission at 1270 nm. However, the higher energy state of molecular oxygen (<sup>1</sup>Σ<sub>g</sub><sup>+</sup>) also exists, which is a singlet as well.<sup>16</sup> It is an energetically unstable form of molecular singlet oxygen that requires higher energy to be formed (~157 kJ/mol, see Figure 4.8) and quickly deactivates to <sup>1</sup>Δ<sub>g</sub> (~94 kJ/mol) due to the shorter lifetime (8.2 ps in H<sub>2</sub>O and 42 ps in D<sub>2</sub>O).<sup>17</sup>

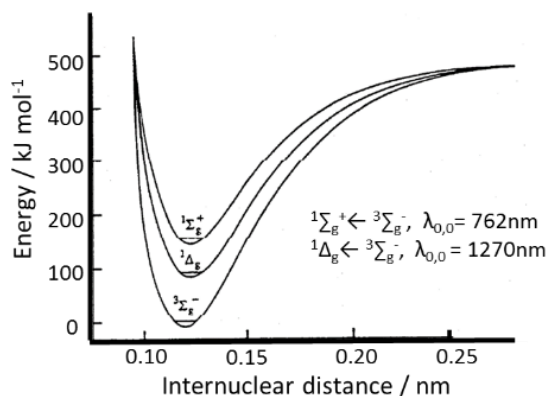


**Figure 4.8:** Potential energy curve for molecular oxygen:  $^3\Sigma_g^-$ ,  $^1\Delta_g$  and  $^1\Sigma_g^+$ <sup>18</sup>

Ground state of molecular oxygen is a triplet state which is a rare electronic structure for the molecules in ground state.<sup>17</sup> It has two unpaired valence electrons in two orbitals where spins are oriented in the same direction. In excited state the spins get paired in opposite directions in one orbital and form highly reactive  $^1\Delta_g$  oxygen. Unstable singlet sigma has also two unpaired electrons in two molecular orbitals but spins are oriented in opposite directions as can be seen from Figure 4.9.

	$^3\Sigma_g^-$	$^1\Delta_g$	$^1\Sigma_g^+$
$\sigma_p^*$	—	—	—
$\pi_x^* \pi_y^*$	$\uparrow \uparrow$	$\uparrow\downarrow$ —	$\uparrow \downarrow$
$\pi_x \pi_y$	$\uparrow\downarrow \uparrow\downarrow$	$\uparrow\downarrow \uparrow\downarrow$	$\uparrow\downarrow \uparrow\downarrow$
$\sigma_p$	$\uparrow\downarrow$	$\uparrow\downarrow$	$\uparrow\downarrow$
$\sigma^*(2s)$	$\uparrow\downarrow$	$\uparrow\downarrow$	$\uparrow\downarrow$
$\sigma(2s)$	$\uparrow\downarrow$	$\uparrow\downarrow$	$\uparrow\downarrow$
$\sigma^*(1s)$	$\uparrow\downarrow$	$\uparrow\downarrow$	$\uparrow\downarrow$
$\sigma(1s)$	$\uparrow\downarrow$	$\uparrow\downarrow$	$\uparrow\downarrow$

**Figure 4.9:** Electronic configuration of molecular oxygen in the ground triplet state and excited singlet states<sup>19</sup>

**Table 4.2:** The lifetime of  $^1\Delta_g$  in different solvents <sup>21</sup> (\*<sup>20</sup>)

Solvents	$\tau$ , $\mu\text{s}$
H <sub>2</sub> O	3.5*
D <sub>2</sub> O	68*
CH <sub>3</sub> OH	10
CD <sub>3</sub> OD	227
C <sub>6</sub> H <sub>6</sub>	31
C <sub>6</sub> D <sub>6</sub>	628

The singlet sigma ( $^1\Sigma_g^+$ ) has characteristic luminescence emission at 762nm due to the  $^1\Sigma_g^+ \rightarrow ^3\Sigma_g^-$  transition, and the emission at 1925 nm characteristic of the  $^1\Sigma_g^+ \rightarrow ^1\Delta_g$  transition (20 ns).<sup>16</sup> These transitions can be monitored in solution by spectroscopic techniques. The



lifetime decay of  $^1\Delta_g \rightarrow ^3\Sigma_g^-$  transition depends on the nature of the solvent (see Table 4.2). It has been shown that the predominant excited oxygen  $^1\Delta_g$  shows 20 times lower lifetime in water compare to deuterated water. This perturbation is explained by the energy transfer from  $^1\Delta_g$  to H-O stretching vibration. Thus, solvents with O-H and C-H groups can convert the electronic energy of  $^1\Delta_g$  into vibrational energy of the solvent and decrease the lifetime.<sup>20</sup>

Ogilby et al.<sup>22-25</sup> performed different photophysical studies on cells incubated in D<sub>2</sub>O and H<sub>2</sub>O, which are based on the detection of  $^1\Delta_g \rightarrow ^3\Sigma_g^-$  phosphorescence decay at 1275 nm, to characterize the photophysical behavior of singlet oxygen in intracellular environment. Time resolved studies on single cell showed that the lifetime of singlet oxygen in cells incubated in D<sub>2</sub>O is in the range of 15-30  $\mu$ s, which is much smaller than the lifetime in pure D<sub>2</sub>O (68  $\mu$ s). On the other hand, the lifetime calculated as 3  $\mu$ s for cells incubated in H<sub>2</sub>O is not much different than the lifetime in neat water (3.5  $\mu$ s).<sup>25</sup> However, in early studies the intracellular singlet oxygen lifetime was reported to be around 10-300 ns, as calculated from indirect methods.<sup>17,26,27</sup> Ogilby and co-workers<sup>25</sup> have also estimated that the singlet oxygen has a spherical 100 nm activity radius in the cell which is estimated from an intracellular oxygen diffusion coefficient ( $2-4 \times 10^{-6} \text{ cm}^2\text{s}^{-1}$ ). Thus the toxicity of singlet oxygen is limited for one cell and cannot diffuse for a long distance and damage healthy cells since the diameter of eukaryotic cells are in the range of 10-30  $\mu$ m. Consequently, shorter diffusion length increases the selectivity of Photodynamic Therapy.

#### 4.1.3.1 Detection of singlet oxygen in the solution

There are several methods<sup>18</sup> to calculate the singlet oxygen generation quantum yield ( $\Phi_\Delta$ ). However, the most frequently used ones are the direct detection of singlet oxygen signal at 1270nm by spectroscopic techniques and the chemical trapping method.<sup>28</sup> Both methods are comparative and require the use of a reference compound.

The first method is based on the direct detection of the singlet oxygen phosphorescence curve by time-resolved NIR fluorimeter.<sup>29</sup> In this technique,  $\Phi_\Delta$  can be calculated from Equation 4.10 by using optically matched photosensitizer.

$$\Phi_\Delta^X = \Phi_\Delta^R \frac{I_x A_R \tau_R}{I_R A_x \tau_x} \quad (4.10)$$

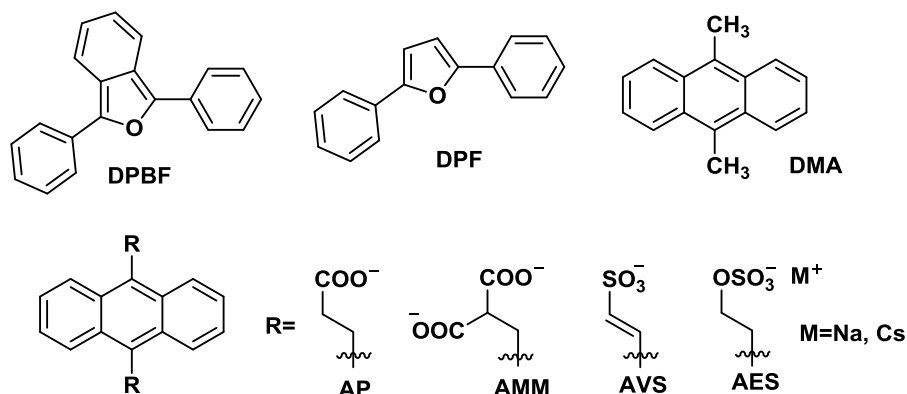
Where I is the emission intensity of  $^1\text{O}_2$  (at 1270nm), A is the absorption of the solution,  $\tau$  is the lifetime of the  $^1\text{O}_2$  phosphorescence in the selected solvent, X and R indices refer to the sample and reference compound, respectively.<sup>18,29-32</sup>

The chemical trapping method is the mostly preferred photometric detection method in the literature to determine  $^1\text{O}_2$  generation yield.<sup>14,30,31,33,34</sup> It is a useful technique especially for the detection of small quantities of singlet oxygen in solution. The method is based on the photobleaching of the  $^1\text{O}_2$  scavenger molecule under monochromatic light irradiation. During light irradiation, with an appropriate wavelength for the PTS,  $^1\text{O}_2$  is formed in the solution and immediately reacts with the trapping molecule, and consequently decreases its absorption band.<sup>30</sup> The photobleaching rate constant, which is proportional to  $\Phi_\Delta$ , can be obtained by monitoring the absorption change as a function of time. Moreover, by using a reference molecule with known quantum yield of singlet oxygen generation,  $\Phi_\Delta$  of the sample can be calculated by the following equation:

$$\Phi_\Delta^X = \Phi_\Delta^R \left( \frac{m_x F_R}{m_R F_x} \right) \quad (4.11)$$

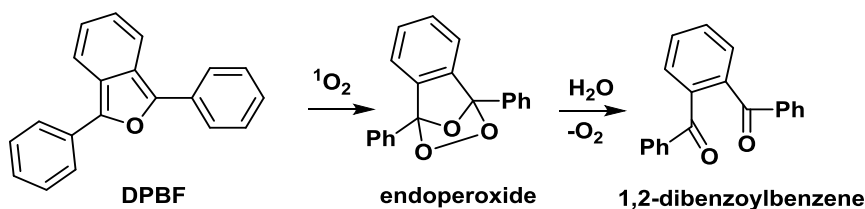
Where  $m$  is the photobleaching rate of the trap molecule and  $F$  is the optical density of PTS at irradiation wavelength, X and R indices refer to the sample and reference compound, respectively.

After the discovery of existence of singlet state molecular oxygen ( $^1\text{O}_2$ ), many trapping molecules have been reported in the early 1970s.<sup>35-40</sup> Among these reported trapping molecules furan analogues and anthracene derivatives are the mostly used scavengers to the best of our knowledge (see Scheme 4.1).



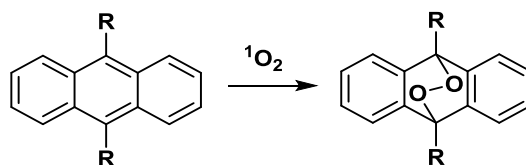
**Scheme 4.1:** Library of singlet oxygen traps: 1,3-diphenylisobenzofuran (DPBF)<sup>40</sup>, 2,5-diphenylfuran (DPF)<sup>36</sup>, 9,10-dimethylanthracene (DMA)<sup>41</sup>, 9,10-bis(propionate)anthracene (AP)<sup>14</sup>, 9,10-bis(methylmalonate)anthracene (AMM)<sup>33</sup>, 9,10-bis-(vinylsulfonate)anthracene (AVS)<sup>42</sup> and sodium or cesium salt of anthracene-9,10-bisethanesulphonic acid (AES)<sup>37,43</sup>

Although 1,3-diphenylisobenzofuran (DPBF) was reported in 1975 by Howard et al.,<sup>40</sup> it is still the most widely used molecule to quantify the singlet oxygen generation.<sup>34</sup> It can simultaneously react with singlet oxygen *via* [1+4] cycloaddition reaction in organic solvent and form endoperoxide, which degrades to 1,2-dibenzoylbenzene in the presence of water as shown in Scheme 4.2. The photodegradation process can be followed by the decrease of the absorption band at 429 nm. However, its application is limited due to the lack of solubility in water and low singlet oxygen selectivity since it has been reported that it can also react with other reactive oxygen species (ROS).<sup>44</sup> Despite the fact that a derivative of furan with reduced aromaticity, 2,5-diphenylfuran (DPF), was proposed as a water soluble  $^1\text{O}_2$  trapping molecule, it also possess reactivity toward other ROS as well.<sup>36</sup>



**Scheme 4.2:** Oxidation of DPBF in the presence of singlet oxygen

Several studies reported in literature<sup>42,43</sup> show that water (AP, AMM, AVS, AES etc., see Scheme 4.1) and organic (DMA etc.) soluble anthracene derivatives are more stable in the different environments and show more selectivity toward singlet oxygen. In the presence of singlet oxygen in the solution they simultaneously react *via* [4+2] cycloaddition reaction and form endoperoxides (Scheme 4.3).



**Scheme 4.3:** [4+2] cycloaddition reaction of anthracene with  $^1\text{O}_2$

Water soluble singlet oxygen traps have an important role in biology in term of quantification of  $^1\text{O}_2$  yield by mimicking the cellular environment. 9,10-bis-(vinylsulfonate) anthracene (AVS) water soluble singlet oxygen indicator gained more attention owing to the easy synthesis and higher trapping efficacy.<sup>43</sup> The comparative rates of  $^1\text{O}_2$  total removal between 9,10-bis(propionate)anthracene (AP), 9,10-bis(methylmalonate)anthracene (AMM) and AVS by  $^1\text{O}_2$  phosphorescence quenching experiments show that AVS has the higher rate constant (K) of  $^1\text{O}_2$  removal compared to two other anthracene derivatives (Table 4.3).<sup>42</sup>

**Table 4.3:** Rate constant of total removal of  $^1\text{O}_2$  in water <sup>42</sup>

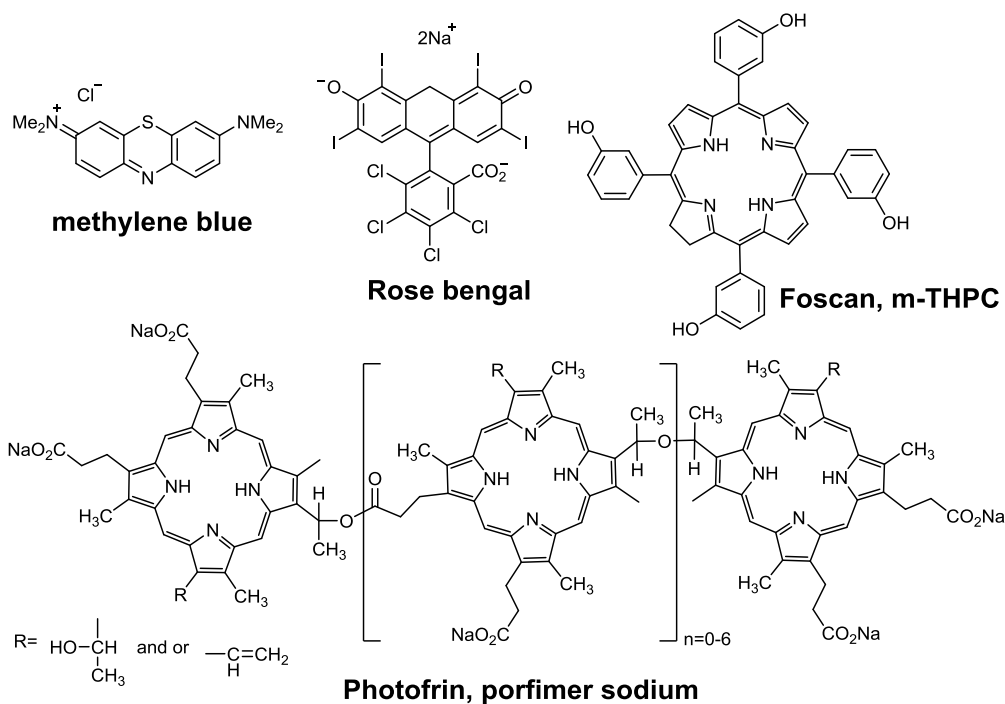
$^1\text{O}_2$ traps	$K_T \times 10^6$ [ $\text{M}^{-1} \text{s}^{-1}$ ]
AP	17
AMM	13
AVS	44

#### 4.1.4 Photophysical properties of clinically used photosensitizers for photodynamic therapy

Besides the biocompatibility and lower dark toxicity, good photophysical properties are also important to increase the therapeutic efficacy of photosensitizers. A good photosensitizer should have strong absorption in the range 650-800nm, higher extinction coefficient ( $\epsilon$ ), higher singlet oxygen generation yield ( $\Phi_\Delta$ ), good water solubility and higher circulation lifetime in the blood stream.<sup>13</sup>

Photofrin<sup>®</sup> is the first FDA approved photosensitizer (in 1999) which is known as first generation photosensitizer and belongs to the porphyrin family.<sup>13</sup> It consists of a mixture of ester or ether linked dimers, trimers and oligomers of porphyrin units as depicted in Scheme 4.4.<sup>45</sup> However, the synthesis and purification of Photofrin<sup>®</sup> is challenging and it lacks water solubility. Moreover, it has poor photophysical properties and causes many side effects during treatment. Due to these drawbacks many studies have been reported to develop new photosensitizers for photodynamic therapy to reduce the unwanted side effects and increase the photoactivity (Table 4.4).<sup>46-50</sup>

The attempts to use charged molecules like cationic methylene blue (MB) and anionic Rose Bengal (RB) also were not successful due to the high inherent dark toxicity and low absorption wavelength.<sup>34,48,51</sup> However, MB and RB are used *ex-vivo* in clinics for the treatment of some cancer types, bacterial and viral infections by PDT. Moreover, these dyes are used for staining living organisms in biology and medicine.



**Scheme 4.4:** Molecular structure of some clinically used photosensitizers

The second generation photosensitizer Foscan<sup>®</sup> (meta-tetra (hydroxyphenyl) chlorin, m-THPC) was approved for cancer treatment by EU in 2001.<sup>52,53</sup> It belongs to the chlorin family which differs from porphyrins by two extra hydrogen atoms on the pyrrole ring. Easy synthesis, purification and enhanced photophysical properties make it a better candidate for PDT compared to Photofrin<sup>®</sup>. Moreover, skin sensitization period after treatment is shorter than Photofrin<sup>®</sup> treatment. To decrease the side effect of Foscan<sup>®</sup>, liposome encapsulated m-THPC vesicles<sup>49</sup> and PEG coated liposomal m-THPC particles<sup>54</sup> have been also investigated.

During the therapy, the duration of the light irradiation and the dose of the administered PDT therapeutics are determined according to the type, stage, location of the cancer and several other parameters depending on the patient. Thus, all these variables make the comparison between the different systems rather difficult.

Still, there are many studies under clinical trials to improve the therapeutic efficacy, decrease dark toxicity and increase the localization of the drug in the cancer site.

**Table 4.4:** Properties and application of some approved photosensitizers<sup>13</sup>

Compounds	$\lambda_{\text{abs}}$ (nm)	$\epsilon$ ( $\text{M}^{-1} \cdot \text{cm}^{-1}$ )	$\Phi_{\Delta}$	Application
Methylene blue	666	82 000	0.5 in $\text{H}_2\text{O}$ <sup>51</sup>	melanoma, basal cell carcinoma, Kaposi's sarcoma
Rose Bengal	549	100 000	0.76 in $\text{H}_2\text{O}$ <sup>18</sup>	breast carcinoma, melanoma
Photofrin <sup>®</sup>	630	3 000	0.25 (PB + 1% TX100) <sup>55</sup>	bladder cancer esophageal cancer, lung cancer, Barrett's esophagus, cervical cancer, endobronchial cancer
Foscan <sup>®</sup>	650	39 000	0.31 (PBS + 10% FCS) <sup>55</sup>	neck and head cancer

*PB* Phosphate buffer pH 7.4, *PBS* Phosphate buffered saline, *TX100* Triton X100, *FCS* Fetal calf serum

#### 4.1.5 Photophysical properties of BODIPYs and heavy atom effect

As mentioned in Chapter 2 modification of BODIPY core tremendously affects their optical properties. Depending on the attached group on the BODIPY core the absorption of the dye can be blue shifted or red shifted and inhibits intense fluorescence emission which makes them good candidates for fluorescence imaging, bio-labeling and sensing applications. However, these dyes rarely exhibit phosphorescence properties due to the slow intersystem crossing (ISC) rate. Takatoshi and co-workers<sup>56</sup> have reported that iodination of BODIPY core at the 2 and 6 positions can increase ISC yield due to the internal heavy atom effect. Although this process ends up with a reduction of fluorescence quantum yield, no phosphorescence can be observed. It was shown that upon excitation of halogenated BODIPYs, they transfer their energy in triplet state to the molecular triplet oxygen and excite it into the singlet oxygen state which is relaxed back by red luminescence emission (Figure 4.10). It is known that the presence of molecular oxygen can cause 99.9% phosphorescence quenching due to the energy transfer or electron transfer from triplet state.<sup>2</sup>

It was reported that the iodine substituted BODIPY 21-BOD<sup>56</sup> generates 1.34 times more singlet oxygen compared to Rose Bengal (RB,  $\Phi(^1\text{O}_2) = 0.8$  in MeOH) and exhibits good photostability as shown in Figure 5.10. The same approach was observed in aza-BODIPY derivatives. Moreover, the longer absorption and emission wavelength make them efficient dyes or PTS for *in vivo* applications. O'Shea and co-workers<sup>34</sup> investigated the internal heavy atom effect on singlet oxygen generation by placing halogen at different position in the molecule. The study shows that the bromination of aza-BODIPY core increases the singlet oxygen quantum yield compared to the bromination of aromatic rings. This is explained by the fact that bromination of aromatic rings causes distortion of planarity of the molecule whereas bromination of the core does not cause any distortion according to X-ray studies.<sup>34</sup>

Singlet oxygen generation efficacy of **31** was calculated by the comparative method using methylene blue (MB,  $\Phi_{\Delta} = 0.5$ -0.65 in MeOH) as a reference compound and monitored by singlet oxygen acceptor DPBF photoperoxidation. According to this study, **31** can generate 7.7

times more singlet oxygen in methanol compared to MB. Mcclenaghan and coworkers<sup>57</sup> have reported the detailed photophysical characterization of **30** and **31** by real time measurements in acetonitrile. A significant decrease in fluorescence quantum yield and fluorescent lifetime (**30** ( $\tau=2.2$  ns) and **31** ( $\tau=550$  ps)) was observed after the bromination as a result of enhanced ISC rate.<sup>57</sup> The ISC quantum efficacy, in other word the triplet state quantum yield of **31**, was calculated as 0.72 (triplet lifetime 21  $\mu$ s) and absolute singlet oxygen generation calculated as 74%.<sup>57</sup> Overall, these characterizations prove **31** as an efficient photosensitizer for PDT. Moreover, it shows relatively low dark toxicity and 100 fold higher efficacy under light excitation compared to **30** according to the in vitro studies on HeLa cells.<sup>34, 46</sup>

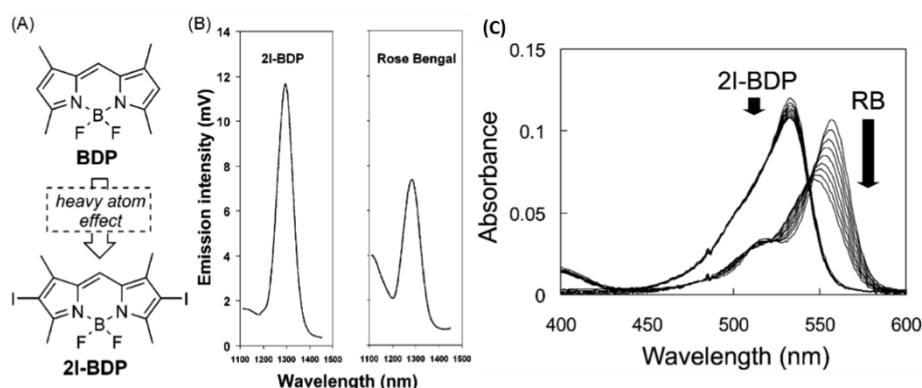
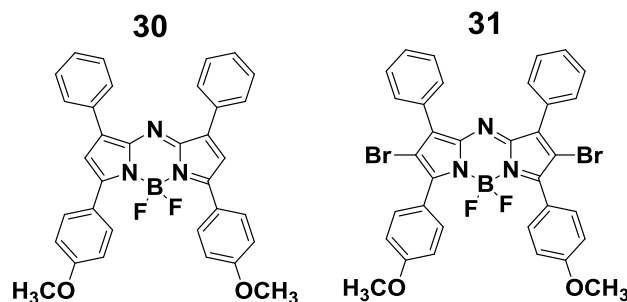


**Figure 4.10:** A) Structure of BODIPYs B) Singlet oxygen luminescence of 2I-BODIPY and Rose Bengal ( $5 \times 10^{-5}$  M in MeOH,  $\lambda_{ex} = 515$  nm,  $^1O_2$   $\lambda_{em} = 1268$  nm) B) photostability of 2I-BODIPY and Rose Bengal ( $1 \times 10^{-6}$  M in MeOH,  $\lambda_{ex} = 546$  nm, 8 cycle)<sup>56</sup>



**Scheme 4.5:** Molecular structure of aza-BODIPYs<sup>34</sup>

**Table 4.5:** Photophysical properties of **30** and **31**<sup>34</sup>

compounds	$\lambda_{abs}$ (nm)		$\lambda_{em}$ (nm)		$\Phi_F$	$\epsilon$ ( $M^{-1} \cdot cm^{-1}$ )
	H <sub>2</sub> O/CrEL	CHCl <sub>3</sub>	H <sub>2</sub> O/CrEL	CHCl <sub>3</sub>		
<b>30</b>	696	688	727	715	0.36	85000
<b>31</b>	683	679	719	714	0.1	75000

CrEL – emulsifier cremophor EL

## **4.2 Results**

### **4.2.1 Overall photophysical properties of the PTS, PTS-PBLG conjugates and PTS functionalized block copolymers**

The fluorescence quantum yield (QY), fluorescence lifetime, absorption coefficient, triplet state QY and singlet oxygen generation QY of the Aza-BODIPYs, their PBLG conjugates and block copolymers were measured. These characterizations allow us to evaluate the photophysical changes of the PTS during chemical modifications, and its behavior after self-assembly in water. Overall results are shown in Table 4.6 which will be discussed in detail in following sections of this chapter.

**Table 4.6:** Overall results from photophysical characterization

	$\lambda_{\text{abs}}$ (nm)	$\lambda_{\text{em}}$ (nm)	$\Phi_{\text{F}}$	$\tau$ (ns)	$\varepsilon$ [M <sup>-1</sup> ·cm <sup>-1</sup> ]	$\Phi_{\text{T}}$	$\Phi_{\Delta}$ DCM
<b>23</b>	689	719	0.36	2.4	83900		
<b>24</b>	675	712	0.08	0.59(0.41%)1.02 (0.59%)	71700	0.57	0.66
<b>25</b>	676	718	0.07	0.6	69300	0.6	
PTS- PBLG <sub>53</sub>	675	712	0.08	0.62(0.42%)1.73 (0.58%)	46300	0.58	
PTS- PBLG <sub>49</sub>	671	707	0.06	0.41(0.65%)1.26 (0.35%)	40200	0.62	
PBLG <sub>53</sub> - PTS- <i>b</i> - PEG <sub>45</sub>	677	712	0.11	0.65(0.43%) 2.01(0.57%)	23700	0.5	0.53
PBLG <sub>53</sub> - PTS- <i>b</i> - PEG <sub>113</sub>	677	712	0.08	0.67(0.45%)2.03 (0.55%)	30300	0.45	0.39
PTS- PBLG <sub>49</sub> - <i>b</i> - PEG <sub>45</sub>	672	707	0.06	0.49(0.40%) 1.6(0.60%)	23900	0.6	0.30
PTS- PBLG <sub>49</sub> - <i>b</i> - PEG <sub>113</sub>	672	707	0.05	0.48(0.37%)1.55 (0.63%)	26500	0.62	0.56

$\lambda_{\text{abs}}$  absorption maxima,  $\lambda_{\text{em}}$  emission maxima,  $\tau$  fluorescence lifetime,  $\varepsilon$  extinction coefficient,  $\Phi$  is quantum yield of F- fluorescence, T- triplet state and  $\Delta$ -singlet oxygen



Red emitting fluorophores have an important role in biology and medicine owing to the reduced autofluorescence signals from complex tissues in this wavelength range. They provide an easy way for *in vivo* fluorescence imaging and histological studies at cellular level.

In our study we developed NIR emitting asymmetric Aza-BODIPY dyes and introduced bromine groups on 2, 6 positions to enhance the singlet oxygen generation which is the main parameter of interest for efficient PDT. An optical characterization at each step of chemical modification of aza-BODIPY shows narrow absorption and emission spectra (Figure A4.1). The core modification leads to a decrease of fluorescence quantum yield and extinction coefficient as expected (Figure 4.11). On the other hand, this process increases the yield of triplet state that interferes with the sensitization of molecular oxygen (see Table 4.6).

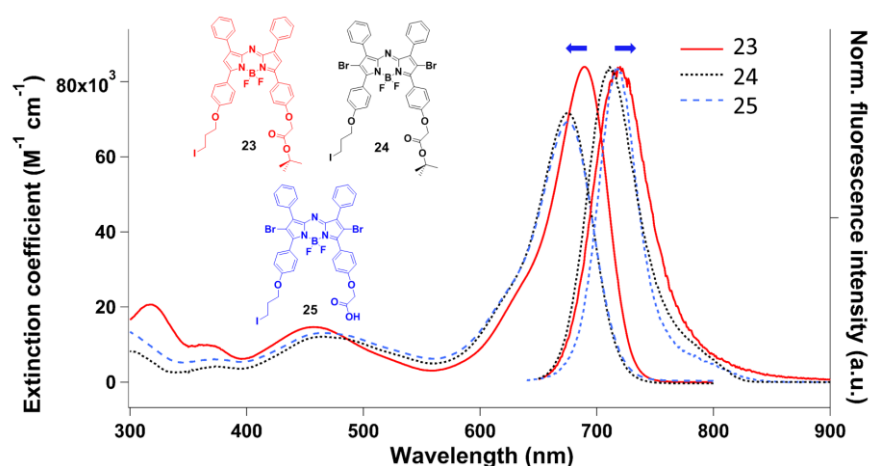


**Figure 4.11:** Overlaid UV–Vis spectra and fluorescence spectra of aza-BODIPY before and after bromination and after deprotection of carboxylic group ( $\lambda_{\text{ex}} = 630 \text{ nm}$  in THF)

The photon absorption and emission maxima of aza-BODIPYs before and after bromination, and after deprotection of the carboxylic group show small shifting due to the chemical modification and solvatochromic nature in the two solvents (Table 4.7).

Extinction coefficients of PTS decrease show the same trend (Figure 4.12) in both types of block copolymer after the addition of PBLG and PEG chains. However, it should be taken in consideration that the molar mass of the polymers, which is involved in the calculation of the extinction coefficient, is less precisely determined compared to free Aza-BODIPYs, what could play important role in extinction coefficient determination error.

**Table 4.7:** Absorption maxima and fluorescence wavelengths of non-brominated, brominated and deprotected aza-BODIPYs.

compounds	$\lambda_{\text{abs}}$ (nm)		$\lambda_{\text{em}}$ (nm)	
	THF	DCM	THF	DCM
<b>23</b>	689	683	719	715
<b>24</b>	675	674	712	720
<b>25</b>	676	670	718	709

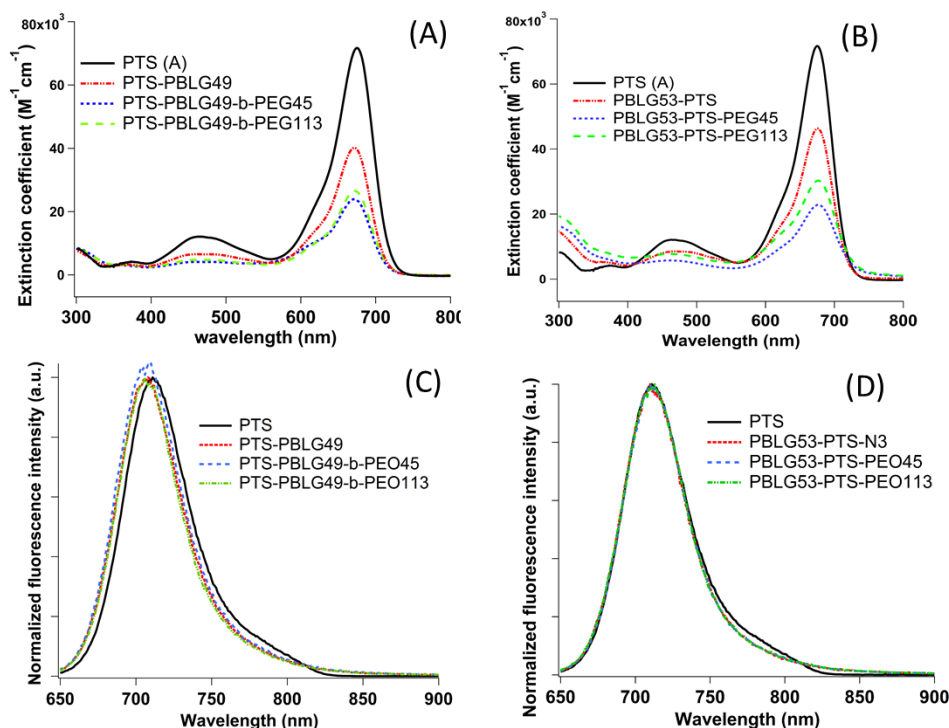


**Figure 4.12:** Overlaid absorption of (A) PTS, PTS-PBLG49 and PTS-PBLG-*b*-PEG type block copolymers (B) PTS, PBLG53-PTS-N3 and PBLG-PTS-PEG type block copolymers; fluorescence of (C) PTS, PTS-PBLG49 and PTS-PBLG-*b*-PEG type block copolymers (D) PTS, PBLG53-PTS-N3 and PBLG-PTS-*b*-PEG type block copolymers ( $\lambda_{\text{ex}} = 630 \text{ nm}$  in THF)

The fluorescence emission spectra show that the conjugation of polymer chains to the side groups of Aza-BODIPY does not cause distinguishable changes in the emission maxima of PTS in PBLG-PTS-PEO type block copolymers. However, a small blue shift of 5 nm was observed in chain-end functionalized PTS-PBLG-*b*-PEG type block copolymer spectra. This small difference can be due to the presence of iodine group on the side chain of the Aza-BODIPY in PTS-PBLG-*b*-PEG type block copolymers or mobility difference in the solvent.

#### 4.2.2 Fluorescence quantum yield calculations

The fluorescence quantum yields (QY) of the aza-BODIPY dyes, before and after bromination, and after deprotection of the carboxylic group were measured in THF by the comparative method. One of the early reported non-brominated aza-BODIPY derivative (**1**, BF<sub>2</sub> chelate of [5-(4-methoxyphenyl)-3-phenyl-1H-pyrrol-2-yl]-[5-(4-methoxyphenyl)-3-phenylpyrrol-2-ylidene]amine,  $\Phi_{\text{F}} = 0.35$  in THF)<sup>34</sup> was used as a reference compound. Expectedly, we observed the decline in fluorescence QY of brominated aza-BODIPY, due to the higher ISC yield. To investigate the polymer conjugation and localization effects, the fluorescence QYs of the PTS, PTS-PBLG conjugates, PTS-PBLG-*b*-PEG and PBLG-PTS-*b*-PEG were also measured. We found out that the modification caused only ~3-5% difference in THF (Table 4.6).

The fluorescence QYs of micelles was calculated by using an integrating sphere. We observed fluorescence quenching after self-assembly of PTS bearing block copolymers in water, probably due to the  $\pi$ - $\pi$  stacking of the PTS molecules. In order to reduce interaction of aza-BODIPYs inside the nano-assemblies we mixed PTS-bearing block copolymers, in 3 different ratios (Table 4.6 and 4.8), with non-PTS functionalized block copolymers of the same

composition. It was observed that as PTS bearing polymer content decreases the fluorescence QY and lifetime increase due to the dilution effect. However, increasing of the non-PTS functionalized polymer content to more than 50% in the nano-assemblies causes a polydispersity problem of the nano-assemblies as mentioned in Chapter 3.

#### 4.2.3 Time-resolved emission and transient absorption measurements

The fluorescence lifetime measurements were performed in THF (Table 4.6) and water (nano-assemblies) on a sub-nanosecond set-up equipped with time resolved luminescence spectrophotometer (Table.4.8). The results show a decline in decay time after bromination of the aza-BODIPY from 0.36 ns to 0.08 ns. The aza-BODIPY molecules show mono-exponential luminescence decay in the free state in THF as depicted in Figure 4.13 and bi-exponential fluorescence decay in PBLG-PTS-*b*-PEG and PTS-PBLG-*b*-PEG type block copolymers (Figure A4. 3).

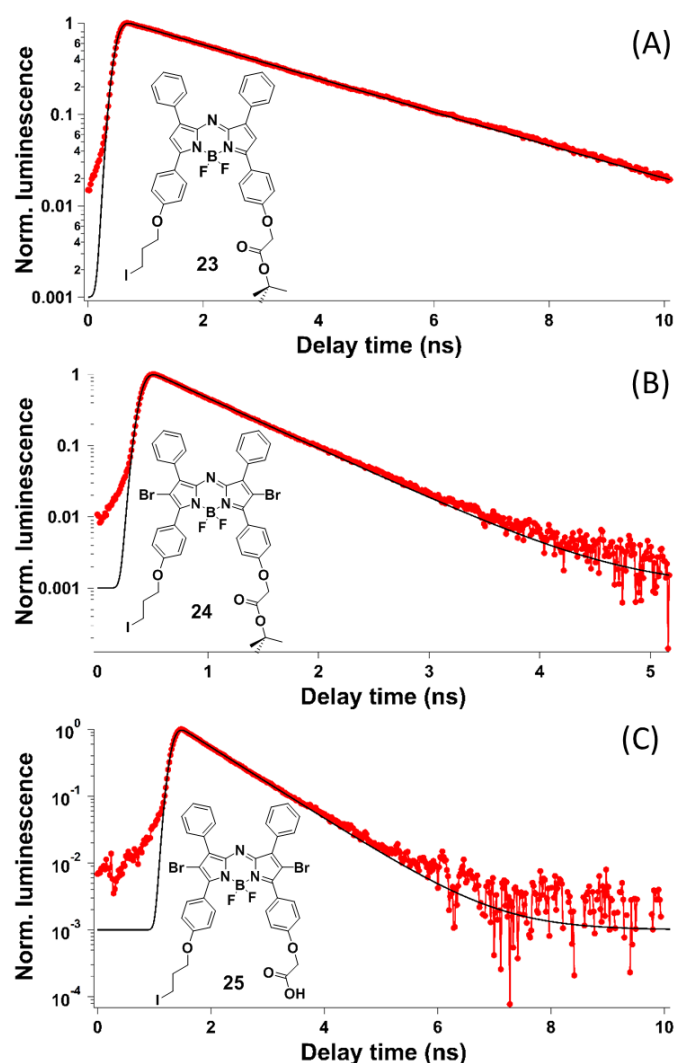


**Figure 4.13:** Time resolved emission decay of aza-BODIPY (A) **23** (C) **24** and (C) **25** in THF ( $\lambda_{exc} = 630 \text{ nm}$ ,  $\lambda_{ob} = 700 \text{ nm}$ )

The time-resolved transient absorption (TRABS) measurements were performed on diluted and degassed solutions (by freeze-thaw-freeze cycles) of PTS, PTS-PBLG conjugates and PTS-PBLG-*b*-PEG/ PBLG-PTS-*b*-PEG type block copolymers in distilled THF. As a result of

TRABS measurement we calculated the triplet state quantum yield of free PTS and its conjugates between 57-62% (Table 4.6).

#### 4.2.4 Singlet oxygen generation

The singlet oxygen generation QYs were calculated *via* two relative methods by using an optically matched dye solution and methylene blue (MB) as standard. In the first method  $^1\text{O}_2$  generation QYs were calculated from direct detection of the  $^1\text{O}_2$  luminescence at 1270 nm in DCM as depicted in Figure 4.14. By using integrated  $^1\text{O}_2$  luminescence intensity and a reference compound ( $\Phi_{\Delta}=0.57$  in DCM)<sup>58</sup>  $\Phi_{\Delta}$  was calculated by applying equation 4.10.

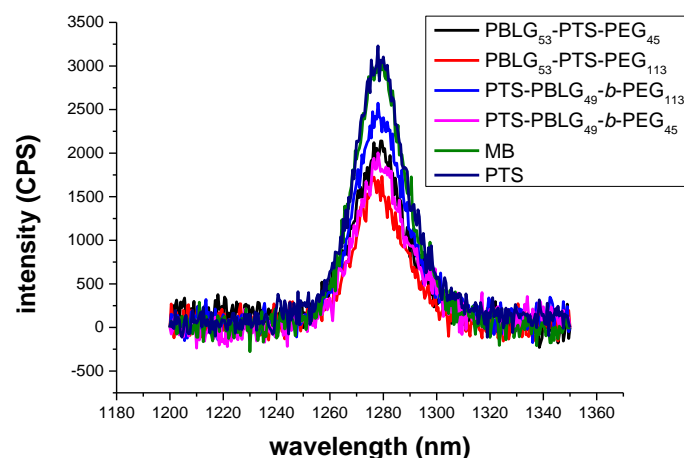


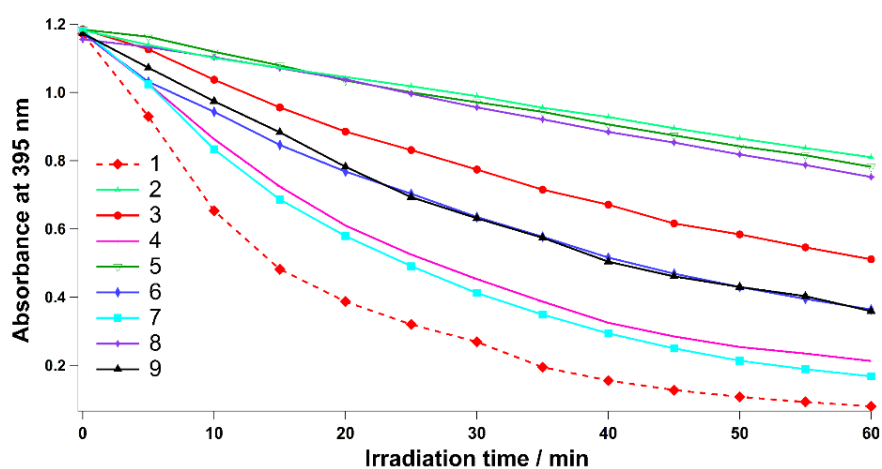
**Figure 4.14:** Luminescence of the  $^1\text{O}_2$  generated by PTS (**24**) functionalized block copolymers, PTS and MB in DCM (dilute solutions, OD 0.1,  $\lambda_{\text{ex}}$  630 nm)

Due to the shorter lifetime of singlet oxygen in water it is hard to detect the luminescence of the  $^1\Delta_g \rightarrow ^3\Sigma_g^-$  transition. The attempt to perform measurements in  $\text{D}_2\text{O}$  also failed due to the instability of nano-assemblies in deuterated water. Owing to these limitations, the singlet oxygen production yield of PTS bearing nano-assemblies was calculated by the chemical trapping method. The relative yield of  $^1\text{O}_2$  generation was quantified by monitoring the photoperoxidation of the anthracene 9,10-divinylsulfonate (**AVS**) sensitized by PTS bearing nano-assemblies over 1h. Optically matched solution of methylene blue (**MB**,  $1.7 \times 10^{-6}$  M) was used as a standard ( $\Phi_{\Delta}=0.52$  in water) and the QYs of singlet oxygen generation were calculated by equation 4.11. To perform photoactivation, we used a 660 nm LED array (power density  $1.33 \text{ mW/cm}^2$ ) as a light source to mimic the clinical therapeutic settings.

In this study we designed micelles and vesicles where the PTS is localized on the surface or inside the PBLG core or membrane to evaluate the dilution, localization and morphological effects on singlet oxygen generation yield of PTS in the nano-assemblies. To study the dilution effect we prepared micellar nano-assemblies (NABs) from the block copolymers PTS-PBLG<sub>49</sub>-*b*-PEG<sub>113</sub> and PBLG<sub>53</sub>-PTS-*b*-PEG<sub>113</sub>, and their co-assembled micelles with PBLG<sub>54</sub>-*b*-PEG<sub>113</sub> in 80 and 50% weight ratio (Figure A4.5 and 4.15). Comparison of photoperoxidation rates of the same amount of PTS ( $2 \times 10^{-5}$  M) in the pure NABs and co-assembled NABs with MB showed that the relative rate of singlet oxygen production is increasing as dilution of PTS is increasing (Figure 4.14). The maximum  $^1\text{O}_2$  production yield was observed in 1:1 ratio mixed NABs where it increases 3-4 times compared to pure PTS functionalized NABs. However, in terms of PTS localization we did not observe significant difference between both types of functionalized copolymers (see Table 4.8). This study shows that we are able to enhance the

photochemical reactivity of PTS in the nano-assemblies by adjusting its concentration in the particles.

After optimization of the best conditions for PDT with the micelles, we calculated the  $^1\text{O}_2$  generation QY of the vesicles in the same conditions. The vesicles were prepared by co-assembling PTS-PBLG<sub>49</sub>-*b*-PEG<sub>45</sub> and PBLG<sub>53</sub>-PTS-*b*-PEG<sub>45</sub> block copolymers with PBLG<sub>54</sub>-*b*-PEG<sub>45</sub> in 1:1 weight ratio. As can be clearly seen from Figures 4.15 and 4.16 the rate and QY of  $^1\text{O}_2$  generation of vesicles are lower compared to micelles. Moreover, a  $^1\text{O}_2$  generation QY three times higher was observed for the vesicles prepared from PTS-PBLG<sub>49</sub>-*b*-PEG<sub>45</sub> where the PTS is localized inside of the thin membrane of the vesicles. The lower photoactivity in vesicles with PTS localized on the surface of the membrane could be explained by increased interactions of PTS with water (see Table 4.9). Even though, PTS in nano-assemblies exhibit lower  $^1\text{O}_2$  yield compared to MB, they show higher photostability during 1h LED irradiation (see Figure 4.15). This parameter is very important in a context of a clinical use of PDT in order to maintain an active PTS on the tumor for a long period of time.

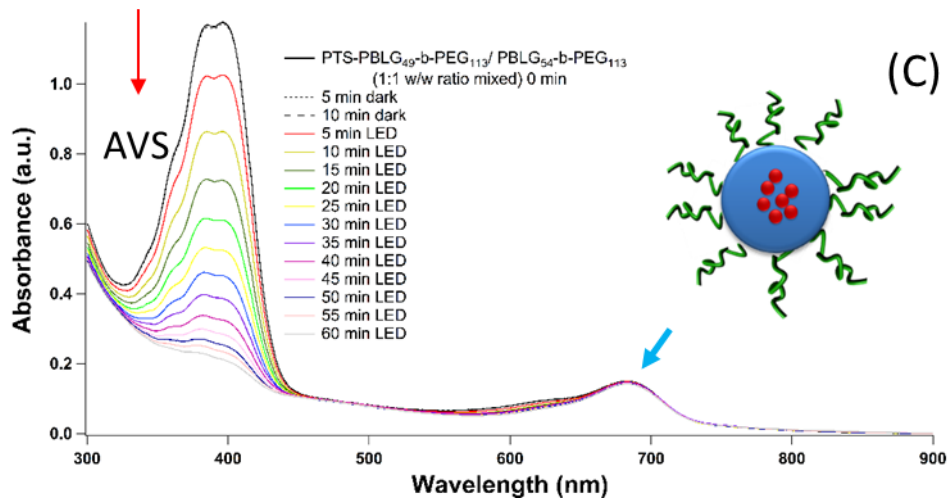
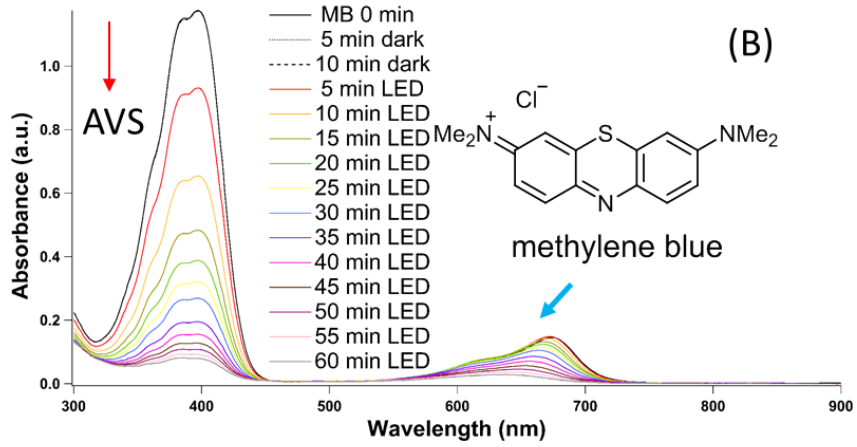
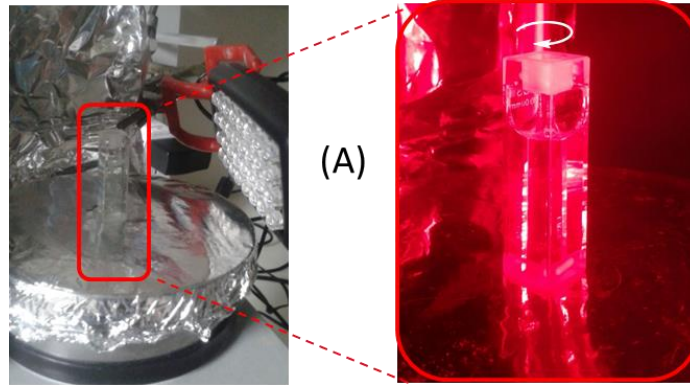


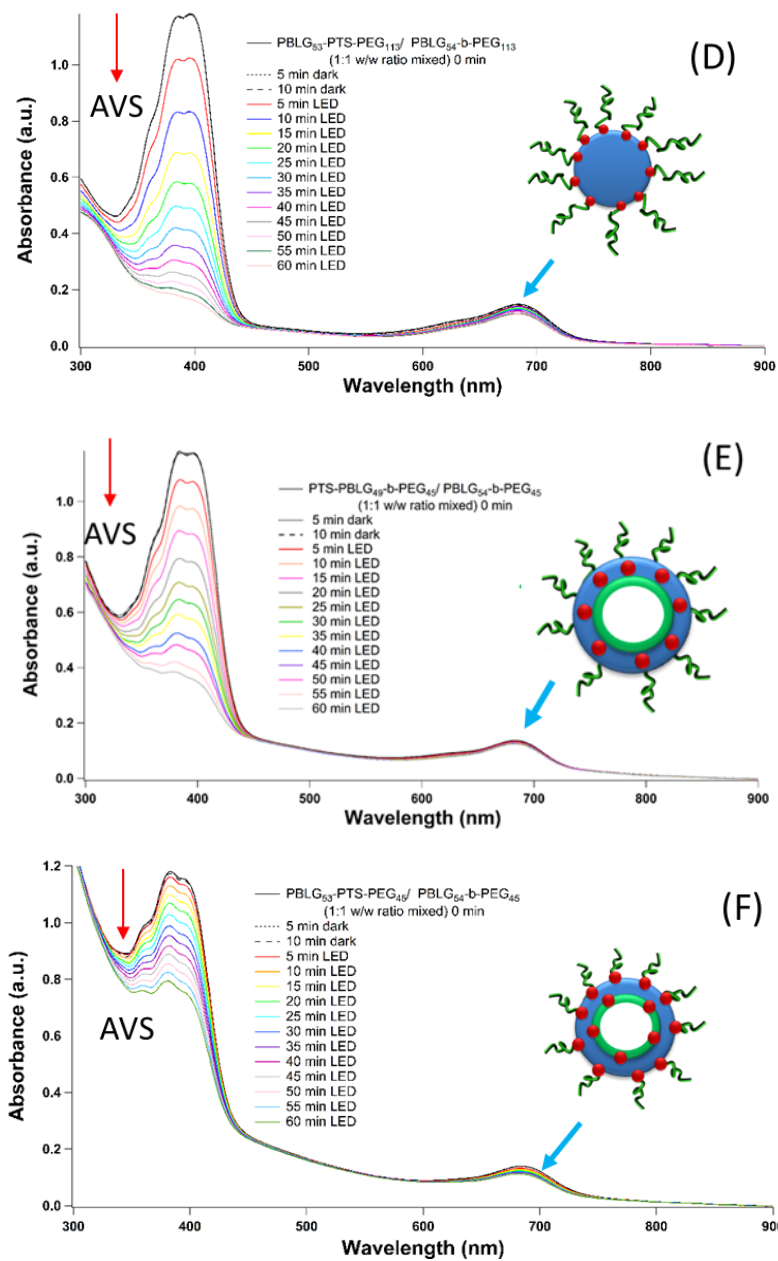
Compounds	1	2	3	4	5	6	7	8	9
	MB	100%	80%	50%	100%	80%	50%	50%	50%
Relative rate	1	0.15	0.37	0.71	0.17	0.48	0.75	0.51	0.15

% indicates the weight percent of PTS functionalized block copolymer in the nano-assemblies

**Figure 4.15:** Absorption of  $6.5 \times 10^{-5}$  M AVS at 395 nm as a function of irradiation time in the presence of: 1) Methylene Blue ( $1.8 \times 10^{-6}$  M) 2) PTS-PBLG<sub>49</sub>-*b*-PEG<sub>113</sub> 3) PTS-PBLG<sub>49</sub>-*b*-PEG<sub>113</sub> 80% weight ratio 4) PTS-PBLG<sub>49</sub>-*b*-PEG<sub>113</sub> 50% weight ratio 5) PBLG<sub>53</sub>-PTS-*b*-PEG<sub>113</sub> 6) PBLG<sub>53</sub>-PTS-*b*-PEG<sub>113</sub> PEG<sub>113</sub> 80% weight ratio 7) PBLG<sub>53</sub>-PTS-PEG<sub>113</sub> 50% weight ratio 8) PTS-PBLG<sub>49</sub>-*b*-PEG<sub>45</sub> 50% weight ratio 9) PBLG<sub>53</sub>-PTS-*b*-PEG<sub>45</sub> 50% weight ratio nano-assemblies in Milli-Q water over time period of 60 min LED exposure ( $\lambda_{\text{exc}} = 660$  nm LED array, PTS concentration in the nano-assemblies is approximately  $2 \times 10^{-5}$  M)

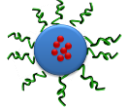
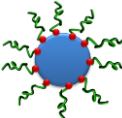
As a result of this study, we obtained PTS-conjugated micelles with 2 times higher  $^1\text{O}_2$  generation QYs compared to conventional clinically used photosensitizer Photofrin<sup>®</sup> (0.25 in D<sub>2</sub>O, lower in H<sub>2</sub>O). Moreover, these nano-assemblies have the advantage of having a large size, which is important for targeting (EPR effect), should have longer circulation lifetime in the blood (PEG shell), PTS protection inside polymer matrix, and no PTS leaking concern.





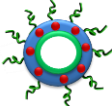
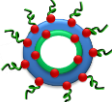
**Figure 4.16:** Overlay of UV-Visible spectra of an irradiated solution of AVS in the presence of (A) Methylene Blue (B) picture of the experimental setup ; and 1:1 weight ratio mixed nano-assemblies of (C) PTS-PBLG<sub>49</sub>-b-PEG<sub>113</sub> micelles (D) PBLG<sub>53</sub>-PTS-b-PEG<sub>113</sub> micelle (E) PTS-PBLG<sub>49</sub>-b-PEG<sub>113</sub> vesicles (F) PBLG<sub>53</sub>-PTS-b-PEG<sub>113</sub> vesicles

**Table 4.8:** Overall results of  $^1\text{O}_2$  generation QYs, fluorescence QYs and fluorescence lifetimes of micelles

Micelles	% <sup>a</sup>	$\Phi_{\Delta}$	$\Phi_F$	$\tau$ (ns)	$\lambda_{\text{abs}}$ (nm)	$\lambda_{\text{em}}$ (nm)
PTS-PBLG <sub>49</sub> - <i>b</i> - PEG <sub>113</sub> 	100	0.08	0.030	0.18/ 0.80	684	718
	80	0.21	0.034	0.25/1.10		
	50	0.38	0.046	0.30/1.40		
	20		0.060	0.60/2.20		
PBLG <sub>53</sub> -PTS- <i>b</i> - PEG <sub>113</sub> 	100	0.12	0.002	0.14/0.62	684	715
	80	0.25	0.005	0.18/0.86		
	50	0.41	0.021	0.20/1.40		
	20		0.036	0.43/2.20		

*a* the weight per cent of functionalized copolymer used in co-assembly with PBLG<sub>54</sub>-*b*-PEG<sub>113</sub>

**Table 4.9:** Overall results of  $^1\text{O}_2$  generation QYs, fluorescence QYs and optical properties of the vesicles

Vesicles	% <sup>a</sup>	$\Phi_{\Delta}$	$\lambda_{\text{abs}}$ (nm)	$\lambda_{\text{em}}$ (nm)
PTS-PBLG <sub>49</sub> - <i>b</i> - PEG <sub>45</sub> 	50	0.29	682	718
PBLG <sub>53</sub> -PTS- <i>b</i> - PEG <sub>45</sub> 	50	0.08	682	715

*a* the weight per cent used of functionalized copolymer in co-assembly with PBLG<sub>54</sub>-*b*-PEG<sub>45</sub>

### 4.3 Conclusion

Through this chapter, the characterization of the optical and photophysical properties (molar extinction coefficient, fluorescence quantum yield, efficiency of singlet oxygen generation, fluorescence lifetime...) of free photosensitizer (before and after bromination and deprotection) and after its conjugation to the PBLG has been described. The effects of the PTS localization in the PTS-PBLG-*b*-PEG and PBLG-PTS-*b*-PEG type block copolymers on its properties have been also analyzed, and no big difference was observed in THF. However, after self-assembly in water, the PTS showed changes in its characteristics due to the localization, morphology and concentration effects. It has been observed that dilution of the PTS in the nano-assemblies, by co-assembling the functionalized copolymers with non-functionalized ones, increased the activity of PTS due to the decrease in the stacking of the aza-BODIPY dyes.



## 4.4 Experimental

### Materials

The reference reagent, 3,7-bis(dimethylamino)-5-phenothiazinium chloride hydrate (Methylene blue, Sigma-Aldrich, 82%) has been used without further purification. Dichloromethane (DCM, Sigma-Aldrich, HPLC grade, 99.9%) has been used without further purification and tetrahydrofuran (THF, Fluka, 99.8%) was used after distillation over CaH<sub>2</sub>. The singlet oxygen trap, 9,10-bis-(vinylsulfonate)anthracene (AVS) and reference aza-BODIPY **30** were synthesized at the Institut des Sciences Moléculaires (ISM), University of Bordeaux.

**Fluorescence spectroscopy:** fluorescence and phosphorescence emission spectra of optically diluted solutions were recorded on a Horiba Jobin-Yvon Fluorolog-3 spectrofluorimeter with TCSPC capability. It is equipped with photomultiplier from Hamamatsu Photonics R2658 (185-1100nm range) and R928 (185-1100nm range), iHR-320 spectrograph (150-1500 nm range, 1200 gr/mm grating, blazed at 500nm) and NIR detector H10330-45. For basic fluorescence measurements a Fluorimeter Varian Cary Eclipse was used.

**LED Array:** High Power 660 nm Red 32 LED Array (power density 1.33 mW/cm<sup>2</sup>) was purchased from ELIXA (<http://www.elixa.com/>).

**Transient absorption/ time-resolved fluorescence:** Sub-nanosecond set-up (Figure 5.17) was built at the Institut des Sciences Moléculaires (ISM), University of Bordeaux as follows. A frequency tripled Nd:YAG amplified laser system (30 ps, 30 mJ @1064 nm, 20 Hz, Ekspla model PL 2143) output was used to pump an optical parametric generator (Ekspla model PG 401) producing tunable excitation pulses in the range 410-2300 nm. The white light pulse for sample probing was produced by focusing the residual fundamental laser radiation to high pressure Xe filled breakdown cell. All light signals were analysed by a spectrograph (Princeton Instruments Acton model SP2300) coupled with a high dynamic range streak camera (Hamamatsu C7700). Accumulated sequences (sample emission, probe without and with excitation) of pulses were recorded and treated by HPDTA (Hamamatsu) software to produce two-dimensional maps (wavelength vs delay) of transient absorption intensity in the range 300-800 nm. The typical measurement error is 10<sup>-3</sup> OD.<sup>59,60</sup> The schematic illustration of the set-up is shown below.

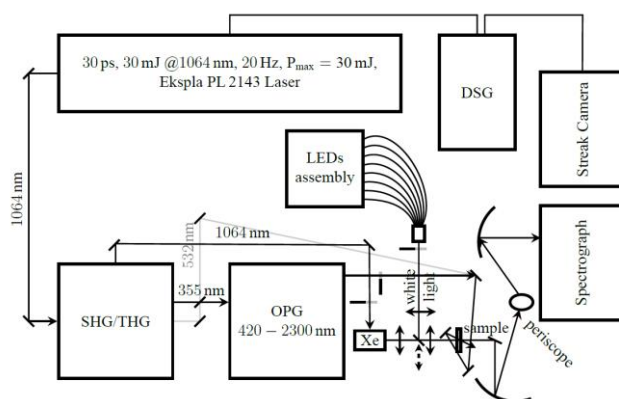


**Figure 4.17:** Sub-nanosecond laser set-up; DSG – digital signal generator, SHG/THG – second/third harmonic generator, LED – light emitting diode and OPG – optical parametric generator<sup>60</sup>

## TRABS and luminescence lifetime measurements

The transient absorbance (TRABS) measurements were performed with a sub-nanosecond set-up on degassed samples. The samples were dissolved in distilled THF and the absorption band of the samples at excitation wavelength adjusted to 1 O.D. and excited with a 620 nm laser pulse. Then, the solutions were transferred to blowtorch sealed quartz cells and degassed by multiple freeze-pump-thaw cycles before the measurements.

Fluorescence lifetimes were determined by time-resolved fluorescence spectroscopy equipped sub-nanosecond set-up, by exciting the samples at 600 nm (PYI) and 405 nm (NCS) with a diode and a laser, respectively. The experimental errors are  $\pm 1$  nm for the wavelengths. All measurements have been performed in very dilute solutions of the samples in distilled THF and in micelle solutions in Milli-Q water. The data analysis was done by LabVIEW program.

## Fluorescence quantum yield measurements

The relative fluorescence quantum yields ( $\Phi_F$ ) were determined by the optically dilute method using aza-BODIPY (BF2 chelate of [5-(4-Methoxyphenyl)-3-phenyl-1H-pyrrol-2-yl]-[5-(4-methoxyphenyl)-3-phenylpyrrol-2-ylidene] amine,  $\Phi_F=0.35$  in THF)<sup>34</sup> in THF as standard. The absorptions of the standard and the samples were adjusted to less than 0.1 O.D. at excitation wavelength and  $\Phi_F$  calculated from equation 4.5. The measurements have been performed with a Horiba Jobin-Yvon Fluorolog-3.

The absolute fluorescence quantum yields ( $\Phi_F$ ) of the self-assemblies in Milli-Q water have been determined by using an integrating sphere (diameter of 100 mm), which provides a reflectance >99% over 400-1500 nm range (>95% within 250-2500 nm). The concentrated micelle solutions (2 mg/mL) were prepared and fluorescence signals were detected IN and OUT of the beam in the cylindrical quartz cuvette (8mm diameter) which is mounted on a Teflon support inside the sphere. The measurement was performed with and without the sample (rotating the holder by 180°), and to reduce the error an average of 15 measurements have been taken and final  $\Phi_F$  calculated from equations 4.6 and 4.7. The measurements have been performed with a Horiba Jobin-Yvon Fluorolog-3 equipped with a Labsphere optical Spectralon.

## The singlet oxygen generation measurement in DCM

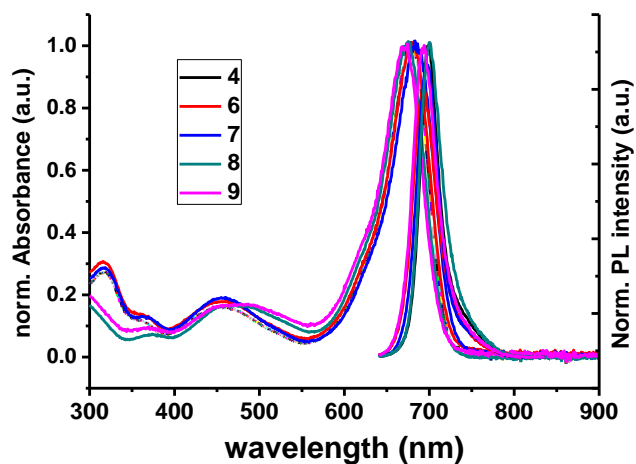
The singlet oxygen luminescence spectra were recorded in air saturated DCM solutions with 630 nm excitation wavelength with an Innolas MOPA-1 variable repetition rate (1–5000 Hz) Nd:YAG laser. The measurements were performed on a Horiba Jobin-Yvon Fluorolog-3 equipped with a Hamamatsu H10330–45 NIR detector configured with a Fastcom P7889 100 ps multistop TDC acquisition card operating at 10 GHz.

As a reference, an optically matched solution of methylene blue (MB) was used ( $\Phi_\Delta=0.57$  in DCM).<sup>58,61</sup> The optical density of the reference MB and the samples at excitation wavelength were adjusted to 0.1 in DCM and excited with 630 nm light. The relative singlet oxygen generation quantum yields were calculated from equation 4.10. Measurements were performed under open air conditions.

### **The singlet oxygen generation measurement of nanoparticles in water**

The quantum yields of singlet oxygen production ( $\Phi_{\Delta}$ ) of PTS bearing self-assemblies (micelles and vesicles) in water were calculated according to the literature.<sup>62</sup> An optically matched photosensitizer, methylene blue was selected as a reference sensitizer with known  $\Phi_{\Delta}$  (0.52) in water.<sup>33</sup> The absorption of PTS in the nanoparticles was adjusted to 0.1 ( $2 \times 10^{-5}$  M) and the absorption of trapping molecule, AVS was adjusted to 1.2 ( $6.5 \times 10^{-5}$  M) in the nanoparticles solution in 1cm quartz cuvette. The absorption spectra were taken in dark over 10min and after each 5min excitation time with 660 nm LED over a time period of 1h. Photodegradation rate of the AVS at 395 nm was subtracted from the spectrum and  $\Phi_{\Delta}$  were calculated from equation 4.11, respectively. All measurements have been performed under the open air conditions.

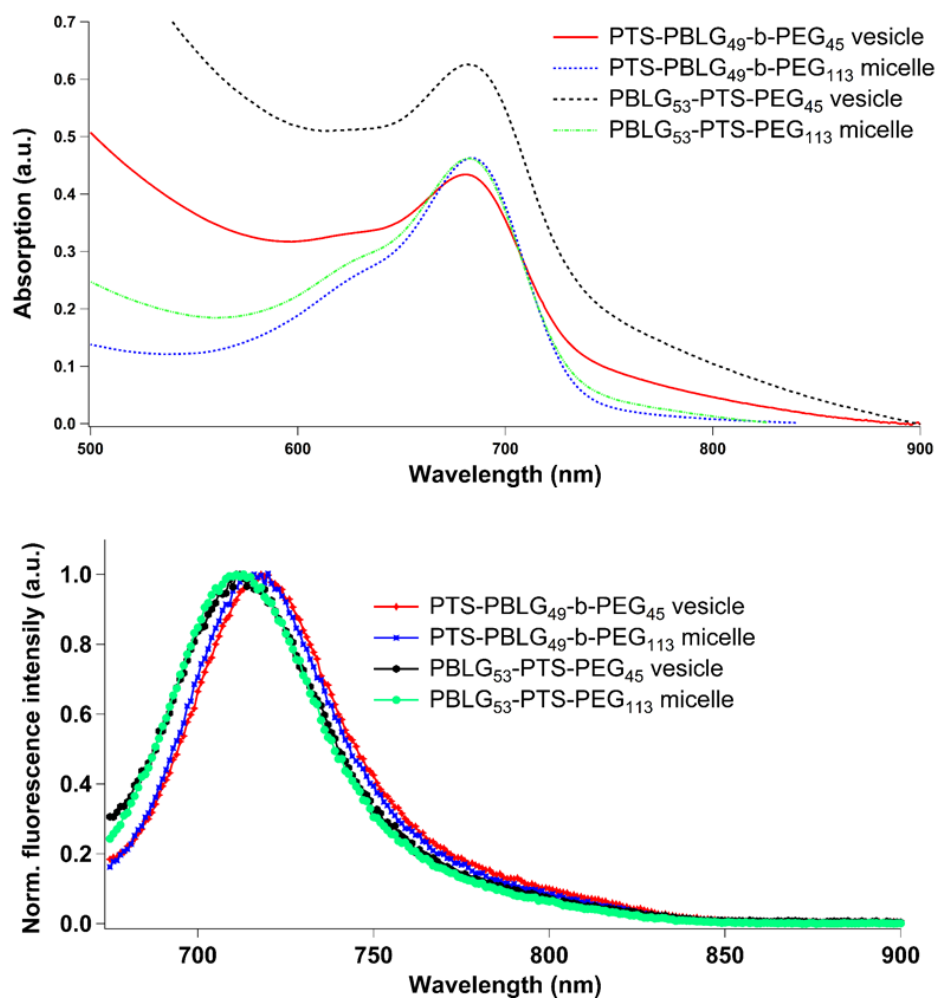
## Appendix 4: CHARACTERIZATION DATA FOR CHAPTER 4



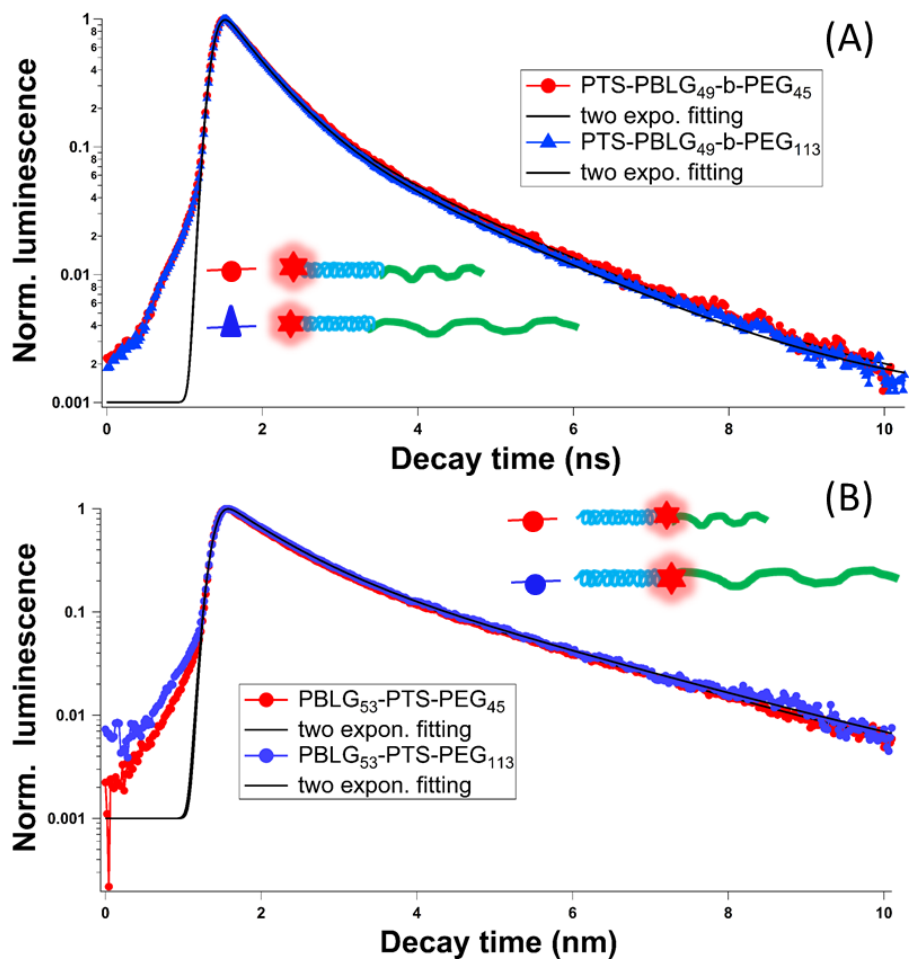
**Figure A4.1:** Overlaid UV-vis spectra and fluorescence spectra of intermediate and the main products **20** (4), **22** (6), **23** (7), **24** (8) and **25** (9) in DCM ( $\lambda_{\text{exc}} = 630$  nm)

**Table A4.1:** Absorption ( $\lambda_{\text{abs}}$ ) and emission ( $\lambda_{\text{em}}$ ) maxima of the intermediate and targeted aza-BODIPYs in DCM ( $\lambda_{\text{exc}} = 630$  nm)

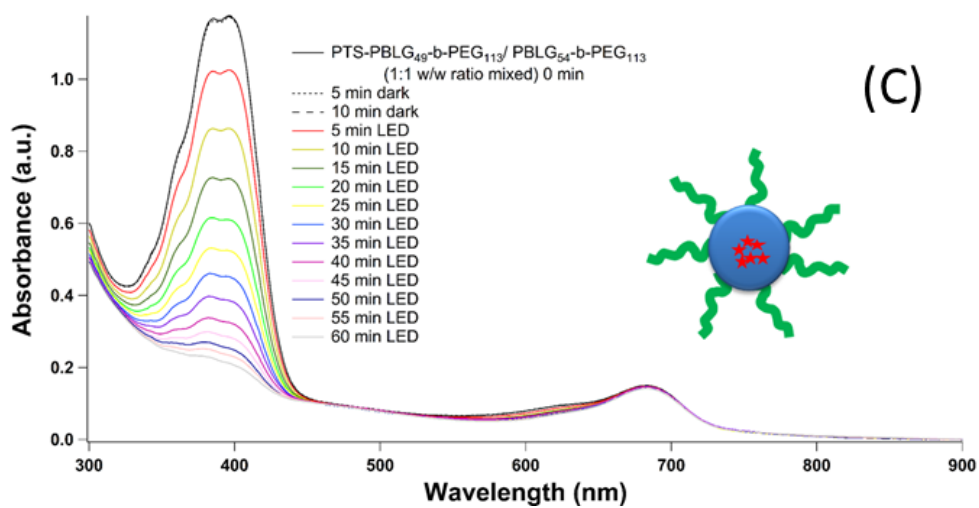
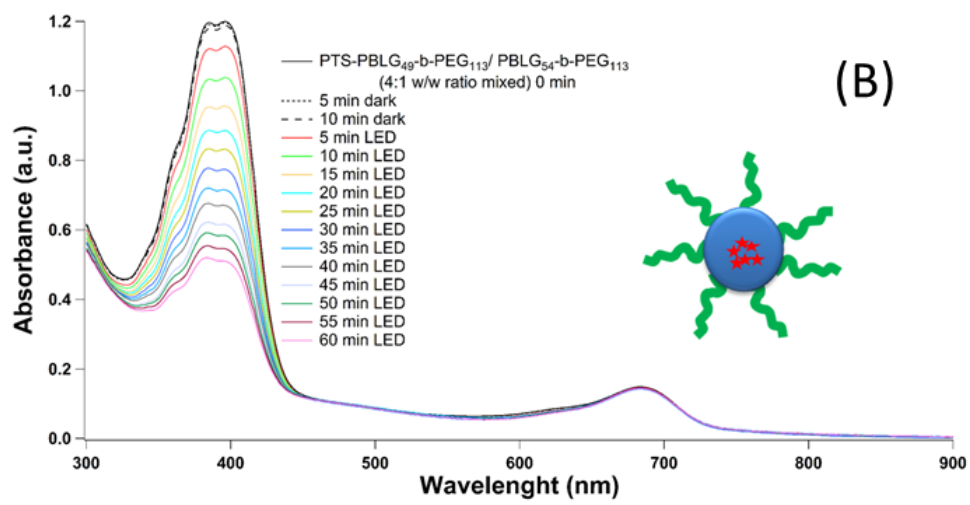
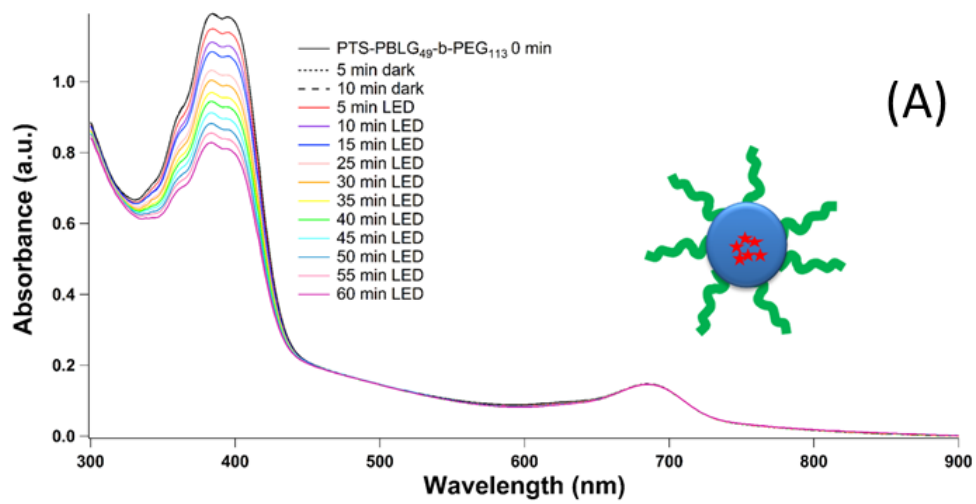
numbers	aza-BODIPYs	$\lambda_{\text{abs}}$ [nm]	$\lambda_{\text{em}}$ [nm]
4	<b>20</b>	678	717
6	<b>22</b>	678	721
7	<b>23</b>	683	715
8	<b>24</b>	674	720
9	<b>25</b>	670	709
10	<b>26</b>	674	715



**Figure A4.2:** Overlaid UV-vis spectra and fluorescence spectra of micelles and vesicles in water ( $\lambda_{exc}= 650$  nm)



**Figure A4.3:** Overlay time resolved emission decays of PTS-PBLG-*b*-PEG and PBLG-PTS-*b*-PEG type block copolymers in THF ( $\lambda_{exc} = 630$  nm,  $\lambda_{ob} = 700$  nm)



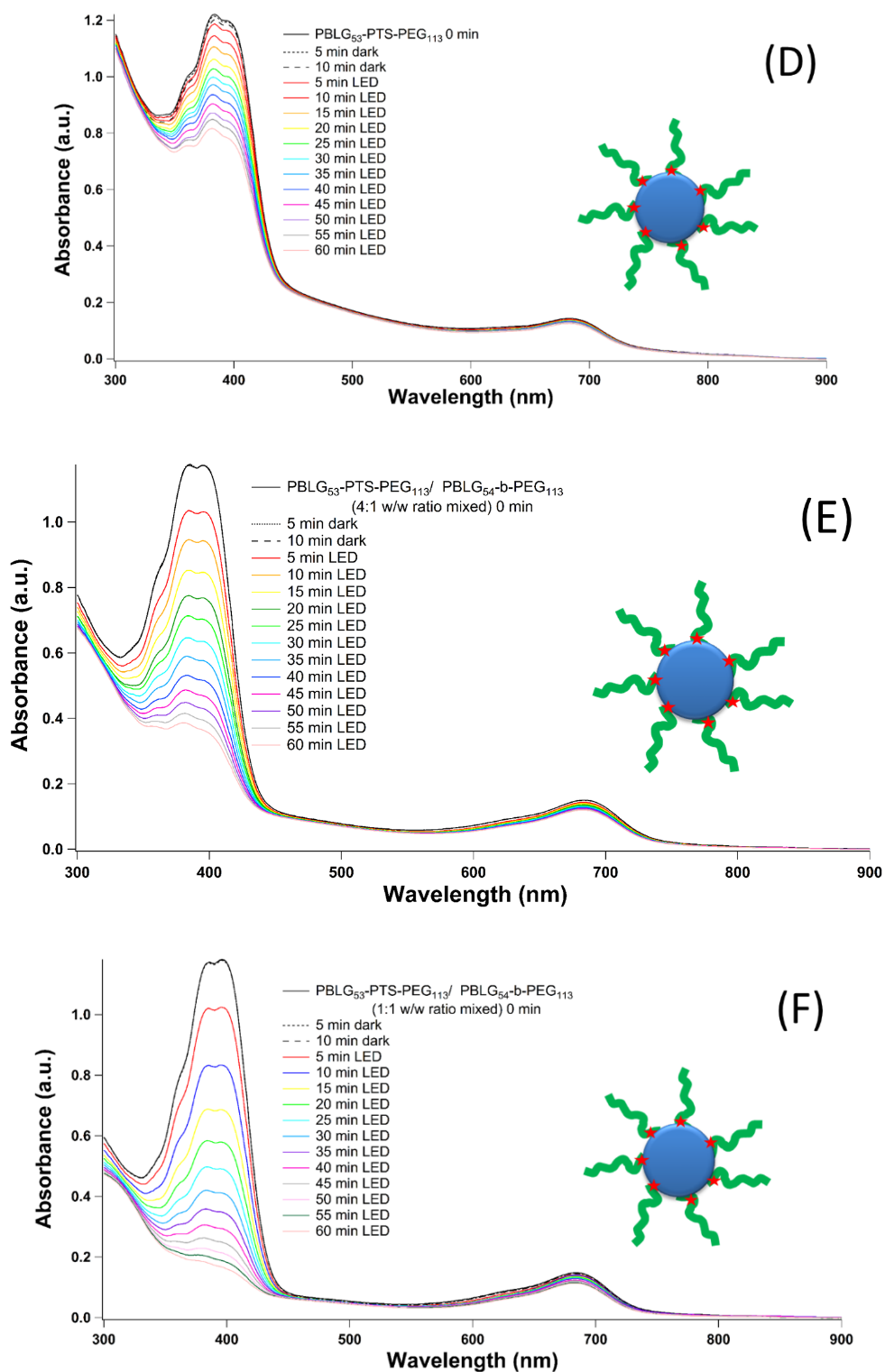


**Figure A4.4:** Overlaid UV-vis spectra of AVS peroxidation in the presence of micelles (A) PTS-PBLG<sub>49</sub>-b-PEG<sub>113</sub> (B) PTS-PBLG<sub>49</sub>-b-PEG<sub>113</sub> / PBLG<sub>54</sub>-b-PEG<sub>113</sub> in 4:1 weight ratio mixed (C) PTS-PBLG<sub>49</sub>-b-PEG<sub>113</sub> / PBLG<sub>54</sub>-b-PEG<sub>113</sub> in 1:1 weight ratio mixed (D) PBLG<sub>53</sub>-PTS-b-PEG<sub>113</sub> (E) PBLG<sub>53</sub>-PTS-b-PEG<sub>113</sub> PEG<sub>113</sub> / PBLG<sub>54</sub>-b-PEG<sub>113</sub> in 4:1 weight ratio mixed (F) PBLG<sub>53</sub>-PTS-b-PEG<sub>113</sub> PEG<sub>113</sub> / PBLG<sub>54</sub>-b-PEG<sub>113</sub> in 1:1 weight ratio mixed in Milli-Q water during 60 min LED exposure ( $\lambda_{exc} = 660$  nm LED array)



## References

- (1) Suppan, P. In *Chemistry and Light*; Suppan, P., Ed.; The Royal Society of Chemistry: 1994, p 11.
- (2) McGlynn, S. P.; Azumi, T.; Kinoshita, M. *Molecular spectroscopy of the triplet state*; Prentice-Hall: Englewood Cliffs, N.J., 1969.
- (3) Workman Jr, J. In *Applied Spectroscopy*; Academic Press: San Diego, 1998, p 3.
- (4) Lakowicz, J. R. *Principles of fluorescence spectroscopy*; Third edition ed.; Springer US: USA, 2006.
- (5) Vo-Dinh, T.; Wiley: New York :, 1984.
- (6) Porrès, L.; Holland, A.; Pålsson, L.-O.; Monkman, A. P.; Kemp, C.; Beeby, A. *Journal of Fluorescence* **2006**, *16*, 267.
- (7) Ishida, H.; Tobita, S.; Hasegawa, Y.; Katoh, R.; Nozaki, K. *Coordination Chemistry Reviews* **2010**, *254*, 2449.
- (8) de Mello, J. C.; Wittmann, H. F.; Friend, R. H. *Advanced Materials* **1997**, *9*, 230.
- (9) Berera, R.; Grondelle, R.; Kennis, J. T. M. *Photosynthesis Research* **2009**, *101*, 105.
- (10) Bækthøj, J. E.; Madsen, L. B. *Physical Review A* **2015**, *92*, 023407.
- (11) Maciejewski, A.; Naskrecki, R.; Lorenc, M.; Ziolk, M.; Karolczak, J.; Kubicki, J.; Matysiak, M.; Szymanski, M. *Journal of Molecular Structure* **2000**, *555*, 1.
- (12) González-Delgado, J. A.; Kennedy, P. J.; Ferreira, M.; Tomé, J. P. C.; Sarmiento, B. *Journal of Medicinal Chemistry* **2015**.
- (13) Ormond, A.; Freeman, H. *Materials* **2013**, *6*, 817.
- (14) Ding, H.; Yu, H.; Dong, Y.; Tian, R.; Huang, G.; Boothman, D. A.; Sumer, B. D.; Gao, J. *J Control Release* **2011**, *156*, 276.
- (15) Usacheva, M.; Swaminathan, S. K.; Kirtane, A. R.; Panyam, J. *Molecular Pharmaceutics* **2014**, *11*, 3186.
- (16) Weldor, D.; Poulsen, T. D.; Mikkelsen, K. V.; Ogilby, P. R. *Photochemistry and Photobiology* **1999**, *70*, 369.
- (17) Ogilby, P. R. *Chemical Society Reviews* **2010**, *39*, 3181.
- (18) Wilkinson, F.; Helman, W. P.; Ross, A. B. *Journal of Physical and Chemical Reference Data* **1993**, *22*, 113.
- (19) Adelhelm, M.; Aristov, N.; Habekost, A. *Journal of Chemical Education* **2010**, *87*, 40.
- (20) Klán, P.; Wirz, J. *Photochemistry of organic compounds: From concepts to practice*; John Wiley & Sons, 2009.
- (21) Rodgers, M. A. J.; Rossbroich, G.; Garcia, N. A.; Braslavsky, S. E.; Gorman, A. A.; Hamblett, I.; Standen, M. C.; Monici, M. In *Primary Photo-Processes in Biology and Medicine*; Bensasson, R. V., Jori, G., Land, E. J., Truscott, T. G., Eds.; Springer US: Boston, MA, 1985, p 181.
- (22) Zebger, I.; Snyder, J. W.; Andersen, L. K.; Poulsen, L.; Gao, Z.; Lambert, J. D. C.; Kristiansen, U.; Ogilby, P. R. *Photochemistry and Photobiology* **2004**, *79*, 319.
- (23) Snyder, J. W.; Skovsen, E.; Lambert, J. D. C.; Poulsen, L.; Ogilby, P. R. *Physical Chemistry Chemical Physics* **2006**, *8*, 4280.
- (24) Kuimova, M. K.; Balaz, M.; Anderson, H. L.; Ogilby, P. R. *Journal of the American Chemical Society* **2009**, *131*, 7948.
- (25) Hatz, S.; Poulsen, L.; Ogilby, P. R. *Photochemistry and Photobiology* **2008**, *84*, 1284.
- (26) Baker, A.; Kanofsky, J. R. *Photochemistry and Photobiology* **1992**, *55*, 523.

- (27) Moan, J.; Berg, K. *Photochemistry and Photobiology* **1991**, *53*, 549.
- (28) Ogilby, P. R. *Photochemistry and Photobiology* **2006**, *82*, 1133.
- (29) Colombo, A.; Dragonetti, C.; Roberto, D.; Valore, A.; Ferrante, C.; Fortunati, I.; Picone, A. L.; Todescato, F.; Williams, J. A. G. *Dalton Transactions* **2015**, *44*, 15712.
- (30) Bonacin, J. A.; Engelmann, F. b. M.; Severino, D.; Toma, H. E.; Baptista, M. S. *Journal of the Brazilian Chemical Society* **2009**, *20*, 31.
- (31) Tang, C.; Hu, P.; Ma, E.; Huang, M.; Zheng, Q. *Dyes and Pigments* **2015**, *117*, 7.
- (32) Wirotius, A.-L.; Ibarboure, E.; Scarpantonio, L.; Schappacher, M.; McClenaghan, N. D.; Deffieux, A. *Polymer Chemistry* **2013**, *4*, 1903.
- (33) Kilic, B.; Yesilgul, N.; Polat, V.; Gercek, Z.; Akkaya, E. U. *Tetrahedron Letters* **2016**, *57*, 1317.
- (34) Gorman, A.; Killoran, J.; O'Shea, C.; Kenna, T.; Gallagher, W. M.; O'Shea, D. F. *J Am Chem Soc* **2004**, *126*, 10619.
- (35) Aubry, J. M.; Rigaudy, J.; Cuong, N. K. *Photochemistry and Photobiology* **1981**, *33*, 149.
- (36) Takayama, K.; Noguchi, T.; Nakano, M.; Migita, T. *Biochemical and Biophysical Research Communications* **1977**, *75*, 1052.
- (37) Botsivali, M.; Evans, D. F. *Journal of the Chemical Society, Chemical Communications* **1979**, 1114.
- (38) Kraljić, I.; Mohsni, S. E. *Photochemistry and Photobiology* **1978**, *28*, 577.
- (39) Matheson, I. B. C.; Etheridge, R. D.; Kratoch, N. R.; Lee, J. *Photochemistry and Photobiology* **1975**, *21*, 165.
- (40) Howard, J. A.; Mendenhall, G. D. *Canadian Journal of Chemistry* **1975**, *53*, 2199.
- (41) Albitar, E.; Alfaro, S.; Valenzuela, M. A. *Photochemical & Photobiological Sciences* **2015**, *14*, 597.
- (42) Lebrun, V.; Tron, A.; Scarpantonio, L.; Lebrun, C.; Ravanat, J.-L.; Latour, J.-M.; McClenaghan, N. D.; Sénèque, O. *Angewandte Chemie International Edition* **2014**, *53*, 9365.
- (43) Nardello, V.; Aubry, J.-M.; Johnston, P.; Bulduk, I.; de Vries, A. H. M.; Alsters, P. L. *Synlett* **2005**, *2005*, 2667.
- (44) Carloni, P.; Damiani, E.; Greci, L.; Stipa, P.; Tanfani, F.; Tartaglioni, E.; Wozniak, M. *Research on Chemical Intermediates* **1993**, *19*, 395.
- (45) Dougherty, T. J. *Photochemistry and Photobiology* **1987**, *46*, 569.
- (46) Killoran, J.; Allen, L.; Gallagher, J. F.; Gallagher, W. M.; O'Shea, D. F. *Chem Commun (Camb)* **2002**, 1862.
- (47) Gallagher, W. M.; Allen, L. T.; O'Shea, C.; Kenna, T.; Hall, M.; Gorman, A.; Killoran, J.; O'Shea, D. F. *Br J Cancer* **2005**, *92*, 1702.
- (48) Tardivo, J. P.; Del Giglio, A.; de Oliveira, C. S.; Gabrielli, D. S.; Junqueira, H. C.; Tada, D. B.; Severino, D.; de Fátima Turchiello, R.; Baptista, M. S. *Photodiagnosis and Photodynamic Therapy*, *2*, 175.
- (49) Garrier, J.; Bezdetnaya, L.; Barlier, C.; Gräfe, S.; Guillemin, F.; D'Hallewin, M.-A. *Photodiagnosis and Photodynamic Therapy* **2011**, *8*, 321.
- (50) Garcia-Diaz, M.; Sanchez-Garcia, D.; Soriano, J.; Sagrista, M. L.; Mora, M.; Villanueva, A.; Stockert, J. C.; Canete, M.; Nonell, S. *MedChemComm* **2011**, *2*, 616.
- (51) Junqueira, H. C.; Severino, D.; Dias, L. G.; Gugliotti, M. S.; Baptista, M. S. *Physical Chemistry Chemical Physics* **2002**, *4*, 2320.

- (52) Paszko, E.; Ehrhardt, C.; Senge, M. O.; Kelleher, D. P.; Reynolds, J. V. *Photodiagnosis and Photodynamic Therapy* **2011**, *8*, 14.
- (53) Senge, M. O.; Brandt, J. C. *Photochemistry and Photobiology* **2011**, *87*, 1240.
- (54) Petri, A.; Kyriazi, M.; Alexandratou, E.; Rallis, M.; Gräfe, S.; Yova, D. 2009; Vol. 7373, p 73731I.
- (55) Kamkaew, A.; Lim, S. H.; Lee, H. B.; Kiew, L. V.; Chung, L. Y.; Burgess, K. *Chemical Society Reviews* **2013**, *42*, 77.
- (56) Yogo, T.; Urano, Y.; Ishitsuka, Y.; Maniwa, F.; Nagano, T. *Journal of the American Chemical Society* **2005**, *127*, 12162.
- (57) Batat, P.; Cantuel, M.; Jonusauskas, G.; Scarpantonio, L.; Palma, A.; O'Shea, D. F.; McClenaghan, N. D. *J Phys Chem A* **2011**, *115*, 14034.
- (58) Mirenda, M.; Strassert, C. A.; Dixelio, L. E.; Román, E. S. *ACS Applied Materials & Interfaces* **2010**, *2*, 1556.
- (59) Batat, P.; Cantuel, M.; Jonusauskas, G.; Scarpantonio, L.; Palma, A.; O'Shea, D. F.; McClenaghan, N. D. *The Journal of Physical Chemistry A* **2011**, *115*, 14034.
- (60) Denisov, S., Université de Bordeaux, 2014.
- (61) Cakmak, Y.; Kolemen, S.; Duman, S.; Dede, Y.; Dolen, Y.; Kilic, B.; Kostereli, Z.; Yildirim, L. T.; Dogan, A. L.; Guc, D.; Akkaya, E. U. *Angew Chem Int Ed Engl* **2011**, *50*, 11937.
- (62) Cakmak, Y.; Kolemen, S.; Duman, S.; Dede, Y.; Dolen, Y.; Kilic, B.; Kostereli, Z.; Yildirim, L. T.; Dogan, A. L.; Guc, D.; Akkaya, E. U. *Angewandte Chemie* **2011**, *123*, 12143.

---

# CHAPTER 5

---

## IN VITRO TESTING OF PTS-CONJUGATED NANO-ASSEMBLIES

### *Abstract*

*Fluorescent molecules have an important role in medicine to selectively visualize and diagnose many diseases. When combined with therapeutics (theranostics) they increase the selectivity and efficacy of the treatment. In this context, in the introduction part of this chapter the applications of aza-BODIPY dyes in fluorescence imaging are reviewed. Moreover, the concepts of cell activity (MTT assay test) and cell internalization quantification (using flow cytometry) are introduced. In the end of this chapter, preliminary in vitro test results on the four different PTS bearing nano-assemblies are discussed.*



## 5.1 INTRODUCTION

Diagnosis of diseases is one of the biggest challenges in medicine. Indeed, the early diagnosis of some life threatening diseases like cancer is highly important. Therefore, several imaging techniques like magnetic resonance imaging (MR), optical imaging, positron emission tomography (PET), single-photon emission computed tomography (SPECT), computerized tomography (CT), ultrasound imaging (US), etc. have been developed (see Figure 5.1).<sup>1,2</sup>

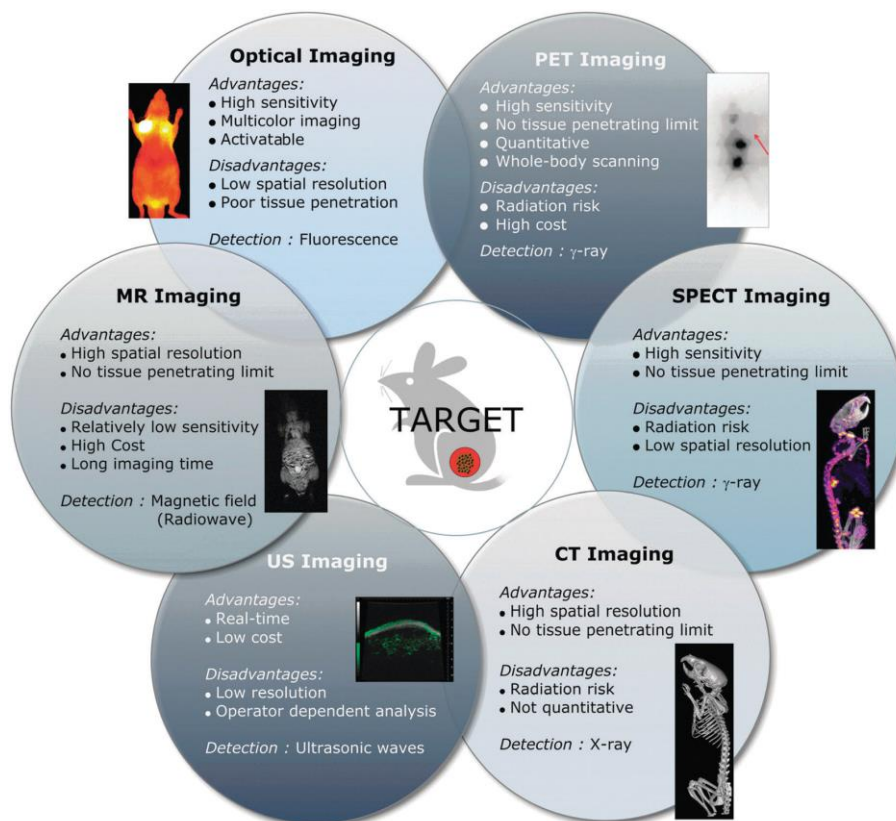


**Figure 5.1:** Imaging techniques and their characteristics<sup>1</sup>

Differently from other imaging techniques, fluorescence imaging<sup>3</sup> provides an opportunity for a histological examination which brings along an easy monitoring of the intracellular localization of the delivered therapeutic particles, and other changes in the cells during treatment.<sup>4,5,6</sup> Optical imaging requires the use of fluorescent molecules (i.e., cyanine dyes, rhodamine dyes, etc.) and is mostly used in preclinical studies. Beside the medical use, it is applied in analysis of food, water pollution, criminology, etc.<sup>6</sup>

For the development of drugs, optical imaging helps to examine the pharmacological profiles of new therapeutics.<sup>7</sup> Moreover, in nanomedicine, it is used in combination with other imaging techniques or therapeutic methods, which provides an opportunity to detect and treat the disease simultaneously.<sup>8</sup> In addition, it helps to increase the efficiency of the treatment and decreases the damage to healthy tissues. The nanomaterials that combine one or more than one diagnostic method and therapy are referred as theranostics.<sup>9,10</sup>

To give an example, the clinically used therapeutic Metvix<sup>®</sup> cream can visualize several skin diseases like basal cell carcinoma, squamous cell carcinoma, multiple actinic keratosis, Bowen's disease, etc. and treat them with photodynamic therapy (PDT) in multiple sessions (Figure

5.2).<sup>11</sup> In the applied area, the methyl aminolevulinate, which is the main ingredient in Metvix<sup>®</sup> cream, is selectively absorbed through the skin by cancer cells. It is then converted into porphyrins in the cells, which can be detected due to their fluorescence property. Through continuous irradiation by 570-670nm LED light, they generate reactive oxygen species (ROS) which cause the clearance of cancer cells.<sup>12</sup>



**Diagnosis    Therapy**

**Figure 5.2:** Fluorescence diagnosis of squamous cell carcinoma with Metvix<sup>®</sup> cream and treatment with photodynamic treatment <sup>11</sup>

### 5.1.1 Application of aza-BODIPYs in fluorescence imaging

Although there are many fluorescent molecules in the literature, only non-toxic, photostable dyes with high fluorescence quantum yield ( $\Phi_{Fl}$ ) can be used in bioimaging applications.<sup>13</sup> For *in vivo* imaging, besides those requirements, dyes should be near-infrared (NIR) emitting (650-800nm) to reduce the autofluorescence problem and have an efficient light penetration through the tissues. In this context, it has been reported that aza-BODIPY dyes have 60-fold higher photostability compared to conventional BODIPY dyes (see Figure 5.3).<sup>14</sup> Moreover, they are NIR emitting dyes, have low toxicity and they are also good photosensitizers for PDT application as described in Chapter 2 and 4.

Wu and O'Shea have reported on the synthesis of the water soluble asymmetric dye **32** as a NIR fluorescence imaging probe by attaching a sulfonate group (Scheme 5.1). *In vitro* testing on HeLa cells showed an efficient localization of the dye in the cytosol.<sup>15</sup> Collado and co-workers<sup>16</sup> have reported on a neutral water soluble PEGylated aza-BODIPY **33** by attaching tetraethylene glycol subunits at the para-position of phenyl groups. *In vitro* testing on HeLa cells showed a faster internalization and localization in the cytoplasm. The charge free fluorophores offer an opportunity to conjugate them to biomolecules without causing any chemical distortion to them. Tasior and O'Shea<sup>17</sup> have reported on an asymmetric water soluble derivative of aza-BODIPY dye **34** (Scheme 5.2) that can be further conjugated to fluorescent probe for biomolecule labeling. This dye bears a tri(ethylene glycol) subunit on one phenyl ring to enhance the water solubility, and an activated ester group (sulfonated N-hydroxysulfosuccinimide sodium salt) on the other phenyl ring for conjugation. It has been experimentally shown that in water (at pH=8.3) this fluorophore has potential for effective amine conjugation with amino acids and proteins (lysozyme and trypsin).

In the literature, several pH responsive aza-BODIPY derivatives have also been reported for NIR fluorescence imaging. Murtagh et al.<sup>18</sup> introduced a pH responsive "off-on" fluorescence switchable galactose conjugated derivative of aza-BODIPY **35** (Scheme 5.2). The fluorescence is switched on at low pH (6.6) and switched off at high pH (8) due to phenol/phenolate interconversion in the cell (Figure 5.4). The response to low pH is an attractive feature to

selectively detect cancer cells since they are known to have lower pH profile (6.5-6.8) compared to healthy cells (pH 7.4).<sup>18</sup>

Zhank and coworkers<sup>19</sup> have also reported on a pH responsive “off-on” fluorescence switchable dye **36a** for *in vivo* cell tracking application. This dye has an enhanced membrane permeability and can switch the bright NIR fluorescence on in neutral and basic hydrophobic microenvironments in living cells (see Scheme 5.3). McDonnell et al.<sup>20</sup> have reported on the pH responsive dibrominated analog **36b** for selective PDT applications. In an acidic intracellular environment, **36b** gets protonated and switches on the weak fluorescence and higher PDT activity, selectively in the cancer cells (Scheme 5.3).

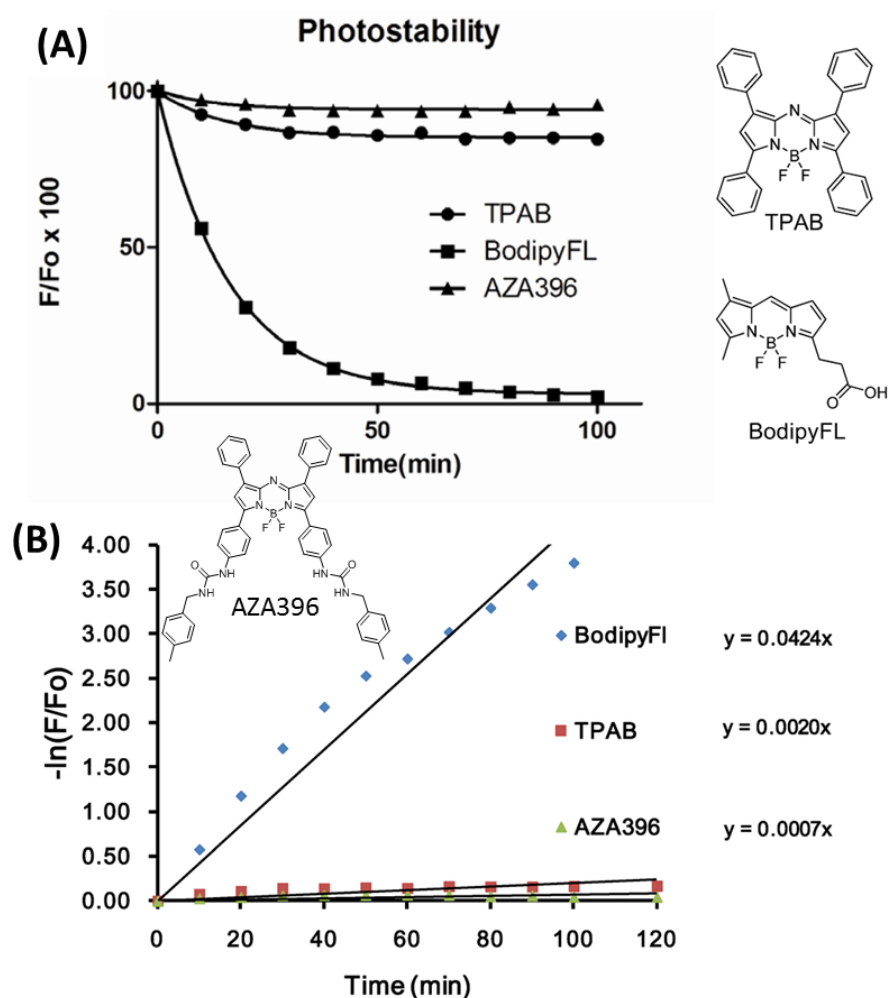
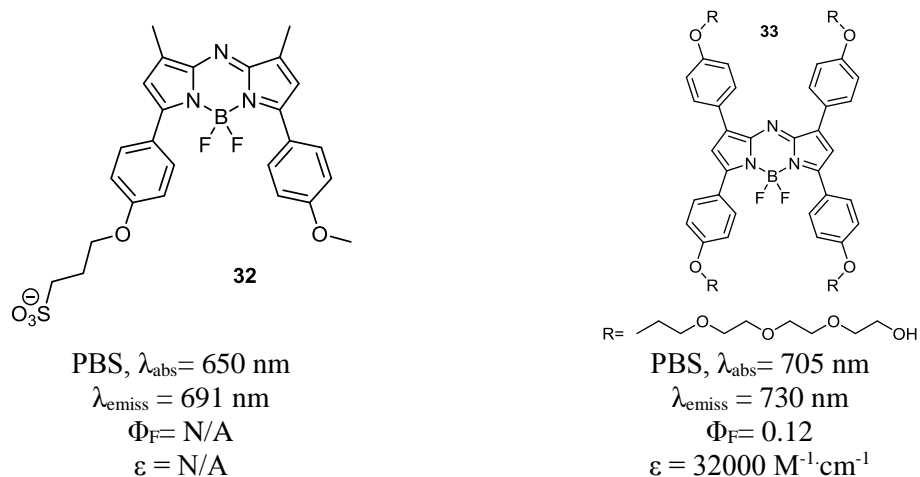
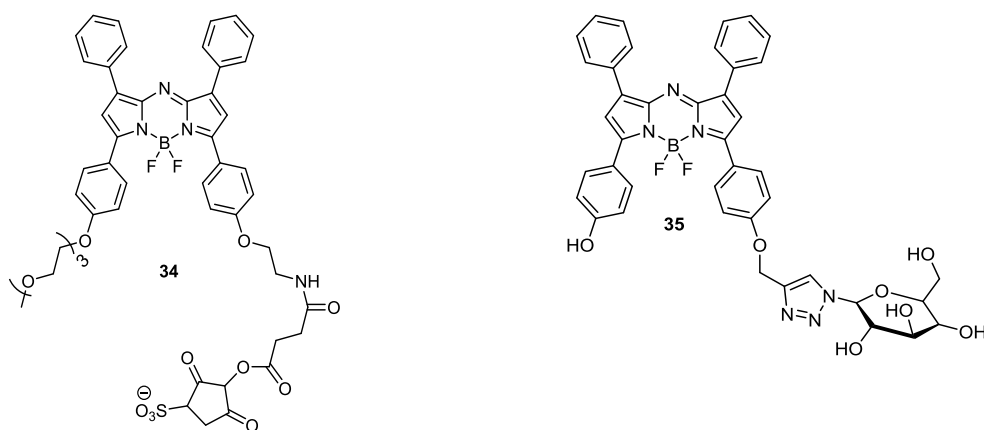


**Figure 5.3:** Photostability of the aza-BODIPYs compared to conventional BODIPY dye under 100min continuous irradiation with 365nm UV light in DMSO<sup>14</sup>





**Scheme 5.1:** Chemical structures of water soluble aza-BODIPYs based fluorescent probes.<sup>15,16</sup>



**Scheme 5.2:** Chemical structure of conjugable **3**<sup>17</sup> and pH sensitive **4**<sup>18</sup> fluorescent probes.

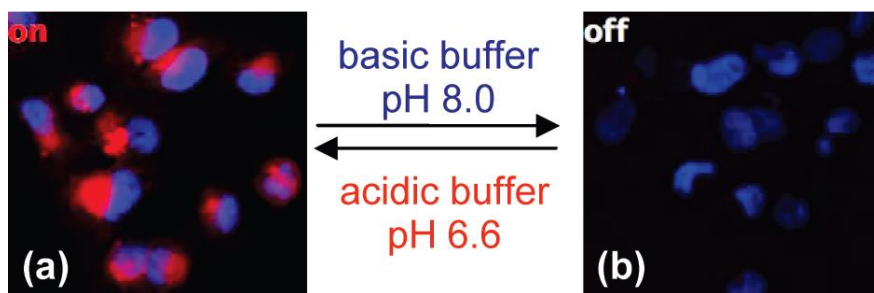
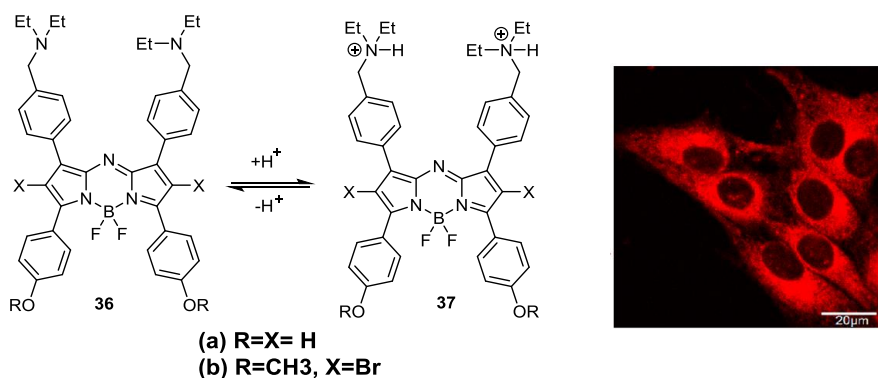
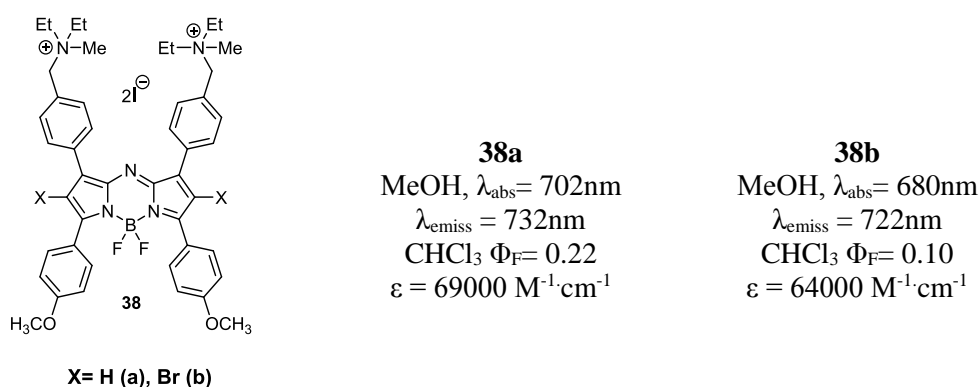


**Figure 5.4:** Confocal laser scanning microscopy (CLSM) images of MDA-MB-231 cells incubated with **35** over 1h. Blue fluorescence is due to the nuclei staining with 4,6-diamidino-2-phenylindole (DAPI).<sup>18</sup>



**Scheme 5.3:** pH sensitive “off-on” aza-BODIPY derivatives<sup>20</sup> and confocal image of **36a** incubated (3h, 0.1µM) in MDA-MB-435 cells.<sup>19</sup>



**Scheme 5.4:** Chemical structure of the fluorescence imaging probe **38a**, antimicrobial PDT agent **38b** and their optical properties in MeOH and CHCl<sub>3</sub>.<sup>21</sup>

In addition, Frimannsson and coworkers<sup>21</sup> reported on the water soluble bis-cationic fluorescence probes (**38a,b**) with very low dark toxicity. Dye **38b** could be used as an antimicrobial PDT agents for Gram-positive and -negative bacterial strains and pathogenic yeasts infections due to the singlet oxygen generation property. These dyes were functionalized with bis-ammonium salt to enhance the cellular uptake (10min) and brominated to increase the PDT activity.

Besides the *in vitro* imaging aza-BODIPY derivatives have also been used in *in vivo* imaging applications. O’Shea’s group<sup>21</sup> has reported on the synthesis of a water soluble maleimide bearing aza-BODIPY **39**, which is capable of thiol conjugation with several peptides in water. In this work, **39** is covalently linked to the cancer specific cyclic cRGD peptide sequence (**39a**) to selectively visualize the solid tumor in rats with Eca-109 subcutaneous tumor. RGD peptide is known to have specific binding property to receptors ( $\alpha_v\beta_3$  integrin heterodimeric cell surface receptors) that are overexpressed in tumor cells. Due to this property, the selective localization of **39a** has been observed in 1h after the intravenous administration (1mg/kg). The fluorescence signal, which persisted even after 4 h, was also detected from liver and other tissues, but was completely cleared from the body after 48h (see Figure 5.5).

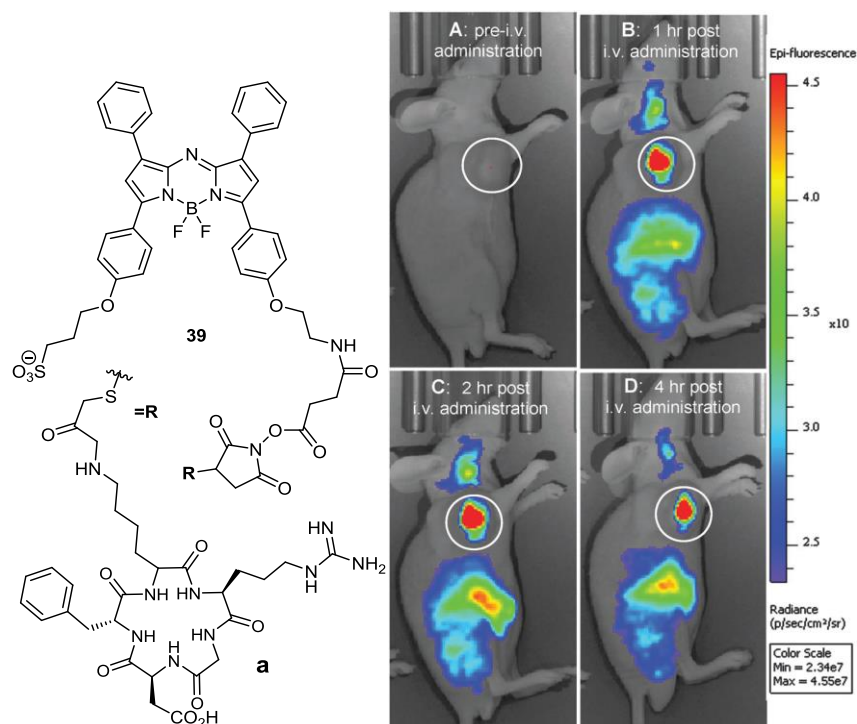
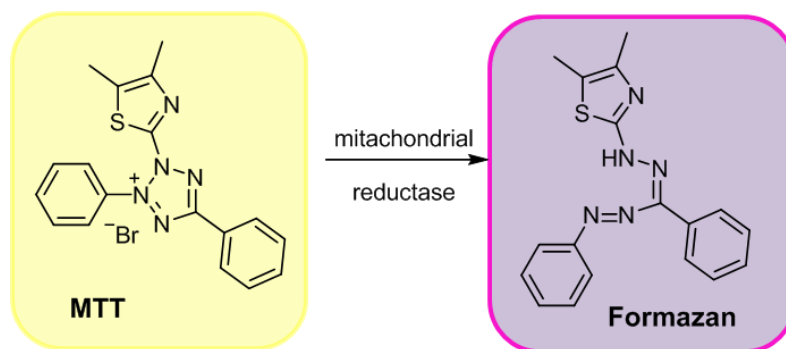


**Figure 5.5:** Chemical structure of **39** (a) and in vitro imaging application of **39a** (selective localization in Eca-109 subcutaneous tumor (circle indicates the tumor),  $\lambda_{exc} = 630\text{nm}$ ,  $\lambda_{emiss} = 700\text{ nm}$  ).<sup>21</sup>

### 5.1.2 MTT assay test

MTT is a quantitative colorimetric assay which is used to assess the metabolic activity of the living cells<sup>22</sup> and has wide applicability in many types of mammalian cells. It is used to quantitatively measure cytotoxicity of therapeutics or toxic compounds and proliferation of the living cells by measuring the color change from pale yellow to purple, which can be detected by optical plate readers (500-600nm). The reduction of soluble MTT 3-(4,5-dimethylthiazol-2-yl)-2,5-diphenyltetrazolium bromide) to insoluble formazan ((E,Z)-5-(4,5-dimethylthiazol-2-yl)-1,3-diphenylformazan) can take place only in metabolically active living cells (Scheme 5.5).<sup>23</sup> The limitation of this method is the use of organic solvents (usually DMSO) to dissolve the produced formazan in the cells to homogenize the solution for optical measurements, which causes irreversible damage to the live cells.



**Scheme 5.5:** Scheme of a reduction of tetrazolium salt (pale yellow) to formazan (purple) in live cells.

### 5.1.3 Flow cytometry

Flow cytometry (FACS) analysis provides fast, qualitative and quantitative fluorescent measurements of cells. It can measure simultaneously the multiple characteristics (i.e., optical characteristics, physical properties, internal complexity, etc.) of a single cell flowing in a stream of fluid.<sup>24</sup> During FACS analysis, fluorescently labeled cells pass through an interrogation point one-by-one due to the laminar flow of the stream through the narrow cytometer (see Figure 5.6). At this point, individual cells absorb the monochromatic light and emit photons in all directions. The cells are then collected and isolated according to the emission wavelength of the fluorescent labels in the cell. The final result could be displayed either as histograms or scatterplots (two dimensional).<sup>24</sup> This technique has very broad applications in biology and clinical laboratories like cell sorting,<sup>25</sup> DNA content analysis, determination of blood neutrophil fraction,<sup>26</sup> etc. It is also used to study the kinetics of cellular internalization of fluorescent labeled molecular therapeutics or nanoparticles.<sup>27</sup>

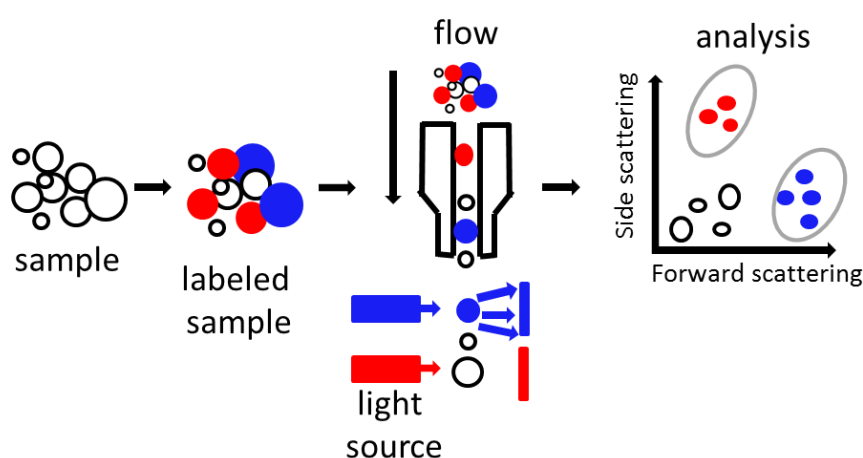


**Figure 5.6:** Simplified schematic representation of flow cytometry (adapted from ref. <sup>28</sup>).

## 5.2 Results

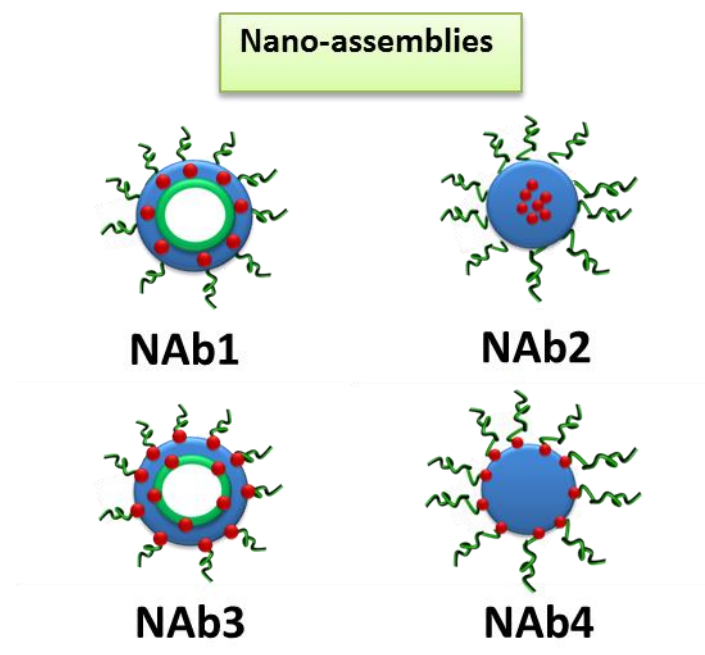
In order to test the cellular internalization, toxicity and therapeutic efficacy of the nano-assemblies and evaluate the difference between those particles, preliminary *in vitro* experiments have been performed which will be discussed in detail in the following sections.

### 5.2.1 Cellular internalization test by flow cytometry

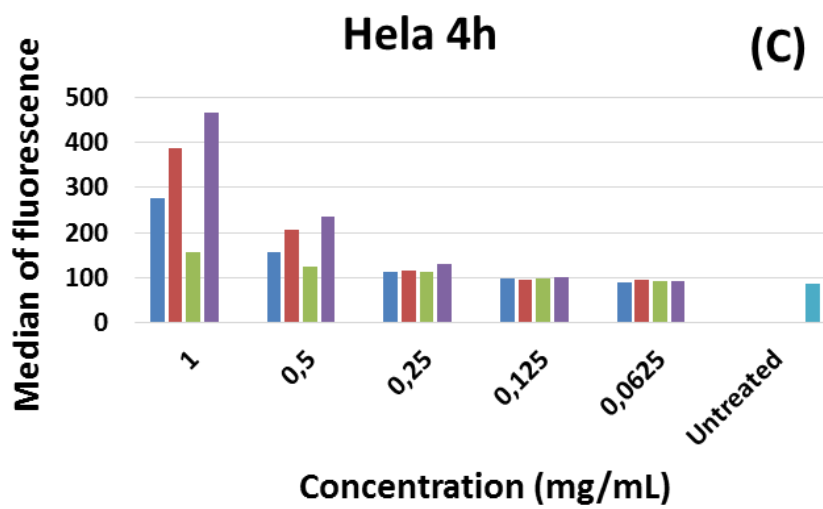
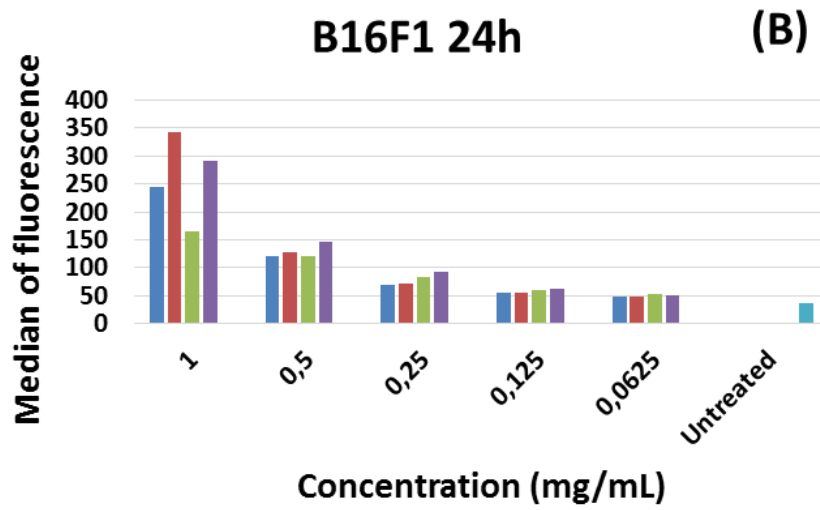
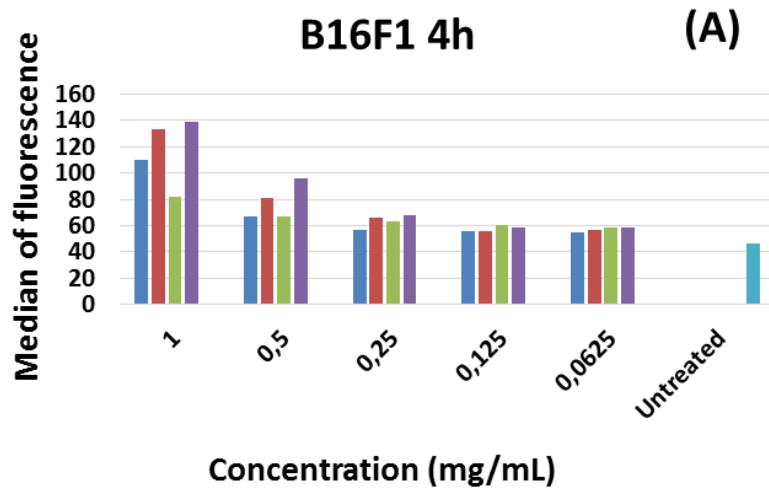
The time and concentration dependent internalization tests for four different nano-assemblies (see Figure 5.7) were performed on two cell lines (B16F1 and HeLa) by using FACS technique. The cells were incubated with PTS-PBLG<sub>49</sub>-*b*-PEG<sub>45</sub> (**NAb 1**), PTS-PBLG<sub>49</sub>-*b*-PEG<sub>113</sub> (**NAb 2**), PBLG<sub>53</sub>-PTS-*b*-PEG<sub>45</sub> (**NAb 3**) and PBLG<sub>53</sub>-PTS-*b*-PEG<sub>113</sub> (**NAb 4**) nano-assemblies during 4 and 12h with five different concentrations of nano-assemblies (Figure 5.8). It is known that the internalization of nanoparticles is size<sup>29</sup> and shape<sup>30</sup> dependent. NAb 1 and NAb 3 showed a slow internalization compared to NAb 2 and NAb 4. The reason for this difference in internalization is probably due to the morphological difference between the nano-assemblies since they all have size in the same range ( $R_h \sim 100\text{nm}$ ) as mentioned in Chapter 3.

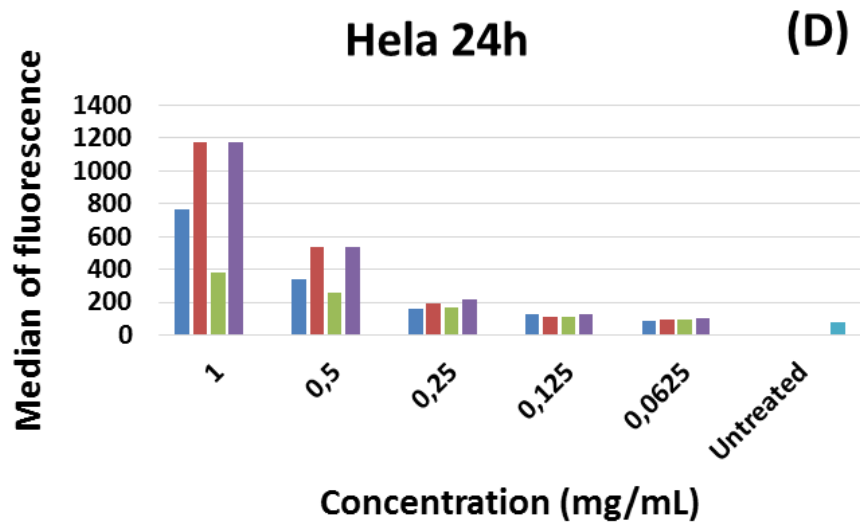
In addition, fluorescence imaging conformed the internalization of the NAb and localization in the cytosol in both cell line (B16F1 and HeLa).

It is also important to mention that the internalization is in general rather low, because of the stealth character of the nanoparticle. Indeed, pegylated and colloïdally stable nanoparticles in serum are not design to internalize fast in *in vitro* testing, but to benefit from the EPR effect and accumulate in the tumor environment *in vivo*.

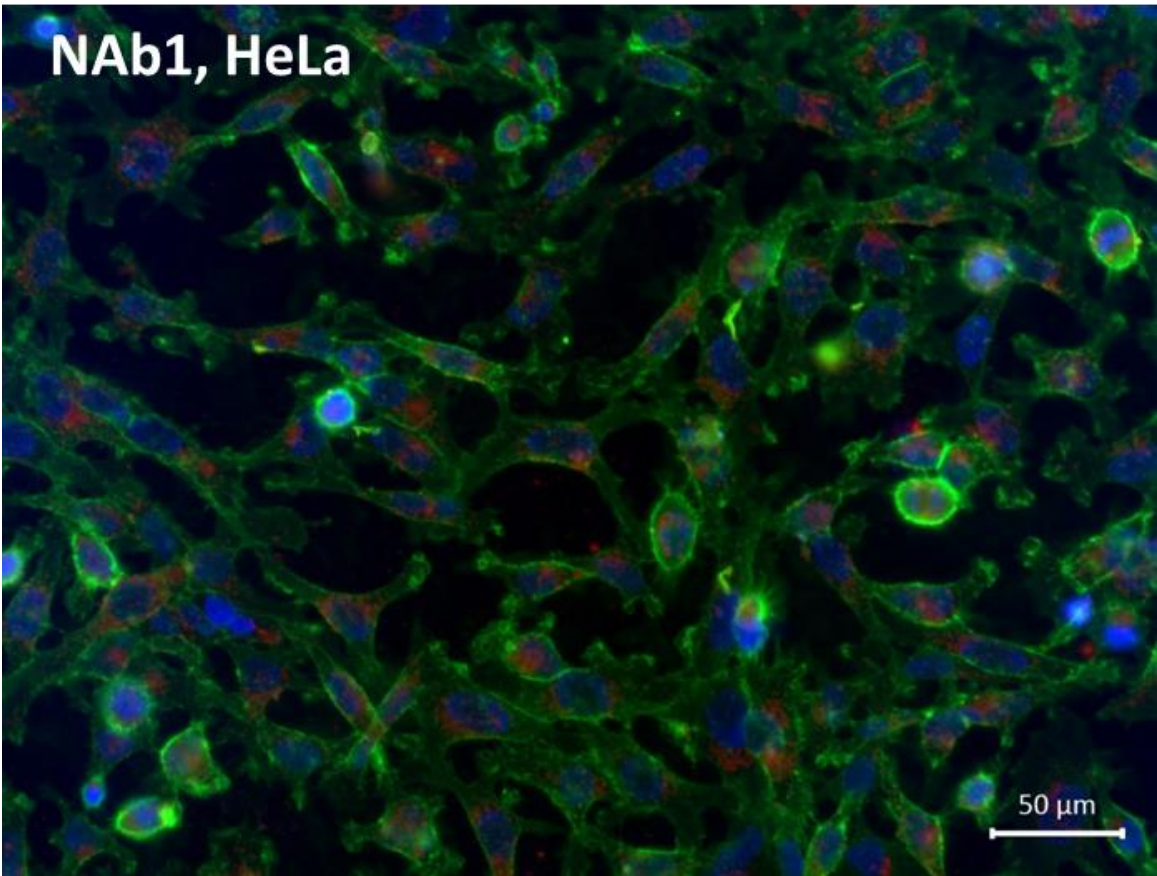
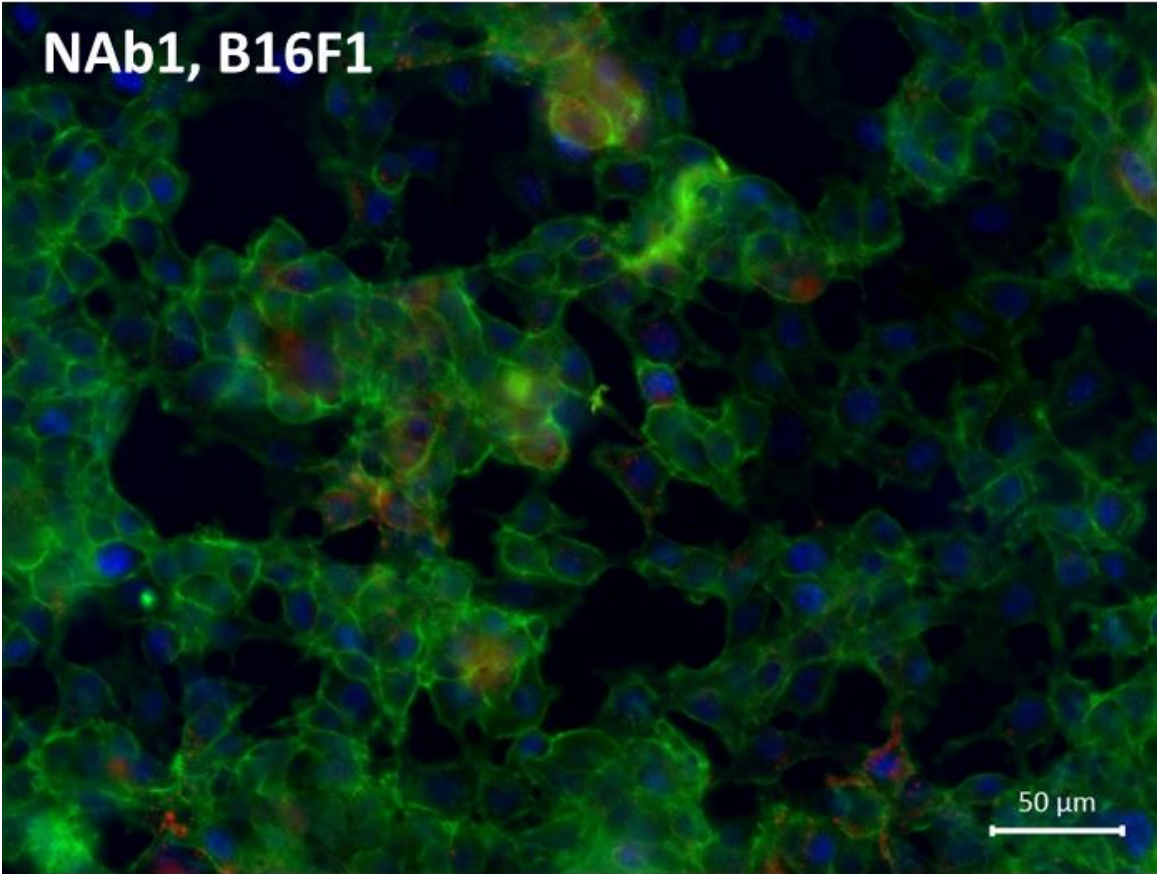


**Figure 5.7:** Schematic illustration of PTS-PBLG<sub>49</sub>-*b*-PEG<sub>45</sub> (**NAb 1**), PTS-PBLG<sub>49</sub>-*b*-PEG<sub>113</sub> (**NAb 2**), PBLG<sub>53</sub>-PTS-*b*-PEG<sub>45</sub> (**NAb 3**) and PBLG<sub>53</sub>-PTS-*b*-PEG<sub>113</sub> (**NAb 4**) nano-assemblies.

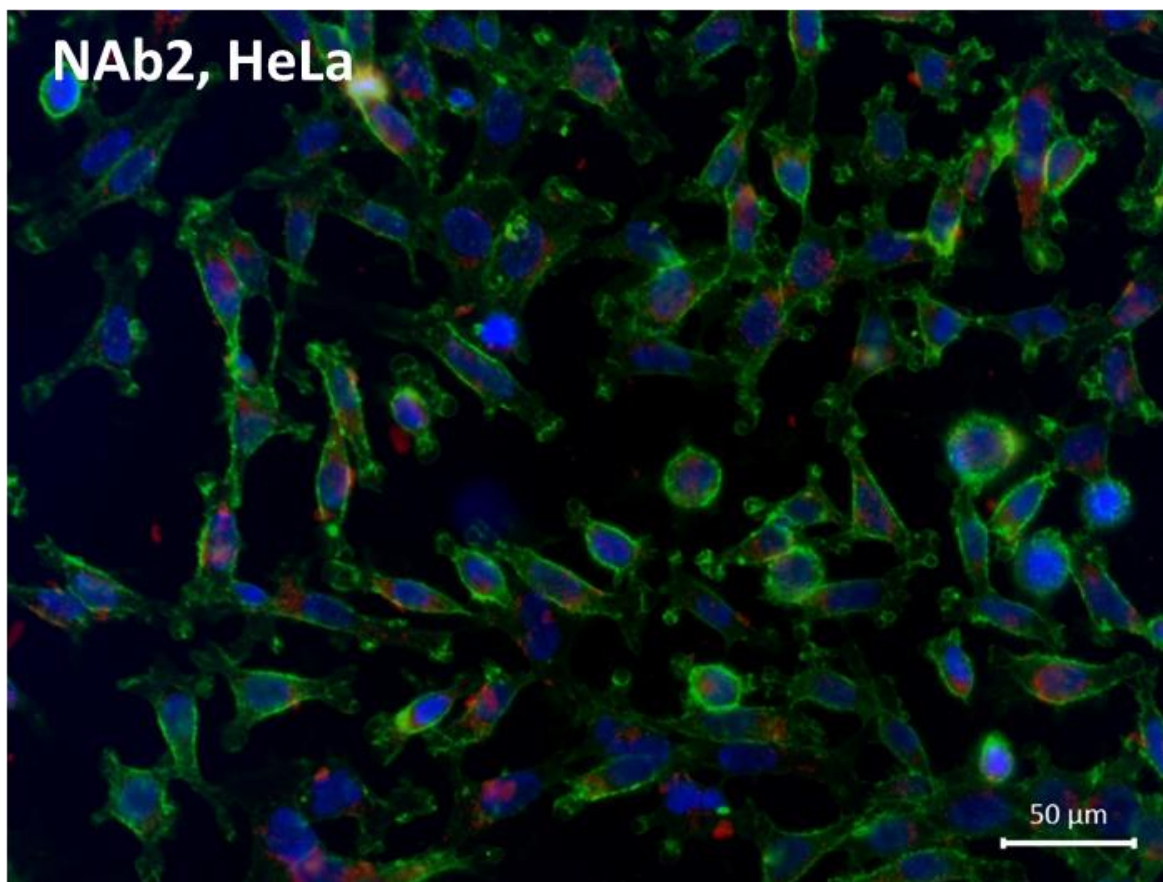
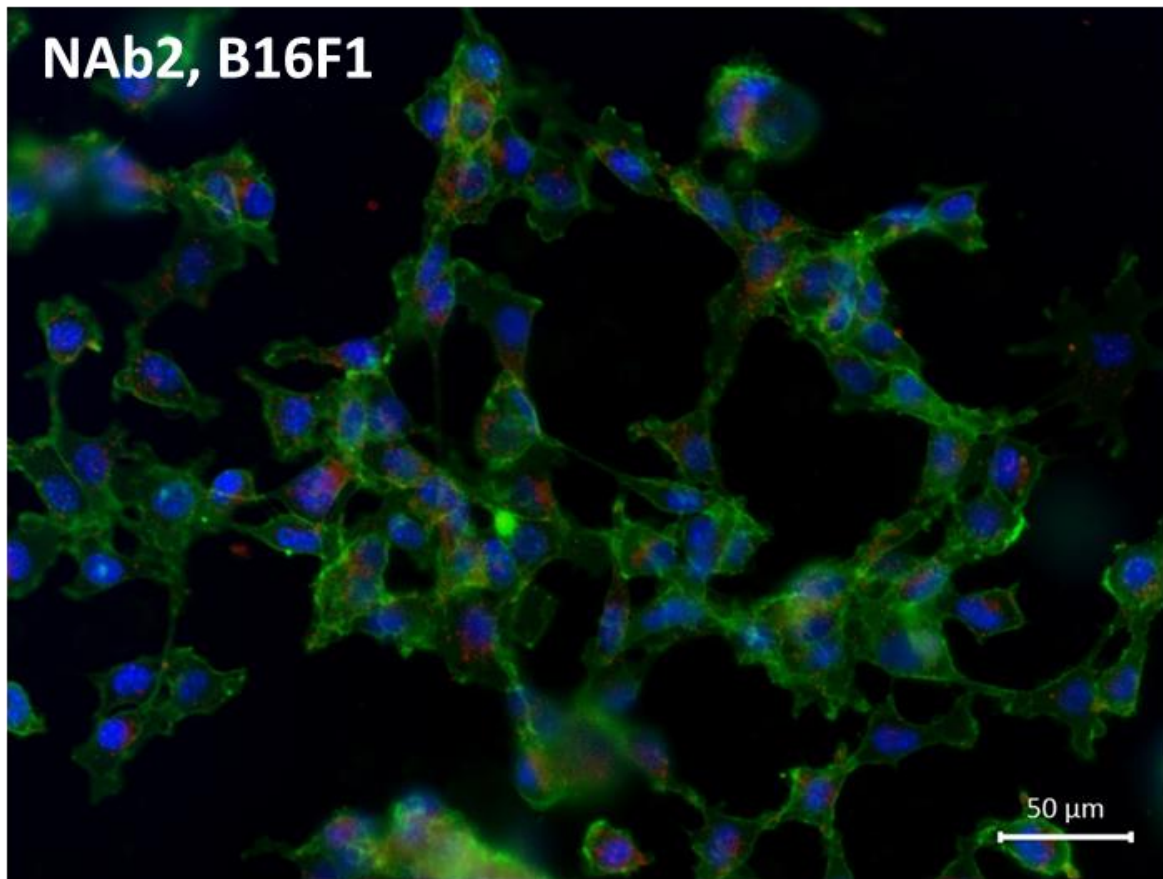


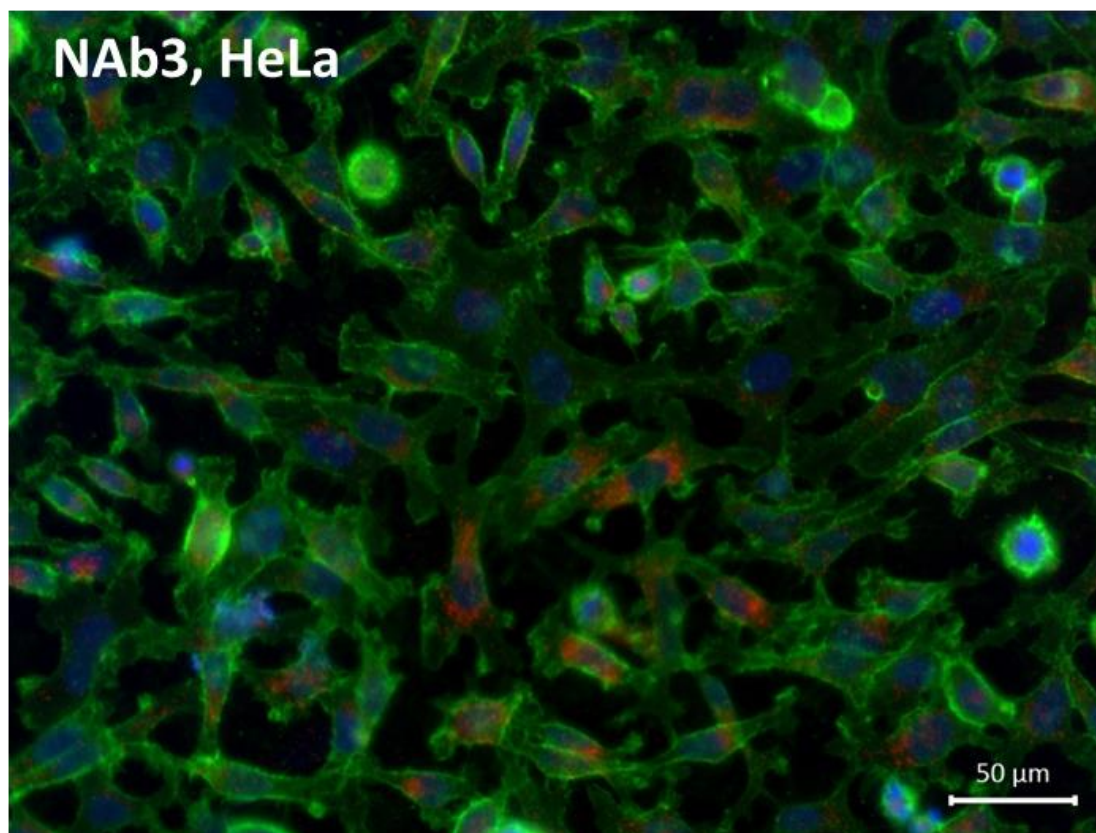
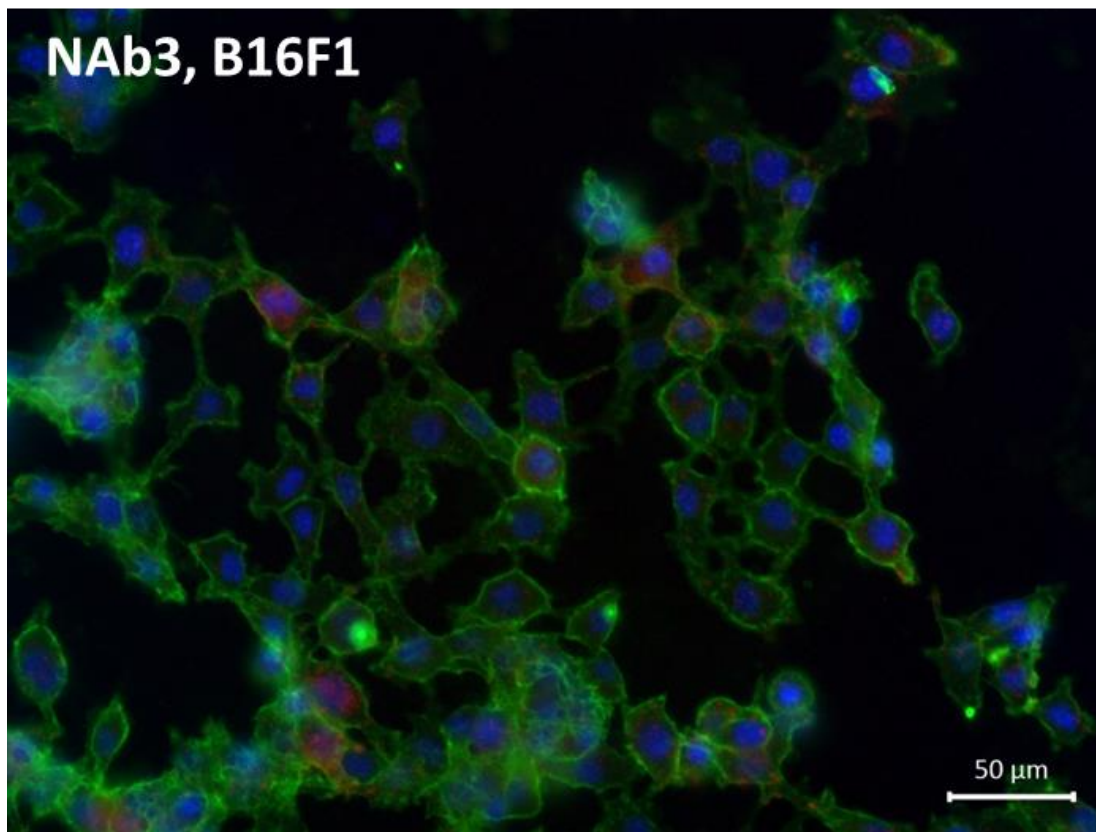


**Figure 5.8:** Time and concentration dependent internalization of the nano-assemblies in B16F1 (A and B) and HeLa cells (C and D). Blue: PTS-PBLG<sub>49</sub>-*b*-PEG<sub>45</sub> (NAb 1), red: PTS-PBLG<sub>49</sub>-*b*-PEG<sub>113</sub> (NAb 2), green: PBLG<sub>53</sub>-PTS-*b*-PEG<sub>45</sub> (NAb 3), purple: PBLG<sub>53</sub>-PTS-*b*-PEG<sub>113</sub> (NAb 4)









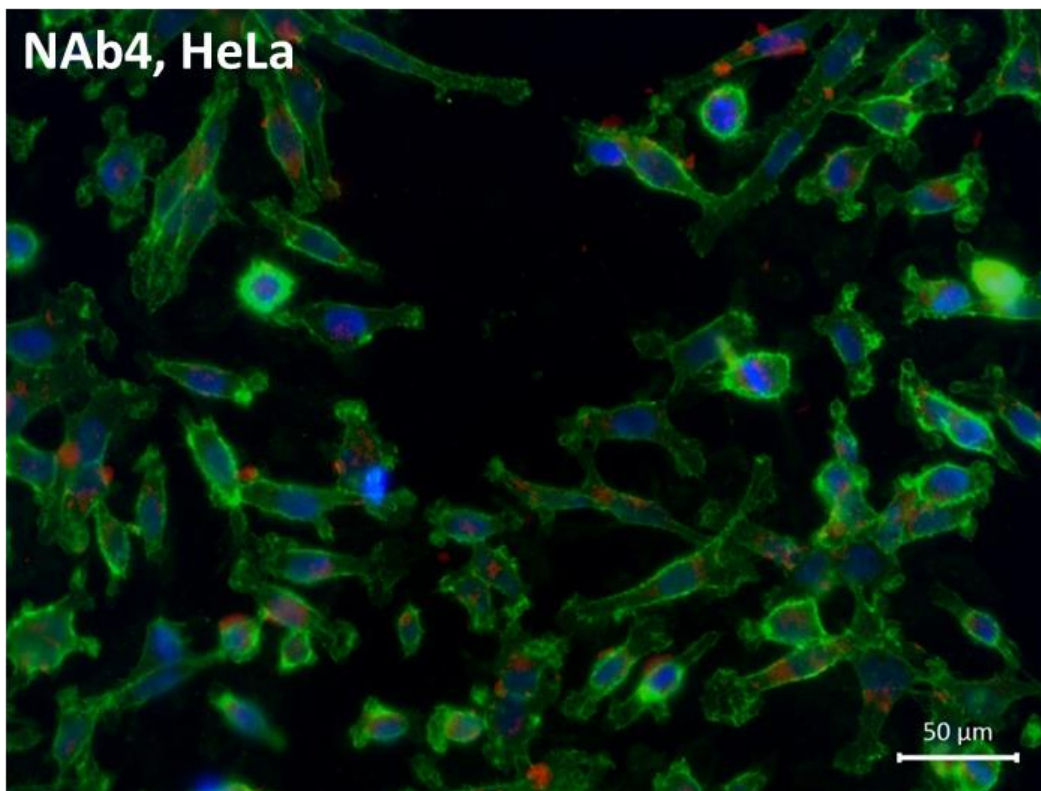
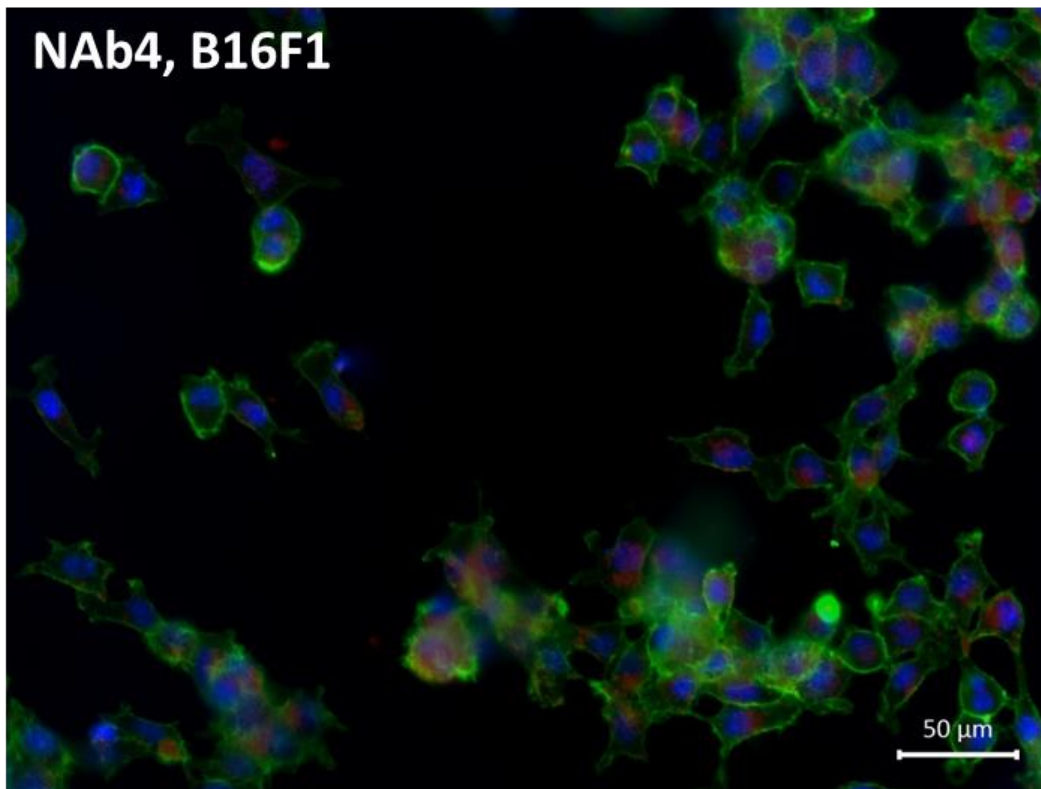


**Figure 5.9:** Confocal laser scanning microscopy (CLSM) images of B16F1 and HeLa cells incubated with NABs over 24h. Blue fluorescence is due to the nuclei staining with 4,6-diamidino-2-phenylindole (DAPI), green fluorescence is due to the membrane staining with AlexaFluor488-conjugated concanavalin A and red fluorescence is due to the PTS fluorescence in the NABs.

### 5.2.2 *In vitro* cytotoxicity

Cell viability tests on B16F1 and HeLa cells were performed in order to evaluate the therapeutic activity of the NAbs. In first a step, their dark toxicity was tested at different concentrations of nano-assemblies by using a MTT cell proliferation assay (see Figure 5.10). The cells were incubated with eight different concentrations of NAbs over 12h to have efficient internalization, washed with cell medium and followed by cell viability tests. We observed that without light activation, NAbs exhibit a small toxicity at high concentration (1mg/mL). Moreover, they displayed higher viability for B16F1 cells compared to HeLa cells.

The experiments were repeated under the same conditions but before performing MTT test, cells were irradiated with 660nm LED lamp (power density 1.33 mW/cm<sup>2</sup>) during 15 (1.2 J/cm<sup>2</sup>), 30 (2.4 J/cm<sup>2</sup>) and 60 (4.8 J/cm<sup>2</sup>) minutes time periods to induce the toxicity by activating the PTS in the NAbs (see Figure 5.11 and 5.12). Indeed, after these examinations we found out that activity of the PTS in the cell varies depending on its localization in the NAbs, morphology of the NAbs and irradiation time. The NAbs that have PTS in the core or in the membrane (NAb 1 and NAb 2) exhibited lower photoactivity in both cell lines. However, their toxicity increased at high concentration (1mg/mL) and longer light excitation period (1h). Contrary to these NAbs, the nano-assemblies that have PTS at the interface (NAb 3 and NAb 4) cause 100% cell death even at low concentration (0.125 mg/mL) at 1h irradiation time for both cell lines. Moreover, PBLG<sub>53</sub>-PTS-PEG<sub>45</sub> (**NAb 3**) nano-assembly caused even 100% cell death for the minimum light dose (1.2 J/cm<sup>2</sup>) at 0.125mg/mL (PTS concentration in the nano-assembly is 3μg/mL, 15pM) concentration, whereas no toxicity was evidenced at the same concentration without light activation. However, NAb 3 showed lower singlet oxygen generation yield (0.08) compared to NAb1, NAb2 and NAb4 as described in Chapter 4. The opposing trend between *in vitro* test results and singlet oxygen generation yield is difficult to explain on the basis of the available data. It could be explained by the formation of additional radical species compared to free <sup>1</sup>O<sub>2</sub>, which would induce a higher toxicity and couldn't be detected by singlet oxygen trap AVS.

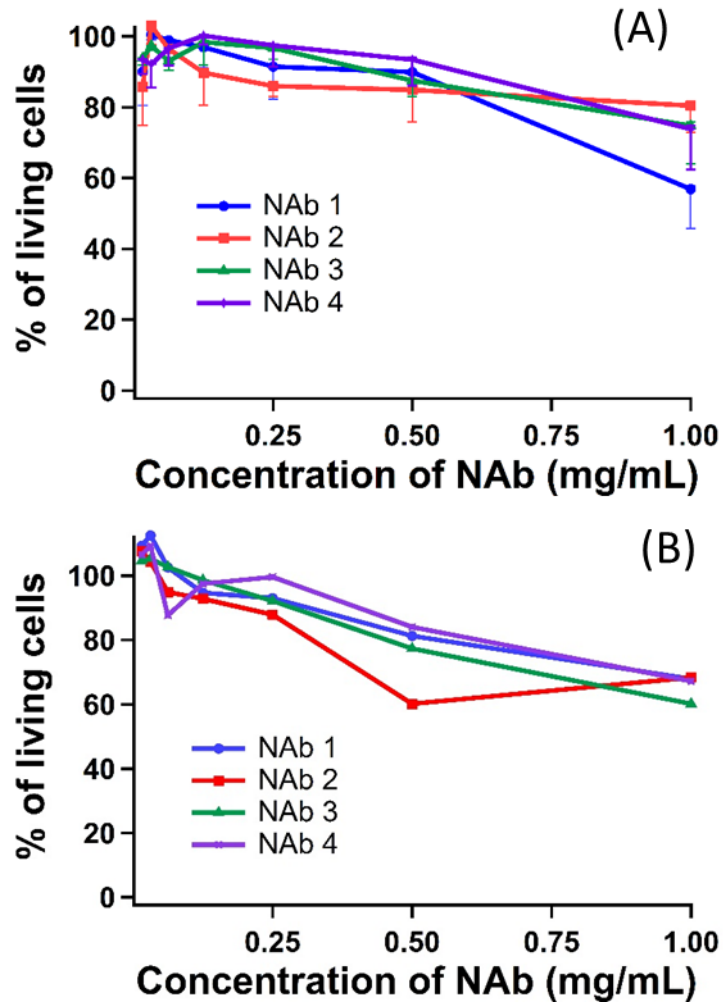


**Figure 5.10:** Cytotoxicity tests of the NABs as a function of concentration on (A) B16F1 (triplicated) and (B) HeLa cells (in dark)

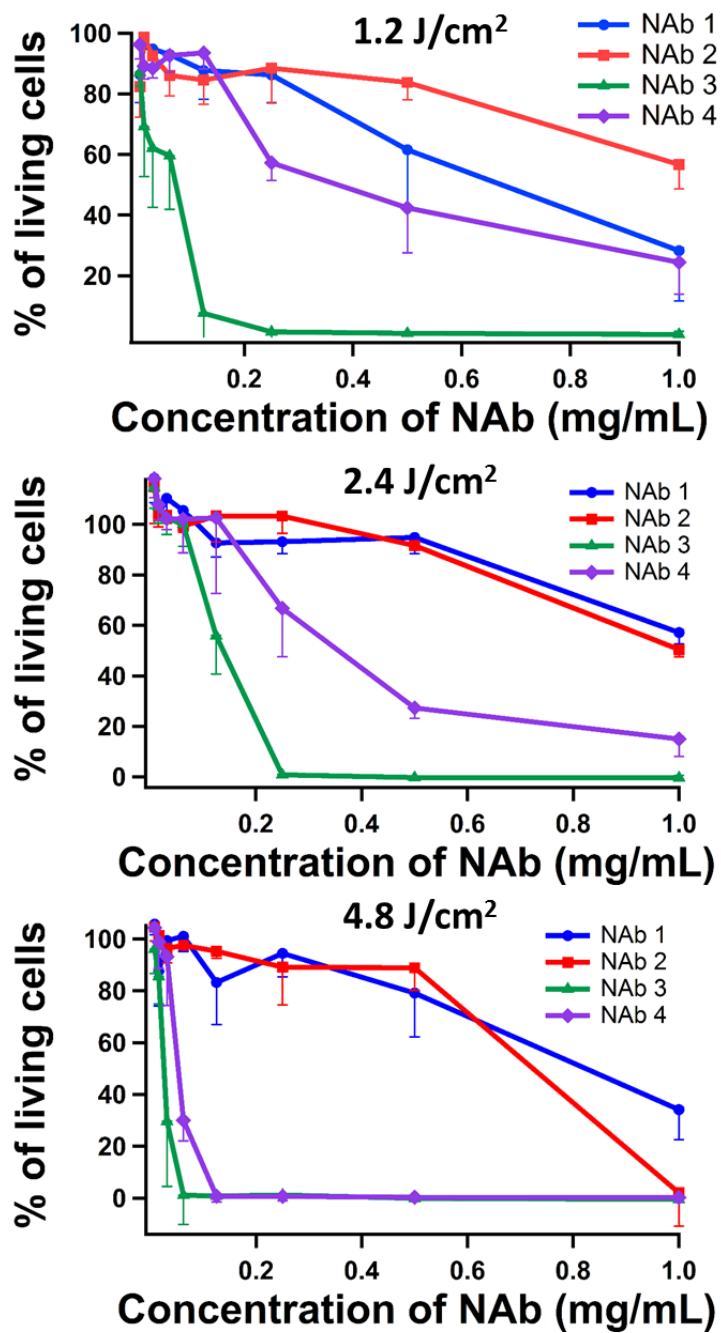


**Figure 5.11:** Cytotoxicity tests of the NABs under 660 nm LED irradiation as a function of light dose and NABs concentration (B16F1 cells, the measurements have been repeated three times)

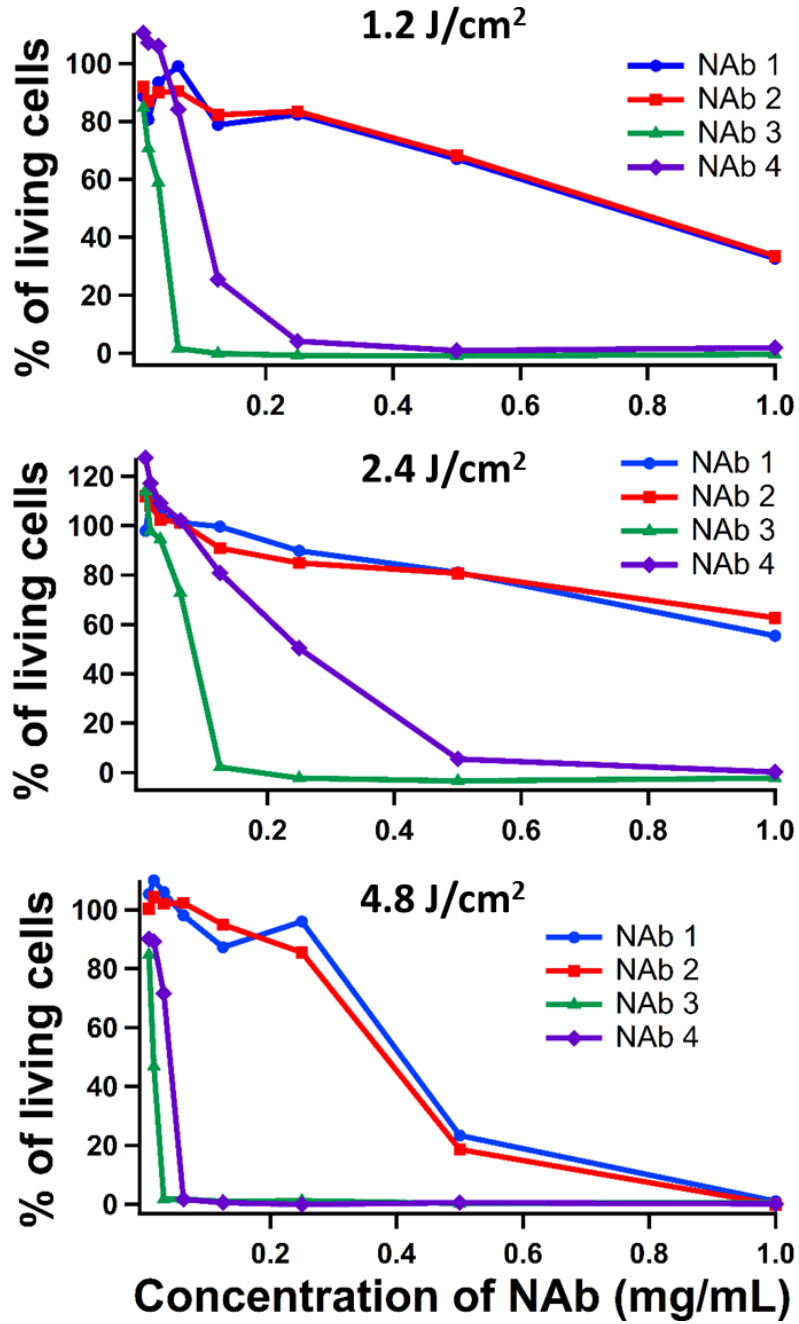


**Figure 5.12:** Cytotoxicity tests of the NABs under 660 nm LED irradiation as a function of light dose and NABs concentration (HeLa cells)

Compared to literature results, the phototoxicity of the NAb 3 nano-assemblies is much higher at lower concentration. Garcia-Diaz and coworkers<sup>31</sup> have performed *in vitro* PDT tests on HeLa cells by using DMSO loaded Temocene and clinically used PTS Foscan®. As can be seen from their MTT assay results (Figure 5.13), both PTS have higher viability and lower phototoxicity at 0.5  $\mu\text{M}$  concentration, which is  $\sim 10^5$  times higher than the PTS concentration in NAb 3 nano-assemblies (15pM). Moreover, a 3 times higher light dose was applied to enhance the phototoxicity of Temocene and Foscan®.

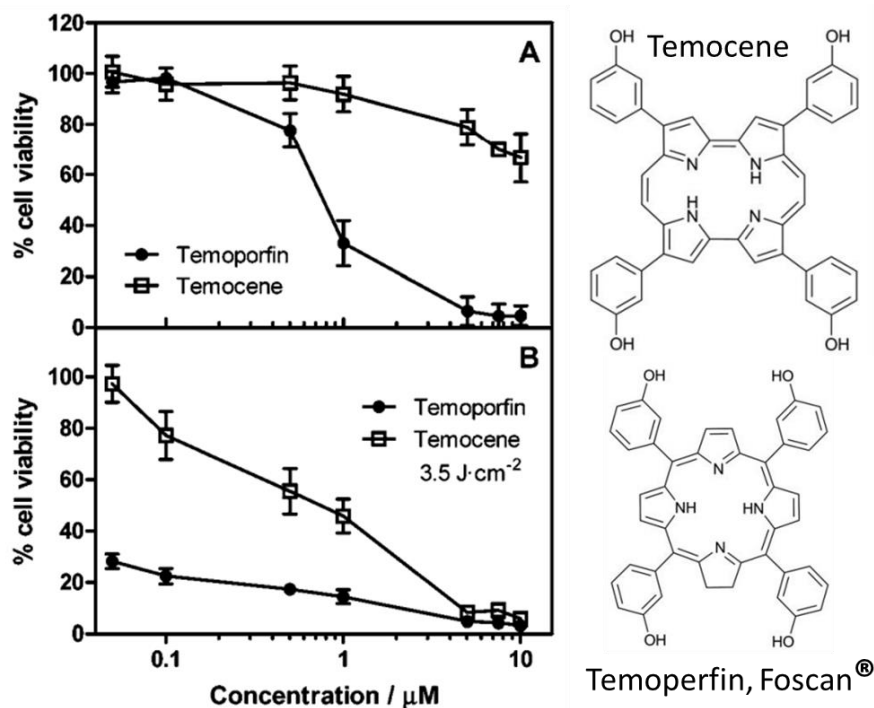


**Figure 5.13:** MTT assay test after 18h incubation with Foscan® and Temocene on HeLa cells (A) in dark and (B) after 625 nm LED irradiation.<sup>31</sup>

Moreover, Petri et al.<sup>32</sup> have evaluated the therapeutic activity of Foscan® and Fospeg® at different light dose on LNCaP cells. They observed only 20% cell death at 540 mJ/cm<sup>2</sup> light dose (652 nm LED) for Foscan®, and 70% cell death from Fospeg® incubated cells at 0.15 $\mu\text{g}/\text{mL}$  concentration. This study also showed that the encapsulation of the PTS increases its therapeutic activity, in agreement with our observations, since Fospeg® is a Temoporfin encapsulated lipid based nanoparticle which is coated with PEG after micellization to induce the stealth property.

### 5.3 Conclusion

In this chapter preliminary *in vitro* tests were performed to evaluate the biocompatibility of the nano-assemblies, their internalization. B16F1 skin cancer cells were chosen for the potential application and HeLa cells were used to compare the results with the literature examples. The phototoxicity of the nano-assemblies after PDT treatment was assessed by MTT colorimetric assay, and we found out that therapeutic activity of the PTS depends on its localization in the nano-assemblies and the morphology of the latter. The maximum cell toxicity in minimum photoactivation time (15min) was observed in PBLG<sub>53</sub>-PTS-PEG<sub>45</sub> (NAb 3) nano-assemblies where the PTS concentration is 3 $\mu\text{g}/\text{mL}$  in 0.125mg/mL nano-assembly solution. Due to the



covalent linking of PTS we can control the PTS concentration quantitatively and protect it from degradation before reaching the targeted site. In addition, we demonstrated that both the localization and shape of the self-assemblies can influence both the internalization efficiency and dark/light toxicity. The phototoxicity can be gently moderated with time and light dose (NAb 1 and 2) when the PTS molecule is preferentially localized in the hydrophobic domains of the nanoparticles. On the opposite, when the PTS is at the nanoparticle/water interface, it is much more efficient and high toxicity can be rapidly reached upon illumination at low dose. As a result of this study we designed PDT agents that have higher phototoxicity and lower dark toxicity at lower PTS concentration compared to previously reported systems, which could open a new door for the development of new therapeutics for cancer treatment.

## **5.4 Experimental**

### **Materials and methods**

#### **Materials**

The following reagents have been used as received: Minimum essential medium (MEM, Thermo Fisher Scientific), minimum essential medium (MEM Alpha Medium (1X) + GlutaMax, Thermo Fisher Scientific), 3-[4,5-dimethylthiazol-2-yl]-2,5-diphenyltetrazolium bromide (thiazolyl blue; MTT, Sigma-Aldrich), phosphate-buffered saline (PBS, Thermo Fisher Scientific), 4',6-diamidino-2-phenylindole (DAPI, Thermo Fisher Scientific)

#### **Methods**

##### **Cell Culture**

For in vitro tests two human epithelial adenocarcinoma cell line HeLa and skin cancer cell line B16F1 were used. HeLa cervix cancer cells were cultured at 37 °C for 24 hours in Minimum essential medium (MEM) supplemented with 10% heat-inactivated FBS and 100U/ml penicillin–streptomycin, in 5% CO<sub>2</sub>-humidified atmosphere. B16F1 skin cancer cells were cultured at 37 °C for 24 hours in minimum essential medium (MEM Alpha Medium (1X)+ GlutaMax) supplemented with 10% heat-inactivated FBS and 100U/ml penicillin–streptomycin, in 5% CO<sub>2</sub>-humidified atmosphere.

##### **Cellular uptake**

Cellular uptake of nano-assemblies was quantified by flow cytometry. HeLa and B16F1 cells were seeded in two different 24-well plates ( $5 \times 10^4$  cells/ well) 24h before the experiment. Cells were incubated with nano-assemblies for 4 and 24h at concentrations of 1, 0.5, 0.25, 0.125, 0.062mg/mL. Then, cells were rinsed with phosphate-buffered saline (PBS) solution, trypsinized and diluted with cell medium. After centrifugation (250 RPM, 5 min, 4 °C), the cell pellet was resuspended in 200μL PBS. The measurements were done on a FACSCalibur cytometer (BD Biosciences, Erembodegem, Ex: 640 nm / Em: 660 nm). After obtaining the best internalization at 24h the experiment was repeated two more times for 24h incubation time at concentrations of 1, 0.5, 0.25, 0.125, 0.062 mg/mL. Finally, the data were analyzed using Flow Jo software.  $5 \cdot 10^3$  cells were analyzed in each measurement.

## Cell viability in dark

The HeLa and B16F1 cells were seeded on two different 96-well plate and incubated for 24h at 37°C. Then the cells were incubated with 1mg/mL and 0.5mg/mL nano-assembly solutions for 24h. After the cells were washed with cell medium and 0.5mg/mL of MTT solution was added and the cells were incubated for 3h. The formazan that is produced in the cells was dissolved in 100µL dimethylsulfoxide (DMSO) and read at OD 560nm via Multiskan Ex plate reader (Thermo Fisher Scientific).

## Cell viability after LED irradiation (in vitro PDT)

The HeLa and B16F1 cells were seeded on two different 96-well plates and incubated for 24h at 37°C. Then the cells were incubated with 1mg/mL and 0.5mg/mL nano-assembly solutions for 24h. To activate the photosensitizers in the nano-assemblies the plates were irradiated with LED light (660 nm, power density 1.33 mW/cm<sup>2</sup>) for 15, 30 and 60min. The cells were incubated 24 more hours and to identify the cell viability 0.5mg/mL of MTT solution was added and the cells were incubated for 3h. The formazan that is produced in the cells were dissolved in 100µL dimethylsulfoxide (DMSO) and read at OD 560 nm via Multiskan Ex plate reader.

## Fluorescence microscopy

The HeLa and B16F1 cells were seeded in cover slip containing 12-well plates (10<sup>5</sup> cells/well) and incubated for 24h. Then, the cells were incubated with the nano-assemblies for 24h with 1 mg/mL concentration, then fixed with fresh paraformaldehyde (2% (w/v) in PBS) and rinsed three times with PBS solution. The cell nuclei was stained by 4',6-diamidino-2-phenylindole (DAPI; 0.1µg/mL). After 5 min incubation, the cells were rinsed with PBS solution three times. The cells were incubated for 1h with AlexaFluor488-conjugated concanavalin A (5µg/mL in PBS, Molecular Probes) to stain the cell membranes. After washing, the cover slips were placed on a slide using the Vectashield® mounting medium. The slides were imaged using a structured illumination AxioImager microscope equipped with an Apotome module (Zeiss, Germany, magnification40x).

## References

- (1) Lee, D.-E.; Koo, H.; Sun, I.-C.; Ryu, J. H.; Kim, K.; Kwon, I. C. *Chemical Society Reviews* **2012**, *41*, 2656.
- (2) Mulder, W. J. M.; Strijkers, G. J.; van Tilborg, G. A. F.; Cormode, D. P.; Fayad, Z. A.; Nicolay, K. *Accounts of Chemical Research* **2009**, *42*, 904.
- (3) Michel, B. W.; Lippert, A. R.; Chang, C. J. *J Am Chem Soc* **2012**, *134*, 15668.
- (4) Zhu, H.; Fan, J.; Li, M.; Cao, J.; Wang, J.; Peng, X. *Chemistry* **2014**, *20*, 4691.
- (5) Johnson, J. R.; Fu, N.; Arunkumar, E.; Leevy, W. M.; Gammon, S. T.; Piwnicka-Worms, D.; Smith, B. D. *Angew Chem Int Ed Engl* **2007**, *46*, 5528.
- (6) Valeur, B. In *Molecular Fluorescence*; Wiley-VCH Verlag GmbH: 2001, p 3.
- (7) Stockhofe, K.; Postema, J.; Schieferstein, H.; Ross, T. *Pharmaceuticals* **2014**, *7*, 392.
- (8) Kunjachan, S.; Ehling, J.; Storm, G.; Kiessling, F.; Lammers, T. *Chemical Reviews* **2015**, *115*, 10907.
- (9) Melancon, M. P.; Zhou, M.; Li, C. *Acc Chem Res* **2011**, *44*, 947.
- (10) Shi, D.; Bedford, N. M.; Cho, H.-S. *Small* **2011**, *7*, 2549.
- (11) Abdel-Kader, M. H., Ed.; Springer: Berlin :, 2014.

- (12) <http://www.dermnetnz.org/procedures/metvix-pdt.html>.
- (13) Andersson-Engels, S.; Klinteberg, C.; Svanberg, K.; Svanberg, S. *Physics in medicine and biology* **1997**, *42*, 815.
- (14) Lee, S.-C.; Zhai, D.; Mukherjee, P.; Chang, Y.-T. *Materials* **2013**, *6*, 1779.
- (15) Wu, D.; O'Shea, D. F. *Org Lett* **2013**, *15*, 3392.
- (16) Collado, D.; Vida, Y.; Najera, F.; Perez-Inestrosa, E. *RSC Advances* **2014**, *4*, 2306.
- (17) Tasiar, M.; O'Shea, D. F. *Bioconjugate Chemistry* **2010**, *21*, 1130.
- (18) Murtagh, J.; Frimannsson, D. O.; O'Shea, D. F. *Org Lett* **2009**, *11*, 5386.
- (19) McDonnell, S. O.; Hall, M. J.; Allen, L. T.; Byrne, A.; Gallagher, W. M.; O'Shea, D. F. *J Am Chem Soc* **2005**, *127*, 16360.
- (20) Zhang, X.-X.; Wang, Z.; Yue, X.; Ma, Y.; Kiesewetter, D. O.; Chen, X. *Molecular Pharmaceutics* **2013**, *10*, 1910.
- (21) Wu, D.; Cheung, S.; Devocelle, M.; Zhang, L.-J.; Chen, Z.-L.; O'Shea, D. F. *Chemical Communications* **2015**, *51*, 16667.
- (22) Mosmann, T. *Journal of Immunological Methods* **1983**, *65*, 55.
- (23) Berridge, M. V.; Tan, A. S. *Archives of biochemistry and biophysics* **1993**, *303*, 474.
- (24) Brown, M.; Wittwer, C. *Clinical Chemistry* **2000**, *46*, 1221.
- (25) Ibrahim, S. F.; van den Engh, G. In *Cell Separation: Fundamentals, Analytical and Preparative Methods*; Kumar, A., Galaev, I. Y., Mattiasson, B., Eds.; Springer Berlin Heidelberg: Berlin, Heidelberg, 2007, p 19.
- (26) Škrajnar, Š.; Lasnik, M. A.; Zavec, A. B. *Journal of the American Association for Laboratory Animal Science : JAALAS* **2009**, *48*, 152.
- (27) Gratton, S. E. A.; Ropp, P. A.; Pohlhaus, P. D.; Luft, J. C.; Madden, V. J.; Napier, M. E.; DeSimone, J. M. *Proceedings of the National Academy of Sciences* **2008**, *105*, 11613.
- (28) <http://www.bioinformin.net/cytometry.php>.
- (29) REJMAN, J.; OBERLE, V.; ZUHORN, I. S.; HOEKSTRA, D. *Biochemical Journal* **2004**, *377*, 159.
- (30) Chen, L.; Xiao, S.; Zhu, H.; Wang, L.; Liang, H. *Soft Matter* **2016**, *12*, 2632.
- (31) Garcia-Diaz, M.; Sanchez-Garcia, D.; Soriano, J.; Sagrista, M. L.; Mora, M.; Villanueva, A.; Stockert, J. C.; Canete, M.; Nonell, S. *MedChemComm* **2011**, *2*, 616.
- (32) Petri, A.; Kyriazi, M.; Alexandratou, E.; Rallis, M.; Gräfe, S.; Yova, D. 2009; Vol. 7373, p 7373II.

---

# CHAPTER 6

---

## GENERAL CONCLUSION AND PERSPECTIVE

*Abstract*

*In this final chapter, all the results are summarized and concluding remarks are indicated. Finally, the future perspectives of this project are discussed*



## 6.1 GENERAL CONCLUSION AND PERSPECTIVES

Photodynamic therapy (PDT) is a very promising noninvasive method which has emerged as one of the important therapeutic options in management of cancer and other diseases. The attractiveness of PDT comes mainly from its fundamental specificity and selectivity, since in theory only the tissues that are irradiated with light of an appropriate wavelength will be exposed to the toxic species, limiting therefore strongly side effects. However, the administration mode of the photosensitizer (PTS) is not yet optimal and often leads to a nonspecific accumulation of the PTS in normal tissues, inducing a general photosensitivity of the patient (especially the skin). To overcome this problem, the use of delivery carriers such as liposomes, polymer conjugates, polymer nanoparticles, or block copolymer micelles has been proposed. In the great majority of these cases, the PTS was not covalently bonded to its carrier which may still pose leakage problems. Therefore, in this project we developed polypeptide based model systems (self-assembled nanoparticles) where PTS is covalently bounded to the building blocks of the nano-assemblies to solve the existing problems in PDT and propose new clues for the development of new therapeutics for PDT with minimum toxicity and maximum efficacy.

Overall this thesis work consists of four steps. In the first step the building blocks were synthesized and characterized, in the second part optical and photophysical properties of the products and of the nano-assemblies were investigated, and in third part the self-assembly behavior of four different polypeptide based amphiphilic block copolymers was optimized. In the final step, we performed *in vitro* tests on two cancer cell lines (HeLa and B16F1) to investigate the dark toxicity of the nano-assemblies and their localization in the cell. In addition, cellular level PDT was performed to test the therapeutic efficiency and investigate the difference between them.

In the first part of the project (Chapter 2) building blocks: asymmetric aza-BODIPY, PBLG and PEG, were synthesized and modified. As photosensitizer an aza-BODIPY bearing the appropriate functional groups for its incorporation in the copolymer chains (carboxylic acid and azide) has been synthesized. These compounds are indeed known to be excellent photosensitizers for the generation of singlet oxygen, have very high molar extinction coefficients, are photostable, and have absorption and emission properties in the 650-750 nm range, i.e. directly in the near-infrared range. Two poly( $\gamma$ -benzyl-L-glutamate) (PBLG, DP ~50) with different appropriate chain-ends were synthesized by ring-opening N-carboxyanhydride (NCA) polymerization and coupled to the aza-BODIPY via a peptidic coupling reaction which was optimized to achieve the maximum functionalization. Moreover, commercially available PEGs were functionalized at the chain-end to introduce the desired reactive groups for Copper catalyzed azide-alkyne cycloaddition click reaction. In the final step of the synthetic part, copolymers presenting two types of structure were synthesized via a synthetic strategy involving orthogonal coupling reactions: copolymers bearing the photosensitizer at the end of the PBLG block (PTS-PBLG-*b*-PEG) and copolymers bearing the photosensitizer at the junction of PBLG and PEG blocks (PBLG-PTS-*b*-PEG). Polypeptide based copolymers have been selected in this project since they are particularly interesting for the construction of micelles and vesicles targeted for biological applications.

The second step of the project (Chapter 3) is focused on the self-assembly of PTS-PBLG-*b*-PEG/PBLG-PTS-*b*-PEG copolymers in aqueous solutions into several nano-assemblies. The PBLG block is hydrophobic and thus forms the insoluble compartment (core) of the nano-assemblies. The PEG is hydrophilic and forms the corona of the nano-assemblies. In addition

to the composition of the copolymers (PEG chain length), parameters such as ionic strength (self-assembly in PBS), solvent nature, concentration, flow rate, stirring speed... were varied to obtain well-defined nano-assemblies of controlled size. Sizes of a few tens of nanometers (20-200) were targeted in order to benefit from passive targeting to tumors thanks to the enhanced permeability and retention (EPR) effect. All nano-assemblies were prepared by nano-precipitation technique by fixing the flow rate, stirring speed and concentration. This technique allowed us to easily control the formation of the nano-assemblies. After optimization of the self-assembly behaviors of four different PTS functionalized block copolymers (PTS-PBLG<sub>49</sub>-*b*-PEG<sub>45</sub>, PTS-PBLG<sub>49</sub>-*b*-PEG<sub>45</sub>, PBLG<sub>53</sub>-PTS-*b*-PEG<sub>45</sub>, PBLG<sub>53</sub>-PTS-*b*-PEG<sub>113</sub>), they were co-assembled with non-functionalized block copolymers of the same composition (PBLG<sub>54</sub>-*b*-PEG<sub>45</sub>, PBLG<sub>54</sub>-*b*-PEG<sub>113</sub>) in order to dilute the concentration of PTS in the nano-assemblies. Moreover, the physicochemical stability of the nano-assemblies in a simulated biological environment (10% serum in Milli-Q water) was tested, and no aggregate formation was observed. The obtained nano-assemblies were characterized by dynamic light scattering (DLS) and transmission electron microscopy (TEM) via RuO<sub>4</sub>, I<sub>2</sub> and ammonium molybdate staining.

Chapter 4 was dedicated to the optical and photophysical characterization (molar extinction coefficient, fluorescence quantum yield, efficiency of singlet oxygen generation, fluorescence lifetime...) of PTS, PTS-PBLG conjugates, and PTS functionalized nano-assemblies. These characterizations confirmed that brominated **24** is suitable to be used in NIR imaging and as photosensitizer (PTS) for biomedical application. The brominated and non-brominated aza-BODIPYs exhibited a high extinction coefficient of 71702 and 83900M<sup>-1</sup>.cm<sup>-1</sup> in THF, respectively. Although the fluorescence quantum yield dropped from 0.36 to 0.08 after the addition of two bromine groups to the aza-BODIPY core on the 2,6-positions, its singlet oxygen generation yield increased to 0.66. Weak fluorescence property will allow the detection of fluorescence signals from the tissues or from the skin and perform PDT selectively. We observed minor changes in optical and photophysical properties of PTS after conjugating the polymer chains. However, in water it showed different characteristics due to the localization, morphology and concentration effects. In the nano-assemblies, the aza-BODIPY is located in the core of the nano-assemblies if end-functionalized copolymers are used, or at the core/corona interface if copolymers bearing the aza-BODIPY at the junction of the two blocks are used. In particular, the influence of the localization of the aza-BODIPY in the nano-assemblies and dilution effects (with non-functionalized copolymer) on the photophysical properties of the aza-BODIPY were investigated by spectroscopic techniques. This difference in localization and morphology indeed had an impact on the singlet oxygen generation and fluorescence quantum yield, considering the difference in the environments and in oxygen concentration. The singlet oxygen generation quantum yield calculations showed that micelles exhibit higher yield compared to vesicle structure. Moreover, the PTS dilution, by co-assembling the functionalized copolymers with non-functionalized ones, increases the activity of PTS in terms of <sup>1</sup>O<sub>2</sub> generation. In addition, nano-assemblies prepared from PBLG<sub>53</sub>-PTS-*b*-PEG<sub>45</sub> showed less activity compared to PTS-PBLG<sub>49</sub>-*b*-PEG<sub>45</sub> nano-assemblies, probably due to the increased interaction with water molecules.

The obtained four different multifunctional nano-assemblies have been tested in preliminary *in vitro* experiments; uptake by human epithelial adenocarcinoma cell line HeLa and skin cancer cell line B16F1, cytotoxicity measurements, and therapeutic efficiency. Time and concentration dependent cellular uptake of the nano-assemblies were quantified by flow cytometry where the nano-assemblies PTS-PBLG<sub>49</sub>-*b*-PEG<sub>113</sub> (**NAb 2**) and PBLG<sub>53</sub>-PTS-*b*-PEG<sub>113</sub> (**NAb 4**) showed faster internalization compared to PTS-PBLG<sub>49</sub>-*b*-PEG<sub>45</sub> (**NAb 1**) and PBLG<sub>53</sub>-PTS-*b*-PEG<sub>45</sub> (**NAb 3**) nano-assemblies. They showed the maximum uptake at 1mg/mL concentration after

24h incubation time. As mentioned in Chapter 5, morphological difference of NAb 1 and NAb2 compared to micelles are the main reason of the slow internalization since all nano-assemblies have the similar size ( $R_h \sim 100\text{nm}$ ). The dark toxicity of the nano-assemblies was quantified by MTT cell proliferation assay tests at different concentration. A small dark toxicity at high concentration ( $1\text{mg/mL}$ ) of nano-assemblies was observed. Moreover, this test was repeated after performing *in vitro* PDT to determine the potential therapeutic efficacy of the nano-assemblies after photoactivation. Indeed, we did observed a difference in activity due to the localization of the photosensitizer in 15 and 30 min irradiation ( $1.2\text{ J/cm}^2$  and  $2.4\text{ J/cm}^2$  light dose). The higher cell death percentage was observed on the PBLG<sub>53</sub>-PTS-*b*-PEG<sub>113</sub> and PBLG<sub>53</sub>-PTS-*b*-PEG<sub>45</sub> nano-assemblies where PTS is localized at the interface. Among the two nano-assemblies which have PTS at the interface, PBLG<sub>53</sub>-PTS-*b*-PEG<sub>45</sub> nano-assemblies caused 100% apoptosis of both cell lines even at low concentration ( $0.125\text{mg/mL}$ ) of nano-assembly (PTS concentration in the nano-assembly is  $3\mu\text{g/mL}$ ,  $15\text{pM}$ ) for 15min ( $1.2\text{ J/cm}^2$  light dose) irradiation time. In addition, after 1h LED irradiation time all nano-assemblies have also showed a high toxicity at  $1\text{mg/mL}$ .

To sum up, in this study we developed four different polypeptide based model nanoparticles that can open a new door for the development of a new generation of therapeutics to improve the limitations existing in current clinical PDT agents. These nano-assemblies offer a control on size distribution, morphology, PTS concentration and localization. By covalently linking the photosensitizer to amphiphilic block copolymers in different order we can quantitatively control the concentration in the nano-assemblies, control the PTS localization and protect it in the hydrophobic polymer matrix from degradation in different biological microenvironments before reaching the cancer site. Moreover, by changing the localization and PEG chain length in the block copolymers, we revealed that PTS shows more biological activity under LED activation when it is located at the interface of the nano-assemblies and even better efficacy with shorter PEG chain corona. This strategy also allows the increase of the therapeutic efficacy by using very small quantities of photosensitizer. Having higher efficacy at lower concentration is also of great importance in pharmaceutical industry to reduce both the possible side-effects and the cost of currently existing, highly expensive anticancer therapeutics.

As a perspective of this project, therapeutic activity of the nano-assemblies needs to be investigated *in vivo* to monitor the targeting property and investigate pharmacokinetic/pharmacodynamics profile. Moreover, the self-assembly behavior of block copolymers with shorter polypeptide chains also need to be investigated. Shortening of the hydrophobic block can increase the water solubility of the block copolymers which can help to get rid of the use of toxic organic solvents (THF, DMSO) during the self-assembly process. THF could be replaces with small quantity of EtOH to better solubilize the block copolymer or even organic solvent free self-assembly could be achieved. This will help to discard the time consuming dialysis step. Easy preparation is also important for manufacturing the therapeutics and to increase their processability for clinical applications.

Contrast agent for MRI (magnetic resonance imaging), superparamagnetic iron nanoparticles, could also be embedded in the micelles and vesicles to have multimodal imaging for better diagnosis purposes. This could be done during the copolymer self-assembly step. Nanoparticles of  $\gamma\text{-Fe}_2\text{O}_3$  (maghemite)<sup>1</sup> could be used since they are nontoxic, they show no remanent magnetization due to their superparamagnetic behavior, and well established preparation protocols exist allowing the control of their size and coating (hydrophilic or hydrophobic).<sup>2,3</sup> In the case of micelles, the nanoparticles can be located in the core, and in the case of vesicles in the membrane or in the internal compartment. In this way, nano-assemblies being able to act



both as probes for multimodal imaging (MRI and fluorescence) and as therapeutic agents could be obtained. This last point will come mainly from PDT, but the embedded iron oxide nanoparticles can also allow the use of the hyperthermia effect to further weaken resistant cancer cells.

To achieve active targeting property, nano-assemblies could be functionalized with cancer specific receptors and anticancer drug molecules (i.e., doxorubicin, epirubicin, etc.) could be loaded to achieve multiple therapy. Potentially, PEG also could be replaced with hyaluronan as hydrophilic segment, as this oligosaccharide presents not only a stealth behavior, but also some targeting properties regarding CD44 glycoproteins that are overexpressed in cancer cells.<sup>4</sup> Moreover, to have a selective targeting, PEG chains could be functionalized with RGD peptide which has a specific binding property to receptors ( $\alpha_v\beta_3$  integrin heterodimeric cell surface receptors) that are overexpressed in tumor cells.

## References

- (1) a) C. Sanson, O. Diou, J. Thevenot, E. Ibarboure, A. Soum, A. Brulet, S. Miraux, E. Thiaudière, S. Tan, A. Brisson, V. Dupuis, O. Sandre, S. Lecommandoux, *ACS Nano* **2011**, 5, 1122; b) S. Lecommandoux, O. Sandre, F. Chécot, J. Rodriguez-Hernandez, R. Perzynski, *Adv. Mater.* **2005**, 17, 712.
- (2) D. Yoo, J.H. Lee, T.H. Shin, J. Cheon, *Acc. Chem. Res.* **2011**, 44, 863.
- (3) C.S.S.R. Kumar, F. Mohammad, *Adv. Drug Deliv. Rev.* **2011**, 63, 789.
- (4) a) K.K. Upadhyaya, A.N Bhatt, A.K Mishra, B.S. Dwarakanath, S. Jain, C. Schatz, J.F. Le Meins, A. Farooque, G. Chandraiah, A.K Jain, A. Misrac, S. Lecommandoux, *Biomaterials* **2010** 31, 3882; b) K.K. Upadhyay, A.K. Mishra, K. Chuttani, A. Kaul, C. Schatz, J.F. Le Meins, A. Misra, S. Lecommandoux, *Nanomedicine: Nanotechnology, Biology and Medicine* **2012**, 8, 71.

### Publications

B. Baykal, **V. Ibrahimova**, G. Er, E. Bengu and D. Tuncel, Dispersion of multi-walled carbon nanotubes in an aqueous medium by water-dispersible conjugated polymer nanoparticles, *Chemical Communications* **2010**, 46, 6762

E.-J. Park, T. Erdem, **V. Ibrahimova**, S. Nizamoglu, H. V. Demir, and D. Tuncel, White-Emitting Conjugated Polymer Nanoparticles with Cross-Linked Shell for Mechanical Stability and Controllable Photometric Properties in Color-Conversion LED Applications, *ACS NANO*, **2011**, 5(4), 2483

**V. Ibrahimova**, S. Ekiz, O. Gezici and D. Tuncel, Facile synthesis of cross-linked patchy fluorescent conjugated polymer nanoparticles by click reactions, *Polymer Chemistry* **2011**, 2, 2818

**V. Ibrahimova**, M. E. Kocak, A. M. Onal, D. Tuncel, Optical and Electronic Properties of Fluorene-Based Copolymers and Their Sensory Applications, *PART A: Polymer Chemistry* **2013**, 51(4), 815

T. Erdem, **V. Ibrahimova**, D.-W. Jeon, I.-H. Lee, D. Tuncel, H. V. Demir, Morphology-Dependent Energy Transfer of Polyfluorene Nanoparticles Decorating InGaN/GaN Quantum-Well Nanopillars, *The Journal of Physical Chemistry C* **2013**, 117(36), 18613

B. Guzelturk, P. L. Hernandez Martinez, V. K. Sharma, Y. Coskun, **V. Ibrahimova**, D. Tuncel, A. O. Govorov, X. Sun, Q. Xiong, H. V. Demir, Study of Exciton Transfer in Dense Quantum Dot Nanocomposites, *Nanoscale* **2014**, 6(19), 11387

### Poster and oral communications

V. Ibrahimova, D. Tuncel, 3rd EuCheMS Chemistry Congress, poster presentation, August 29-September 2 2010, Nurnberg, Germany.

V. Ibrahimova, D. Tuncel, S.C.A.N. 2010 synthesis, characterization and applications of nanomaterials Workshop and School, poster presentation, Bilkent University, September 30-October 6 2010, Ankara, Turkey.

V. Ibrahimova, D. Tuncel, Summer School Cellular Systems, Oral Presentation, Heidelberg University, 24-30 August 2011, Heidelberg, Germany.

V. Ibrahimova, D. Tuncel, 7<sup>th</sup> Nanoscience and Nanotechnology Conference, Oral Presentation, Sabanci University, June 27- July 1 2011, Istanbul, Turkey.

V. Ibrahimova, S. Lecommandoux and C.-A. Fustin, International Doctoral School in Functional Materials for Energy, Informational Technology and Health, Third Training School, Oral Presentation, 17-22 March 2013, Annecy, France.

V. Ibrahimova, S. Lecommandoux and C.-A. Fustin International Doctoral School in Functional Materials for Energy, Informational Technology and Health, Forth Training School, Oral and Poster Presentation, 16-21 March 2014, Spa, Belgium.

V. Ibrahimova, S. Lecommandoux, and C.-A. Fustin, PhD Students' day 2014, Poster presentation, 17 July 2014, Louvain-la-Neuve, Belgium

V. Ibrahimova, N. D. McClenaghan, S. Lecommandoux, and C.-A. Fustin, BPG ANNUAL MEETING 2014, Poster presentation, 19-20 May 2014, Ghent, Belgium

V. Ibrahimova, N. D. McClenaghan, S. Lecommandoux, and C.-A. Fustin, International Doctoral School in Functional Materials for Energy, Informational Technology and Health, Fifth Training School, Oral and Poster Presentation, 15-20 March 2015, Vallendar, Germany.

V. Ibrahimova, N. D. McClenaghan, S. Lecommandoux, and C.-A. Fustin, Supramolecular Photochemistry Faraday Discussion, Poster presentation, Downing College, 15-17 September 2015, Cambridge, United Kingdom

V. Ibrahimova, N. D. McClenaghan, S. Lecommandoux, and C.-A. Fustin, PhD Students' day 2016, Oral presentation, 20 May 2016, Louvain-la-Neuve, Belgium

V. Ibrahimova, N. D. McClenaghan, S. Lecommandoux, and C.-A. Fustin, Annual Meeting of the Belgian Polymer Group BPG, Oral presentation, 23-24 May 2016, Hasselt, Belgium

V. Ibrahimova, N. D. McClenaghan, S. Lecommandoux, and C.-A. Fustin, MACRO2016, Oral presentation, 18-20 July 2016, Istanbul, Turkey

## TITRE : Développement de Nano-Structures Multifonctionnelles à Base de Polypeptide pour une Approche Théranostique

**Résumé :** Dans ce travail, nous avons développé des nanostructures théranostics à base de polypeptides fonctionnalisées avec un photosensibilisateur (PTS) dans le but d'être utilisées en thérapie photodynamique (PDT). La génération d'oxygène singulet et les propriétés de fluorescence du PTS peuvent ainsi à la fois diagnostiquer et traiter une tumeur.

Un dérivé asymétrique et multifonctionnel de l'aza-dipyrrrométhènes difluorure de bore chélate (aza-BODIPY) fluorogène a été synthétisé pour être utilisé comme photosensibilisateur en raison de ses propriétés non toxiques, son insensibilité à l'environnement biologique externe, sa production d'oxygène singulet élevée et son important rendement quantique de fluorescence. Pour permettre au photosensibilisant d'atteindre la tumeur, quatre copolymères à blocs amphiphiles différents en termes de localisation du PTS et de la longueur de la chaîne PEG ont été synthétisés. Les blocs amphiphiles sont constitués de segments poly( $\gamma$ -benzyl-L-glutamate) (PBLG, DP ~ 50) et poly(éthylène glycol) (PEG, DP = 45 et 113). Ces copolymères sont en outre capables de s'auto-assembler en micelles et en vésicules. Nous avons développé une stratégie de synthèse permettant la liaison covalente du PTS pour les copolymères à blocs amphiphiles, empêchant ainsi une fuite du PTS avant que les nanoparticules atteignent le site de la tumeur. En outre, nous avons étudié l'activité du PTS en fonction de la concentration, de la morphologie des nanoparticules et de la localisation du PTS dans les nanoparticules. Enfin, l'efficacité des nanoparticules a été évaluée *in vitro* sur des cellules HeLa et B16F1.

**Mots-clés:** nanoparticules polymériques, des polypeptides, amphiphile copolymère bloc d'auto-assemblage, photosensibilisateurs, aza-BODIPY, thérapie photodynamique

Laboratoire de Chimie des Polymères  
Organiques (LCPO)  
16 avenue Pey Berland  
F-33607 Pessac  
France



Institute of Condensed Matter and  
Nanosciences (IMCN)  
Bio and soft matter division (BSMA)  
Place Louis Pasteur 1  
1348 Louvain-la-Neuve  
Belgium

